

Spin wave excitations in magnetic helices and skyrmion lattices

Dissertation
Johannes Waizner



Spin wave excitations in magnetic helices and skyrmion lattices

Inaugural-Dissertation

zur

Erlangung des Doktorgrades

der Mathematisch-Naturwissenschaftlichen Fakultät

der Universität zu Köln

vorgelegt von

Johannes Waizner

aus Köln



Köln 2017

Berichterstatter:
(Gutachter)

PD Dr. Markus Garst
Prof. Dr. Achim Rosch

Tag der mündlichen Prüfung: 16.1.2017

ABSTRACT

Chiral magnets are materials that lack inversion symmetry in their crystal structure and contain a number of different magnetic phases. In this thesis we focus on cubic crystals. Besides a field-polarized phase for strong applied magnetic fields and a paramagnetic phase above a critical temperature, there are the more interesting helical and conical phases as well as, most prominently, a trigonal lattice of topologically stable magnetic whirls, so-called skyrmions. Their recent discovery in MnSi has sparked a great interest in them, largely because of their topological nature and the prospects of novel applications, for instance in future magnetic storage devices. The last three mentioned phases are spin textures due to the Dzyaloshinskii-Moriya spin-orbit interaction which is induced by the aforementioned lack of inversion symmetry. We theoretically study spin wave excitations with a focus on these phases, which are essential to understand for dynamic applications.

Part I is an introductory chapter to chiral magnets, their phases, and their static properties. The skyrmions deserve special attention as they are the most complex phase and necessitate the introduction of concepts from topology. We conclude this overview by a theoretical description of chiral magnets in terms of a Ginzburg-Landau theory. To study the dynamics, we work in a mean-field limit with added Gaussian fluctuations. The latter are also necessary to stabilize the skyrmion lattice phase with respect to the conical phase.

In **part II** we introduce and prepare expressions and concepts relevant for the study of spin waves. The first two sections cover their fundamental origin and two experimental methods, namely microwave excitation with coplanar waveguides and inelastic neutron scattering. Collaborators employed those two methods to measure spin waves in various chiral magnets. Their data are also presented in the course of this thesis and compared to theory.

Part III addresses spin waves in the helical/conical phase, so-called helimagnons, and first focuses on homogeneous spin waves at the Γ -point of the one dimensional magnetic Brillouin zone. We find two modes whose resonance frequencies are decisively influenced by dipole-dipole interaction. They are, in particular, degenerate without it. An astonishing effect is their perfectly linear polarization at zero field. This can be used to excite the two modes individually. Their resonance frequencies can also be calculated analytically for which we employed a non-linear σ model, opposed to the Ginzburg-Landau model for numerical calculations. The

latter is then used to calculate the helimagnon spectrum in the remainder of the Brillouin zone. We also calculate spectral weights in correspondence with neutron scattering experiments. In the longitudinal spectrum we find three branches whose detection depends on the ability to detect spin-flip and non-spin-flip scattering.

The structure of [part IV](#) resembles the previous one but covers magnons in the skyrmion lattice. At the Γ -point there are two gyration and a breathing mode. The spectrum with finite momentum exhibits a plethora of modes. The weight distribution for neutron scattering spreads over all of them in a way, that on average resembles the three helimagnon branches. Finally, we calculate topological invariants called Chern numbers with good confidence for the lowest 14 bands. Four of them have Chern number zero, the remaining ones have Chern number one.

———— KURZZUSAMMENFASSUNG ————

Chirale Magnete sind Materialien ohne Inversionssymmetrie in ihrer Kristallstruktur, die aufgrund dessen eine Vielzahl von unterschiedlichen, magnetischen Phasen aufweisen. In dieser Arbeit stehen chirale Magnete mit kubischer Kristallstruktur im Vordergrund. Neben einer feldpolarisierten Phase bei starken angelegten Magnetfeldern und einer paramagnetischen Phase oberhalb einer kritischen Temperatur, gibt es die interessanteren helischen und konischen Phasen, sowie die wohl prominenteste Phase, nämlich die sogenannte Skymionphase. Skymionen sind in einem Dreiecksgitter angeordnete, topologisch stabile, magnetische Wirbel. Ihre kürzliche Entdeckung in MnSi erzeugte großes Interesse, besonders wegen ihrer topologischen Natur und die dadurch erhoffte Aussicht auf neuartige Anwendungen, beispielsweise in zukünftigen, magnetischen Datenträgern. Die letzten drei genannten Phasen sind Spinstrukturen, die durch die auf Spin-Bahn-Kopplung basierende Dzyaloshinskii-Moriya Wechselwirkung bedingt sind. Letztere ist wiederum durch die fehlende Inversionssymmetrie induziert ist. Wir untersuchen theoretisch die Spinwellenanregungen in diesen Phasen, deren Verständnis unabdingbar für dynamische Anwendungen ist.

Part I ist eine Einführung über chirale Magnete, ihre Phasen und statischen Eigenschaften. Die Skymionen bedürfen besonderer Aufmerksamkeit, da sie die komplexeste Phase ausmachen für die Konzepte der Topologie von Bedeutung ist. Wir schließen diese Übersicht mit der theoretischen Beschreibung chiraler Magnete mithilfe einer Ginzburg-Landau Theorie ab. Die Dynamik untersuchen wir basierend auf einer Molekularfeldtheorie mit zusätzlichen Gaußschen Fluktuationen. Letztere sind außerdem notwendig um das Skymion-Gitter im Vergleich zur konischen Phase zu stabilisieren.

In **Part II** bereiten wir Ausdrücke und Konzepte vor, die relevant für das Studium von Spinwellen sind. Die ersten zwei Sektionen behandeln ihren fundamentalen Ursprung und stellen zwei experimentelle Methoden vor, nämlich Mikrowellenanregungen mit ko-planaren Wellenleitern, und inelastische Neutronenstreuung. Kollegen aus der Experimentalphysik benutzten diese zwei Methoden um Spinwellen in verschiedenen, chiralen Magneten zu messen. Ihre Daten werden auch im Rahmen dieser Arbeit vorgestellt und mit der Theorie verglichen.

Part III behandelt Spinwellen in der helischen und konischen Phase, sogenannte Helimagnonen, und konzentriert sich zuerst auf homogene Spinwellen am Γ -Punkt der hier eindimensionalen, magnetischen Brillouin-Zone. Wir finden zwei Moden,

deren Resonanzfrequenzen bestimmend durch die Dipol-Dipol-Wechselwirkung beeinflusst werden. Ohne sie sind die beiden Moden entartet. Ein erstaunlicher Effekt ist ihre perfekte, lineare Polarisation im Nullfeld. Dieser kann ausgenutzt werden um die Moden unabhängig voneinander anzuregen. Ihre Resonanzfrequenzen können analytisch bestimmt werden, wofür wir ein nichtlineares σ -Modell, im Gegensatz zu dem Ginzburg-Landau-Modell für numerische Rechnungen, anwenden. Letzteres benutzen wir um das Helimagnonspektrum im restlichen Bereich der Brillouin-Zone zu berechnen. Außerdem berechnen wir spektrale Gewichte, die Ergebnissen inelastischer Neutronenstreuung entsprechen. Im longitudinalen Spektrum gibt es drei Zweige deren Detektion von der Einstellung abhängt Spin-Flip- und nicht-Spin-Flip-Streuung zu messen.

Part IV ähnelt strukturell dem vorherigen, behandelt jedoch Magnonen im Skyrmion-Gitter. Am Γ -Punkt finden sich zwei rotierende und eine atmende Mode, während das Spektrum bei endlichem Impuls eine Unmenge an Moden aufweist. Die Gewichtsverteilung der inelastischen Neutronenstreuung verteilt sich über ihnen in einer Art und Weise die gemittelt den drei Zweigen des Helimagnonspektrums ähnelt. Abschließend berechnen wir topologische Invarianten, genannt Chern Zahlen, für die 14 tiefsten Bänder. Vier von ihnen haben den Wert Null, die anderen Chern Zahlen den Wert eins.

PUBLICATIONS

PUBLISHED

- T. SCHWARZE, J. WAIZNER, M. GARST, A. BAUER, I. STASINOPOULOS, H. BERGER, C. PFLEIDERER, AND D. GRUNDLER
 “Universal helimagnon and skyrmion excitations in metallic, semiconducting and insulating chiral magnets”
Nature Materials **14**, 478-483 (2015)
- M. KUGLER, G. BRANDL, J. WAIZNER, M. JANOSCHEK, R. GEORGII, A. BAUER, K. SEEMANN, A. ROSCH, C. PFLEIDERER, P. BÖNI, AND M. GARST
 “Band Structure of Helimagnons in MnSi Resolved by Inelastic Neutron Scattering”
Physical Review Letters **115**, 097203 (2015)
- S. ZHANG, I. STASINOPOULOS, T. LANCASTER, F. XIAO, A. BAUER, F. RUCKER, A. BAKER, A. FIGUEROA, Z. SALMAN, F. PRATT, S. BLUNDELL, T. PROKSCHA, A. SUTER, J. WAIZNER, M. GARST, D. GRUNDLER, G. VAN DER LAAN, C. PFLEIDERER, AND T. HESJEDAL
 “Room-temperature helimagnetism in FeGe thin films”
Scientific Reports **7**(1), 123 (2017)
- M. GARST, J. WAIZNER AND D. GRUNDLER
 “Topical Review: Collective spin excitations of helices and magnetic skyrmions: review and perspectives of magnonics in non-centrosymmetric magnets”
Journal of Physics D: Applied Physics **50**, 29 (2017)
- I. STASINOPOULOS, S. WEICHELBAUMER, A. BAUER, J. WAIZNER, H. BERGER, S. MAENDL, M. GARST, C. PFLEIDERER, AND D. GRUNDLER
 “Low spin wave damping in the insulating chiral magnet Cu_2OSeO_3 ”
Applied Physics Letters **111**, 032408 (2017)
- I. STASINOPOULOS, S. WEICHELBAUMER, A. BAUER, J. WAIZNER, H. BERGER, M. GARST, C. PFLEIDERER, AND D. GRUNDLER
 “Linearly polarized GHz magnetization dynamics of spin helix modes in the ferromagnetic insulator Cu_2OSeO_3 ”
Scientific Reports **7**, 7037 (2017)

SUBMITTED

- T. WEBER, J. WAIZNER, R. GEORGII, G. TUCKER, M. KUGLER, A. BAUER, M. GARST, P. BÖNI
 “Field-dependence of the helimagnon dispersion in the chiral magnet MnSi”
Physical Review B

CONTENTS

GENERAL INTRODUCTION	1
I. CHIRAL MAGNETS	3
1. INTRODUCTION	5
1.1. Definition of Chirality	5
1.2. Typical Magnetic Phases	7
1.3. Materials & Properties	8
2. SKYRMIONS	15
2.1. Historical Origin	15
2.2. Topological Aspects of Skyrmions	17
2.3. Experimental Realization and Application	21
3. THEORETICAL DESCRIPTION	23
3.1. Conventions	23
3.2. Ginzburg-Landau Theory	25
3.3. Dipolar Interactions	27
3.4. Crystal Anisotropies	31
3.5. Free Energy of Chiral Magnets	34
3.6. Mean-Field Analysis & Fluctuations	35
II. BASIC ASPECTS OF SPIN WAVES	39
4. INTRODUCTION TO SPIN WAVES	41
4.1. Precession	42
4.2. Ferromagnetic Resonance	44
4.3. Ellipticity	50
4.4. Types of Spin Waves	51
4.5. Damon Eshbach Physics	54
5. EXPERIMENTAL METHODS	57
5.1. Coplanar Waveguides	57

Contents

5.2. Neutron Scattering	58
6. LINEAR RESPONSE DYNAMICS	63
6.1. Derivation of Resonance Frequencies	63
6.2. Formulation in Momentum Space	64
6.3. Spectral Weights	70
III. HELIMAGNONS	77
7. RESONANCE AT THE Γ -POINT	79
7.1. Excitation Modes	79
7.2. Ellipticity & Magnetic Linear Dichroism	83
8. NON-LINEAR σ MODEL	89
8.1. Mean-Field and Parameterization	90
8.2. Fluctuations	91
8.3. Eigenmodes	95
8.4. Uniform Chiral Magnetic Resonances	96
9. FINITE MOMENTUM SPIN WAVES	99
9.1. Analysis via the Non-Linear σ Model	99
9.2. Extended Analysis with Numerical Input	101
9.3. Resonances Close to H_{c2}	106
10. COMPARISON TO EXPERIMENTS	109
10.1. Ferromagnetic Resonances	109
10.2. Neutron Scattering	110
IV. MAGNONS IN THE SKYRMION LATTICE	115
11. RESONANCES AT THE Γ -POINT	117
11.1. Excitation Modes	117
11.2. Ellipticity and Weight Distribution	120
12. SPECTRUM	123
12.1. Spectrum within the 1. Brillion Zone	123
12.2. Spectrum beyond the 1. Brillion Zone	130
12.3. \mathbf{k} perpendicular to the 1. Brillion Zone	134
12.4. Weights for Neutron Scattering	136
13. CHERN NUMBERS	141
13.1. Definition and Means of Calculation	142
13.2. Results	146

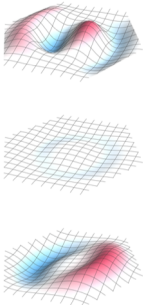
14. CONCLUSIONS AND OUTLOOK	153
V. APPENDIX	157
A. DERIVATION OF DIPOLE-DIPOLE INTERACTION	159
B. GROUND STATE ON MEAN-FIELD LEVEL	163
C. COMPLEX RESONANCES IN THE FERROMAGNET	167
D. AUXILIARY CALCULATIONS IN THE NON-LINEAR σ MODEL	171
D.1. Derivation of Equation (8.7)	171
D.2. Identities for Chiral Basis Vectors	172
D.3. \mathcal{F}_{ex} Expansion to 4 th Order	173
D.4. Fourier Transformation of $\hat{n}(r)$	177
D.5. Quadratic order of \mathcal{S}_{dip} in π	178
BIBLIOGRAPHY	187
LIST OF FIGURES	199
LIST OF TABLES	201
INDEX	203
DANKSAGUNG	205

GENERAL INTRODUCTION

All around us in everyday life ranging from staircases to flower patterns, shapes of animals and more, one encounters a sense of handedness or chirality. It is the fundamental property responsible for all the fascinating effects that we will explore in this thesis and they are not only present at macroscopic but also microscopic length scales and occur in materials and places which may not be that obvious. In the following parts and chapters we will explore a category of such materials, namely cubic chiral magnets, or helimagnets, and study their spin wave excitations.

Arguably the most prominent chiral magnet is manganese silicide, MnSi, which has been intensively studied since the 60's. At that time MnSi was still considered mainly a ferromagnet [1, 2] while the helimagnetic behavior was discovered later in 70's [3, 4]. In the helimagnetic phase, the magnetization forms an arrangement of screws that either align with certain crystal directions when applied external magnetic fields are low (helical phase), or align with the field direction for higher fields (conical phase). Eventually, for increasing field strength, there is a 2nd order phase transition into a field polarized phase. First experiments to probe spin waves have also been performed during that time using neutron scattering [5] covering the extent of the nuclear Brillouin zone. MnSi was still full of surprises like the non-Fermi liquid behavior at high pressures [6], which drove further studies. The most relevant discovery to our studies, was the discovery of a lattice of topologically stable, magnetic whirls, so-called skyrmions, in 2009 [7]. The description of their topological structure goes back to a proposal of nuclear physicist Tony H. R. Skyrme in the late 50's to think of neutrons and protons as non-linear excitations of pion fields [8]. While he used a three dimensional field description in his work, the corresponding structure in MnSi, or as we now know many other materials as well, is two dimensional and therefore sometimes called a "baby-skyrmion". Such a description was proposed by Bogdanov and Yablonskii in 1989 [9].

After said discovery the community studying skyrmion hosting materials, like the bulk chiral magnets we consider in this thesis, grew substantially. This was not least because of the prospect of novel applications in future magnetic storage devices like racetrack memory as suggested by Stuart Parkin et al. [10]. A big advantage of skyrmions is their comparably very low threshold current density of the order of $j \sim 10^6 \text{ A/m}^2$ above which the skyrmion lattice texture gets



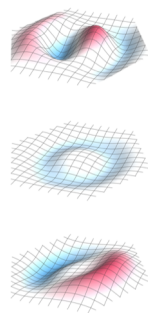
unpinned from disorder. This is ultra-low compared to a current density of around $j \sim 10^{11}$ A/m² needed to move ordinary domain walls, which is used in current devices [11].

Equally important to information storage in information technology is the ability to carry information. This is where spin waves or magnons have gained increased attention [12]. Magnons usually refer to the particle-like spin excitation in a magnetic material while the wave-like part is referred to as spin waves. Spin waves offer the possibility to transmit and process information without moving electrical charge carriers which can lead to unwanted heating effects. Magnonic devices also offer an integration with microwave electronics. A big advantage is that the wavelength of spin waves corresponds to the practically relevant frequencies within the GHz to THz range. This offers prospects for miniaturization [13]. Before one is able to build devices that can exploit such benefits, detailed fundamental research is a prerequisite, which is the objective of this thesis.

After giving more detailed introductions to helimagnets, their magnetically ordered phases and basic aspects of spin waves in [parts I](#) and [II](#), we will discuss in detail the spin wave modes and spectra in chiral magnets. In [part III](#) we will focus on spectra in the helical and conical phases while the focus in [part IV](#) is on spin waves in the skyrmion lattice phase. Unique to [part III](#) is an analytical calculation based on a non-linear σ model which yields an exact formula for uniform spin wave resonances including dipolar interactions. Additionally, we also get good analytical approximations for the helimagnon spectrum for momenta longitudinal and perpendicular to the helix pitch. The non-trivial topological nature of skyrmions motivates us in [part IV](#) to also address and calculate topological invariants, called Chern numbers, of the magnon bands in the skyrmion phase.

PART I.

CHIRAL MAGNETS



1

INTRODUCTION

1.1. DEFINITION OF CHIRALITY

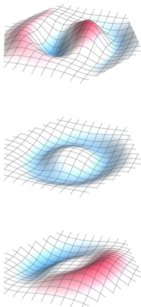
The word *chirality* is derived from the Greek word $\chiείρ$ (Kheir) which means *hand*. It is a property of asymmetry and, like a hand, a chiral object is non-superposable on its mirror image [14]. After creating the mirrored image of such an object, it is hence not possible to map it onto the original image just by rotations and translations alone. Ultimately, there is a right and left sense of handedness like that of right and left feet depicted in [figure 1.1](#). Rotating and translating one of the feet will never generate the other.

Chiral objects occur in several branches of science like Biology and Chemistry in the form of chiral molecules, but also in many parts of Physics ranging from left and right handed quarks in Particle Physics to chiral magnets which are the center of attention in this thesis. The latter are, as the name suggests, magnets that possess a certain sense of chirality or handedness intrinsic to the atomic lattice structure. It is achieved by having neither mirror nor inversion symmetry. Examples of such materials are the metal MnSi [16] and the insulator Cu₂OSeO₃ [17]. In [section 1.3](#) we elaborate more on these and on more materials and their properties.



Figure 1.1: Left and right feet as examples of chiral objects. The image shows a logo of a famous band of Cologne called *De Bläck Fööss* which translates to *The Naked Feet* [15].

In the model description of chiral magnets, an interaction term in the free energy, called Dzyaloshinskii-Moriya interaction, is responsible for the occurrence of chirality. Ordinary (anti-)ferromagnets on the other hand are non-chiral and well described by the exchange interaction between spins [18]. Exchange interaction is



1. Introduction

well modeled by the Heisenberg model¹ in which the exchange Hamiltonian for spins \mathbf{S} on a lattice is given by

$$\mathcal{H}_{\text{Heisenberg}} = - \sum_{i,j} \mathcal{J}_{ij} \mathbf{S}_i \cdot \mathbf{S}_j, \quad (1.1)$$

summing over lattice sites i and j . The exchange integral \mathcal{J}_{ij} is a measure for the strength of the interaction. In many models, it is sufficient to only consider interaction between neighboring sites which is usually denoted by $\langle i, j \rangle$ and also an isotropic exchange, i.e., $\mathcal{J}_{ij} = \mathcal{J}$. The ferromagnetic case is then realized for $\mathcal{J} > 0$ as the energy will be lowest for a parallel spin-alignment. Depending on the lattice structure, a negative \mathcal{J} can, for example, yield an anti-ferromagnetic state, but it can become arbitrarily complicated, for example when frustration plays a role in an Ising-spin model.

In the systems that we focus on in this thesis, the magnetization varies on a length scale much larger than the lattice spacings. It is hence permitted to use a continuum approach for the magnetization $\mathbf{M}(\mathbf{r})$ as a continuous function of space. In that context, a Ginzburg-Landau theory is often used, see [sections 3.2](#) and [3.5](#). There, equilibrium thermodynamics are completely determined by the free energy functional F that depends on temperature and the (local) order parameter, here $\mathbf{M}(\mathbf{r})$. Deviations from parallel alignment get penalized by finite gradients:

$$F_{\text{Heisenberg}} = \int d\mathbf{r} \, J (\nabla \mathbf{M}(\mathbf{r}))^2. \quad (1.2)$$

The *Dzyaloshinskii-Moriya* interaction can also be written in a discrete and continuous version which read

$$\mathcal{H}_{\text{DM}} = \sum_{i,j} \mathbf{D}_{ij} \cdot (\mathbf{S}_i \times \mathbf{S}_j) \quad (1.3)$$

$$F_{\text{DM}} = \int d\mathbf{r} \, D \mathbf{M}(\mathbf{r}) \cdot (\nabla \times \mathbf{M}(\mathbf{r})). \quad (1.4)$$

Equation (1.3) was part of Moriya's initial publication [20], which was an extension of Dzyaloshinskii's study on *weak* ferromagnetism in $\alpha\text{-Fe}_2\text{O}_3$, MnCO_3 and CoCO_3 via a phenomenological Landau-theory of second order phase transitions. Therein, \mathbf{D} is a constant vector pointing along the trigonal axis of $\alpha\text{-Fe}_2\text{O}_3$, an axis fixed by the crystal structure. Spins then prefer a canted arrangement, that would even be perpendicular, if (1.3) would be the solely relevant term. Perpendicular to each other and to \mathbf{D} . Left- or right-handed chirality is determined by an overall negative or positive sign of \mathcal{H}_{DM} , respectively.

Both Heisenberg- and DM interaction are present in chiral- or helimagnets. They compete against each other and the result of that competition is a helical structure with neither parallel nor perpendicular neighboring spins.

¹In the Heisenberg model, spins have an O_3 symmetry, meaning they can rotate any way in three dimensions. This stands in contrast to the Ising-model with a \mathbb{Z}_2 symmetry, where spins variables are only allowed to take two values, either up or down. A mixture between those two can be realized via a clock model that has a \mathbb{Z}_N symmetry [19].

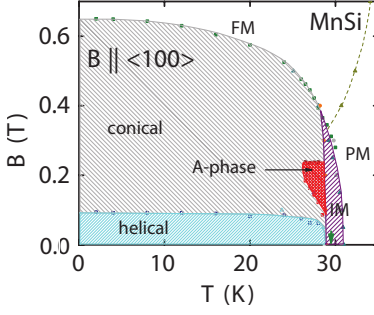


Figure 1.2: Typical magnetic phase diagram of the exemplary chiral magnet MnSi. Picture taken from [21].

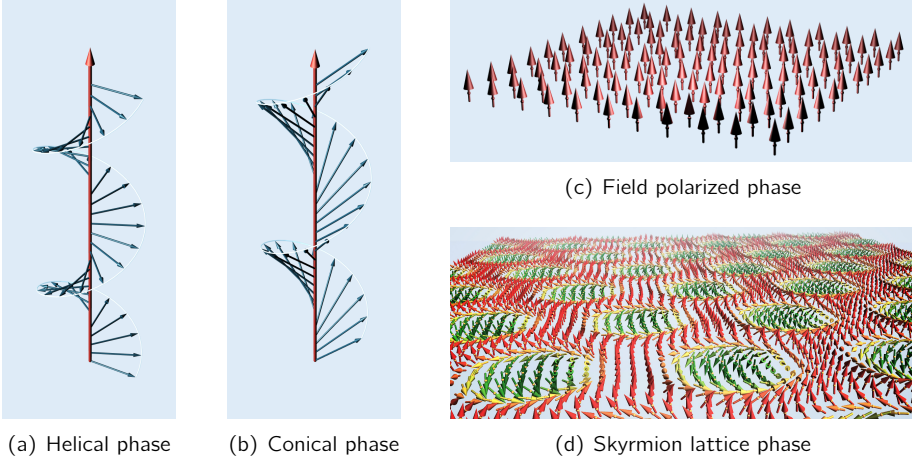


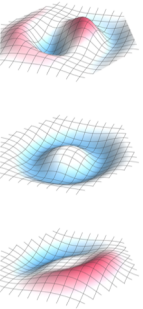
Figure 1.3: Magnetically ordered phases in chiral magnets.

1.2. TYPICAL MAGNETIC PHASES

A well known chiral magnet, and probably the most studied one for its availability of high-quality single crystals, is MnSi. Therefore, we use its phase diagram for the discussion of magnetic phases generally present in chiral magnets. More detailed properties of MnSi and further materials, which also contain the same or similar magnetic phases, are listed and described in [section 1.3](#). For now, let us focus on a typical phase diagram as shown in [figure 1.2](#).

At high temperatures, the system is in a paramagnetic state (PM) where local magnetization points in arbitrary directions and the net-magnetization is zero. Lowering the temperature, one first enters an intermediate regime (IM), i.e., the fluctuation disordered regime [22–24]. It is a crossover region between the paramagnetic and magnetically ordered phases. On a mean-field level one obtains a second-order phase transitions, but fluctuations drive it to first order.

After said first order transition at a critical temperature T_c one enters an ordered phase. At zero magnetic field this is the *helical phase* where magnetization forms



1. Introduction

a twisted structure as shown in [figure 1.3\(a\)](#). Note, that the local magnetization is perpendicular to the helix pitch and hence does not carry any mean magnetization. At zero field, the pitch direction is determined by cubic anisotropies [\[25, 26\]](#) and the formation of domains with different pitch directions is possible. Upon applying and increasing an external magnetic field \mathbf{H}^{ext} , the system transitions from a helical into a conical arrangement. First, all pitch vectors start to align with the direction of \mathbf{H}^{int} , which generally comprises of \mathbf{H}^{ext} , demagnetization and anisotropy effects, but mostly corresponds to the direction \mathbf{H}^{ext} , especially for higher fields. This process is completed at a critical field strength H_{c1} . For more details see [section 3.4](#). After that, the magnetization tilts towards \mathbf{H}^{int} forming a conical shape, as shown in [figure 1.3\(b\)](#), and generating a finite mean magnetization also pointing towards \mathbf{H}^{int} . This is the *conical phase*.

Increasing the magnetic field makes the cone more and more acute until it vanishes and a *field polarized* or *ferromagnetic state* (FM) is obtained, [figure 1.3\(c\)](#). This happens at a critical field H_{c2} and the phase transition is of second order, i.e., the magnetization changes continuously.

Just below T_c and at a finite magnetic field between H_{c1} and H_{c2} , roughly at $0.5 H_{c2}$, there exists a small phase pocket indicated as the *A-phase* in [figure 1.2](#). It contains a trigonal lattice of magnetic whirls, so-called skyrmions. An impression of this *skyrmion lattice* or *skyrmion crystal phase* is shown in [figure 1.3\(d\)](#). More details are given in [chapter 2](#).

1.3. MATERIALS & PROPERTIES

By today, many materials exhibiting the previously described phases have been found and investigated. The initial spark that ignited growing interest and research on, at first, chiral magnets, was the discovery of a skyrmion lattice phase in MnSi [\[7\]](#). From then on, a lot of effort has been put into creating and studying materials that might be able to host skyrmions natively, cf. [chapter 2](#).

The focus of this thesis lies on models that apply to study bulk chiral magnets with corresponding experiments being conducted by collaborators on MnSi, $\text{Fe}_{1-x}\text{Co}_x\text{Si}$ and Cu_2OSeO_3 . The first two crystallize in a cubic B20 alloy structure, which is a name for the FeSi-structure type, but all three have the space group $P2_13$ of point group 23, cf. No. 198 in [\[27\]](#). This space group lacks a center of inversion, which leads to the existence of both left and right handed versions of the crystals. The selection process can depend on the substrate or seed on top of which the crystals are grown. It hands down their own chirality to the sample. In the following, we describe those three materials in more detail. Characteristic parameters are summarized in [table 1.1](#) on page [14](#).

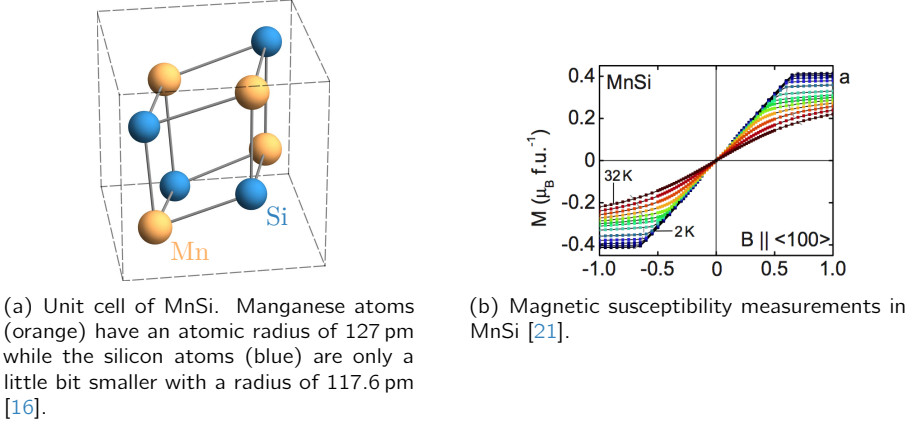


Figure 1.4: B20 crystal structure and magnetization measurements of MnSi.

MANGANESE SILICIDE: MnSi

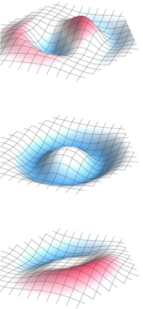
This material is a metallic, itinerant-electron magnet [3]. The cubic structure has an edge length of $a_{\text{MnSi}} = (4.5480 \pm 0.0002) \text{ \AA}$ [16] forming a cube containing eight atoms per unit cell, i.e., four formula units, and their positions are defined by the following coordinates:

$$\left((u, u, u); \left(\frac{1}{2} + u, \frac{1}{2} - u, \bar{u} \right); \left(\frac{1}{2} - u, \bar{u}, \frac{1}{2} + u \right); \left(\bar{u}, \frac{1}{2} + u, \frac{1}{2} - u \right) \right) \quad (1.5)$$

with $u_{\text{Mn}} = 0.138$ and $u_{\text{Si}} = 0.845$ [5], cf. figure 1.4(a). The magnetization in the ferromagnetic state comprises $0.4 \mu_{\text{B}}$ per Mn atom [28].

Furthermore, MnSi can be grown in an ultra-pure form with a mean free path of up to 5000 Å which suggests a good description by Fermi-liquid theory, a theoretical model dating back to Landau that is able to describe the normal state of most metals at sufficiently low temperatures. MnSi, however, shows an uncharacteristic behavior for Fermi-liquids above a critical pressure p_c . At lower pressures, when the system is weakly spin polarized, the resistivity ρ depends quadratically on temperature as is expected by Fermi-liquid-theory. When magnetic order is suppressed at $p > p_c$, this behavior changes abruptly to $\rho \propto T^{3/2}$ [6, 29–33]. Note that this phenomenon is not only confined to an area close to the quantum critical point but over a wider area of the phase diagram. Reasons for the appearance of this non-Fermi-liquid phase are still unknown and its understanding is sometimes referred to as the holy grail of MnSi.

The magnetic phase diagram of MnSi was already shown in figure 1.2. Below a critical temperature of $T_c \approx 29 \text{ K}$, the system exhibits helical magnetic order at zero or small magnetic field [3, 34, 26]. The pitch vector \mathbf{Q} is pinned to a



1. Introduction

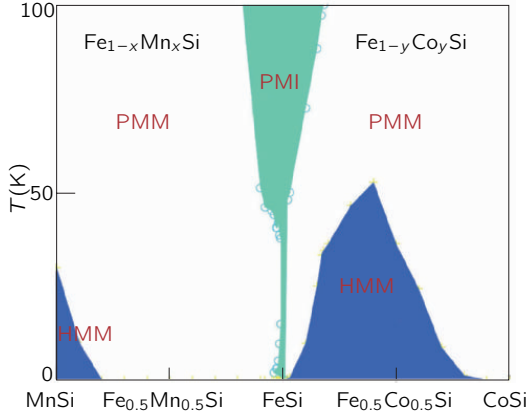


Figure 1.5: Effects of doping and temperature on $\text{Fe}_{1-x}\text{Mn}_x\text{Si}$ (left) and $\text{Fe}_{1-y}\text{Co}_y\text{Si}$ (right). Paramagnetic metallic (PMM), paramagnetic insulating (PMI) and helimagnetic metallic at zero field (HMM) phases are possible [38].

$\langle 111 \rangle$ direction in the helical phase via cubic anisotropies and the corresponding wavelength is approximately 180 Å long and almost temperature independent. In terms of chirality it can be said that a left handed chirality of the crystal structure corresponds to a left handed magnetic chirality [35, 36].

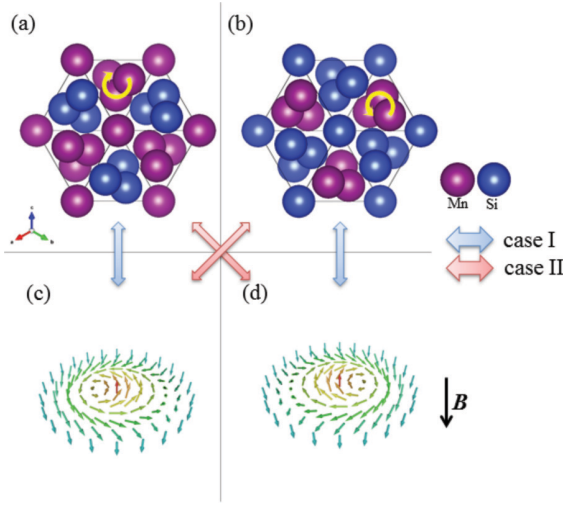
Another important property concerns the magnetic susceptibility in the conical phase χ_{con} . The striking feature is a constant behavior at low temperatures. Measurements have, for example, been performed by Bauer *et al.* [21] and are shown in figure 1.4(b). The slope of magnetization vs. applied field is truly linear for temperatures around 2 K, but softens out a little bit for higher temperatures. This is still fine for small fields, but needs to be kept in mind for situations with comparably high temperatures and fields. As the magnetic field inside of a macroscopic sample depends on the strength of the shape dependent demagnetization field, χ_{con} is also shape dependent. Said field can be characterized via a demagnetization factor N_z corresponding to a principal axis in field direction, cf. section 3.3. A shape independent constant, however, can be extracted via [37]

$$\chi_{\text{con}}^{\text{int}} = \frac{1}{\chi_{\text{con}}^{-1} - N_z}. \quad (1.6)$$

The material constant $\chi_{\text{con}}^{\text{int}}$ of MnSi has a value of 0.34. The property of a constant conical susceptibility is not reserved for MnSi alone, but occurs in the other chiral magnets as well. Values for other materials are listed in table 1.1.

IRON COBALT SILICIDE: $\text{Fe}_{1-x}\text{Co}_x\text{Si}$

The magnetic and conducting properties of $\text{Fe}_{1-x}\text{Co}_x\text{Si}$ depend on doping and temperature as can be seen in figure 1.5. When interested in helimagnets, most experiments are therefore conducted with a doping between $x = 0.2$ and $x = 0.5$. Like MnSi, both FeSi and CoSi also crystallize in a B20 structure which allows the full doping range.



The helix pitch is weakly oriented along $\langle 100 \rangle$ and in some measurements even a random distribution has been found [40].

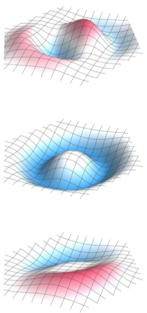
Figure 1.6 shows a B20 structure like iron cobalt silicide in both chiralities, illustrated by yellow arrows.

Contrary to MnSi, the handedness of the magnetic spin structure does not always correspond to the handedness of the atomic crystal structure, i.e., a left handed crystal structure does not mean that magnetic helices or skyrmions have a left handed chirality as well (case I in figure 1.6), but can be exactly the opposite (case II). In Fe_{1-x}Co_xSi the association between crystal and magnetic chirality is doping dependent. That means choosing a fixed crystal chirality and changing the doping strength will flip the sign of the Dzyaloshinskii-Moriya interaction at a doping strength around $x = 0.65$ [41].

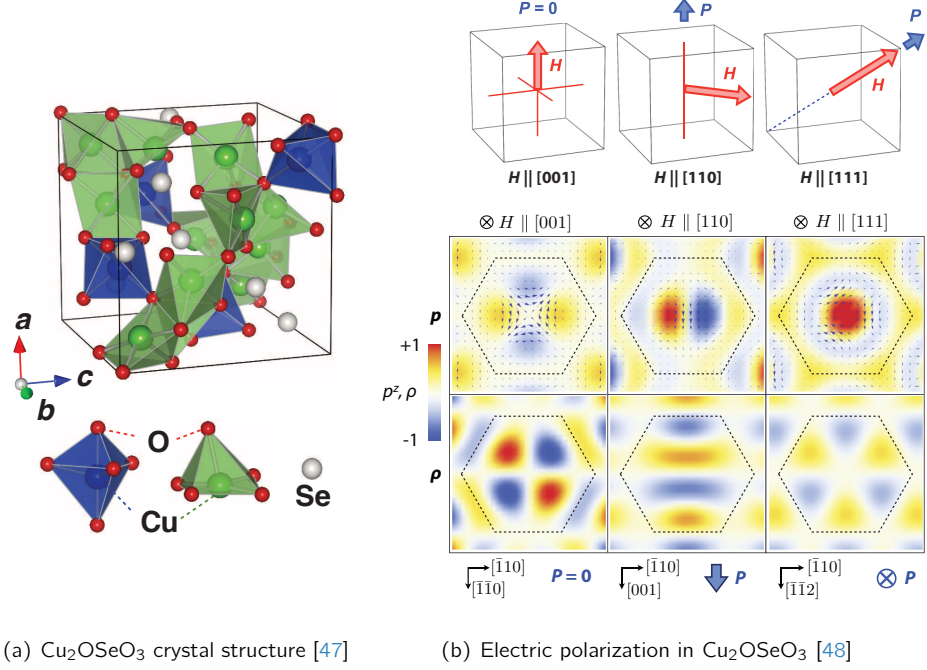
The change of the Dzyaloshinskii-Moriya interaction D also influences the pitch length leading to a variation of the helix wavelength $\lambda_{\text{hel}} \propto 1/D$ between 200 and 2300 Å [42–44]. Dependent on doping, λ_{hel} first decreases but soon increases with increasing x [40].

COPPER(II)-OXO-SELENITE: Cu₂OSeO₃

Below a critical temperature of 58.8 K CuSeO₄ shows spontaneous magnetization [45]. Copper(II)-oxo-selenite in general can appear in a multitude of crystal structures going from monoclinic and triclinic forms of Cu₄O(SeO₃)₃ to Cu₂O(SeO₃), which can be monoclinic and even cubic. The latter is the type we focus on. The material in question is a dark olive green multiferroic and magnetoelectric insulator. Comparing to MnSi, it crystallizes similar to the B20 structure but with a different coordination number. It contains eight formula units per unit



1. Introduction



(a) Cu_2OSeO_3 crystal structure [47]

(b) Electric polarization in Cu_2OSeO_3 [48]

Figure 1.7: (a) The empirical formula of Cu_2OSeO_3 contains two Cu^{2+} ions. They are characterized by a different oxygen coordination.

(b) Top: depending on the direction of an applied magnetic field \mathbf{H} with respect to the atomic lattice, a finite mean electric polarization \mathbf{P} is able to form with a direction also dependent on the direction of \mathbf{H} .

(b) Bottom: besides a possibly finite mean polarization, the skyrmion phase experiences also a modulating local one that induces a local charge distribution ρ plotted in the bottom row of (b).

cell of edge length $a_{\text{Cu}_2\text{OSeO}_3} = (8.9250 \pm 0.0001) \text{ \AA}$ [17]. A picture of the crystal structure is shown in figure 1.7(a). The helical magnetic modulation has a length of $(616 \pm 45) \text{ \AA}$ and is pinned to a $\langle 100 \rangle$ direction at zero field [46].

In a magnetoelectric material, an external magnetic field influences electric polarization [49]. Although Cu_2OSeO_3 does not show spontaneous ferroelectric polarization, it can be induced by an external magnetic field [50]. For the setup used here, this polarization can locally be written as [51]

$$\mathbf{P} = \alpha \begin{pmatrix} M_y M_z \\ M_z M_x \\ M_x M_y \end{pmatrix}. \quad (1.7)$$

The direction of the average polarization depends on the direction of applied magnetic field and may also vary on strength. When the system is in the skyrmion

phase, then also the local polarization varies significantly with respect to the direction of the magnetic field. Both effects are shown in the top and bottom parts of [figure 1.7\(b\)](#), respectively. Electric forces are generally much stronger than magnetic forces, but the induced polarization has, nevertheless, only a small effect as can be seen, for example, when comparing magnetic and electric dipolar energies. Seki *et al.* measured a saturation magnetization between $0.5 \mu_{\text{B}}/\text{Cu}^{2+}$ at 5 K and $0.2 \mu_{\text{B}}/\text{Cu}^{2+}$ at $57 \text{ K} \approx T_c$ for $\mathbf{H} \parallel [111]$ [47]. This corresponds to approximately $16 \mu\text{C}/\text{m}^2$ and $1 \mu\text{C}/\text{m}^2$ at $H = H_{c2}$, respectively. Having eight formula units per unit cell providing 16 copper ions responsible for the magnetic moments per unit cell, leads to

$$P_{[111]}^{T=5\text{K}} = 16 \frac{\mu\text{C}}{\text{m}^2}$$

$$M_{[111]}^{T=5\text{K}} = 0.5 \frac{\mu_{\text{B}}}{\text{Cu}^{2+}} \cdot \frac{16 \text{ Cu}^{2+}}{710.8 \text{ \AA}} \approx 104\,000 \frac{\text{A}}{\text{m}}$$

giving corresponding dipolar energies of

$$E_{\text{dipole},\text{electric}} = \frac{1}{8\pi\epsilon_0} \left(P_{[111]}^{T=5\text{K}} \right)^2 \approx 1 \frac{\text{J}}{\text{m}}$$

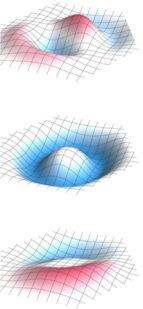
$$E_{\text{dipole},\text{magnetic}} = \frac{\mu_0}{8\pi} \left(M_{[111]}^{T=5\text{K}} \right)^2 \approx 540 \frac{\text{J}}{\text{m}}.$$

There are hence at least two to three orders of magnitude between those energies. But because Cu_2OSeO_3 is insulating, electric fields can still influence the magnetic structure without needing to worry about affecting itinerant charge carriers.

SUMMARY AND OTHER NOTEWORTHY MATERIALS

[Table 1.1](#) summarizes typical values of the materials above. One should mention, that temperature generally plays a role in all obtained data. It is ultimately a matter of focus which allows us to approximate some values as constant opposed to others. For example the lattice constants and hence the $V_{\text{f.u.}} (\text{\AA}^3)$ depend on temperature. We chose to mention low temperature values in the text, while values in [table 1.1](#) correspond to ambient temperatures. Their discrepancies are fairly small at about one percent. The pitch length varies more significantly with around 10% between 0 K and T_c [52]. The biggest influence of temperature can, however, be observed in H_{c2} which is around a factor of two. Therefore, the other temperature dependencies can be regarded as constant compared to $H_{c2}(T)$.

Apart from those three materials, there are, for one, more B20-type alloys like FeGe [57] or MnGe [58] that host skyrmions. To a great deal driven by the need for skyrmions at room temperature to be able to use them in applications and novel computer technologies (cf. [section 2.3](#)), other approaches were explored. For example Heusler compounds like Mn_2RhSn of space group $I\bar{4}m2$ (No. 119), as an example of other non-centrosymmetric magnets, are studied [59], but also



1. Introduction

	MnSi	Fe _{0.8} Co _{0.2} Si	Cu ₂ OSeO ₃	FeGe
	metallic	semi-conducting	insulating	metallic
T_c (K)	29	28	58	278.2
$H_{c2}^{\text{int}}(T=0) (\frac{T}{\mu_0})$	0.60	0.15	0.08	0.93 at $T=271$ K
$2\pi/Q$ (Å)	180	340	600	700
pitch alignment	$\langle 111 \rangle$	weakly $\langle 100 \rangle$	$\langle 100 \rangle$	$\langle 100 \rangle_{\text{high } T}$ $\langle 111 \rangle_{\text{low } T}$
$\chi_{\text{con}}^{\text{int}}$	0.34	0.64	1.76	3.43
$V_{\text{f.u.}} (\text{Å}^3)$	24.02	22.52	89.02	103.80
Z	4	4	8	4
g	2.0	2.1	2.1	1.9

Table 1.1: Summary of material properties. The number Z equals the number of formula units per unit cell and note that *pitch alignment* refers to the direction of \mathbf{Q} at zero field in the helical phase. Most values are taken from samples used in [37], the remaining sources are mentioned in the text and [53–56]. Note that the listed data for FeGe are for its low-temperature B20 structure.

centrosymmetric magnets, where Dzyaloshinskii-Moriya interaction does not play a role but the interplay between magnetic dipole–dipole interaction and uniaxial anisotropy causes the formation of a skyrmion spin texture. Also, broken inversion symmetry at interfaces can lead to the formation of skyrmions as can be seen in [60] where the authors create a square, atomic-scale skyrmion lattice in a one-atomic iron film on top of an iridium (111) surface. For a collection of materials see [61, chapter 2].

Although near-room temperature formation of a skyrmion lattice was already achieved in thin-films of FeGe [57], skyrmions at and beyond room temperature were first found in a different family of chiral magnets: β -Mn-type Co–Zn–Mn alloys. One example is Co₁₀Zn₁₀, which belongs to the cubic chiral space group $P4_132$ or $P4_332$ depending on its handedness containing 20 atoms in the unit cell and the critical temperature lies at $T_c \approx 462$ K [62]. Doping with manganese systematically decreases T_c until Co₆Mn₆Zn₈ does not show ferromagnetic behavior any longer. The authors effectively detect skyrmions at 283 K and 345 K respectively for Co₈Zn₈Mn₄ and Co₈Zn₁₀Mn₂.

2

SKYRMIONS

2.1. HISTORICAL ORIGIN

Skyrmions date back to studies by T. H. R. Skyrme in the late 1950's and early 1960's [8, 63–67]. He developed a unified field theory of K- and π -mesons and baryons. It turned out to be a non-linear theory of self-interacting (boson) meson fields, which admit states that have phenomenological properties of fermion particles, interacting with mesons. This was achieved by separating the field into meson-like and particle-like parts.

In the following we sketch his original work in a rough fashion and mainly follow the beginning of [67]. Let the initial field at any point be characterized by a unitary symbol U :

$$UU^\dagger = U^\dagger U = 1. \quad (2.1)$$

While he also discussed simpler, one-dimensional models where U corresponds to a complex number $e^{i\alpha}$, in the physically relevant case U is a quaternion¹, which can also be written in terms of four real fields ϕ_α :

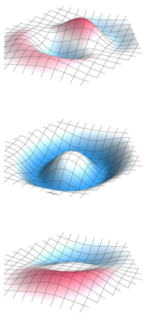
$$U = \phi_4 + i \sum_{\alpha=1}^3 \tau^\alpha \phi_\alpha \quad (2.2)$$

where the coefficients τ^α are a set of three Pauli matrices. In his model, the three independent pion field amplitudes are replaced by such four fields, that interact symmetrically with the nuclear field. The vector composed of those fields is then constrained to have constant length:

$$\sum_{\alpha=1}^4 \phi_\alpha^2 = 1. \quad (2.3)$$

The domain of U is hence the surface of a unit-sphere in a four-dimensional Euclidean space. A constant of motion called N , that can be interpreted as a

¹Quaternions can be seen as an extension of the complex numbers. They have been discovered by Sir William Rowan Hamilton (1805–65) and are the first non-commutative algebra to be studied [68].



2. Skyrmions

particle number, has the global meaning of the number of times that the field distribution $U(x)$ maps the 3-dimensional configuration space onto this domain. U has to obey the boundary condition

$$U(\infty) = 1 \quad (2.4)$$

to ensure an integer particle number. In a state where there is one particle, U has to wrap around the sphere at least once and therefore take the value of -1 at least once. This leads to a native definition of the position of the particle, namely at $x = x_0$ when $U(x_0) = -1$. He then separates U into a *mesonic* part \hat{U} that never takes the value -1 , and a *particle* part, that is only significant in the vicinity of x_0 . He gives

$$\hat{U} = \frac{1 + \varepsilon + U}{1 + \varepsilon + U^\dagger}, \quad (2.5)$$

which is unequal to -1 for $\varepsilon > 0$. As $\varepsilon \rightarrow 0$ \hat{U} approaches U almost everywhere. Because \hat{U} is particle free, i.e., $N = 0$, a separation can be made as

$$U = \hat{U} S. \quad (2.6)$$

Except near the positions x_0 of particles, the new field $S = 1$. Near particles S can be written as

$$S = -\frac{\varepsilon + i\tau^\alpha B_i^\alpha (x - x_0)_i}{\varepsilon - i\tau^\alpha B_i^\alpha (x - x_0)_i}. \quad (2.7)$$

τ^α are the Pauli matrices and B_i^α are proportional to the field gradients of U at $x = x_0$:

$$\frac{\partial U}{\partial x_i} = i\tau^\alpha B_i^\alpha U \quad (2.8)$$

$$B_i^\alpha = (1/2i) \text{Tr}(U^\dagger \tau^\alpha \frac{\partial U}{\partial x_i}). \quad (2.9)$$

It then needed to be shown that singularities like S , describing the branch points of \sqrt{U} , behave like Dirac particles coupled to the residual meson field U . Those are some longer calculations that we will not address here. Still noteworthy is a derived expression for the particle number (in the limit of $\varepsilon \rightarrow 0$)

$$N = -\text{sgn} \det B_i^\alpha(x_0). \quad (2.10)$$

At this point he believed that the particle operators have many fermionic properties but did not show it explicitly. He did, however, demonstrate this for the one-dimensional model in [65] where neutrino-like properties were evident.

In retrospect Skyrme's particle solutions, the now so-called skyrmion solutions, were the first example of a topological soliton model of a particle [69]. Seen in a broader context, they emerged from the Yukawa model which describes how heavy spin- $\frac{1}{2}$ nucleons interact through pion exchange. He reconsidered the pion

exchange which leads to a Lagrangian with a topological structure, that allowed a topologically stable soliton solution. He saw that these solutions had rotational degrees of freedom and the key was that when quantized, the state was allowed to carry spin- $\frac{1}{2}$. Hence, a bosonic field theory could lead to fermionic states.

While skyrmions occurred here as field configurations on a 3-sphere as defined by (2.12), the concept and their topological properties can be generalized to other dimensions, in particular to the 2-sphere S^2 . This brings us back to the texture shown in figure 1.3(d), the skyrmions present in chiral magnets. Because they are formulated in one dimension less than the original skyrmions, they are sometimes called baby-skyrmions. In contrast to objects in other magnetic phases present in chiral magnets they are topologically non-trivial. This aspect is elucidated in the following.

2.2. TOPOLOGICAL ASPECTS OF SKYRMIONS

Skyrmions or magnetic textures in general are described by a vector field, i.e., a mapping between two manifolds, in this example position and spin-direction. This paragraph follows [69] to introduce topological characteristics and their application on the skyrmion structure.

Let

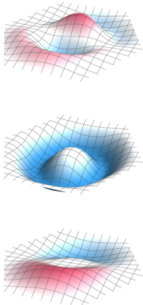
$$\begin{aligned}\Psi_0: X &\rightarrow Y \\ \mathbf{x} &\mapsto \mathbf{y}\end{aligned}\tag{2.11}$$

be a map between two manifolds X and Y . In particular, let there be points $\mathbf{x}_0 \in X$ and $\mathbf{y}_0 \in Y$. In the following, we consider based maps, i.e., maps $\Psi_0(\mathbf{x}_0) = \mathbf{y}_0$. To formulate topological aspects in a proper way, the concept of homotopy is important. Ψ_1 homotopic to Ψ_0 means, that Ψ_0 can be continuously deformed into Ψ_1 . *Homotopic* is symmetric, transitive and reflexive, which are the properties of an equivalence relation. Proof can be found in [70]. Therefore, maps can be classified in homotopy classes. The constant class, for example, contains all maps that are homotopic to the constant map $\Psi(\mathbf{x}) = \mathbf{y}_0$ for all $\mathbf{x} \in X$.

Of special interest to us are maps from a sphere to a target manifold.

$$S^n = \{x \in \mathbb{R}^{n+1} : \|x\| = 1\}\tag{2.12}$$

is the definition of an n -sphere, a sphere embedded in $n + 1$ dimensions [71]. Based maps $\Psi: S^n \rightarrow Y$ from such a sphere are of a class in $\pi_n(Y)$, which has a group structure for $n \geq 1$. In particular $\pi_1(Y)$ is known as the fundamental group.



2. Skyrmions

EXAMPLE: $\pi_1(Y)$

$\pi_1(Y)$ is the class containing all maps of circles or loops that get mapped to a target Y . If Y is a connected manifold and $\pi_1(Y) = \{e\}$, where $\{e\}$ is the trivial group containing only the identity element, then Y is simply connected. This means, that all loops can be smoothly contracted to a single point. This, in turn, implies that Y does not have any holes.

If the target is a circle or loop itself, i.e., $Y = S^1$, then there exists a map $f: S^1 \rightarrow S^1$ with $f(1) = 1$. A map $\tilde{f}: \mathbb{R} \rightarrow S^1$ is clearly induced by $\tilde{f}(t) = f(e^{it})$. It can be shown that due to $\pi_1(\mathbb{R}) = 0$ every map $g: \mathbb{R} \rightarrow S^1$ with $g(0) = 1$ can be uniquely lifted to a map $\hat{g}: \mathbb{R} \rightarrow \mathbb{R}$ with $\hat{g}(0) = 0$ [71]. In particular, there exists a unique map \hat{f} with $\hat{f}(0) = 0$ such that the diagram

$$\begin{array}{ccccc} & & & \mathbb{R} & \\ & & \nearrow \tilde{f} & \downarrow p & \\ \mathbb{R} & \xrightarrow[t \mapsto e^{it}]{} & S^1 & \xrightarrow{f} & S^1, \end{array}$$

commutes.

Clearly, there exists $k \in \mathbb{Z}$ that $\hat{f}(2\pi) = 2\pi k$. The number k can be seen as a winding number that counts the number of times the image of f winds around S^1 . It follows from the uniqueness of the lifting property that the winding number is well-defined.

The statement of the second part of the example can be generalized and reads

$$\pi_n(S^n) = \mathbb{Z} \quad \forall n \geq 1. \quad (2.13)$$

For Skyrme's original skyrmions $n = 3$. The case of baby skyrmions, which we will simply call skyrmions in the remainder of the text, of course also falls into the same set of classes, only with $n = 2$. In that context, they can easily be drawn as arrows on a sphere like in the upper part of [figure 2.1](#). The magnetic texture in chiral magnets is, however, set on a planar surface and not the surface of a sphere. That transition is achieved via a stereographic projection of S^2 onto \mathbb{R}^2 . Let \mathbf{p} be the north pole of the sphere, then there exists a homeomorphism $\mathbb{R}^2 \rightarrow S^2 \setminus \{\mathbf{p}\}$. A complete correspondence is obtained by adding a single point at infinity to \mathbb{R}^2 and identifying it with the image of \mathbf{p} . A based map $\Psi: S^2 \mapsto S^2$, or to any other target manifold for that matter, is hence a continuous extension of a map $\Psi: \mathbb{R}^2 \rightarrow S^2$ provided that $\lim_{\mathbf{x} \rightarrow \infty} \Psi(\mathbf{x}) = \mathbf{p}$. Of course, the occurring skyrmions have a finite extent, but a contraction of \mathbb{R}^2 is easily done, for example by applying the map $\rho \mapsto \tan^{-1} \rho$, or other less distorting functions, where ρ is the distance to the origin of \mathbb{R}^2 . The result after such transformations is shown in the lower part of [figure 2.1](#). On the left hand side so-called Néel-skyrmions are shown. They are characterized by having always outward-pointing spins on the sphere. Combing those spins around the axis connecting north and south pole of the sphere yields a sense of chirality that is, of course, also present in the

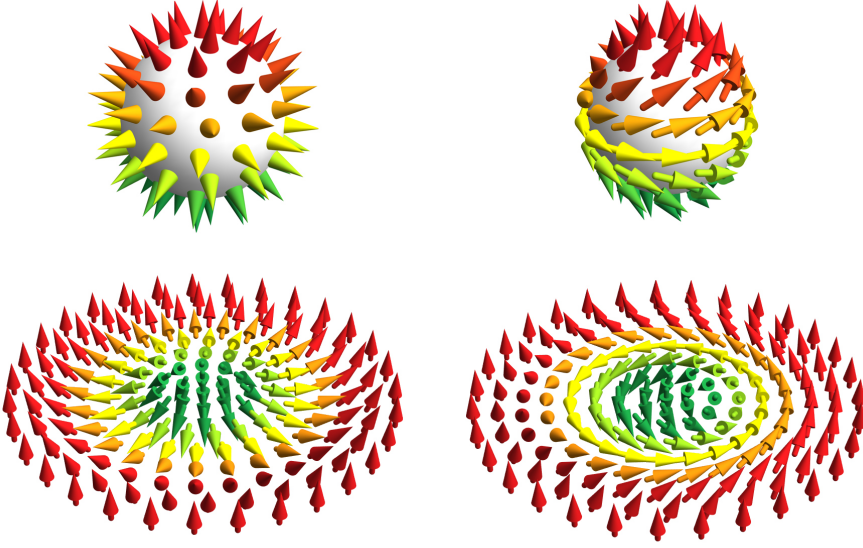


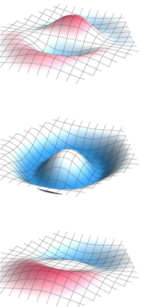
Figure 2.1: Stereographical projections of (baby) skyrmions. The south pole of the sphere is mapped to the origin of \mathbb{R}^2 while the north pole is mapped to infinity. Via the map $\rho \mapsto \tan^{-1}(\rho)$ one can map \mathbb{R}^2 onto a finite sized disk, where ρ is the distance to the origin. **Left:** Néel-skyrmion. Note the similarity to Néel-type domain walls, in which spins rotate in a plane perpendicular to the domain boundary. **Right:** Chiral- or Bloch-type skyrmion. Note the similarity to Bloch-type domain walls, in which spins rotate in a plane parallel to the domain boundary. It evolves from a Néel-skyrmion by first *combing* the spherical hedgehog arrangement around the axis defined by the north and south poles of the sphere before projecting it onto a plane. This type is the one observed in chiral magnets.

projected version. This texture is then called chiral skyrmion and it is the type of texture that occurs in chiral magnets and therefore the kind of skyrmion that we refer to in the remainder of the thesis unless explicitly stated otherwise.

At this point, it is appropriate to give another quantity that characterizes the skyrmion. This is its *winding number*. In the general mathematical scheme it is rooted in the concept of the *topological degree*, which is defined for an everywhere continuously differentiable map $\Psi : X \rightarrow Y$ between two oriented and closed manifolds of the same dimension. Then the topological degree is defined as the integral over the pullback Ψ^* of a normalized volume form Ω on the target Y :

$$\deg \Psi = \int_X \Psi^*(\Omega). \quad (2.14)$$

The topological degree is an integer number and therefore a homotopy invariant. It also does not depend on Ω [69].



2. Skyrmions

To make the transition from this abstract definition to the skyrmion configuration, let us specify the integrand of (2.14). Given $\Omega = \beta(\mathbf{y}) dy^1 \wedge dy^2$ with $\mathbf{y} \in Y$ and let the map Ψ be represented by $\mathbf{y}(\mathbf{x})$, then the integrand is written in terms of local coordinates as

$$\begin{aligned}\Psi^*(\Omega) &= \beta(\mathbf{y}(\mathbf{x})) \frac{\partial y^1}{\partial x^j} dx^j \wedge \frac{\partial y^2}{\partial x^k} dx^k \\ &= \beta(\mathbf{y}(\mathbf{x})) J(\mathbf{x}) dx^1 \wedge dx^2\end{aligned}\tag{2.15}$$

with $J(\mathbf{x}) = \det \left(\frac{\partial y^i}{\partial x^j} \right)$ and $i, j, k \in \{1, 2\}$.

In the physical context the map describes the local magnetization $\mathbf{M}(\mathbf{x}) \equiv \mathbf{y}(\mathbf{x})$ and, when normalized, $(\hat{\mathbf{M}})$ can be described by angles ϑ and φ of the standard spherical coordinates. Using those coordinates the normalized volume form specifies to $\Omega = \frac{1}{4\pi} \sin(\vartheta) d\vartheta \wedge d\varphi$. We now need to pull this integration over a sphere back to an integration over \mathbb{R}^2 in Cartesian coordinates by inverting the spherical coordinate representation. To avoid an abundance of indices we set $(x, y) = (x^1, x^2) \in X$.

$$\vartheta = \arcsin \sqrt{\hat{M}_x^2 + \hat{M}_y^2}\tag{2.16}$$

$$\varphi = \arctan \frac{\hat{M}_x}{\hat{M}_y}\tag{2.17}$$

Also, the explicit dependence on (x, y) has been dropped for clarity, i.e., $M_x = M_x(x, y)$ is the first component of the magnetization at position (x, y) . Using those coordinates in (2.15) and evaluating the derivatives in the second step yields

$$\begin{aligned}\deg \mathbf{M} &= \frac{1}{4\pi} \int_{\mathbb{R}^2} \sin \vartheta \sqrt{M_x^2 + M_y^2} \left(\frac{\partial \vartheta}{\partial x} \frac{\partial \varphi}{\partial y} - \frac{\partial \varphi}{\partial x} \frac{\partial \vartheta}{\partial y} \right) dx dy \\ &= \frac{1}{4\pi} \int_{\mathbb{R}^2} \frac{1}{\sqrt{1 - \hat{M}_x^2 - \hat{M}_y^2}} \left(\frac{\partial \hat{M}_x}{\partial x} \frac{\partial \hat{M}_y}{\partial y} - \frac{\partial \hat{M}_y}{\partial x} \frac{\partial \hat{M}_x}{\partial y} \right) dx dy \\ &= \frac{1}{4\pi} \int_{\mathbb{R}^2} \frac{1}{\sqrt{1 - \hat{M}_x^2 - \hat{M}_y^2}} \left(\frac{\partial \hat{\mathbf{M}}}{\partial x} \times \frac{\partial \hat{\mathbf{M}}}{\partial y} \right)_z dx dy.\end{aligned}\tag{2.18}$$

The normalization of \mathbf{M} is encoded in $M_z = \sqrt{1 - M_x^2 - M_y^2}$. Furthermore, it can be shown that the last line can be written as a triple product, which results in the common form used to calculate the skyrmion *winding number* W :

$$W = \frac{1}{4\pi} \int_{\mathbb{R}^2} \hat{\mathbf{M}} \cdot \left(\partial_x \hat{\mathbf{M}} \times \partial_y \hat{\mathbf{M}} \right) dx dy.\tag{2.19}$$

This number counts how often the magnetization wraps around a sphere. Applying (2.19) to a texture as shown in the bottom half of figure 2.1, one obtains $W = -1$. Strictly speaking this object is called an *anti-skyrmion*. The minus sign appears because magnetization at the center is pointing *down*.

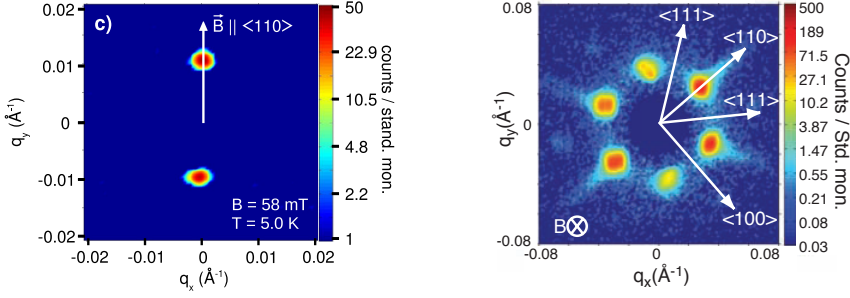
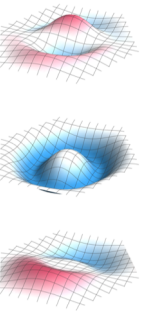


Figure 2.2: Structure factors obtained via neutron scattering. **Left:** Helical/conical phase of the helimagnet Cu_2OSeO_3 [46]. Two peaks are clearly visible aligned with the magnetic field along which they represent the helical modulation. **Right:** Skymion phase in MnSi [7]. Six major peaks are visible indicating a superposition of three helices. Additionally, smaller higher order peaks are recognizable. A more thorough study on them can be found in [74].

2.3. EXPERIMENTAL REALIZATION AND APPLICATION

Around the early 90's, Bogdanov *et al.* showed, that such skyrmions may occur as a thermodynamically stable system of magnetic vortices in magnetically ordered crystals with an easy axis [9, 72, 73]. The vortices themselves form a lattice similar to that of type-II superconductors and can be stabilized by a so-called Dzyaloshinskii-Moriya interaction. Besides tetragonal materials like Tb_3Al_2 , the authors also suggested cubic magnets like $\text{Fe}_x\text{Co}_{1-x}\text{Si}$ and, in particular, MnSi as possible candidates to exhibit skyrmions.

In 2009, MnSi was subject to studies by a research group in Munich where Mühlbauer *et al.* performed small angle neutron scattering experiments (cf. section 5.2) on it while applying a magnetic field and thus inducing an easy axis of magnetization [7]. Contrary to previous experiments, they did not apply the incident neutron beam perpendicular to the magnetic field, but in parallel. Unlike two peaks in the structure factor that one expects at intermediate fields in the perpendicular setup indicating the conical phase, the result were six major peaks forming a hexagon around the center, cf. figure 2.2. Having a spirally modulated structure in mind when observing two opposing peaks it seemed natural to superpose three of them when seeing six peaks. Doing exactly that and properly fixing the relative phases amounts to the magnetic lattice structure shown in figure 1.3(d). This actually three dimensional texture is translation invariant in the direction parallel to the magnetic field, i.e., perpendicular to the shown plane, thus forming a tube-like structure similar to the Abrikosov vortex lattice of type-II superconductors. Atomic scale skyrmion have also been realized by using a surface Dzyaloshinskii-Moriya interaction [60]. There, the chirality is not an intrinsic property of a material but arises because of material differences between the substrate and the studied layer on top of it.



2. Skyrmions

Skyrmions have the prospect of becoming a key ingredient in future computer technology. Their topological structure leads to an emergent electrodynamics which can be used to couple them very efficiently to currents. Due to their incommensurability and large extent compared to the atomic lattice, skyrmion lattices can be moved by currents a million times smaller than needed to move ordinary magnetic domain walls [11, 75]. Novel ideas about applying single skyrmions range from racetrack memories [10, 76, 77] to entire logic elements.

3

— THEORETICAL DESCRIPTION —

The magnetic structure in bulk chiral magnets can be described by several methods. In this thesis we primarily choose a description via a Ginzburg-Landau theory which we introduce in this chapter. In [part III](#) we also employ a description via a non-linear σ model, which restricts the magnetization to be normalized. Before turning to the description of the theoretical model we introduce necessary quantities.

3.1. CONVENTIONS

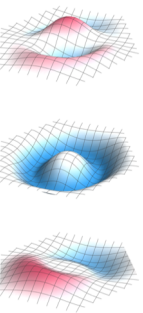
In the following chapters we compare our models to data obtained by different experimental methods: ferromagnetic resonance and neutron scattering experiments. The first applies an oscillating external magnetic field, which enters the relevant equations, while the latter method focuses on much shorter length scales which makes it convenient to use the internal magnetic field in the describing equations. At this point we establish a connection between these quantities and define notation.

External quantities will be indicated by the index “ext” and internal quantities by an index “int”. Magnetic fields and inductions are therefore denoted by \mathbf{H}^{ext} and \mathbf{H}^{int} respectively \mathbf{B}^{ext} and \mathbf{B}^{int} . While vectors are written in bold letters, their norms will mostly be denoted by normal font and omitted absolute value bars.

Magnetic moments are indicated by $\boldsymbol{\mu}$ and magnetization, which has units of magnetic moment over volume, by a capital \mathbf{M} . When encountering spatially homogeneous quantities, they will carry an index “0”, i.e., \mathbf{M}_0 or \mathbf{H}_0 . Furthermore, (static) mean-field solutions carry an index “mf” like \mathbf{M}^{mf} .

In the vacuum, the two magnetic fields \mathbf{B} and \mathbf{H} are just scaled versions of each other related by the permeability of free space $\mu_0 = 4\pi \times 10^{-7} \text{ N/A}^2$:

$$\mathbf{B} = \mu_0 \mathbf{H}. \quad (3.1)$$



3. Theoretical Description

Inside a magnetic solid, their relation is more complex and the general relationship is given by

$$\mathbf{B} = \mu_0(\mathbf{H} + \mathbf{M}) \quad (3.2)$$

with magnetization \mathbf{M} , which is defined as the magnetic moment per unit volume and therefore usually considered in the continuum limit and seen as a smooth vector field. In the special case that the magnetization is linearly dependent on \mathbf{H} , one can write

$$\mathbf{M} = \mathbf{M}' + \chi \mathbf{H} \quad (3.3)$$

where χ a dimensionless quantity and called *magnetic susceptibility*. The term \mathbf{M}' stands for a spontaneous magnetization in the absence of an applied field. The linear relation of (3.3) also keeps the relation between \mathbf{H} and \mathbf{B} linear:

$$\mathbf{B} = \mu_0(1 + \chi)\mathbf{H} = \mu_0\mu_r\mathbf{H} \quad (3.4)$$

where $\mu_r = (1 + \chi)$ is called the relative permeability and is the ratio of the permeability of a specific medium to the permeability of free space: $\mu_r = \frac{\mu}{\mu_0}$. When dealing with the description of magnetizable media, one needs to be cautious to define those fields, as they can differ significantly inside and outside of the media. In free space, it is simple and

$$\mathbf{B}^{\text{ext}} = \mu_0 \mathbf{H}^{\text{ext}} \quad (3.5)$$

holds. The field inside a sample, that enters the above fields, is changed via a demagnetization field \mathbf{H}^{dem} (more information in [section 3.3](#)):

$$\mathbf{H}^{\text{int}} = \mathbf{H}^{\text{ext}} + \mathbf{H}^{\text{dem}}. \quad (3.6)$$

Note that a magnetized sample also influences the magnetic field around it. For para- or diamagnetic samples of ellipsoidal shape this can be neglected as stray-fields cancel each other. The internal magnetic induction then reads

$$\mathbf{B}^{\text{int}} = \mu_0(\mathbf{H}^{\text{int}} + \mathbf{M}) = \mathbf{B}^{\text{ext}} + \mu_0(\mathbf{H}^{\text{dem}} + \mathbf{M}). \quad (3.7)$$

Fourier transformations are performed with the following convention:

$$\mathbf{M}(\mathbf{r}) = \frac{1}{\nu} \sum_{\mathbf{k}} \mathbf{m}_{\mathbf{k}} e^{i\mathbf{k} \cdot \mathbf{r}} \quad \mathbf{m}_{\mathbf{k}} = \int_{\nu} d\mathbf{r} \mathbf{M}(\mathbf{r}) e^{-i\mathbf{k} \cdot \mathbf{r}} \quad (3.8)$$

$$\mathbf{M}(\mathbf{r}) = \int_{\nu} d\mathbf{r}' \delta(\mathbf{r} - \mathbf{r}') \mathbf{M}(\mathbf{r}') \quad \mathbf{m}_{\mathbf{k}} = \sum_{\mathbf{k}'} \delta_{\mathbf{k}, \mathbf{k}'} \mathbf{m}_{\mathbf{k}'} \quad (3.9)$$

$$\delta(\mathbf{r} - \mathbf{r}') = \frac{1}{\nu} \sum_{\mathbf{k}} e^{i\mathbf{k} \cdot (\mathbf{r} - \mathbf{r}')} \quad \delta_{\mathbf{k}, \mathbf{k}'} = \frac{1}{\nu} \int_{\nu} d\mathbf{r} e^{i(\mathbf{k} - \mathbf{k}') \cdot \mathbf{r}} \quad (3.10)$$

where ν is the integration volume.

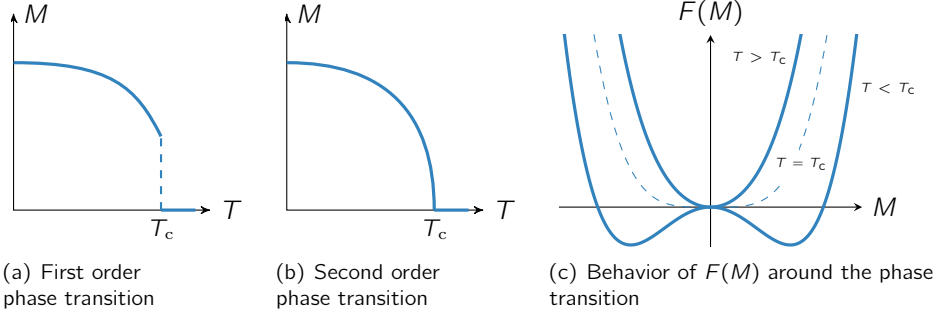


Figure 3.1: Temperature dependence of order parameter M at first order (a) and second order (b) phase transitions. Designs taken from [19]. Panel (c) shows the behavior of the free energy around a second order phase transition at T_c . Above and at T_c the order parameter M vanishes. For $T > T_c$, a finite magnetization arises.

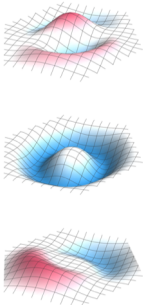
3.2. GINZBURG-LANDAU THEORY

Originally formulated as a model for superconductivity, Ginzburg-Landau theory is now widely used throughout solid state physics to describe phase transitions. It is based on Lev Landau’s phenomenological mean-field theory to describe second order phase transitions, which is based on a power series expansion of the free energy in terms of *spatially uniform* order parameters for the transition of interest [19, 78]. The series expansion is motivated, because the order parameter is small around the phase transition. For example, the textbook free energy of Landau-theory, sometimes simply called Landau function, of ferromagnetism, is given by [79]

$$F(\mathbf{M}) = F_0 + a(T)\mathbf{M}^2 + b\mathbf{M}^4. \quad (3.11)$$

Because states *up* and *down* are energetically the same due to time reversal symmetry, only even powers occur. While $a(T)$ is temperature dependent, F_0 and b are constants with $b > 0$ assumed. Second order phase transitions are characterized by a continuous change in the order parameter at a critical temperature T_c from zero in the disordered phase ($T > T_c$) to a finite value in the ordered phase ($T < T_c$), cf. figure 3.1(b). In Landau-theory, the quantity with such a behavior is the minimum position or mean-field \mathbf{M}^{mf} of the free energy (3.11). The parameter $a(T)$ is constructed proportional to $(T - T_c)$, so that $a(T) > 0$ corresponds to $T > T_c$ and $a(T) < 0$ to $T < T_c$. Those two cases are shown in figure 3.1(c). Note that Landau-theory is a mean-field theory, which means, that all spins “feel” the same averaged field generated by all their neighbors, here proportional to the magnetization.

In studying fluctuations, which we will see later play a significant role in stabilizing the skyrmion lattice, the more general case of *spatially dependent* local



3. Theoretical Description

order parameters needs to be addressed, i.e., $\mathbf{M}(\mathbf{r})$ in this case. Following and using notations of [7, 80], the free energy G can generally be described by the partition function Z via

$$Z = e^{-G} = \int \mathcal{D}\mathbf{M} e^{-F[\mathbf{M}]}. \quad (3.12)$$

$F[\mathbf{M}]$ is called the free energy functional and respects the fundamental symmetries of the system. The free energy depends on magnetic field and temperature, and the state that minimizes G is the one taken by the system in thermal equilibrium. The mean-field approximation is then obtained by applying the stationary-phase approximation to (3.12), leading to

$$e^{-G} \approx e^{-F[\mathbf{M}^{\text{mf}}]} \\ G \approx \min_{\mathbf{M}(\mathbf{r})} F[\mathbf{M}] \equiv F[\mathbf{M}^{\text{mf}}]. \quad (3.13)$$

where the stationary solution \mathbf{M}^{mf} satisfies the mean-field equation

$$\left. \frac{\partial F[\mathbf{M}]}{\partial \mathbf{M}} \right|_{\mathbf{M}^{\text{mf}}} = 0. \quad (3.14)$$

Going beyond mean-field means to include corrections in terms of thermal fluctuations. The leading order correction is given by Gaussian fluctuations and the free energy takes the form

$$G \approx F[\mathbf{M}^{\text{mf}}] + \frac{1}{2} \ln \det \left(\frac{\delta^2 F}{\delta \mathbf{M} \delta \mathbf{M}} \right) \Big|_{\mathbf{M}^{\text{mf}}}. \quad (3.15)$$

The formulation with a now spatially dependent order parameter $\mathbf{M}(\mathbf{r})$ leads to the difference between Landau- and Ginzburg-Landau theory, namely non vanishing gradient terms in the free energy functional. The admissibility of their order and kind depends on the symmetries of the system of interest. The Ginzburg-Landau free energy functional of a ferromagnet analogous to (3.11) reads

$$F[\mathbf{M}(\mathbf{r})] = \int d\mathbf{r} \left(r_0 \mathbf{M}(\mathbf{r})^2 + J(\nabla \mathbf{M}(\mathbf{r}))^2 + U \mathbf{M}(\mathbf{r})^4 - \mathbf{B} \mathbf{M}(\mathbf{r}) \right) \quad (3.16)$$

where $\mathbf{M}(\mathbf{r})^4 = (\mathbf{M}(\mathbf{r}) \cdot \mathbf{M}(\mathbf{r}))^2$ and the gradient term is written in a shorthand notation for $(\nabla \mathbf{M}(\mathbf{r}))^2 = \partial_{r_i} M_j(\mathbf{r}) \partial_{r_i} M_j(\mathbf{r})$. Note, that the gradient term corresponds to the exchange term (1.2) already mentioned in section 1.1. Again, the pre-factor U of the highest power of \mathbf{M} needs to be chosen positive to obtain a stable system. \mathbf{B} is the magnetic field which makes $-\mathbf{B} \mathbf{M}(\mathbf{r})$ the well known Zeeman-term. As already mentioned in the summary of section 1.3, in real systems everything depends somewhat on temperature and so do all these pre-factors. As we are interested in the vicinity of the phase transition, one can

linearize all temperature dependencies around the critical temperature. In this phenomenological theory, only a linear temperature dependence of r_0 remains, i.e., $r_0 \propto (T - T_c)$ like $a(T)$ was in (3.11). Because of this linearization and even negligence of smaller temperature dependences, the mean-field critical temperature varies slightly compared to the true experimental critical temperature.

At zero magnetic field, (3.16) possesses symmetries with respect to $\mathbf{M}(\mathbf{r}) \rightarrow -\mathbf{M}(\mathbf{r})$ and is translationally and rotationally invariant with an $O(3)$ -symmetry. An applied magnetic field reduces that symmetry to $O(2)$, leaving only rotations around the axis defined by \mathbf{B} . Also, only a combined symmetry transformation of $\mathbf{M}(\mathbf{r}) \rightarrow -\mathbf{M}(\mathbf{r})$ and $\mathbf{B} \rightarrow -\mathbf{B}$ is allowed. An emphasis should be put on spatial symmetries, that are not only translation and rotation symmetries, but especially inversion symmetry $\mathbf{r} \rightarrow -\mathbf{r}$. This is the key symmetry that is broken in chiral magnets.

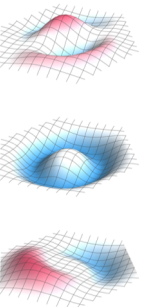
Before we write down the full Ginzburg-Landau free energy functional for chiral magnets including the aforementioned Dzyaloshinskii-Moriya interaction equation (1.4), two additional types of contributions to the free energy functional are first presented and discussed in more detail: dipolar interactions and crystal anisotropies

3.3. DIPOLAR INTERACTIONS

In contrast to the exchange and Dzyaloshinskii-Moriya interactions, dipolar interaction has a long-range nature generally resulting in the need for a more elaborate effort in calculations and especially simulations. Their ramifications, however, have significant consequences. In this thesis, we find them in particular responsible for the splitting of resonance peaks in the conical phase which otherwise would be degenerate. But already on the mean-field level, their influences are quite noticeable, especially when dealing with skyrmions, whose magnetic profile changes due to them. The space in the phase diagram taken by skyrmions in thin films increases with increasing dipole-dipole strength [81].

For the discussions in this text, their influences on magnons and in particular ferromagnetic resonances is important. Already in 1947, Charles Kittel studied their influence in a ferromagnet [82]. In that paper, he commented on experiments conducted by J. H. E. Griffiths in the 1940s which showed unexpected values of resonance frequencies, that were two to six times larger than the Larmor frequency, cf. equation (4.13) later in the text. Kittel became aware that magnetization was large and a differentiation between internal and external fields had to be made. The former is strongly influenced by the sample geometry. Before giving a more detailed account of this revelation, we first provide a more general introduction to magnetic dipoles and dipolar interaction.

Microscopic magnetic dipoles can be introduced in two different, but equivalent ways [83]. One option is to see a dipole as a circular current loop whose radius



3. Theoretical Description

is decreased while simultaneously increasing the current strength keeping the magnetic dipole moment constant. The second possibility is to consider two magnetic monopoles¹ which approach each other while their magnetic charge is increased to keep its dipole moment here constant as well. Both approaches ultimately result in a point-like object, that creates the magnetic field

$$\mathbf{B}(\mathbf{r}) = \frac{\mu_0}{4\pi} \frac{3\hat{\mathbf{r}}(\boldsymbol{\mu} \cdot \hat{\mathbf{r}}) - \boldsymbol{\mu}}{|\mathbf{r}|^3} \quad (3.17)$$

given in SI-units. cgs-units lack the pre-factor of $\frac{\mu_0}{4\pi}$. The magnetic dipole moment is given by $\boldsymbol{\mu}$, μ_0 is the magnetic vacuum permeability and the point-dipole is situated at the origin. The energy contribution of a magnetic dipole to an external magnetic field reads

$$E_{\text{dipole}} = -\boldsymbol{\mu} \cdot \mathbf{B}^{\text{ext}}. \quad (3.18)$$

If the external field is generated by a second dipole $\boldsymbol{\mu}_2$, then the energy between those two dipoles is given by

$$E_{\text{DD}} = -\frac{\mu_0}{4\pi} \boldsymbol{\mu}_1 \cdot \frac{3\hat{\mathbf{r}}(\boldsymbol{\mu}_2 \cdot \hat{\mathbf{r}}) - \boldsymbol{\mu}_2}{|\mathbf{r}|^3} = \frac{\mu_0}{4\pi} \boldsymbol{\mu}_1 \left(\frac{1_3 - 3\hat{\mathbf{r}} \otimes \hat{\mathbf{r}}}{|\mathbf{r}|^3} \right) \boldsymbol{\mu}_2. \quad (3.19)$$

The operation \otimes is the tensor product and 1_3 is the unit-matrix in 3 dimensions. With electrons, having an intrinsic magnetic moment of about one μ_B and typical distances on the length scale of \AA , yields energies of no more than 10^{-4} eV [18], it is quite small compared to the electrostatic interaction and also, typically, a thousand times smaller than the exchange coupling. But because exchange interaction is short- and dipolar interaction long-ranged, as it only falls off as the inverse cube of the separation, dipolar interaction becomes important for large samples and is especially responsible for the domain formation in ferromagnets.

DEMAGNETIZATION FIELDS AND FACTORS

In macroscopic solids, there exists a vast number of either electrons or atoms, that carry spins contributing to the dipole-dipole energy. This makes it virtually impossible to calculate the true magnetic field created by all those microscopic dipoles. Luckily, ellipsoidal samples pose a special case. When a sample is brought into an external magnetic field \mathbf{H}^{ext} parallel to one of the (semi-)principal axes of the sample, then all spins align and collectively form a field, the so-called *demagnetization field* \mathbf{H}^{dem} , that points exactly opposite to \mathbf{H}^{ext} . The internal field is given by simply adding these both fields:

$$\mathbf{H}^{\text{int}} = \mathbf{H}^{\text{ext}} + \mathbf{H}^{\text{dem}}. \quad (3.20)$$

¹So far, magnetic monopoles as elementary particles have never been observed. The closest thing are Dirac monopoles [84], which are monopoles with an infinitesimally thin flux line connecting two magnetic monopoles of opposite charge. As an example, they can be found in spin-ice [85, 86]. In chiral magnets, monopoles may also occur from an emergent magnetic field which is due to an emergent electrodynamics in the skyrmion phase [87]. There, individual skyrmions carry a quantized amount of emergent flux.

3.3. Dipolar Interactions

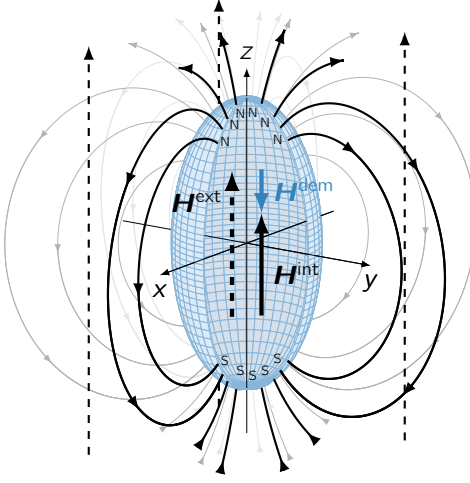


Figure 3.2: This figure illustrates the demagnetization effect inside an ellipsoidal, magnetizable sample. When subjected to an external magnetic field \mathbf{H}^{ext} (dashed lines), the microscopic elementary magnets align. Due to this alignment, neighboring “north and south poles” cancel each other, except at the boundaries of the sample. Between these open ends, a magnetic field arises similar to an electric charge polarization. This is the *demagnetization field* \mathbf{H}^{dem} . Because it is anti-parallel to the external magnetic field, the internal magnetic field \mathbf{H}^{int} is reduced.

This opposing direction can be explained as follows and is illustrated in [figure 3.2](#). When subjected to \mathbf{H}^{ext} , a magnetized body produces effective magnetic surface charges. This is because, when all microscopic internal elementary magnets align, neighboring “north and south poles” cancel each other everywhere except at the boundaries of the sample. From the outside, this results in a collective magnetic moment which aligns parallel to \mathbf{H}^{ext} . Inside the material, the surface charges, too, create a field with field lines also starting at the accumulated effective surface charges. This direction is now opposite to \mathbf{H}^{ext} .

The demagnetization field can be characterized by demagnetization factors N_x , N_y and N_z which respectively correspond to the directions of the (semi-)principal axes \hat{x} , \hat{y} and \hat{z} of the sample. Then \mathbf{H}^{dem} can be written as

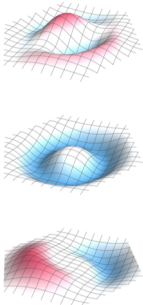
$$\mathbf{H}^{\text{dem}} = - \begin{pmatrix} N_x & 0 & 0 \\ 0 & N_y & 0 \\ 0 & 0 & N_z \end{pmatrix} \cdot \mathbf{M} =: -\underline{N} \cdot \mathbf{M}. \quad (3.21)$$

The demagnetization factors do not depend on the size of the sample, but only on its shape and proportions. They abide the restriction that their sum equals unity in SI-units and 4π in cgs-units. Here, we use the former:

$$N_x + N_y + N_z = 1. \quad (3.22)$$

EXAMPLES OF DEMAGNETIZATION FACTORS:

To familiarize oneself with their values, we give three typical shapes as examples: a perfect sphere, a rod and a disk. The sphere is rotationally invariant which means, that all directions should be treated equally, i.e., also their demagne-



3. Theoretical Description

tization factors are equal, namely $N_x = N_y = N_z = \frac{1}{3}$. Having the picture of surface charges in mind, that generate the demagnetizing field, it is natural that this field becomes weaker, when those charges are further apart. The demagnetization factor corresponding to an axis along an otherwise rotationally symmetric rod should therefore decrease compared to the other two. In an infinitely long rod, this would yield zero for that direction, e.g., $N_x = N_y = 0$ and $N_z = 1$. For a disc, or a finitely thick but infinitely extended plane, the opposite case applies. The two directions of infinite or very large extent correspond to a vanishing demagnetization factor, while the remaining one becomes unity.

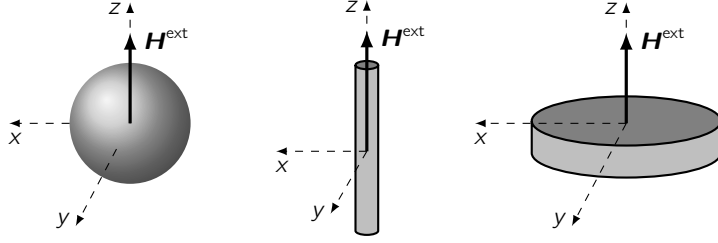


Figure 3.3: Examples of three different shapes and their corresponding demagnetization factors.

Left: perfect sphere with $N_x = N_y = N_z = \frac{1}{3}$,

Middle: rod or infinite cylinder with $N_x = N_y = \frac{1}{2}$ and $N_z = 0$,

Right: disk or infinite surface (dark gray) with $N_x = N_y = 0$ and $N_z = 1$.

Remembering the relation $\mu_0 \mathbf{H}^{\text{eff}} = -\frac{\delta F}{\delta \mathbf{M}}$ between free energy, effective magnetic field and magnetization, gives a contribution of

$$F_{\text{DD}, |\mathbf{k}| \ll 1/L}[\mathbf{M}] = \int d\mathbf{r} \frac{1}{2} \mu_0 \mathbf{M} \cdot \underline{\mathbf{N}} \cdot \mathbf{M} \quad (3.23)$$

to the free energy. The index $|\mathbf{k}| \ll 1/L$ indicates, that this is the homogeneous contribution. Homogeneous in the sense, that the modulation is small compared to the sample size L .

Note, that this is not only true for a strictly parallel spin alignment, but also for modulated spin textures like a helix. In such a case, \mathbf{M} has to be replaced by only the homogeneous net-component \mathbf{M}_0 of \mathbf{M} to obtain the internal magnetic field. Changes in the external field that are of a homogeneous nature, i.e., with zero wave-vector $\mathbf{k} = 0$ or at least $|\mathbf{k}| \ll 1/L$ like in ferromagnetic resonance experiments, imply a homogeneous change of magnetization inside the sample. Therefore, this dynamics can be described using demagnetization factors as well. For local excitations, i.e., $|\mathbf{k}| \gg 1/L$, one needs to take a closer look at the field generated by the spins themselves, and the explicit dipole-dipole interaction needs to be considered.

FULL DIPOLE-DIPOLE INTERACTION

Calculating the full contribution in real space in a microscopic way is more complicated, especially due to its long ranged influence. Even in small and discrete systems, dipole-dipole interaction can pose cumbersome problems. Calculations in Fourier space offer a less expensive approach, which we will therefore use throughout this thesis. The contribution to the free energy is given by

$$F_{\text{DD}, |\mathbf{k}| \gg 1/L}[\mathbf{m}] = \frac{1}{2} \frac{\mu_0}{\nu} \sum_{\mathbf{k}} \frac{(\mathbf{m}_{\mathbf{k}} \cdot \mathbf{k})(\mathbf{m}_{-\mathbf{k}} \cdot \mathbf{k})}{|\mathbf{k}|^2}. \quad (3.24)$$

A detailed derivation is given in [appendix A](#). Note that this expression is valid for 3-dimensional bulk samples. In the 2-dimensional case, for a plane perpendicular to the $\hat{\mathbf{e}}_z$ -direction, of finite thickness d and infinite extent, things change to [\[81\]](#)

$$F_{\text{DD}, |\mathbf{k}| \gg 1/L}^{2\text{-dim}}[\mathbf{m}] = \frac{\mu_0}{2\nu} d \sum_{\mathbf{k}} \mathbf{m}_{\mathbf{k}} \left[\hat{\mathbf{e}}_z \otimes \hat{\mathbf{e}}_z + \left(1 - \frac{e^{d|\mathbf{k}|}}{d|\mathbf{k}|} \right) (\mathbf{k}_z \otimes \mathbf{k}_z - \hat{\mathbf{e}}_z \otimes \hat{\mathbf{e}}_z) \right] \mathbf{m}_{-\mathbf{k}} \quad (3.25)$$

with $\mathbf{k} \in \mathbb{R}^2$.

Together with results from the previous paragraph we can obtain the expression

$$F_{\text{DD}}[\mathbf{m}] = \frac{1}{2} \frac{1}{\nu} \sum_{\mathbf{k}} \mathbf{m}_{\mathbf{k}}^i \chi_{\text{dip}, ij}^{-1} \mathbf{m}_{-\mathbf{k}}^j \quad (3.26)$$

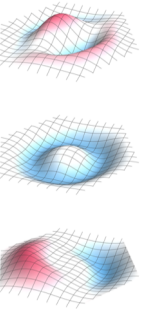
with

$$\chi_{\text{dip}, ij}^{-1}(\mathbf{k}) = \mu_0 \begin{cases} \frac{\mathbf{k}_i \mathbf{k}_j}{|\mathbf{k}|^2} & \text{for } |\mathbf{k}| \gg 1/L \\ N_{ij} & \text{for } |\mathbf{k}| \ll 1/L \end{cases} \quad (3.27)$$

for the free energy of dipolar interactions in the limits of very large or very small wavelengths compared with the sample size L . The intermediate regime is more difficult to address because then explicit surface terms enter the calculations. Note, that the demagnetization matrix with $\text{Tr}[N_{ij}] = 1$ is technically speaking only diagonal when coordinate axes align with the principal axes of the ellipsoid. Cases where this is not true are, however, not considered in this work.

3.4. CRYSTAL ANISOTROPIES

In terms of energy scales (see [section 3.5](#)) crystal anisotropies form the lower end, hence only play a minor role and can often be neglected in effective calculations. However, they play a big phenomenological role as they are responsible for pinning directions of helix pitches at zero or low magnetic fields, as well as skyrmion lattice \mathbf{Q} -vectors.



3. Theoretical Description

Studies on the theory of crystal anisotropies in ferromagnets have been performed already around the 1930's by, for example, Akulov [88]. The energy term deemed to determine the preferred direction of the spontaneous magnetization for temperatures below the Curie temperature has the form [89, 90]

$$f_{K'} = K'(\alpha_1^2\alpha_2^2 + \alpha_2^2\alpha_3^2 + \alpha_3^2\alpha_1^2) = -\frac{K'}{2}(\alpha_1^4 + \alpha_2^4 + \alpha_3^4) \quad (3.28)$$

$$= -\frac{K'}{2}(\sin^2 2\vartheta + \sin^4 \vartheta \sin^2 2\varphi). \quad (3.29)$$

Terms α_i are the direction cosines of the direction of the magnetization with respect to the cubic edges being the coordinate axes. In the last line one passed to an angle description with ϑ and φ respectively being the angle between \mathbf{M} and the main axis and the angle in the basal plane, cf. figure 4.3 on page 49. $f_{K'}$ is the work per cm^3 necessary to rotate the magnetization from $[100]$ to the direction $\alpha_1, \alpha_2, \alpha_3$. A more modern representation is given by

$$F_{\text{cub}_0}[\mathbf{M}(\mathbf{r})] = K \int d\mathbf{r} \frac{1}{M^4} (M_x^4 + M_y^4 + M_z^4) \quad (3.30)$$

with *anisotropy constant* $K = -K'/2$. This term may fix the direction of spontaneous magnetization and defines easy and hard axes, but does not necessarily give a preferred direction of the helix pitch.

In section 1.3 we have already seen that, at zero field, helices in chiral magnets can orient along a $\langle 111 \rangle$ direction, like in MnSi, or along $\langle 100 \rangle$, like in Cu_2OSeO_3 . While F_{cub_0} also does the job, there exist further popular terms and one of the free energy functional in lowest order spin-orbit coupling, that describes this behavior, is given by

$$\begin{aligned} F_{\text{cub}_1}[\mathbf{M}(\mathbf{r})] &= c_1 \int d\mathbf{r} \mathbf{M}(\mathbf{r}) (\partial_x^4 + \partial_y^4 + \partial_z^4) \mathbf{M}(\mathbf{r}) \\ &= c_1 \frac{1}{\nu} \sum_{\mathbf{q}} (q_x^4 + q_y^4 + q_z^4) |\mathbf{m}_{\mathbf{q}}|^2. \end{aligned} \quad (3.31)$$

The sign of the pre-factor determines the pinning direction, which in turn can easily be seen by minimizing the q -sum for a fixed $\mathbf{q} \equiv \mathbf{Q}$ that is the helix pitch. Therefore, a minimum for a negative (positive) pre-factor is obtained for $\mathbf{Q} \parallel \langle 111 \rangle$ ($\mathbf{Q} \parallel \langle 100 \rangle$).

Of course, there are many more possible anisotropy terms which are allowed by symmetries of the $P2_13$ space group. An organized list can be found in appendix A of [80]. At this point, we would like to mention one more term also considered in one of the original theory of helical magnetic structures by Bak and Jensen

[26], namely

$$\begin{aligned} F_{\text{cub}_2} [\mathbf{M}(\mathbf{r})] &= c_2 \int d\mathbf{r} \left((\partial_x M_x(\mathbf{r}))^2 + (\partial_y M_y(\mathbf{r}))^2 + (\partial_z M_z(\mathbf{r}))^2 \right) \\ &= c_2 \frac{1}{\nu} \sum_{\mathbf{q}} (q_x^2 m_{\mathbf{q}}^x m_{-\mathbf{q}}^x + q_y^2 m_{\mathbf{q}}^y m_{-\mathbf{q}}^y + q_z^2 m_{\mathbf{q}}^z m_{-\mathbf{q}}^z). \end{aligned} \quad (3.32)$$

It also fixes the helix pitch direction to $\langle 111 \rangle$ for $c_2 < 0$ and to $\langle 001 \rangle$ for $c_2 > 0$.

An interesting consequence of cubic anisotropies in cubic chiral magnets is a crossover between the purely helical and the conical phase at a particular magnetic field strength H_{c1} . Without anisotropies, an infinitesimally small magnetic field suffices to align the helices along said field. Given cubic anisotropies, for example F_{cub_1} with a negative pre-factor, it is not completely clear from the start where the helices ultimately point to at small magnetic fields, but depends on several factors. One big factor is the difference between field-cooling (fc) with a subsequent lowering of the magnetic field and zero-field-cooling (zfc) followed by an increase of the magnetic field.

Considering MnSi with its preferred $\langle 111 \rangle$ direction as an example, the following cases can occur. Field-cooling the sample into the conical phase with $\mathbf{H} \parallel \langle 111 \rangle$ and then decreasing the magnetic field down to zero actually does not yield a phase transition at all, because the helix already points in the preferred crystal direction. As soon as \mathbf{H} deviates from that direction, the story is different. \mathbf{H} close to a $\langle 111 \rangle$ direction leads to a simple rearrangement of the pitch towards the closest $\langle 111 \rangle$ direction for fields below H_{c2} . For fields along other high symmetry directions like $\langle 110 \rangle$ (red line in figure 3.4) and $\langle 100 \rangle$ (blue line in figure 3.4), the helix “does not know” which $\langle 111 \rangle$ direction to take and domains with helices pointing in different directions get created. As a result, two kinds of domains arise for $\mathbf{H} \parallel \langle 110 \rangle$ and even four for $\mathbf{H} \parallel \langle 100 \rangle$. The result is a spontaneous transition, i.e., of second order [91].

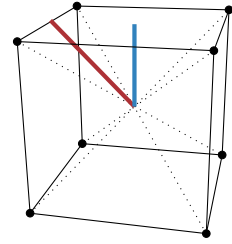
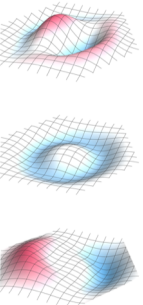


Figure 3.4: Special high symmetry directions (see text for details).

Dotted: $\langle 111 \rangle$
Red: $\langle 110 \rangle$
Blue: $\langle 100 \rangle$

Zero-field-cooling the sample achieves already an initial multi-domain state with four domains. What happens when increasing the magnetic field then also depends on the direction of \mathbf{H} with respect to high symmetry directions. Ultimately, there is always a transition at a finite critical field H_{c2} for fields oriented along high symmetry directions [92]. These phenomena can therefore lead to different phase diagrams depending on the process used to trace and traverse transitions.

Because the critical field depends on temperature and, depending on the material, may have a non-zero slope with respect to temperature, the cooling process itself may already suppress the helical phase.



3. Theoretical Description

The orientation of the skyrmion lattice is characterized by the direction of the applied magnetic field to which this two dimensional lattice lies perpendicular with the center spin of a skyrmion pointing anti-parallel to the field direction. This leaves rotational degrees of freedom around the field axis. This liberty is destroyed by cubic anisotropies that, again, try to align pitch vectors and certain crystal directions. To fix the arbitrary rotation angle ϕ to a preferred direction, one needs an effective potential of the form $\cos(6n\phi + \phi_0)$ with $n = 1, 2, \dots$ and constant phase ϕ_0 , to accommodate the six-fold symmetry of the skyrmion lattice. One example of such a term in lowest order perturbation theory is [75]

$$F_{\text{cub}_3}[\mathbf{M}(\mathbf{r})] = c_3 \int d\mathbf{r} \left((\partial_x^3 \mathbf{M}(\mathbf{r}))^2 + (\partial_y^3 \mathbf{M}(\mathbf{r}))^2 + (\partial_z^3 \mathbf{M}(\mathbf{r}))^2 \right). \quad (3.33)$$

3.5. FREE ENERGY OF CHIRAL MAGNETS

In this section, we present the Ginzburg-Landau description of chiral magnets, which is the basis for numerical calculations throughout this thesis. The relevant terms of the free energy functional have already been introduced in previous sections. They will be partly summarized and collected and rescaled, following the supplementary information of [7] as well as [80, 93], to reduce the number of parameters of the theory.

The free energy functional of an ordinary ferromagnet was stated in [section 3.2](#). As chiral magnets lack spatial inversion symmetry, additional and in particular odd powered gradient terms are allowed. The most relevant one was introduced in [section 1.1](#), the Dzyaloshinskii-Moriya interaction

$$F_{\text{DM}}[\mathbf{M}(\mathbf{r})] = \int d\mathbf{r} 2D\mathbf{M} \cdot (\nabla \times \mathbf{M}). \quad (3.34)$$

The additional factor of two has been introduced to yield a helix pitch of unity in later calculations. Together with dipolar interaction $F_{\text{DD}}[\mathbf{M}]$ and cubic anisotropy $F_{\text{cub}}[\mathbf{M}]$ terms, the free energy is given by

$$F[\mathbf{M}, t] = F_0[\mathbf{M}] + F_{\text{DD}}[\mathbf{M}] + F_{\text{cub}}[\mathbf{M}] + F_{\text{excitation}}[\mathbf{M}, t]. \quad (3.35)$$

The term $F_0[\mathbf{M}]$ contains the quadratic and quartic Ginzburg-Landau terms, as well as exchange, Dzyaloshinskii-Moriya and Zeeman interaction terms:

$$F_0[\mathbf{M}] = \int d\mathbf{r} \left(r_0 \mathbf{M}^2 + J(\nabla \mathbf{M})^2 + 2D\mathbf{M} \cdot (\nabla \times \mathbf{M}) + U(\mathbf{M}^2)^2 - \mu_0 \mathbf{H}^{\text{ext}} \cdot \mathbf{M} \right) \quad (3.36)$$

It alone would suffice to generate the sought-after magnetic structures. The time dependent term $F_{\text{excitation}}[\mathbf{M}, t]$ represents additional contributions of, for

example, oscillating magnetic or electric fields, that may excite the system. For now, we focus on $F_0[\mathbf{M}]$ and introduce a rescaling of variables to lower the number of unknown parameters. We follow hereby [7].

As was previously motivated, Dzyaloshinskii-Moriya and exchange interaction compete against each other resulting in a helical arrangement. Its pitch Q is given by $Q = D/J$ and is therefore quite small since we consider D to be much smaller than J , which is also a necessary requirement for the validity of this gradient expansion of the free energy. Such a representation is valid for magnetic structures, where the magnetization is locally almost ferromagnetic [26]. Remember also, that D and J are temperature dependent which is transferred to Q as well. The first step of rescaling is to measure distances in units of helix pitch, namely $\tilde{r} = Q\mathbf{r}$. Reducing the number of parameters is achieved by rescaling magnetization and magnetic field as $\tilde{\mathbf{M}} = [U/JQ^2]^{1/2}\mathbf{M}$ and $\tilde{\mathbf{H}}^{\text{ext}} = [U/(JQ^2)^3]^{1/2}\mathbf{H}^{\text{ext}}$. This leads to a constant global pre-factor $\kappa = J^2Q/U$ and a new parameter $t = r_0/(JQ^2) - 1 \propto T - T_c$, which is a measure for the distance to the mean-field phase transition at $t = 0$. Negative t then yields a finite order parameter. The finite result is given by

$$F_0[\tilde{\mathbf{M}}] = \kappa \int d\tilde{r} \left((t+1)\tilde{\mathbf{M}}^2 + (\nabla\tilde{\mathbf{M}})^2 + 2\tilde{\mathbf{M}} \cdot (\nabla \times \tilde{\mathbf{M}}) + (\tilde{\mathbf{M}}^2)^2 - \mu_0\tilde{\mathbf{H}}^{\text{ext}} \cdot \tilde{\mathbf{M}} \right) \quad (3.37)$$

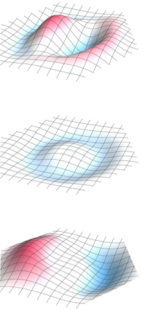
Note, that only a linear explicit temperature dependence is kept in the parameters, because one linearizes all T dependencies around T_c in the Ginzburg-Landau approach. Dipolar interaction (3.26) obtains an additional pre-factor of $1/(JQ^2) =: 1/\alpha$ when using rescaled quantities. That means, that whenever a quantity is expressed in rescaled units $\alpha = 1$, and whenever considering physical units $\alpha = JQ^2$. See also [appendix A](#).

3.6. MEAN-FIELD ANALYSIS & FLUCTUATIONS

On a mean-field level, the conical or helical state is always the state with the lowest minimum. This is especially important in comparison to the skyrmion lattice state. At this point we only give summarized statements but a more detailed discussion can be found in [appendix B](#), as well as in [7, 80, 93]. The necessary steps to see that the ground state is achieved by a helical solution is to rewrite $F_0[\mathbf{M}]$ as a sum of a constant and several quadratic terms creating a lower bound. Plugging in a helical ansatz like

$$\tilde{\mathbf{M}}_{\text{hel}}[\mathbf{r}] = \begin{pmatrix} A \cos Qz \\ A \sin Qz \\ \tilde{M}_0 \end{pmatrix} \quad (3.38)$$

with $\mathbf{H}^{\text{ext}} \parallel \hat{\mathbf{e}}_z$ then minimizes all the quadratic terms individually. Another significant result is the border of the phase transition between the helical/conical



3. Theoretical Description

and the field polarized phase. The critical field value \tilde{H}_{c2} follows a square root behavior:

$$\mu_0 \tilde{H}_{c2} = \sqrt{-2t}. \quad (3.39)$$

The zero-field phase transition happens at $t = 0$ which is obvious due to its construction as a parameter proportional to $T - T_c$. Including dipolar interaction does not change this square root behavior, merely the pre-factor:

$$\mu_0 \tilde{H}_{c2} = \sqrt{-2t} \left(1 + \frac{\mu_0 N_z}{2\alpha} \right). \quad (3.40)$$

It can, however, be absorbed when considering the internal field H_{c2}^{int} . Rescaling leads to a helix pitch $Q = 1$. Choosing the chiral basis²

$$\hat{e}_{\pm} = \frac{1}{\sqrt{2}}(\hat{e}_x \pm i\hat{e}_y)$$

lets us rewrite [equation \(3.38\)](#) in the form

$$\tilde{M}_{\text{hel}}(\mathbf{r}) = \tilde{M}_0 \hat{e}_z + A \hat{e}^- e^{i\mathbf{Q}\mathbf{r}} + A^* \hat{e}^+ e^{-i\mathbf{Q}\mathbf{r}} \quad (3.41)$$

leads us more easily to an expression for the homogeneous magnetization of the form

$$\tilde{M}_0 = \frac{\mu_0 \tilde{H}_z}{2 + \frac{\mu_0}{\alpha} N_z}. \quad (3.42)$$

This leads to an almost temperature independent susceptibility ($\chi_{\text{con}} = M_0/H_z$) in the conical phase

$$\tilde{\chi}_{\text{con}} = \frac{\mu_0}{2 + \frac{\mu_0}{\alpha} N_z}. \quad (3.43)$$

Compared to the dominating temperature dependence of H_{c2} , the conical susceptibility can indeed be seen as a constant [21]. The translation to physical units is done via $\chi_{\text{con}} = \tilde{\chi}_{\text{con}}/\alpha$ and results in

$$\chi_{\text{con}} = \frac{\mu_0}{2\alpha + \mu_0 N_z}, \quad (3.44)$$

where one should keep in mind, that the pre-factor conventions of the free energy functional play a role and are responsible for the maybe surprising appearance of the number 2 when compared to [37, 94]. These conventions, however and most importantly, were used in numerical implementations with regard to this thesis. Furthermore, since this section of the text still serves as an introduction to chiral magnets, we thought it be a good point to make the reader aware of different conventions. When discussing helimagnons in [part III](#), we will revisit the above quantities in a form which used in the cited publications.

²More and proper information on the chiral basis is given later in [section 8.2](#) and a list of identities can be found in [appendix D.2](#).

As basic helical approaches like (3.38) and (3.41) have proven to be the global minimum of the simple free energy defined by (3.37) or (3.36), a skyrmion solution like

$$\mathbf{M}_{\text{sky}}(\mathbf{r}) = \mathbf{M}_0 + \sum_{i=1}^{\infty} (\mathbf{M}_{\mathbf{Q}_i} e^{i\mathbf{Q}_i \cdot \mathbf{r}} + \text{c.c.}) \quad (3.45)$$

$$\approx \mathbf{M}_0 + \sum_{i=1}^3 |A_i| \left(\hat{\mathbf{n}}'_{\mathbf{Q}_i} \cos(\mathbf{Q}_i \cdot \mathbf{r} + \phi_i) - \hat{\mathbf{n}}''_{\mathbf{Q}_i} \sin(\mathbf{Q}_i \cdot \mathbf{r} + \phi_i) \right) \quad (3.46)$$

can obviously not be a global minimum on the mean-field level. Here, $\mathbf{M}_{\mathbf{Q}_i} = A_i(\hat{\mathbf{n}}'_{\mathbf{Q}_i} + i\hat{\mathbf{n}}''_{\mathbf{Q}_i})/2$ with complex amplitudes $A_i = |A_i| \exp(i\phi_i)$. The vectors $\hat{\mathbf{n}}'_{\mathbf{Q}_i}$ and $\hat{\mathbf{n}}''_{\mathbf{Q}_i}$ are orthogonal to each other.

To motivate the occurrence of a skyrmion lattice, we need to consider two points. First, an ansatz $\mathbf{M}_{\text{sky}}(\mathbf{r})$ like (3.45), which can be approximated to first order by the superposition of just three helices as in (3.46), is a local minimum of the free energy. Second, already Gaussian fluctuations around the mean-field lead to a small pocket in the phase diagram, where this skyrmion ansatz is favored compared to a helical ansatz. Those two points were addressed in [7]. Regarding the first point, the authors found that the phenomenological approximation (3.46), due to the six major peaks in the structure factor, locally minimizes the free energy. In particular, the three wave vectors \mathbf{Q}_1 , \mathbf{Q}_2 and \mathbf{Q}_3 form a tripod with mutual angles of 120° and the phases ϕ_i are fixed in a way so that the magnetization in the center of a skyrmion points anti-parallel to the external magnetic field. Furthermore, the three superposing helices are of identical chirality, leading to $\hat{\mathbf{n}}'_{\mathbf{Q}_i} \times \hat{\mathbf{n}}''_{\mathbf{Q}_i} = \mathbf{Q}_i$, and have the same amplitudes, i.e., $|A_1| = |A_2| = |A_3|$.

The previously mentioned angle of 120° between the helices is also a consequence of the minimization process, but can easier be motivated by an analogy to crystal formation out of a liquid phase. The latter is often driven by cubic interactions and can be written in momentum space as [19]

$$\sum_{\mathbf{G}, \mathbf{G}', \mathbf{G}''} \rho_{\mathbf{G}} \rho_{\mathbf{G}'} \rho_{\mathbf{G}''} \delta(\mathbf{G} + \mathbf{G}' + \mathbf{G}''),$$

with densities $\rho_{\mathbf{G}}$ and the \mathbf{G} are in some reciprocal lattice. If a finite uniform magnetization \mathbf{M}_0 is present, a similar mechanism can arise in chiral magnets as well. Some of the quartic terms of (3.38) have hence a similar structure and these terms cause a gain in energy, when the momenta form the proclaimed tripod as shown in figure 3.5, so that the delta function vanishes:

$$\sum_{\mathbf{Q}, \mathbf{Q}', \mathbf{Q}''} (\mathbf{M}_0 \cdot \mathbf{M}_{\mathbf{Q}}) (\mathbf{M}_{\mathbf{Q}'} \cdot \mathbf{M}_{\mathbf{Q}''}) \delta(\mathbf{Q} + \mathbf{Q}' + \mathbf{Q}'').$$

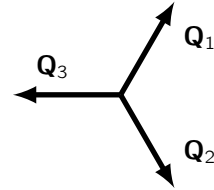
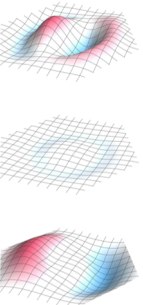


Figure 3.5: Basis vectors of the spin order in the skyrmion lattice phase.



3. Theoretical Description

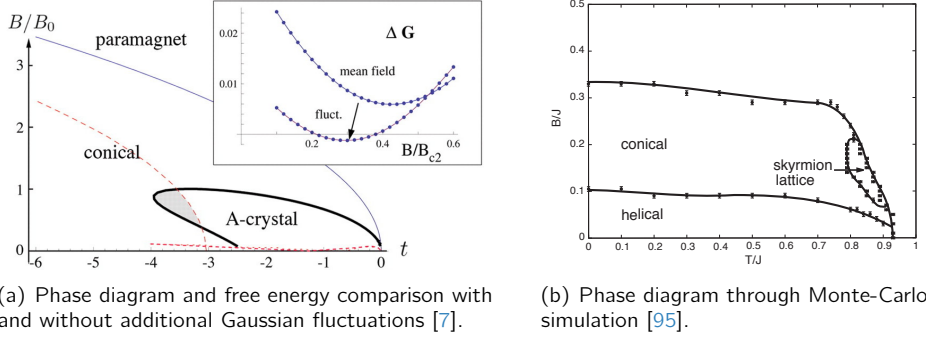


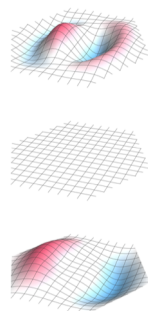
Figure 3.6: (a): The inset compares the energy of the skyrmion lattice and conical phase as a function of magnetic field for $t = -3.5$. Including Gaussian fluctuations leads to a small region, where the skyrmion lattice is energetically favorable. While in the main plot this region is the larger area labeled *A-crystal*, this part of the phase diagram needs to be subjected to the Ginzburg criterion, which is a measure for the reliability of the theory around the phase transition. The gray-shaded area indicates the part that is proven to be reliable leading to a stable, global minimum of the skyrmion lattice phase. (b): Performing Monte-Carlo simulations to obtain the magnetic phase diagram means to also include all orders of thermal fluctuations. While the method from (a) proves the existence of a skyrmion lattice phase, a Monte-Carlo simulation almost exactly reproduces the experimental phase diagram. Temperature and magnetic field were gauged to the ferromagnetic exchange coupling J .

FLUCTUATIONS

To address the second point, the authors of [7] considered Gaussian fluctuations around the mean-field, cf. [equation \(3.15\)](#), as a first order correction. This inclusion already suffices to obtain a pocket in the phase diagram, where a skyrmion lattice is energetically favored. This is shown in [figure 3.6\(a\)](#). The gray-shaded area of the phase diagram indicates the region in which not only the energy of the skyrmion solution is lower than the conical solution when including Gaussian fluctuations, but also is reliable according to the Ginzburg criterion. [Figure 3.6\(b\)](#) shows an even better calculation of the phase diagram via a classical Monte-Carlo study that natively incorporates higher order thermal fluctuations [95]. It resembles almost exactly the experimental phase diagrams.

PART II.

BASIC ASPECTS OF SPIN
WAVES



4

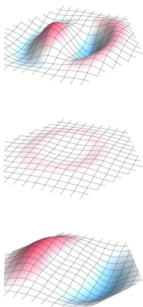
— INTRODUCTION TO SPIN WAVES —

This part draws on introductory chapters of references [96, 89, 13] and summarizes key points and properties of spin waves that widely overlap with the topic of this thesis.

A big motivation behind studying spin waves is their capability of carrying and processing information on the nanoscale, which is a similar goal to that of spintronics¹. A nice additional feature is the lack of necessity to move charge carriers to transfer information. This field is called magnonics and combines the study of waves and magnetism. Spin waves are interesting because of several characteristics that differ to those of light and sound waves. Their dispersion relation $\omega(\mathbf{k})$, for example, is highly dispersive, generally exhibits a gap, and can be anisotropic even if the magnetic medium is isotropic. It is not those aspects alone that spark the interest in spin waves, but also the prospect of miniaturization of technical devices, because the wavelengths of spin waves is several orders of magnitude smaller compared to electromagnetic waves [13]. Another advantage of magnonic devices is the ease with which they can be manipulated by an applied magnetic field.

The concept of spin waves was developed by Bloch around the year 1930 [97]. In his description they consist of one flipped spin compared to, and coherently distributed over, a large number of otherwise aligned spins. Most generally, they can be seen as excitations in a magnetic material. Classically, they are represented by a phase-coherent precession of microscopic magnetization vectors [13]. Holstein and Primakoff [98] as well as Dyson [99] were the first to interpret spin waves as quasiparticles called *magnons*, which turned out to be of bosonic nature. While those coherent magnons usually have distinct values for wave vector \mathbf{k} and energy $\hbar\omega$, where ω is the frequency of the exciting field, finite temperatures also lead to non-coherent thermal magnons. Their distribution over the \mathbf{k} and energy space is much broader, but they significantly influence thermodynamic properties of magnetically ordered materials. For example, early indirect evidence of spin

¹i.e., spin transport electronics



4. Introduction to Spin Waves

waves was found in thermodynamic properties, like the temperature dependence of magnetization which led to the $T^{3/2}$ Bloch law. Direct measurements of spin waves were, for example, performed by Griffiths in 1946 [100], using ferromagnetic resonance measuring homogeneous spin waves at $\mathbf{k} = 0$. Spin waves with a finite wave vector were verified via light scattering two decades later [101].

Hosts for spin waves are, of course, magnetic materials. Their properties can be well described via the magnetic susceptibility defined by (3.3). When placing a ferro- or ferrimagnetic material in a strong magnetic field, then this field is often strong enough to align all domains of spins parallel to the applied field. Furthermore, this prevents a changing magnetic field along the magnetization direction from affecting the magnetization altogether and the magnetization is said to be saturated. The system is, however, still susceptible to perturbations perpendicular to the field. Rapid changes lead to increasingly larger off-diagonal susceptibility contributions, which in turn lead to a more involved response of the system. Those conditions are typical for the propagation of dipolar spin waves. In case one only considers spin angular momentum, as is the case throughout this thesis, the two main interaction mechanisms are magnetic dipole-dipole coupling and some form of exchange interaction. The former is important for spin excitation with a long wavelength whereas the latter dominates when the wavelength is comparable to the spin-lattice spacing. Before we further elucidate their differences further, we go back and revisit precession and resonance in more detail.

4.1. PRECESSION

The orbital motion and the spin of electrons are almost solely responsible for the magnetic properties of most materials. Magnetic moments stemming from nuclear particles are generally smaller by a factor of 10^3 [96]. Because of the electron's subatomic nature, a rigorous description requires quantum mechanics. Their general behavior can, in the classical limit, be understood by taking a look at the classical analog of a spinning top. There, the force of gravity $\mathbf{F}_g = m\mathbf{G}$ given by the gravitational field \mathbf{G} acting on a mass m , induces a precessional motion that follows the equation of motion

$$\mathbf{d} \times \mathbf{F}_g = \boldsymbol{\tau} = \frac{d\mathbf{J}}{dt}, \quad (4.1)$$

where \mathbf{d} is the vector pointing along the rotation axis of the spinning top, and $\boldsymbol{\tau}$ is the torque generated by \mathbf{F}_g , which is equal to the change in angular momentum \mathbf{J} . This equation can be rewritten in the form

$$\frac{d\mathbf{J}}{dt} = \boldsymbol{\Omega} \times \mathbf{J}, \quad (4.2)$$

where $\boldsymbol{\Omega} = \omega_p \operatorname{sgn}(\mathbf{d} \cdot \mathbf{J})\hat{\mathbf{e}}_z$ points along the negative direction of gravity and ω_p is the angular precession frequency.

Adding an electric charge to the top generates a magnetic moment due to the rotation, which is influenced by magnetic fields. When dealing with elementary particles like electrons, their masses are so small, that one can neglect the effects of gravity and ultimately the magnetic field \mathbf{B} will take the place of the gravitational field \mathbf{G} and the spinning top becomes a magnetic moment $\boldsymbol{\mu}$.

The torque on $\boldsymbol{\mu}$ is given by

$$\boldsymbol{\tau} = \boldsymbol{\mu} \times \mathbf{B}. \quad (4.3)$$

The magnetic moment is proportional to angular momentum \mathbf{J} with proportionality constant γ called *gyromagnetic ratio*:

$$\boldsymbol{\mu} = \gamma \mathbf{J}, \quad (4.4)$$

with $\gamma < 0$ for a negative charge and positive otherwise. For the spinning top this would mean an identification of $\boldsymbol{\Omega} = -\gamma \mathbf{B}$. This leads to the well known precession equation for a magnetic moment in a magnetic field:

$$\frac{d\mathbf{J}}{dt} = \gamma \mathbf{J} \times \mathbf{B}. \quad (4.5)$$

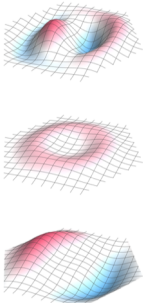
Strictly speaking, $\mathbf{J} = \mathbf{L} + \mathbf{S}$ consists of both orbital (\mathbf{L}) and spin (\mathbf{S}) angular momentum and their individual gyromagnetic ratios differ by a factor of two. Following the appropriate quantum mechanical calculations yields $\gamma_L = \frac{q}{2m_q}$ and $\gamma_S = \frac{q}{m_q}$, respectively, where q is the charge and m_q is the mass of the particle. Together, one can write $\boldsymbol{\mu} = \gamma_L \mathbf{L} + \gamma_S \mathbf{S} = \gamma_L (\mathbf{L} + 2\mathbf{S})$. Also, $\boldsymbol{\mu}$ and \mathbf{J} are not completely parallel anymore, when both kinds of angular momentum are involved. Luckily, only the component of $\boldsymbol{\mu}$ parallel to \mathbf{J} has a well-defined and measurable value, which makes (4.4) still valid with

$$\gamma = g \frac{q}{2m_q} = \text{sgn}(q) g \frac{\mu_B}{\hbar}, \quad (4.6)$$

where g is the so-called *Landé factor* or *g-factor* and μ_B the *Bohr magneton*. The second equality is only valid for electrons or holes with charge q . The Landé factor takes on the value 2 for pure spin and 1 for pure orbital angular momentum. Mixtures of momenta will take on different values representing the projection of $\boldsymbol{\mu}$ onto the direction of \mathbf{J} and they ultimately need to be measured experimentally. Let there be N magnetic moments per unit volume, then multiplying both sides of (4.5) by γN and noting that magnetization $\mathbf{M} = \gamma N \mathbf{J}$ leads to

$$\frac{d\mathbf{M}}{dt} = \gamma \mu_0 \mathbf{M} \times \mathbf{H}^{\text{eff}}. \quad (4.7)$$

Of course, the magnetic field $\mathbf{B}^{\text{eff}} = \mu_0 \mathbf{H}^{\text{eff}}$ can have several types of origin making it an effective magnetic field potentially including anisotropy, demagnetization and other fields as well. Some of these are not real magnetic fields but affect the system similar to one. Equation (4.7) is again called precession equation and is the lossless form of the *Landau-Lifshitz* equation. The precession of magnetization



4. Introduction to Spin Waves

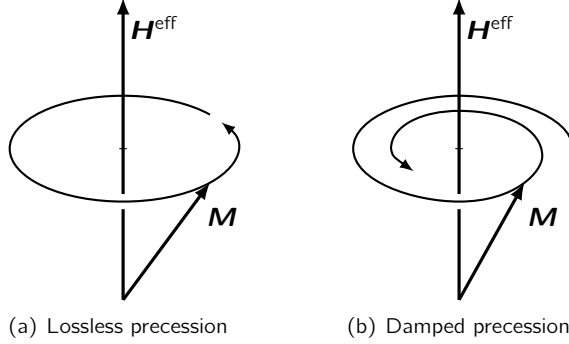


Figure 4.1: Precession of magnetization \mathbf{M} around a static effective magnetic field \mathbf{H}^{eff} .
(a) Lossless precession following the Landau-Lifshitz equation (4.7).
(b) Damped precession following the Landau-Lifshitz-Gilbert equation (4.8).

due to electron spin, i.e., $\gamma < 0$, is visualized in [figure 4.1\(a\)](#). Once magnetization and magnetic field are misaligned, the magnetization would continue to precess indefinitely and never reach the state of minimal energy, i.e., alignment with the field.

A form that includes damping, and thereby solving this issue, was also given by Landau and Lifshitz [102] by adding a comparatively small term that leads to dissipation. It was later refined by Gilbert [103]. Both forms are widely used and nowadays known as the *Landau-Lifshitz-Gilbert* equations [89]. The latter reads

$$\frac{d\mathbf{M}}{dt} = \gamma\mu_0\mathbf{M} \times \mathbf{H}^{\text{eff}} + \frac{\alpha}{M}\mathbf{M} \times \frac{d\mathbf{M}}{dt}. \quad (4.8)$$

The damping parameter is denoted by α . The term $\mathbf{M} \times \frac{d\mathbf{M}}{dt}$ gives an additional component to $\frac{d\mathbf{M}}{dt}$ that points towards the center of motion effectively decreasing the radius of precession until \mathbf{M} is parallel to the field.

4.2. FERROMAGNETIC RESONANCE

Let us now consider a particular dynamical setup by splitting the applied magnetic field into a static part \mathbf{H}_0 and a much smaller, oscillating component $\delta\mathbf{H}(t) \propto e^{-i\omega t}$ perpendicular to it. Furthermore, let us for simplicity consider a simple ferromagnet and let \mathbf{H}_0 be large enough, so that the equilibrium magnetization is saturated, parallel to \mathbf{H}_0 and denoted by \mathbf{M}_s . It will then also only be slightly perturbed and the perturbation $\delta\mathbf{M}$ can be seen as perpendicular to \mathbf{M}_s . In total:

$$\mathbf{H}(t) = \mathbf{H}_0 + \delta\mathbf{H}(t) \quad (4.9)$$

$$\mathbf{M}(t) = \mathbf{M}_s + \delta\mathbf{M}(t). \quad (4.10)$$

Note that since \mathbf{H}_0 and $\delta\mathbf{H}(t)$ are both homogeneous fields, the created wave has zero momentum which ultimately means a spatially uniform precession. Sought-after is a linear relation between an oscillating excitation $\delta\mathbf{H}$ at time t' and the induced oscillating magnetization $\delta\mathbf{M}$ at time t . Because the system is not explicitly time dependent, it follows that the response will only depend on the time difference $t - t'$. Fourier transformation with respect to time gives the important statement that a perturbation acting at a frequency ω results in a system response at the same frequency ω within the linear response regime [68], i.e., $\delta\mathbf{M} \propto e^{-i\omega t}$. Plugging the above ansatz into the Landau-Lifshitz equation (4.7) gives

$$\frac{d\delta\mathbf{M}}{dt} = \gamma\mu_0 (\mathbf{M}_s \times \mathbf{H}_0 + \mathbf{M}_s \times \delta\mathbf{H} + \delta\mathbf{M} \times \mathbf{H}_0 + \delta\mathbf{M} \times \delta\mathbf{H}). \quad (4.11)$$

The first term vanishes, because $\mathbf{M}_s \parallel \mathbf{H}_0$. The last term may also be neglected, since $\delta\mathbf{M}$ and $\delta\mathbf{H}$ are both considered small, making it a perturbation of second order. Assuming that field and magnetization point along $\hat{\mathbf{e}}_z$, the equation above can be written as

$$-i\omega \delta\mathbf{M} = \hat{\mathbf{e}}_z \times (-\omega_M \delta\mathbf{H} + \omega_0 \delta\mathbf{M}), \quad (4.12)$$

with

$$\omega_M = -\gamma\mu_0 M_s \quad \text{and} \quad \omega_0 = -\gamma\mu_0 H_0. \quad (4.13)$$

Note that $\gamma < 0$ for electrons leading to positive frequencies. Solving (4.12) for $\delta\mathbf{H}$ gives

$$\begin{pmatrix} \delta H_x \\ \delta H_y \end{pmatrix} = \frac{1}{\omega_M} \begin{pmatrix} \omega_0 & i\omega \\ -i\omega & \omega_0 \end{pmatrix} \begin{pmatrix} \delta M_x \\ \delta M_y \end{pmatrix}. \quad (4.14)$$

The susceptibility tensor $\underline{\chi}$ is obtained by inverting the equation above giving $\delta\mathbf{M} = \underline{\chi} \cdot \delta\mathbf{H}$ with

$$\underline{\chi} = \begin{pmatrix} \chi_0 & -i\kappa \\ i\kappa & \chi_0 \end{pmatrix} \quad (4.15)$$

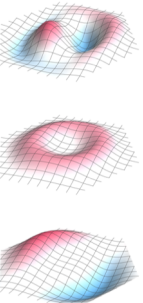
and

$$\chi_0 = \frac{\omega_0 \omega_M}{\omega_0^2 - \omega^2} \quad (4.16)$$

$$\kappa = \frac{\omega \omega_M}{\omega_0^2 - \omega^2}. \quad (4.17)$$

The frequency ω_0 is called *Larmor frequency* and is more generally known as a *resonance frequency* at which the susceptibility has a pole. That means the magnetic response is infinitely large for any excitation at this frequency. As (4.7) is a lossless equation of motion, this can be expected. A more realistic description is provided by (4.8), since the damping term fixes this singular behavior.

In reality, one also needs to differentiate between the internal and external fields of finite but macroscopically sized samples, cf. section 3.3. Let us assume



4. Introduction to Spin Waves

an ellipsoidal sample with the static field $\mathbf{H}_0^{\text{ext}} \parallel \hat{\mathbf{e}}_z$ parallel to a (semi-) principal axis. In the same setup as above the internal field is then given by, cf. [section 3.3](#),

$$\mathbf{H}_0^{\text{int}} = \mathbf{H}_0^{\text{ext}} - N_z \mathbf{M}_s$$

assuming again a saturated magnetization \mathbf{M}_s . With

$$\delta \mathbf{H}^{\text{int}} = \delta \mathbf{H}^{\text{ext}} - \underline{N} \delta \mathbf{M} = \delta \mathbf{H}^{\text{ext}} - \begin{pmatrix} N_x \delta M_x \\ N_y \delta M_y \\ 0 \end{pmatrix} \quad (4.18)$$

and $\delta M_z = 0$ [equation \(4.11\)](#) becomes

$$\frac{d \delta \mathbf{M}}{dt} = \gamma \mu_0 \left(\mathbf{M}_s \times \delta \mathbf{H}^{\text{ext}} - \mathbf{M}_s \times \underline{N} \delta \mathbf{M} + \delta \mathbf{M} \times \mathbf{H}_0^{\text{ext}} - \delta \mathbf{M} \times N_z \mathbf{M}_s \right) \quad (4.19)$$

after the first and last term of [\(4.11\)](#) vanish again for the same reasons as above. Fourier transform and simplification lead to

$$-i\omega \delta \mathbf{M} = \hat{\mathbf{e}}_z \times \left(-\omega_M \delta \mathbf{H}^{\text{ext}} + (\omega_0 - N_z \omega_M + \omega_M \underline{N}) \delta \mathbf{M} \right), \quad (4.20)$$

and, because $\delta M_z = 0$, this equation can also be reduced to two dimensions and solving analogously for $\delta \mathbf{H}$ gives

$$\begin{pmatrix} \delta H_x \\ \delta H_y \end{pmatrix} = \frac{1}{\omega_M} \begin{pmatrix} \omega_0 + \omega_M(N_x - N_z) & i\omega \\ -i\omega & \omega_0 + \omega_M(N_y - N_z) \end{pmatrix} \begin{pmatrix} \delta M_x \\ \delta M_y \end{pmatrix}. \quad (4.21)$$

Here, the demagnetization tensor is assumed to have diagonal form as in [\(3.21\)](#). The susceptibility tensor then looks similar to [\(4.15\)](#), namely

$$\underline{\chi} = \begin{pmatrix} \chi_x & -i\kappa \\ i\kappa & \chi_y \end{pmatrix} \quad (4.22)$$

and

$$\chi_{x/y} = \frac{(\omega_0 + \omega_M(N_{x/y} - N_z)) \omega_M}{(\omega_0 + \omega_M(N_x - N_z)) (\omega_0 + \omega_M(N_y - N_z)) - \omega^2} \quad (4.23)$$

$$\kappa = \frac{\omega \omega_M}{(\omega_0 + \omega_M(N_x - N_z)) (\omega_0 + \omega_M(N_y - N_z)) - \omega^2} \quad (4.24)$$

with a pole at

$$\omega_{\text{Kittel}} = \sqrt{(\omega_0 + \omega_M(N_x - N_z)) (\omega_0 + \omega_M(N_y - N_z))} \quad (4.25)$$

$$= |\gamma| \mu_0 \sqrt{(H_0^{\text{ext}} + (N_x - N_z) M_s) (H_0^{\text{ext}} + (N_y - N_z) M_s)} \quad (4.26)$$

known as the *Kittel formula* for ferromagnetic resonance.

EXAMPLES FOR THE KITTEL FORMULA:

First, let $\mathbf{H}_0^{\text{ext}} \parallel \hat{\mathbf{e}}_z$. Here, we present the three limiting cases of shapes already presented in section 3.3. Those were a perfect sphere with $N_x = N_y = N_z = \frac{1}{3}$ (case 1), an infinite rod or cylinder aligned with the $\hat{\mathbf{e}}_z$ -axis with $N_x = N_y = \frac{1}{2}$ and $N_z = 0$ (case 2), and a disk or infinite surface with $N_x = N_y = 0$ and $N_z = 1$ (case 3). Additionally, we also consider an infinite rod perpendicular to the field, e.g. $N_x = N_z = \frac{1}{2}$ and $N_y = 0$ (case 4), and a disk with a magnetic field parallel to the surface, e.g. $N_x = N_z = 0$ and $N_y = 1$ (case 5).

$$\text{case 1: } \omega = |\gamma| \mu_0 H_0^{\text{ext}} \quad (4.27)$$

$$\text{case 2: } \omega = |\gamma| \mu_0 \left(H_0^{\text{ext}} + \frac{1}{2} M_s \right) \quad (4.28)$$

$$\text{case 3: } \omega = |\gamma| \mu_0 \left(H_0^{\text{ext}} - M_s \right) \quad (4.29)$$

$$\text{case 4: } \omega = |\gamma| \mu_0 \sqrt{H_0^{\text{ext}} \left(H_0^{\text{ext}} - \frac{1}{2} M_s \right)} \quad (4.30)$$

$$\text{case 5: } \omega = |\gamma| \mu_0 \sqrt{H_0^{\text{ext}} (H_0^{\text{ext}} + M_s)} \quad (4.31)$$

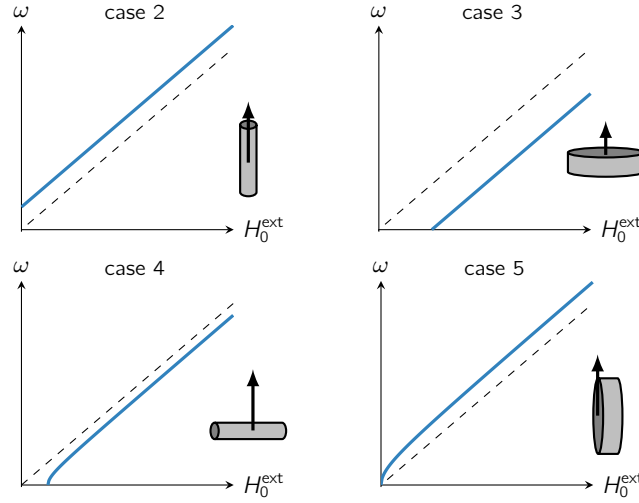
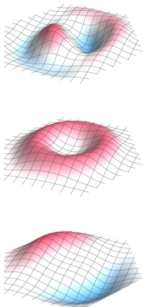


Figure 4.2: Examples of extremal cases of ferromagnetic resonances calculated via the Kittel formula (4.26) for different sample shapes shown as insets. The orientation of the external magnetic field is indicated by a black arrow. The resonance of the perfect sphere, i.e., case 1, equals the Larmor-frequency and is depicted as a dashed line in each panel. The remaining four cases (see text) are indicated by solid blue lines in the panels.

The next step is to include crystal anisotropies into the calculation. Kittel [104] suggested and Macdonald [105] confirmed that not only shape but also crystalline and even strain anisotropies may be taken into account by effective demagnetization factors. Following [89], one needs to choose a coordinate system



4. Introduction to Spin Waves

in which $\hat{\mathbf{e}}_z$ is parallel to the static magnetization and oscillations need to be small. To simplify things here, we still assume that the external field points along the principal axis $\hat{\mathbf{e}}_z$ of the specimen and that the field strength is large enough, so that anisotropies do not notably influence the direction of \mathbf{M}_s . Now, however, the demagnetization tensor might contain off-diagonal terms N_{xy} , taking the form

$$\underline{N}' = \begin{pmatrix} N_x & N_{xy} & 0 \\ N_{xy} & N_y & 0 \\ 0 & 0 & N_z \end{pmatrix}. \quad (4.32)$$

This gives a slightly modified Kittel formula

$$\omega'_{\text{Kittel}} = |\gamma| \mu_0 \sqrt{(H_0^{\text{ext}} + (N_x - N_z)M_s)(H_0^{\text{ext}} + (N_y - N_z)M_s) - N_{xy}^2 M_s^2}. \quad (4.33)$$

In such a setup, demagnetization factors of shape and cubic anisotropy are additive and all N_i in (4.33) need to be replaced by $N_i + N_i^a$ where N_i^a are the effective demagnetization factors due to cubic anisotropies. Starting from an energy density \mathcal{H} containing demagnetization, anisotropy and Zeeman terms, i.e.,

$$\mathcal{H} = \frac{\mu_0}{2} \mathbf{M} \cdot \underline{N}' \cdot \mathbf{M} + \frac{K}{M_s^4} (M_x^4 + M_y^4 + M_z^4) - \mu_0 \mathbf{H}^{\text{ext}} \cdot \mathbf{M}, \quad (4.34)$$

the additive anisotropy contributions take the form [89]²

$$N_x^a = -3 \frac{-2K}{\mu_0 M_s^2} \sin^2 \vartheta \sin^2 2\varphi \quad (4.35)$$

$$N_y^a = -3 \frac{-2K}{\mu_0 M_s^2} \sin^2 2\vartheta \left(1 - \frac{1}{4} \sin^2 2\varphi\right) \quad (4.36)$$

$$N_{xy}^a = -3 \frac{-2K}{\mu_0 M_s^2} \sin^2 \vartheta \cos \vartheta \sin 4\varphi \quad (4.37)$$

$$N_z^a = -\frac{-2K}{\mu_0 M_s^2} (1 + \cos^2 2\vartheta - \sin^4 \vartheta \sin^2 2\varphi) \quad (4.38)$$

The angles ϑ and φ are as defined in figure 4.3. The angle between $[001] = \hat{\mathbf{e}}_z^a$ and magnetization \mathbf{M}_s is ϑ , and φ is the angle between $[100]$ and the projection of \mathbf{M}_s onto the plane spanned by $[100]$ and $[010]$. Since it is common in experiments to apply static and oscillating magnetic fields along principal axes of the sample, \underline{N}' is usually still diagonal, i.e., the principal axes are $\hat{\mathbf{e}}_x$, $\hat{\mathbf{e}}_y$ and $\hat{\mathbf{e}}_z$. One then just needs to know how the crystallographic directions $\hat{\mathbf{e}}_x^a$, $\hat{\mathbf{e}}_y^a$ and $\hat{\mathbf{e}}_z^a$ are rotated with respect to the sample in order to obtain the resonance frequencies.

RESULTS: As results we present two examples where not only the above calculations for shape and cubic anisotropies but additionally the damping from the LLG equation (4.8) has been considered for completion. This lets us obtain

²Note, that there are typographical errors in the cited formulas in this source.

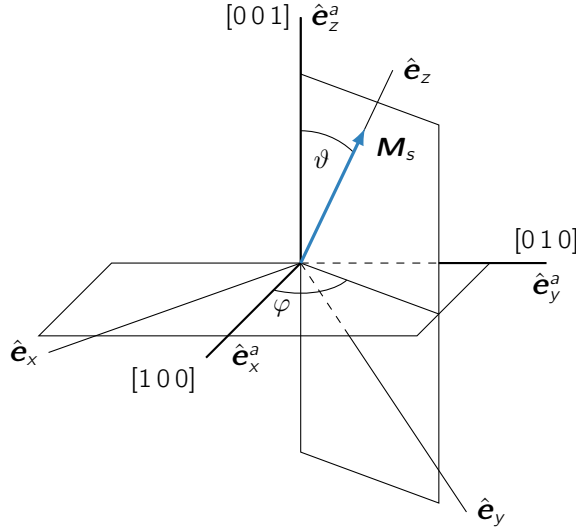


Figure 4.3: Angle definition for cubic anisotropies: ϑ is the angle between $[001] = \hat{\mathbf{e}}_z^a$ and the magnetization \mathbf{M}_s , while angle φ is the angle between $[100]$ and the projection of \mathbf{M}_s onto the plane spanned by $[100]$ and $[010]$. Design taken from [89].

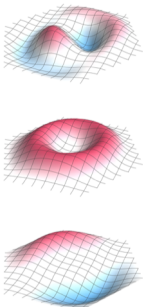
the complex resonance frequency of a ferromagnet with damping to linear order. The extended calculation is provided in [appendix C](#). The angles used in the two examples are shown in [figure 4.3](#).

Case 1: $\mathbf{H}_0^{\text{ext}} \parallel [001]$ with $\vartheta = 0$ and $\varphi = \pi/4$

$$\begin{aligned} \omega_1 &= \omega_{\text{res},1} + i\Gamma_1 \\ &= |\gamma|\mu_0 \sqrt{\left(\frac{4K}{\mu_0 M_0} - (H_0^{\text{ext}} + (N_x - N_z) M_s)\right) \left(\frac{4K}{\mu_0 M_0} - (H_0^{\text{ext}} + (N_y - N_z) M_s)\right)} \\ &\quad - i\gamma\mu_0 \left(\frac{4K}{\mu_0 M_0} - \left(H_0^{\text{ext}} + \frac{(N_x + N_y - 2N_z)}{2} M_s\right)\right) \alpha \end{aligned} \quad (4.39)$$

Case 2: $\mathbf{H}_0^{\text{ext}} \parallel [111]$ with $\vartheta = \arctan \sqrt{2}$ and $\varphi = \pi/4$

$$\begin{aligned} \omega_2 &= \omega_{\text{res},2} + i\Gamma_2 \\ &= |\gamma|\mu_0 \sqrt{\left(\frac{8}{3} \frac{K}{\mu_0 M_0} + (H_0^{\text{ext}} + (N_x - N_z) M_s)\right) \left(\frac{8}{3} \frac{K}{\mu_0 M_0} + (H_0^{\text{ext}} + (N_y - N_z) M_s)\right)} \\ &\quad + i\gamma\mu_0 \left(\frac{8}{3} \frac{K}{\mu_0 M_0} + \left(H_0^{\text{ext}} + \frac{(N_x + N_y - 2N_z)}{2} M_s\right)\right) \alpha \end{aligned} \quad (4.40)$$



4. Introduction to Spin Waves

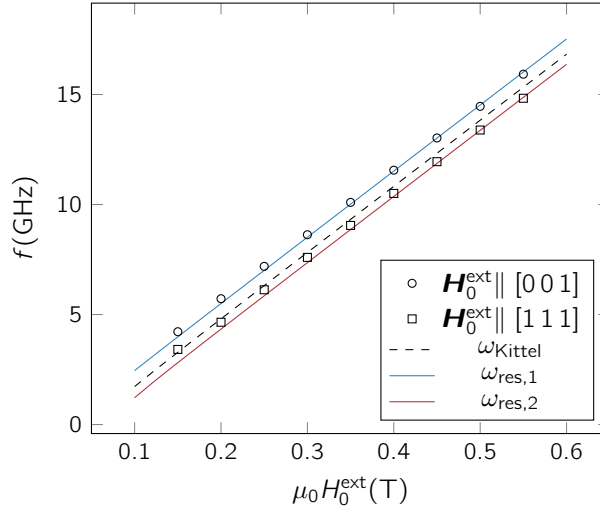


Figure 4.4: Influence of cubic anisotropies on the Kittel mode (dashed line) with an anisotropy constant of $K = -0.6 \times 10^3 \text{ J m}^{-3}$ applied to cases one and two outlined in the text. Data obtained by [106].

Corresponding experiments with coplanar waveguides, cf. [section 5.1](#), have been performed by Ioannis Stasinopolous and collaborators [106] on a rod-like Cu_2OSeO_3 sample with shape demagnetization factors of

$$N_x = 0.0658 \quad N_y = 0.4064 \quad N_z = 0.5278, \quad (4.41)$$

a g-factor of 2.14 and a saturation magnetization of $\mu_0 M_s = 0.131 \text{ T}$. Deviations from the ordinary Kittel mode without anisotropy corrections are clearly noticeable and shown in [figure 4.4](#). A fit results in an anisotropy constant $K = -0.6 \times 10^3 \text{ J/m}^3$.

4.3. ELLIPTICITY

Be it a uniformly precessing mode like in [section 4.2](#) or in later chapters when more complicated magnetic structures oscillate, we meet with the question of polarization of the oscillating magnetization. Although helices and skyrmions consist of twisted magnetic structures, they still have a homogeneous magnetization component, which precesses comparable to the magnetization of a ferromagnet. At this point we would like to introduce a definition for the ellipticity of precessing magnetization. There are several definitions for the *ellipticity* ε of an ellipse mostly just differing by a square. The one we use is given by

$$\varepsilon = \frac{\sqrt{a^2 - b^2}}{a}. \quad (4.42)$$

The longer principal axis is denoted by a and the shorter by b as is shown in figure 4.5. This definition is sometimes also called *eccentricity*. For a perfect circle $\varepsilon = 0$ and for a completely flat ellipse, i.e., linear polarization, $\varepsilon = 1$. When considering a precessing magnetization $\mathbf{M} = \mathbf{M}_0 + \delta\mathbf{M}$ consisting of a static (\mathbf{M}_0) and a dynamic ($\delta\mathbf{M}$) part, then, although the tip of \mathbf{M} potentially traces an ellipse, it is $\delta\mathbf{M}$ that lies in the same plane as that ellipse. It is therefore enough to consider the x and y components of $\delta\mathbf{M}$ if $\mathbf{M}_0 \parallel \hat{\mathbf{e}}_z$ since $\delta\mathbf{M} \perp \mathbf{M}_0$. One can then define

$$\varepsilon_\sigma = \sigma \frac{\sqrt{|\delta M_x|^2 - |\delta M_y|^2}}{\max(|\delta M_x|, |\delta M_y|)} \quad (4.43)$$

In this definition, the principal axes point along the x and y coordinates and δM_x and δM_y are the respective amplitudes of the dynamic part. It turns out to be useful to also define a sign $\sigma = \pm 1$ for ε that indicates along which coordinate axis the longer elliptical axis points. We define

$$\sigma := \begin{cases} +1 & \text{if long axis } \parallel \hat{\mathbf{e}}_x \\ -1 & \text{if long axis } \parallel \hat{\mathbf{e}}_y \end{cases} \quad (4.44)$$

4.4. TYPES OF SPIN WAVES

Spin waves generally do not consist of uniform and homogeneous precession but are usually modulated in space. For their study it is important to know the influence of the dominating spin interactions. Previously mentioned were the two main mechanisms leading to exchange and dipolar spin waves, respectively.

EXCHANGE SPIN WAVES

Exchange interaction has the dominating influence on the spin wave spectrum when wavelengths of spin waves are comparable to the distance between neighboring spins, e.g., atomic lattice spacings. An example is a model chain of spins with basically only nearest neighbor Heisenberg interaction, cf. (1.1). Flipping one spin in a quantum mechanical picture then leads to a proliferation of said flipped state throughout the chain via the Heisenberg exchange, which can be written in terms of a spin exchange operator P for two coupled spins with the property $P\psi_{\uparrow\downarrow} = \psi_{\downarrow\uparrow}$ for spin eigenfunctions ψ , see chapter 2.4 in [96]. The obtained dispersion relation for a chain of ferromagnetic spins, i.e., $\mathcal{J} > 0$, then reads

$$\hbar\omega_{\text{fm}} = \mathcal{J}(1 - \cos ka) \quad (4.45)$$

where a is the lattice spacing between two neighboring spins.

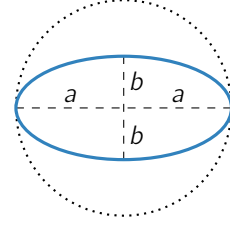
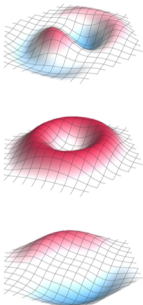


Figure 4.5: Ellipse with indicated principal axes a and b .



4. Introduction to Spin Waves

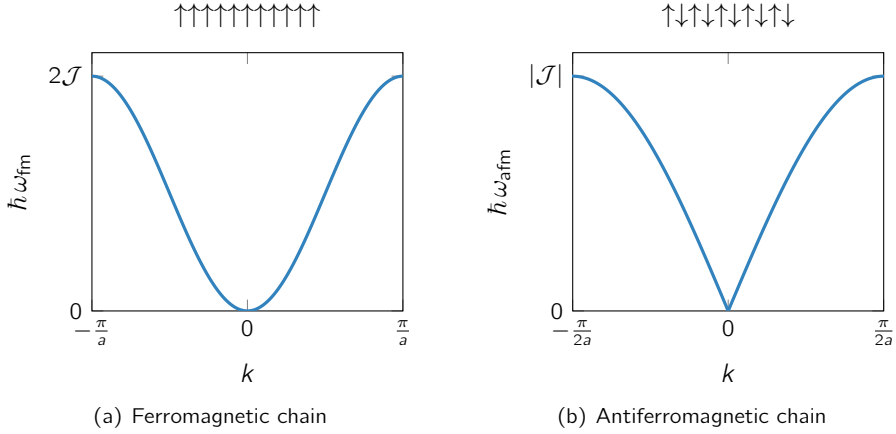


Figure 4.6: Dispersion relations of (a) ferromagnetic and (b) antiferromagnetic chains. Especially noticeable are their differences in the limit $ka \ll 1$ where the ferromagnetic dispersion is quadratic and an the antiferromagnetic dispersion is linear.

Considering an antiferromagnetic system with $\mathcal{J} < 0$, the antiferromagnetic dispersion relation is obtained similarly to the ferromagnetic one by dividing the lattice into two opposing ferromagnetic sublattices [107] and reads

$$\hbar\omega_{\text{afm}} = -\mathcal{J}|\sin ka|. \quad (4.46)$$

Both dispersion relations are shown in [figure 4.6](#). The most pronounced difference between them is observed in the long wavelength limit $ka \ll 1$ where the energy $\hbar\omega_{\text{fm}} \approx \frac{\mathcal{J}}{2}a^2k^2$ is approximately quadratic while $\hbar\omega_{\text{afm}} \approx -\mathcal{J}|ak|$ becomes linear. In this limit, however, exchange interaction loses its influence compared to dipolar interaction and the latter dominate

DIPOLAR SPIN WAVES

Dipolar spin waves dominate at wave lengths much larger than the lattice spacing. To see what they are composed of, we take a look at a plane wave propagating in an arbitrary direction \mathbf{k} in a magnetized medium. The magnetic field can be assumed to be

$$\mathbf{H} = \mathbf{H}_0 + \delta\mathbf{H} = \mathbf{H}_0 + \delta\mathbf{H}e^{i\mathbf{k}\cdot\mathbf{r} - i\omega t}$$

and Maxwell's equations can be written as [96]

$$\mathbf{k} \times \delta\mathbf{H} = -\omega\epsilon\delta\mathbf{E} \quad (4.47)$$

$$\mathbf{k} \times \delta\mathbf{E} = \omega\mu_0(\delta\mathbf{H} + \delta\mathbf{M}), \quad (4.48)$$

where $\delta\mathbf{E}$ is then the electric field associated with the wave. We also assume the magnetized medium to be electrically isotropic with electric permittivity ϵ .

It can be shown, that so-called *slow branches*, i.e., with small phase and group velocities, exist in their spectrum [89]. For certain frequencies, the wavelength inside the material differs significantly from the wavelength of the same wave outside the sample while still having the same frequency in either places, i.e., $|\mathbf{k}| \gg |\mathbf{k}_0| = \omega\sqrt{\mu_0\epsilon}$ and $|\mathbf{k}| \ll |\mathbf{k}_0|$. After employ this approximation [96], Maxwell's equations become

$$\nabla \times \delta \mathbf{H} = 0 \quad (4.49)$$

$$\nabla \times \delta \mathbf{B} = 0 \quad (4.50)$$

$$\nabla \times \delta \mathbf{E} = i\omega(\delta \mathbf{B}). \quad (4.51)$$

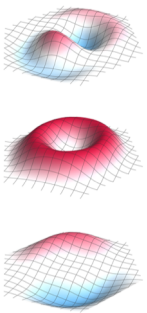
The last line is obtained by solving equations (4.49) and (4.50) for \mathbf{B} and \mathbf{H} , leading to an approximation for the electric field \mathbf{E} . It is therefore called *magnetostatic approximation*. Waves described by these equations are hence called magnetostatic waves. To be a little more precise, these waves propagate in the sample when the frequency lies in the range $\omega_0 \leq \omega \leq \sqrt{\omega_0(\omega_0 + \omega_M)}$ [96] with Larmor frequency $\omega_0 = -\gamma\mu_0 H_0$ and $\omega_M = -\gamma\mu_0 M_s$ where M_s is the saturation magnetization, see also section 4.2.

Unlike the exchange spin waves, the coupling of the spins is here dominated by dipolar fields from the magnetic moments. This is the case when $k \ll \pi/a$. This makes these kind of waves most important to this thesis, because they just meet the criteria in which the dynamical processes, that we study here, occur. Including dipolar interactions alters the dispersion relations of the ferromagnet and antiferromagnet in the small wavelength limit stated in the previous paragraph. The dispersion relation for a cubic ferromagnet of finite size and ellipsoidal shape reads [108–110]

$$(\hbar\omega_{\text{fm}})^2 = \left[\frac{\mathcal{J}}{2}a^2k^2 + g\mu_B\mu_0 (H^{\text{ext}} - N_z M) \right] \times \left[\frac{\mathcal{J}}{2}a^2k^2 + g\mu_B\mu_0 (H^{\text{ext}} - N_z M + M \sin^2 \theta_k) \right] \quad (4.52)$$

$$= \left[\frac{\mathcal{J}}{2}a^2k^2 + g\mu_B\mu_0 H^{\text{int}} \right] \left[\frac{\mathcal{J}}{2}a^2k^2 + g\mu_B\mu_0 (H^{\text{int}} + M \sin^2 \theta_k) \right] \quad (4.53)$$

where cubic anisotropies are neglected and $\mathbf{H}^{\text{ext}} \parallel \hat{\mathbf{e}}_z$. The angle between wave vector \mathbf{k} and magnetization \mathbf{M} is denoted by θ_k . Dipolar interactions hence results in an anisotropy in the $\mathbf{k} \rightarrow 0$ limit. For $\mathbf{k} \parallel \mathbf{M}$ the dispersion $\omega \propto k^2$ is quadratic in k while $\mathbf{k} \perp \mathbf{M}$ results in $\omega \propto k$ a linear dispersion for $H^{\text{int}} = 0$. Due to the finite extend of the sample, one needs to be careful in terms of stability of the magnetically ordered state. When the external field is too small, then there will be a point below which it is favorable to create a state with multiple domains and this formula is not directly applicable anymore. Note also that dipole-dipole interaction alone does not yield a ferromagnetic state [111]. Therefore, the exchange contribution is always present, even though it may only play a minor role in some cases.



4. Introduction to Spin Waves

The dispersion relation for an antiferromagnet is even more complex. There, two branches of the frequency spectrum exist and are given at zero field by [110, 112]

$$(\hbar\omega_{\text{afm}})^2 = \left[\frac{\mathcal{J}}{2} a^2 k^2 \right] \left[\frac{\mathcal{J}}{2} (2 - a^2 k^2) - 2g\mu_B\mu_0 \left(\frac{1}{3} - \sin^2 \theta_k \right) M \right] \quad (4.54a)$$

$$= \left[\frac{\mathcal{J}}{2} a^2 k^2 \right] \left[\frac{\mathcal{J}}{2} (2 - a^2 k^2) - \frac{2}{3} g\mu_B\mu_0 M \right]. \quad (4.54b)$$

4.5. DAMON ESHBACH PHYSICS

Magnetostatic waves can be divided into additional categories. While modes with zero k -vector were addressed in [section 4.2](#), let us here consider waves with non-zero wave vector. Then some of their properties depend on the anisotropy between the directions of the static magnetic field, wave vector \mathbf{k} and the sample shape. In [section 4.4](#) we noted that magnetostatic spin waves propagate inside a sample within frequency range [96]

$$\omega_0 \leq \omega \leq \sqrt{\omega_0(\omega_0 + \omega_M)} \quad (4.55)$$

which corresponds to the region extending from

$$\omega = |\gamma|\mu_0 H^{\text{int}} \quad \text{to} \quad \omega = |\gamma|\sqrt{\mu_0 H^{\text{int}} B^{\text{int}}}.$$

Because this range comprises many waves, it is sometimes called magnetostatic spin wave manifold and contains the dipole-exchange spin wave spectrum like calculated by Herring and Kittel in an unlimited ferromagnetic medium [109]. A finite sample like a film however breaks the translational symmetry in the vicinity of the surface and hence modifies the spin wave spectrum [113]. Considering a thin slab that is either magnetized perpendicular or parallel to the surface ultimately yields different kinds of modes which also depend on the direction of \mathbf{k} . It was found by Damon and Eshbach [114, 115] that the mode spectrum then extends over a wider area from $\omega = |\gamma|\mu_0 H^{\text{int}}$ to $\omega = |\gamma|\mu_0 (H^{\text{int}} + M/2)$ containing the previously mentioned region at the lower end. The other region

$$\sqrt{\omega_0(\omega_0 + \omega_M)} \leq \omega \leq \left(\omega_0 + \frac{\omega_M}{2} \right) \quad (4.56)$$

contains surface modes with exponentially decaying amplitude when going further inside the sample. To describe their key differences one can calculate the wave amplitude distribution, group and phase velocities.

Starting with a normally magnetized slab, as shown in [figure 4.7\(a\)](#), one arrives at the conclusion that phase and group velocities may be different in magnitude, but their directions are the same. Furthermore, the wave amplitude is distributed sinusoidally throughout the sample. Due to those features, they are called *forward volume modes*, which becomes clear when contrasted with the cases discussed next.

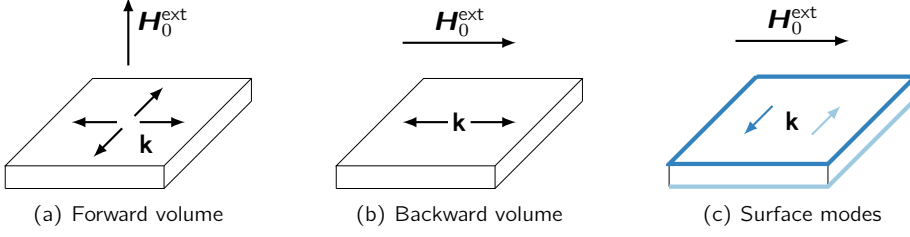
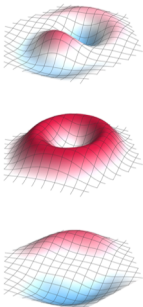


Figure 4.7: Characterization of volume and surface modes of a magnetized slab. Panels (a) and (b) depict volume modes, while panel (c) shows the necessary configuration for surface modes. The slab needs to be magnetized in plane and $\mathbf{k} \perp \mathbf{H}_0^{\text{ext}}$. The two possible configurations for \mathbf{k} are shown with different colors. Note, that one configuration leads to a mode on the top surface while the other configuration with opposite \mathbf{k} leads to a mode on the bottom surface, both also indicated in the corresponding colors. Picture refurbished from [96].

For a tangentially magnetized sample one needs to consider two cases: $\mathbf{k} \parallel \mathbf{H}_0^{\text{ext}}$ and $\mathbf{k} \perp \mathbf{H}_0^{\text{ext}}$. The first one again yields a volume mode, however with opposing group and phase velocities, hence the name *backward volume modes*. When \mathbf{k} is perpendicular to the field, phase and group velocities are again aligned making it a forward mode. However, the wave amplitude is maximal on a surface of the sample and decays exponentially in both directions. This makes it a *surface wave*. Note that this time it is important which sign \mathbf{k} has. If the propagation direction is reversed, the mode shifts from one surface of the thin slab to the other. This is called field displacement non-reciprocity.

Another thing to note about the surface modes is that there is only one surface mode present in a particular frequency range. For the volume modes, there does not exist a finite frequency range, where only one volume mode is present, but there are always several modes close and densely packed to each other. This is at least in the absence of exchange interaction which is, nevertheless, said to be of lower order.



5

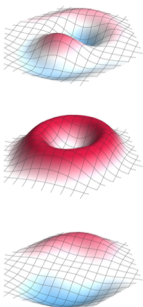
EXPERIMENTAL METHODS

While this work focuses on theoretical descriptions of magnons in chiral magnets, it also forms the link to the experimental methods to probe spin wave dynamics. In collaboration with research groups in Munich and Los Alamos, theoretical and experimental results are brought together. This chapter introduces their different methods. The first uses coplanar waveguides (CPWs) to measure resonance frequencies in the GHz range for wave lengths much larger than intrinsic length scales. So large that one may speak of homogeneous excitations at, or at least very close to, $\mathbf{k} = 0$. Inelastic neutron scattering is the second method and can be used to probe magnon spectra at large momenta compared to the inverse sample size.

5.1. COPLANAR WAVEGUIDES

Waveguides, as stated by the name, are linear structures used to guide waves from one endpoint to the other. CPWs go a little beyond that. They are open structures compared with classic waveguides, which means that materials placed close to it influence the traveling wave dominantly via absorption. A CPW has a number of advantages compared to conventional microstrip lines. They include a simpler fabrication and a reduction of radiation loss, which improves the signal to loss ratio. Furthermore, they offer tailored excitation via appropriate geometrical design and minimize electromagnetic crosstalk with adjacent structures.

They come in different varieties. The kind used in corresponding experiments is called a conventional CPW which ideally consists of a center strip conductor with semi-infinite ground planes on either side. In practical circuits, these ground planes are, of course, of finite extent but still large compared to the signal line. This arrangement is situated on a dielectric substrate [116]. A sketch is shown in [figure 5.1\(a\)](#). Other variants may have an additional ground line beneath the substrate, e.g. the conductor backed CPW, or include layered substrates, etc. Besides being considered a waveguide by itself, CPWs can also be used as inductive input and read out antennas to insert magnetostatic spin waves into a ferrite waveguide. The first CPW inserts a wave at one point after which phase



5. Experimental Methods

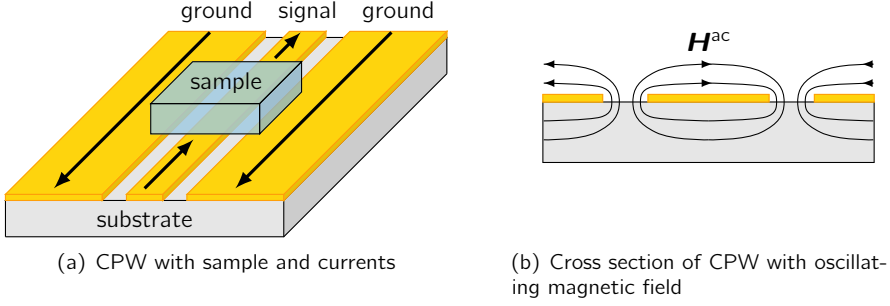


Figure 5.1: Sketches of a coplanar waveguide that consist out of a signal and two ground lines in a coplanar arrangement on top of a dielectric substrate. The sample to study is placed on top of the CPW (a) and absorbs some of the magnetic field created by the CPW shown in (b). Because the sample has a frequency dependent susceptibility influencing the inductive response of the system. These changes are measured between the two end points of the signal line of the CPW.

and/or amplitude are varied. They are later read out at the position of the second CPW [13].

In the experiments conducted in the context of this thesis, the specimen to study is placed on top of one CPW as shown in figure 5.1(a). The arrows indicate the direction of applied alternating currents, which lead to an oscillating magnetic field H^{ac} shown in figure 5.1(b). When examined closely, it is evident that H^{ac} is not completely homogeneous when considered as a whole, but has a certain finite momentum distribution \mathbf{k} . Also the direction of the oscillating magnetic field varies across the cross section. In the middle of the signal line it is parallel to the surface and in the gaps between ground and signal lines it is vertical. This has significant influence on which resonances can be theoretically expected. The sample shown in figure 5.1(a) reaches over both those areas. However, for a more controlled excitation with an oscillating field dominantly in a particular direction, one either needs a sample smaller than the width of the signal line, for the gap to be able to consider the field as unidirectional, or a larger CPW. A larger CPW decreases the momentum distribution towards a more homogeneous excitation field.

5.2. NEUTRON SCATTERING

Neutron scattering has become an invaluable tool to study microscopic properties of solids and liquids. This section introduces some aspects of neutron scattering necessary to understand this work. A more detailed discussion can be found in [117, 118].

The wavelength of neutrons is comparable to interatomic distances, i.e., of the order of Å, which results in interference effects when scattered off the atomic

Quantity	Value
Rest mass m_n	$1.675 \times 10^{-24} \text{ g}$
Spin	$1/2$
Magnetic moment μ_n	$1.913 \mu_N = 1.041 \times 10^{-3} \mu_B$ ¹
Charge	0

Table 5.1: Summarized properties of neutrons [117].

structure. Also, since neutrons do not carry electric charge, there is no Coulomb barrier to overcome and neutrons may penetrate deep into a sample making it possible to study bulk properties. The most important property for us is the fact, that neutrons possess a magnetic moment. This allows interaction with the magnetic structure of a sample and the scattering cross sections includes this information, of course next to the interaction with the nuclei. Quantitative properties of neutrons are collected in [table 5.1](#). Neutrons can be controlled by a moderator that slows them down via collisions with atoms of similar mass. An energy range of 1–100 meV is achieved by a moderator at room temperature, which gives them the name thermal neutrons. These energies lie in the same range of elementary excitations in condensed matter which allows the study of dynamics through the energy transfer into the sample. So-called cold neutrons complement that range.

One usually differentiates between elastic and inelastic scattering. Both processes are sketched in [figure 5.2](#). All scattering experiments are governed by well known momentum and energy conservation laws

$$\mathbf{Q} = \mathbf{k}_f - \mathbf{k}_i \quad (5.1)$$

$$|\mathbf{Q}|^2 = |\mathbf{k}_i|^2 + |\mathbf{k}_f|^2 - 2|\mathbf{k}_i||\mathbf{k}_f|\cos 2\theta_S \quad (5.2)$$

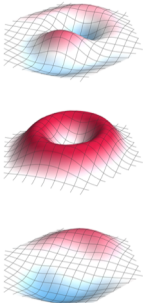
$$\hbar\omega = E_i - E_f. \quad (5.3)$$

Incident and final momenta of neutrons are denoted by \mathbf{k}_i and \mathbf{k}_f , respectively, and their energies by E_i and E_f . The total change in momentum after scattering about an angle θ_S is \mathbf{Q} .

When considering elastic scattering, then $|\mathbf{k}_i| = |\mathbf{k}_f|$. If a circle with radius of this length passes through two points of the reciprocal lattice, then the condition for Bragg scattering is fulfilled. It is called Ewald circle or Ewald sphere in three dimensions. The change of momentum \mathbf{Q} then equals a reciprocal vector \mathbf{G} of the nuclear lattice and

$$|\mathbf{Q}| = |\mathbf{G}| = 2|\mathbf{k}_i| \sin \theta_S = \frac{4\pi}{\lambda_i} \sin \theta_S. \quad (5.4)$$

¹The nuclear magneton is given by $\mu_N = \frac{e\hbar}{2m_p}$ with elementary charge e and proton rest mass m_p . It is the natural unit to express magnetic dipole moments of heavy particles like nucleons, whereas the much larger magnetic dipole moment of electrons is usually expressed in units of the Bohr magneton μ_B .



5. Experimental Methods

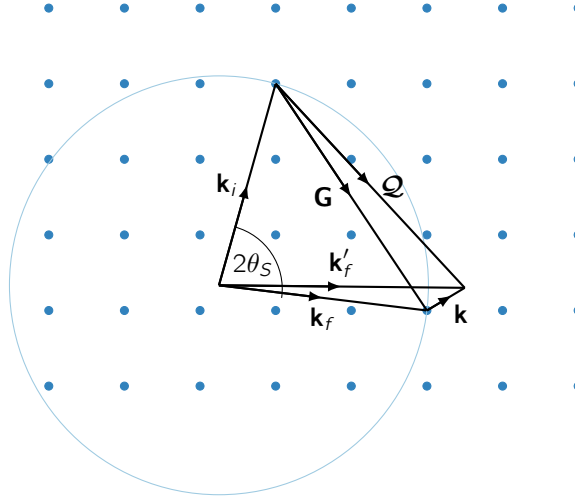


Figure 5.2: Reciprocal space of an atomic lattice showing the Ewald circle and a vector representation of elastic (\mathbf{k}_f) and inelastic (\mathbf{k}'_f) scattering processes for fixed incoming momentum \mathbf{k}_i . For a more detailed description see the main text. The design is adapted from [117].

For inelastic scattering $|\mathbf{k}_i| \neq |\mathbf{k}_f|$ one has to additionally consider a momentum transfer \mathbf{k} onto the sample. In an experiment, usually either \mathbf{k}_i or \mathbf{k}_f remain fixed while the other is varied. The momentum difference is then given by

$$\mathbf{Q} = \mathbf{G} + \mathbf{k}. \quad (5.5)$$

Setups considered in this thesis to measure magnons in helical or skyrmion lattices use inelastic scattering where \mathbf{k} traces a path through the reciprocal *magnetic* lattice. Vectors \mathbf{Q} of these reciprocal lattices are much smaller than the reciprocal vectors of the nuclear lattice and form satellites around nuclear Bragg peaks as pictured in figure 5.3. There, the (one dimensional) reciprocal lattices

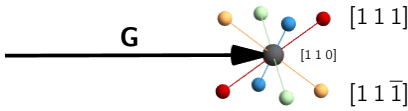


Figure 5.3: Satellites of the magnetic reciprocal lattice of a multi-domain helical state around the nuclear Bragg peak $[1\ 1\ 0]$.

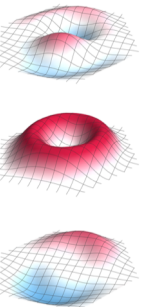
of four different helical domains of, e.g., MnSi, are shown around the nuclear Bragg peak $[1\ 1\ 0]$. A helix is pinned in a general $\langle 1\ 1\ 1 \rangle$ crystal direction which corresponds to four different \mathbf{Q} directions. These are indicated by the colored points. Red and orange points are, as an example, labeled by the specific $[1\ 1\ 1]$ and $[1\ 1\ \bar{1}]$ directions, respectively.

Probably the most important and versatile instrument in neutron scattering spectroscopy is a triple-axis spectrometer. It was invented by Brockhouse [119]

in 1961 and offers controlled measurement of the scattering function $S(\mathbf{Q}, \omega)$ at a very wide range of momentum \mathbf{Q} and energy $\hbar\omega$. Both elastic and inelastic scattering measurable by the triple axis spectrometer, but it is especially suited for inelastic scattering experiments since it was designed to be as flexible as possible. It not only covers a wide range of energies but also renders the rotational parameters accessible. Moreover, it is possible to readily change the energy momentum resolution to accommodate intense and weak patterns.

Resolution in general is a topic that one needs to consider in depth when comparing experimental to plain theoretical data. To compare intensity at a given point in momentum and energy space to theory, say (\mathbf{k}_0, ω_0) , one needs to convolute a four dimensional ellipsoidal region $(\mathbf{k}_0 \pm \Delta\mathbf{k}, \omega_0 \pm \Delta\omega)$ around that point. Those points together contribute to the measured intensity at the given point (\mathbf{k}_0, ω_0) . To obtain a spectrum, one then needs to repeat that process for an array of momenta. This procedure smears out the spectrum initially obtained without the convolution. Minimizing this smearing-out is one of the big challenges for experimentalists as shape and extent of those resolution ellipses depend on numerous factors in the setup.

To conclude this section we want to mention a method well suited for elastic neutron scattering, namely small angle neutron scattering (SANS). The images in [figure 2.2](#) are the result of such measurements. SANS allows to probe spacial correlations in a sample on length scales between nano- and micrometers, i.e. large compared to intrinsic length scales like atomic distances. A small scattering momentum \mathbf{Q} is hence needed and can, according to (5.4), be achieved by increasing the neutron wavelength or decreasing the scattering angle θ_S .



6

— LINEAR RESPONSE DYNAMICS —

This chapter focuses on numerical aspects on how to calculate resonance frequencies not only for a ferromagnet, but also more complicated spin arrangements, in particular helical and skyrmion structures. This has partially been outlined in [93].

6.1. DERIVATION OF RESONANCE FREQUENCIES

Similar to [section 4.2](#) we want to divide the system into a static and a dynamic part. All information about the system we want to study enters the free energy functional F as in (3.35). Schematically, we can split F into a static part F_{stat} and a time dependent part $F(t)$:

$$F = F_{\text{stat}} + F(t). \quad (6.1)$$

The time dependent part contains for example oscillating external magnetic or electric fields, while the static part contains F_0 (cf. (3.36) or (3.37)) plus demagnetization and anisotropy terms. We are looking for the response of the magnetization to time dependent excitations. To be more precise, we are looking for a small deviation of the magnetization away from a mean-field configuration to first order, hence the name linear response. The magnetization \mathbf{M} can therefore be divided into two parts as well

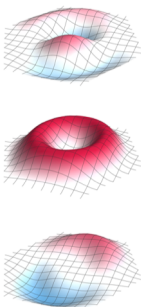
$$\mathbf{M} = \mathbf{M}^{\text{mf}} + \delta\mathbf{M}(t). \quad (6.2)$$

Because exciting and responding frequencies are equal in not explicitly time dependent systems studied via linear response, we can make the following ansatz for the time dependent terms

$$F(\mathbf{r}, t) = \bar{F} e^{i(\mathbf{k} \cdot \mathbf{r} - i\omega t)} \quad (6.3)$$

$$\delta\mathbf{M}(\mathbf{r}, t) = \delta\mathbf{M} e^{i(\mathbf{k} \cdot \mathbf{r} - i\omega t)} \quad (6.4)$$

where \bar{F} and $\delta\mathbf{M}$ are vectorial amplitudes. Due to translational invariance of the system, not only the resonance frequencies are equal, but the statement holds



6. Linear Response Dynamics

in a similar way also for spatial oscillations. Because there is only a discrete translation symmetry, the momenta of excitation and response only coincide up to reciprocal lattice vectors.

Plugging [equations \(6.3\)](#) and [\(6.4\)](#) into the precession equation [\(4.7\)](#) provides a general scheme to calculate resonance frequencies. The effective magnetic field in [\(4.7\)](#) now contains both static and dynamic external fields as well as internal demagnetization fields etc. that are all contained within F . It is calculated via the relation $\mu_0 \mathbf{H}^{\text{eff}} = -\frac{\delta F}{\delta \mathbf{M}}$. This all results in

$$\frac{d\mathbf{M}}{dt} = \gamma\mu_0 \mathbf{M} \times \mathbf{H}^{\text{eff}} = -\gamma \mathbf{M} \times \frac{\delta F}{\delta \mathbf{M}} = -\gamma \mathbf{M} \times \left(\frac{\delta F_{\text{stat}}}{\delta \mathbf{M}} + \frac{\delta F(t)}{\delta \mathbf{M}} \right). \quad (6.5)$$

To be able to collect terms in linear order of $\delta \mathbf{M}$ we need to expand F_{stat} in $\delta \mathbf{M}$ which gives

$$F_{\text{stat}}[\mathbf{M}] = F_{\text{stat}}[\mathbf{M}^{\text{mf}}] + 0 \cdot \delta \mathbf{M} + \frac{1}{2} \delta M_i \left. \frac{\delta^2 F_{\text{stat}}}{\delta M_i \delta M_j} \right|_{\mathbf{M}^{\text{mf}}} \delta M_j + \mathcal{O}(\delta M^3). \quad (6.6)$$

The linear term vanishes due to the mean-field equation of state $\left. \frac{\delta F_{\text{stat}}}{\delta \mathbf{M}} \right|_{\mathbf{M}^{\text{mf}}} = 0$. The next step is to plug this expansion into [\(6.5\)](#) and keep only terms linear in $\delta \mathbf{M}$, \bar{F} and their combinations. Furthermore, $\partial_t \mathbf{M}^{\text{mf}} = 0$ and using the explicit time dependence [\(6.4\)](#) of $\delta \mathbf{M}$ leads to

$$-i\omega \delta \mathbf{M} = -\gamma \left(\mathbf{M}^{\text{mf}} \times \left. \frac{\delta^2 F_{\text{stat}}}{\delta \mathbf{M}^2} \right|_{\mathbf{M}^{\text{mf}}} \delta \mathbf{M} + \mathbf{M}^{\text{mf}} \times \left. \frac{\delta \bar{F}}{\delta \mathbf{M}} \right|_{\mathbf{M}^{\text{mf}}} \right) \quad (6.7)$$

$$\delta \mathbf{M} = \left[\omega + i\gamma \mathbf{M}^{\text{mf}} \times \left. \frac{\delta^2 F_{\text{stat}}}{\delta \mathbf{M}^2} \right|_{\mathbf{M}^{\text{mf}}} \right]^{-1} \cdot \left(i\gamma \mathbf{M}^{\text{mf}} \times \left. \frac{\delta \bar{F}}{\delta \mathbf{M}} \right|_{\mathbf{M}^{\text{mf}}} \right) \quad (6.8)$$

$$\hookrightarrow \omega_{\text{res}} = \text{Im Eigenvalues} [\gamma \mathbf{M}^{\text{mf}} \times \chi_0^{-1}] \quad (6.9)$$

with $\chi_0^{-1} = \left. \frac{\delta^2 F_{\text{stat}}}{\delta \mathbf{M}^2} \right|_{\mathbf{M}^{\text{mf}}}$. The goal was to find resonance, which means to find a maximal $\delta \mathbf{M}$. This is achieved in the second line when the denominator equals zero. $\delta \mathbf{M}$ in this form has an infinite pole like a δ -function because the lossless Landau-Lifshitz equation was used. The weight can therefore not be obtained by calculating the area below the resonance curve, but instead the pre-factor of the pole is taken as the weight. Before continuing with details about the weights in [section 6.3](#), we reformulate the above concept in a more precise form in momentum space. This is then also the form used in numerical calculations.

6.2. FORMULATION IN MOMENTUM SPACE

The magnetic structures studied in this thesis are a skyrmion lattice, a helical/conical phase and a field polarized phase. The first two are periodic structures in space, which means that one can decompose an arbitrary vector \mathbf{k} in momentum space into a reciprocal lattice vector \mathbf{Q} and a vector \mathbf{q} restricted to the

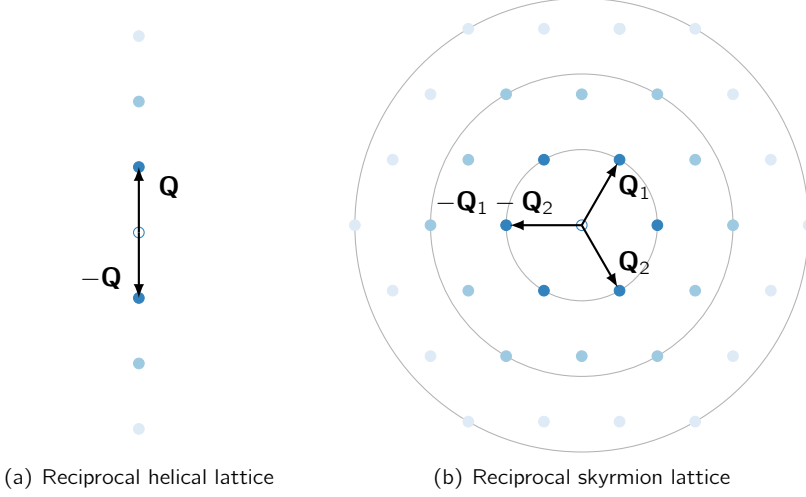


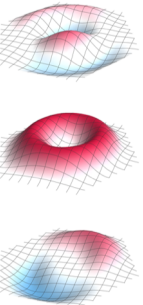
Figure 6.1: Image of the reciprocal lattice in the helical/conical (a) and skyrmion lattice phase (b). The latter is spanned by the two vectors \mathbf{Q}_1 and \mathbf{Q}_2 . The size of the lattice can be defined by rings. Dark blue solid dots define the first ring, mid-toned ones the second ring, light blue ones the third and so forth. Lattice vectors of the i^{th} ring are defined to have a distance to $\mathbf{k} = 0$ between $((i-1)|\mathbf{Q}_1| + \epsilon)$ and $(i|\mathbf{Q}_1| + \epsilon)$, with $\epsilon \ll 1$.

first Brillouin zone (BZ), i.e., $\mathbf{k} = \mathbf{Q} + \mathbf{q}$. The discrete part \mathbf{Q} will also function as a Brillouin zone index in implemented matrices or vectors. For example $v^i(\mathbf{k}) = v_{\mathbf{Q}}^i(\mathbf{q})$ is a vector of potentially infinite dimensions. The index \mathbf{Q} labels sub-vectors of dimension three, whose components are labeled by $i \in \{1, 2, 3\}$ and depend only on $\mathbf{q} \in 1.\text{BZ}$. The multiples of \mathbf{Q} form a reciprocal lattice which is one dimensional in the helical case but two dimensional in the skyrmion lattice case. Those lattices are shown in [figure 6.1](#). In Fourier space, magnetization depends on momentum \mathbf{k} but, because of the periodicity, intrinsic properties only depend on $\mathbf{q} \in 1.\text{BZ}$. However, to realize higher bands in the reduced zone scheme it is rather straight forward to consider many zones in the repeated zone scheme. It later turns out, that the repeated zone scheme is actually necessary when external momenta play a role. This momentum structure of the Fourier transformed magnetization, or any other quantity for that matter, can be organized in a potentially infinite-dimensional vector containing a list of all Fourier components.

We have chosen the following convention for the vectorial structure for the conical phase in momentum space:

$$\mathbf{m}_{\text{con}}(\mathbf{k}) = \left\{ m_0^x, m_0^y, m_0^z, m_{\mathbf{Q}}^x, m_{\mathbf{Q}}^y, m_{\mathbf{Q}}^z, m_{-\mathbf{Q}}^x, m_{-\mathbf{Q}}^y, m_{-\mathbf{Q}}^z; \dots \right\}(\mathbf{q}) \quad (6.10)$$

$$=: \{ \mathbf{m}_0, \mathbf{m}_{\mathbf{Q}}, \mathbf{m}_{-\mathbf{Q}}, \mathbf{m}_{2\mathbf{Q}}, \mathbf{m}_{-2\mathbf{Q}}, \dots \}(\mathbf{q}). \quad (6.11)$$



6. Linear Response Dynamics

The zero momentum Fourier component takes on the first position and the larger $n\mathbf{Q}$ with $n \in \mathbb{Z}$, the larger the position index. Analogously for the skyrmion phase we put the zero- \mathbf{Q} component to the first position, then collect all components of the first ring closest to $\mathbf{Q} = 0$, then of the second ring, etc., and get

$$\mathbf{m}_{\text{sky}}(\mathbf{k}) = \left\{ \mathbf{m}_0, \mathbf{m}_{\mathbf{Q}_1}, \mathbf{m}_{-\mathbf{Q}_1}, \mathbf{m}_{\mathbf{Q}_2}, \mathbf{m}_{-\mathbf{Q}_2}, \right. \\ \left. \mathbf{m}_{\mathbf{Q}_1+\mathbf{Q}_2}, \mathbf{m}_{-\mathbf{Q}_1-\mathbf{Q}_2}, \mathbf{m}_{2\mathbf{Q}_1}, \mathbf{m}_{-2\mathbf{Q}_1}, \dots \right\}(\mathbf{q}). \quad (6.12)$$

Before considering the entire equation of motion in that notation, we first examine individual parts. Following the conventions of [7], i.e., using (3.35) in rescaled units with F_0 as defined in (3.37), the Fourier transform of the fluctuation matrix $\left. \frac{\delta^2 F_{\text{stat}}}{\delta \mathbf{M}^2} \right|_{\mathbf{M}_{\text{mf}}}$ is given by

$$\left. \frac{\delta^2 F_{\text{stat}}}{\delta m^i(-\mathbf{k}) \delta m^j(\mathbf{k}')} \right|_{\mathbf{m}_{\text{mf}}} = 2 g_{\mathbf{k}\mathbf{k}'}^{ij} = 2 g_{\mathbf{Q}\mathbf{Q}'}^{ij}(\mathbf{q}, \mathbf{q}') = (\chi_0^{-1})^{ij}_{\mathbf{Q}\mathbf{Q}'}(\mathbf{q}, \mathbf{q}') \\ \text{with } \begin{matrix} \mathbf{k} = \mathbf{Q} + \mathbf{q} \\ \mathbf{k}' = \mathbf{Q}' + \mathbf{q}' \\ \mathbf{q}, \mathbf{q}' \in 1.\text{BZ} \end{matrix} \\ = \gamma \left[\delta_{\mathbf{q}\mathbf{q}'} \delta_{\mathbf{Q}\mathbf{Q}'} r^{ij}(\mathbf{Q} + \mathbf{q}) + 2 \delta^{ij} \sum_{\mathbf{Q}''} \mathbf{m}_{-\mathbf{Q}''} \cdot \mathbf{m}_{\mathbf{Q}-\mathbf{Q}'+\mathbf{Q}''} \delta_{\mathbf{q}\mathbf{q}'} \right. \\ \left. + 4 \sum_{\mathbf{Q}''} m_{-\mathbf{Q}''}^i m_{\mathbf{Q}-\mathbf{Q}'+\mathbf{Q}''}^j \delta_{\mathbf{q}\mathbf{q}'} \right] = (\chi_0^{-1})^{ij}_{\mathbf{Q}\mathbf{Q}'}(\mathbf{q}) \delta_{\mathbf{q}\mathbf{q}'} \quad (6.13)$$

with $r^{ij}(\mathbf{k}) = (1 + t + \mathbf{k}^2) \delta^{ij} - 2i \epsilon^{ijl} k^l + D^{ij}(\mathbf{k}) + A_{\text{cub}}^{ij}$ where $D^{ij}(\mathbf{k})$ is an additional term representing the contributions from demagnetization field:

$$D^{ij}(\mathbf{k}) = \frac{1}{2} \frac{\mu_0}{\alpha} \begin{cases} \frac{k^i k^j}{|\mathbf{k}|^2} & |\mathbf{k}| \gg 1/L \\ \delta^{ij} N_i & |\mathbf{k}| \ll 1/L \end{cases}. \quad (6.14)$$

The anisotropy terms F_{cub_1} and F_{cub_2} , equations (3.31) and (3.32) can be added, too, if one is interested in the H_{c1} transition between the helical and the conical phase. Their contribution to the fluctuation matrix takes the form

$$A_{\text{cub}}^{ij} = \left[c_1 \left((k^1)^4 + (k^2)^4 + (k^3)^4 \right) + c_2 (k^i)^2 \right] \delta^{ij}. \quad (6.15)$$

Einstein's sum convention is used for the three field dimensions indicated by i, j, l . The sample size is given by L and the parameter α toggles again between the rescaled units ($\alpha = 1$) and physical units ($\alpha = JQ^2$). The next quantity we want

to transform is the effective magnetic field¹

$$\begin{aligned}
 \mu_0 H^{\text{eff},i}(\mathbf{k}) &= \mu_0 H_{\mathbf{Q}}^{\text{eff},i}(\mathbf{q}) = - \sum_{\mathbf{k}'} \frac{\delta^2 F_{\text{stat}}}{\delta m^i(-\mathbf{k}) \delta m^j(\mathbf{k}')} \delta m^j(\mathbf{k}') - \frac{\delta F(t, \mathbf{k})}{\delta m^i(\mathbf{k})} \\
 &= - \sum_{\mathbf{Q}' \mathbf{q}'} (\chi_0^{-1})_{\mathbf{Q} \mathbf{Q}'}^{ij}(\mathbf{q}) \delta_{\mathbf{q} \mathbf{q}'} m_{\mathbf{Q}'}^j(\mathbf{q}') - \frac{\delta F(t, \mathbf{Q} + \mathbf{q})}{\delta m^i_{\mathbf{Q}}(\mathbf{q})} \\
 &= - \sum_{\mathbf{Q}'} (\chi_0^{-1})_{\mathbf{Q} \mathbf{Q}'}^{ij}(\mathbf{q}) \delta m_{\mathbf{Q}'}^j(\mathbf{q}) - \frac{\delta F(t, \mathbf{Q} + \mathbf{q})}{\delta m^i_{\mathbf{Q}}(\mathbf{q})}.
 \end{aligned} \tag{6.16}$$

With these preliminary achievements at the ready, we can recast the initially schematic calculation in Fourier space. Doing the Fourier transform in space via equations (3.8) yields the following expression for (6.5)

$$\begin{aligned}
 \partial_t m^i(\mathbf{k}, t) &= \partial_t \delta m_{\mathbf{Q},t}^i(\mathbf{q}) = \frac{\gamma \mu_0}{\nu} \sum_{\mathbf{Q}' \mathbf{Q}''} \epsilon^{ijl} m_{\mathbf{Q}'}^j H_{\mathbf{Q}''}^{\text{eff},l}(\mathbf{q}, t) \delta_{\mathbf{Q}'+\mathbf{Q}'', \mathbf{Q}} \\
 &= - \frac{\gamma}{\nu} \sum_{\mathbf{Q}''} \underbrace{\left(\sum_{\mathbf{Q}'} \epsilon^{ijl} m_{\mathbf{Q}'}^j \delta_{\mathbf{Q}'+\mathbf{Q}'', \mathbf{Q}} \right)}_{=:(\mathbf{m} \times)_{\mathbf{Q} \mathbf{Q}''}^{il}} \left(-\mu_0 H_{\mathbf{Q}''}^{\text{eff},l}(\mathbf{q}, t) \right) \\
 &= - \frac{\gamma}{\nu} \sum_{\mathbf{Q}'' \mathbf{Q}'''} (\mathbf{m} \times)_{\mathbf{Q} \mathbf{Q}''}^{il} \left((\chi_0^{-1})_{\mathbf{Q}'' \mathbf{Q}'''}^{lb}(\mathbf{q}) \delta m_{\mathbf{Q}'''}^b(\mathbf{q}) + \frac{\delta F(\mathbf{Q}'' + \mathbf{q}, t)}{\delta m_{\mathbf{Q}''}^l(\mathbf{q})} \right).
 \end{aligned} \tag{6.17}$$

Note that \mathbf{k}' was shifted by \mathbf{q} resulting in the Kronecker delta and an \mathbf{m} -term to solely depend on reciprocal lattice vectors. The matrix $(\mathbf{m} \times)_{\mathbf{Q} \mathbf{Q}''}^{il}$ is skew-hermitian (anti-hermitian) due to the anti-symmetric epsilon tensor and has therefore purely imaginary eigenvalues.

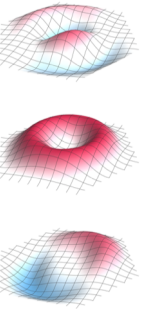
Following the scheme outlined in section 6.1 and now also using Einstein's sum convention for reciprocal lattice momenta lets us obtain an analog expression to (6.7) given by

$$\begin{aligned}
 &-i\omega \delta m_{\mathbf{Q}}^i(\mathbf{q}, \omega) \\
 &= - \frac{\gamma}{\nu} \left[(\mathbf{m}^{\text{mf}} \times)_{\mathbf{Q} \mathbf{Q}''}^{il} \left((\chi_0^{-1})_{\mathbf{Q}'' \mathbf{Q}'''}^{lb}(\mathbf{q}) \delta m_{\mathbf{Q}'''}^b(\mathbf{q}, \omega) + (\mathbf{m}^{\text{mf}} \times)_{\mathbf{Q} \mathbf{Q}''}^{in} \xi_{\mathbf{Q}''}^n(\mathbf{q}, \omega) \right) \right],
 \end{aligned} \tag{6.18}$$

where

$$\xi_{\mathbf{Q}''}^n(\mathbf{q}, \omega) = - \left. \frac{\delta F(\mathbf{Q}'' + \mathbf{q}, \omega)}{\delta m_{\mathbf{Q}''}^n(\mathbf{q})} \right|_{\mathbf{m}^{\text{mf}}} \tag{6.19}$$

¹The general structure is $\mu_0 \mathbf{H}^{\text{eff}} = - \frac{\delta F}{\delta \mathbf{m}} \approx - \frac{\delta^2 F}{\delta \mathbf{m}^2} \delta \mathbf{m}$ and the pair of \mathbf{m} in the denominator are arranged in a $\mathbf{m}(-\mathbf{k})\mathbf{m}(\mathbf{k})$ fashion due to momentum conservation. Hence, the structure of $\frac{\delta^2 F}{\delta \mathbf{m}^2}$ is $\frac{\delta^2 F}{\delta \mathbf{m}(-\mathbf{k}) \delta \mathbf{m}(\mathbf{k})}$.



6. Linear Response Dynamics

contains, for example, the direction and strength of an oscillating field coupling to the magnetization, eg. $\xi(\mathbf{k}, \omega) = \mu_0 \mathbf{H}^{\text{ac}}(\mathbf{k}, \omega)$. Solving for $\delta \mathbf{m}(\mathbf{k})$ returns, in analogy to (6.8),

$$\delta m_{\mathbf{Q}'''}^b(\mathbf{q}, \omega) = \left[\omega \delta^{ib} \delta_{\mathbf{Q}\mathbf{Q}'''} + i \underbrace{\gamma (\mathbf{m}^{\text{mf}} \times)_{\mathbf{Q}\mathbf{Q}''}^{il} (\chi_0^{-1})_{\mathbf{Q}''\mathbf{Q}'''}^{lb}(\mathbf{q})}_{\mathcal{W}_{\mathbf{Q}\mathbf{Q}'''}^{ib}(\mathbf{q})} \right]^{-1} \left(\frac{i\gamma}{\nu} (\mathbf{m}^{\text{mf}} \times)_{\mathbf{Q}\mathbf{Q}''}^{in} \xi_{\mathbf{Q}''}^n(\mathbf{q}, \omega) \right). \quad (6.20)$$

The resonances of the system are therefore eigenvalues $\omega^\alpha(\mathbf{q})$ of \mathcal{W} and obtained in a cleaner form from the eigenvalue equation

$$\sum_{j, \mathbf{Q}'} \mathcal{W}_{\mathbf{Q}\mathbf{Q}'}^{ij}(\mathbf{q}) v^{\alpha, j}(\mathbf{Q}' + \mathbf{q}) = \omega^\alpha(\mathbf{k}) v^{\alpha, i}(\mathbf{k}) \quad (6.21)$$

for $\mathbf{k} = \mathbf{Q} + \mathbf{q}$ and $v^\alpha(\mathbf{k})$ being a normalized eigenvector with

$$\sum_{j, \mathbf{Q}} (v^{\alpha, j}(\mathbf{Q} + \mathbf{q}))^* v^{\beta, j}(\mathbf{Q} + \mathbf{q}) = \delta_{\alpha\beta}$$

where $*$ denotes complex conjugation and α, β label the eigenvalue branches. Due to Bloch's theorem, the eigenvalues are periodic, $\omega^\alpha(\mathbf{k} + \mathbf{Q}) = \omega^\alpha(\mathbf{k})$.

NUMERICAL REFINEMENTS

In principle, the sums in (6.20) extend over infinitely many \mathbf{Q} -vectors. Numerically, a cutoff Λ has to be chosen with $|\mathbf{Q}| \leq \Lambda$. This is reasonable since the magnetic structures are smooth and the free energy approaches a finite value for $\Lambda \rightarrow \infty$ in the mean-field limit plus Gaussian fluctuations [7].

The numerical challenge is to include as many \mathbf{Q} -vectors and corresponding \mathbf{m} -parameters in the calculations as possible, especially in calculations regarding the skyrmion phase. An initial challenge is to compute the mean-field by minimizing the free energy functional with respect to the reciprocal lattice vectors \mathbf{Q}_i and the corresponding Fourier components $\mathbf{m}_{\mathbf{Q}_i}$. The setup discussed so far is very flexible in terms of implementing different field directions even when cubic anisotropies are additionally implemented with respect to which the external field is misaligned. The \mathbf{Q}_i and \mathbf{m} -fields are simply returned as an output in that geometry. This flexibility comes at the cost of calculation time and especially memory because of the plethora of Fourier component parameters. The most dramatic effect occurs in the treatment of the skyrmion lattice which we consider in the following.

The reciprocal skyrmion lattice size can be characterized by the number of *rings* within the cutoff region, cf. figure 6.1 for the definition of rings. To minimize F with respect to the first ring alone, already $3 \cdot 2 \cdot 7 + 2 \cdot 3 = 48$ parameters have to be considered. Three complex Fourier components (= 6 parameters) per lattice

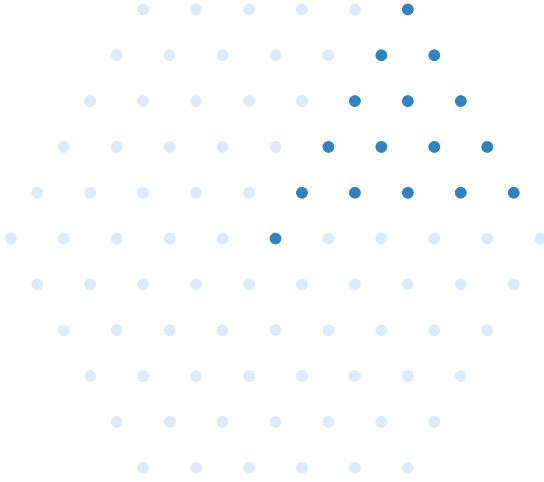
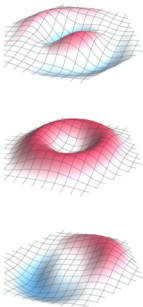


Figure 6.2: Shown in dark are the unique Fourier components that remain after exploiting symmetries. All others can be constructed via simple rotations or complex conjugations.

vector, of which there are seven, plus two lattice vectors with three parameters each. Taking two rings into account leads to 120 parameters, three rings to 228, etc. To calculate resonance frequencies and weights at $\mathbf{k} = 0$, also known as the Γ -point, the computing cost is easily manageable, because the sought-after resonance frequencies already converge almost perfectly between three and four rings, and one can use the advantages of this setup.

However, when studying an extended skyrmion magnon spectrum, this size turns out to be insufficient to emit reliable and convergent results before either the computer runs out of memory, or the user out of patience. Therefore, it is useful to restrict the liberties of the implementation a little, by also reducing the number of parameters significantly by exploiting symmetries.

The first thing one can do is fix the direction of the magnetic field along $\hat{\mathbf{e}}_z$ and one of the \mathbf{Q} vectors along $\hat{\mathbf{e}}_x$. This predefinition already leads to a significant number of vanishing parameters from the start, because $\mathbf{Q}_i \perp \text{Re}(\mathbf{m}_{\mathbf{Q}_i}) \perp \text{Im}(\mathbf{m}_{\mathbf{Q}_i})$, cf. [section 3.6](#). Additionally, it was already shown in [\[7\]](#) that the center spin points opposite to the magnetic field, which fixes another number of parameters. Furthermore, two opposing lattice points with respect to the center, corresponding to a helix, are each others complex conjugates. And last but not least, because the real-space picture has a 120° rotational symmetry, lattice points in the reciprocal lattice connected by a 120° rotation R_{120} around $\hat{\mathbf{e}}_z$ share that symmetry, too, as long as anisotropies are neglected. The consequence for the parameters is that if $R_{120}\mathbf{Q}_i = \mathbf{Q}_j$, then $R_{120}\mathbf{m}_i = \mathbf{m}_j$. For a four ring system size, this reduces the number of parameters from 372 to only 33 in exchange for not being able to use crystal anisotropy terms, which can be neglected in most scenarios anyway, and a more predetermined lattice. The reduction of relevant Fourier modes for a system with a five ring cutoff is shown in [figure 6.2](#).



6.3. SPECTRAL WEIGHTS

The following calculations are closely related to those in the supplementary information of [37]. If an oscillating external field \mathbf{H}^{ac} is present, then (6.20) can be written as

$$\left[\omega \delta^{ib} \delta_{\mathbf{Q}\mathbf{Q}'''} + \mathcal{W}_{\mathbf{Q}\mathbf{Q}'''}^{ib}(\mathbf{q}) \right] \delta m_{\mathbf{Q}'''}^b(\mathbf{q}, \omega) = \frac{i\gamma}{\nu} (\mathbf{m}^{\text{mf}} \times)_{\mathbf{Q}\mathbf{Q}''}^{in} \mu_0 H_{\mathbf{Q}''}^{\text{ac},n}(\mathbf{q}, \omega). \quad (6.22)$$

Expanding $\delta \mathbf{m}$ in the basis of the eigenvectors \mathbf{v} , $\delta m^i(\mathbf{k}) = \sum_{\alpha} c_{\alpha}(\mathbf{k}) v^{\alpha,i}(\mathbf{k})$ with $c_{\alpha}(\mathbf{k} + \mathbf{Q}) = c_{\alpha}(\mathbf{k})$, the expansion coefficients $c_{\alpha}(\mathbf{q})$ of the α^{th} excitation branch are determined by the right hand side of

$$(\omega - \omega^{\alpha}(\mathbf{q})) c_{\alpha}(\mathbf{q}) = \frac{i\gamma\mu_0}{\nu} (v^{\alpha,i}(\mathbf{Q} + \mathbf{q}))^{*} (\mathbf{m}^{\text{mf}} \times)_{\mathbf{Q}\mathbf{Q}'}^{ij} H_{\mathbf{Q}'}^{\text{ac},j}(\mathbf{q}, \omega) \quad (6.23)$$

and determine the sought after spectral weights. They are later encoded in the dot sizes of points in the spectrum. Particularly for magnetic resonance measurements with homogeneous fields \mathbf{H}_0^{ac} only coefficients with $\mathbf{k} = 0$ are finite with

$$(\omega - \omega^{\alpha}(0)) c_{\alpha}(0) = \frac{i\gamma\mu_0}{\nu} (v^{\alpha,i}(\mathbf{Q} + \mathbf{q}))^{*} (\mathbf{m}^{\text{mf}} \times)_{\mathbf{Q},0}^{ij} H_0^{\text{ac},j}(0, \omega). \quad (6.24)$$

A homogeneous field thus measures magnetic excitation frequencies at zero momentum.

Regarding neutron scattering experiments, the scattering cross section for neutrons with a given momentum transfer $\mathbf{Q} = \mathbf{G} + \mathbf{k}$ close to a nuclear reciprocal lattice vector \mathbf{G} is proportional to [120]

$$[1 + n_B(\omega)] \text{Im} \left(\text{Tr} [\chi(\mathbf{k}, \omega + i0)] - \hat{\mathbf{Q}} \chi(\mathbf{k}, \omega + i0) \hat{\mathbf{Q}} \right), \quad (6.25)$$

where $n_B(\omega) = 1/(e^{\hbar\omega/k_B T} - 1)$ is the Bose function. The projection via $\hat{\mathbf{Q}}$ takes into account, that neutrons only couple to the components of χ perpendicular to \mathbf{Q} and stems from the dipole-dipole interaction. It also assumes the valid approximation to neglect multiple scattering events.

To derive a physically correct form of the susceptibility $\chi(\mathbf{k}, \omega)$ we start at the linearized form of the precession equation in real space (4.7)

$$\partial_t \delta \mathbf{M} = -\gamma \mathbf{M}^{\text{mf}} \times \chi_0^{-1} \delta \mathbf{M}, \quad (6.26)$$

and rewrite it in a more suitable way to calculate $\chi^{-1}(\omega)$:

$$\frac{\hat{\mathbf{M}}^{\text{mf}}}{|\mathbf{M}^{\text{mf}}|} \times \partial_t \delta \mathbf{M} = -\gamma \chi_0^{-1} \delta \mathbf{M}. \quad (6.27)$$

Only terms linear in $\delta \mathbf{M}$ are kept.

DERIVATION OF (6.27):

Multiplying (6.27) by $\mathbf{M}^{\text{mf}} \times$ leads to

$$\hat{\mathbf{M}}^{\text{mf}} \times (\hat{\mathbf{M}}^{\text{mf}} \times \partial_t \delta \mathbf{M}) = \gamma \mathbf{M}^{\text{mf}} \times \mathbf{B}^{\text{eff}}$$

with $-\chi_0^{-1} \delta \mathbf{M} = \mathbf{B}^{\text{eff}}$. Rewriting the i th component of the l.h.s. yields

$$\begin{aligned} \epsilon_{ijk} \hat{M}_j^{\text{mf}} \epsilon_{knm} \hat{M}_n^{\text{mf}} \partial_t \delta M_m &= (\delta_{in} \delta_{jm} - \delta_{im} \delta_{jn}) \hat{M}_j^{\text{mf}} \hat{M}_n^{\text{mf}} \partial_t \delta M_m \\ &= \hat{M}_i^{\text{mf}} \hat{M}_j^{\text{mf}} \partial_t \delta M_j - \underbrace{\hat{M}_j^{\text{mf}} \hat{M}_j^{\text{mf}}}_{1} \partial_t \delta M_i \end{aligned}$$

Disregarding longitudinal fluctuations of the magnetization leads to the first term being zero since $\hat{\mathbf{M}}^{\text{mf}} \cdot \partial_t \delta \mathbf{M} = 0$ and it follows (4.7) for $|\mathbf{M}^{\text{mf}}| > 0$. At this point arises a conceptual problem regarding the length of the magnetization. Although the magnetization is, strictly speaking, not fixed to a certain length, it does not vary much and allows for a description of dynamic processes with $|\mathbf{M}| = \text{constant}$, cf. non-linear σ model in chapter 8. In the case above, we do not assume a constant magnetization, but still assume that \mathbf{M} does not fluctuate longitudinally.

Solving (6.27) for $\delta \mathbf{M}$ yields

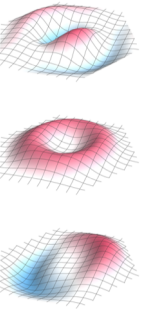
$$0 = \left(\frac{1}{i\gamma} \frac{1}{|\mathbf{M}^{\text{mf}}|^2} (\mathbf{M}^{\text{mf}} \times) \omega + \chi_0^{-1} \right) \delta \mathbf{M} =: \chi^{-1} \delta \mathbf{M}. \quad (6.28)$$

An alternative but equivalent route is to invert the $(\mathbf{M}^{\text{mf}} \times)$ matrix on the r.h.s. of (4.7) and one arrives at

$$0 = \left(\frac{1}{i\gamma} (\mathbf{M}^{\text{mf}} \times)^{-1} \omega + \chi_0^{-1} \right) \delta \mathbf{M} =: \chi^{-1} \delta \mathbf{M}. \quad (6.29)$$

Although both forms may be used, they each pose different kinds of problems regarding the numerical implementation in momentum space. The first equation contains a term $\frac{1}{|\mathbf{M}^{\text{mf}}|^2} (\mathbf{M}^{\text{mf}} \times)$ or $\frac{1}{|\mathbf{M}^{\text{mf}}|} (\hat{\mathbf{M}}^{\text{mf}} \times)$ which is already unhandy when subjected to a Fourier transform as the normalization of \mathbf{M} already poses an impediment let alone the resulting convolution of this product in real space. This makes (6.29) more attractive. However, the implementation is still not straight forward, as $(\mathbf{M}^{\text{mf}} \times)$ is a singular matrix with eigenvalues $\{0, \pm |\mathbf{M}^{\text{mf}}|\}$. Therefore, it cannot be inverted directly. A solution, or workaround, is to focus only on the subspace corresponding to non-zero eigenvalues in which $(\mathbf{M}^{\text{mf}} \times)$ is not singular. In the matrix notation of momentum space, the matrix $(\mathbf{m}^{\text{mf}} \times)_{\mathbf{Q}\mathbf{Q}'}^{ij}$ has a multitude of eigenvalues $\epsilon_{\mathbf{Q}}^{\alpha}$.

Because of the finite cutoff Λ , cf. section 6.2, the distribution of these eigenvalues is not confined to (mostly) three different values but results in a relatively smooth curve when plotted in increasing order. Albeit its continuity most of them do take on values close to 0 and $\pm |\mathbf{M}^{\text{mf}}|$. To be precise, $|\mathbf{M}^{\text{mf}}|$ are the average values



6. Linear Response Dynamics

over space as they may vary a little, especially in the skyrmion case. When sorted with increasing order they form plateaus whose extent grows percentage-wise over the number of eigenvalues approaching a step function. This behavior is shown for the skyrmion lattice and different system sizes in [figure 6.3](#).

To arrive not only at an invertible version of $(\mathbf{M}^{\text{mf}\times})$ in momentum space, but also at stable resonance frequencies that properly converge with increasing system size, it is not only necessary to disregard the subspace where $(\mathbf{M}^{\text{mf}\times})$ has zero eigenvalues, but necessary to consider only the subspace where $\varepsilon_{\times}^{\alpha} \approx \pm|\mathbf{M}^{\text{mf}}|$, i.e. dark blue plateaus in [figure 6.3](#). Let $\tilde{\varepsilon}_{\times}^{\alpha}$ be those eigenvalues and $\tilde{\mathbf{w}}_{\times}^{\alpha}$ their corresponding eigenvectors. Then a matrix \underline{T} can be constructed containing all $\tilde{\mathbf{w}}_{\times}^{\alpha}$ as its columns. The $(\mathbf{M}^{\text{mf}\times})$ matrix restricted to that eigenspace is then given by

$$(\widetilde{\mathbf{M}^{\text{mf}\times}}) = \underline{T}^{\dagger} \cdot (\mathbf{M}^{\text{mf}\times}) \cdot \underline{T} \quad (6.30)$$

where \dagger denotes complex conjugation and transposition. Analogously, χ_0^{-1} needs to be projected onto that subspace via

$$\widetilde{\chi_0^{-1}} = \underline{T}^{\dagger} \cdot \chi_0^{-1} \cdot \underline{T} \quad (6.31)$$

leading to a physical susceptibility

$$\widetilde{\chi^{-1}}(\mathbf{k}, \omega) = \left(\frac{1}{i\gamma} (\widetilde{\mathbf{M}^{\text{mf}\times}})^{-1} \omega(\mathbf{k}) + \widetilde{\chi_0^{-1}}(\mathbf{k}) \right). \quad (6.32)$$

The frequencies $\omega^{\alpha}(\mathbf{k})$ at which $\widetilde{\chi^{-1}}(\mathbf{k}, \omega)$ is evaluated to obtain the corresponding weights are easily calculated via [equation \(6.9\)](#) after substituting [\(6.30\)](#) and [\(6.31\)](#) into it. One hence has the eigenvalue equation

$$\left(-i\gamma (\widetilde{\mathbf{M}^{\text{mf}\times}}) \cdot \widetilde{\chi_0^{-1}}(\mathbf{k}) \right) \mathbf{w}_{\alpha} = \varepsilon_{\alpha} \mathbf{w}_{\alpha} \quad (6.33)$$

with $\mathbf{w}_{\alpha}^{\dagger} \mathbf{w}_{\beta} = \delta_{\alpha\beta}$ for eigenvectors \mathbf{w}_{α} . With their help it is possible to construct a Lehmann representation of χ which makes it easy to identify the weights corresponding to a particular frequency ε_{α} . One starts by multiplying with \mathbf{w}_{α} from the right hand side of

$$\widetilde{\chi^{-1}}(\mathbf{k}, \omega) = \frac{1}{i\gamma} (\widetilde{\mathbf{M}^{\text{mf}\times}})^{-1} \left[\omega + i\gamma (\widetilde{\mathbf{M}^{\text{mf}\times}}) \cdot \widetilde{\chi_0^{-1}}(\mathbf{k}) \right] \quad (6.34)$$

and using [equation \(6.33\)](#) to arrive at

$$\widetilde{\chi^{-1}}(\mathbf{k}, \omega) \mathbf{w}_{\alpha} = (\omega - \varepsilon_{\alpha}) \frac{1}{i\gamma} (\widetilde{\mathbf{M}^{\text{mf}\times}})^{-1} \mathbf{w}_{\alpha}. \quad (6.35)$$

In the next step we contract with $\mathbf{w}_{\alpha}^{\dagger}$ by, in particular, summing over α leading to

$$\widetilde{\chi^{-1}}(\mathbf{k}, \omega) = \frac{1}{i\gamma} (\widetilde{\mathbf{M}^{\text{mf}\times}})^{-1} \sum_{\alpha} (\omega - \varepsilon_{\alpha}) \mathbf{w}_{\alpha} \mathbf{w}_{\alpha}^{\dagger}. \quad (6.36)$$

Now, we take the inverse of this equation which can be shown to equal

$$\tilde{\chi}(\mathbf{k}, \omega) = \sum_{\alpha} \frac{1}{\omega - \varepsilon_{\alpha}} \left[\mathbf{w}_{\alpha} \mathbf{w}_{\alpha}^{\dagger} \left(i\gamma(\widetilde{\mathbf{M}^{\text{mf}} \times}) \right) \right] \quad (6.37)$$

with $\tilde{\chi}\chi^{-1} = \chi^{-1}\tilde{\chi} = 1$. The weight corresponding to frequency ε_{α} can now be extracted from $\left[\mathbf{w}_{\alpha} \mathbf{w}_{\alpha}^{\dagger} \left(i\gamma(\widetilde{\mathbf{M}^{\text{mf}} \times}) \right) \right]$. The formal calculation employs the familiar Dirac identity

$$\lim_{\eta \searrow 0} \frac{1}{x \pm i\eta} = \mp i\pi\delta(x) + \mathcal{P}\left(\frac{1}{x}\right) \quad (6.38)$$

after shifting the frequency ω slightly above the real axis forming a retarded response. $\mathcal{P}\left(\frac{1}{x}\right)$ is the principal value integral of $\frac{1}{x}$. We can then define the spectral matrix function to be

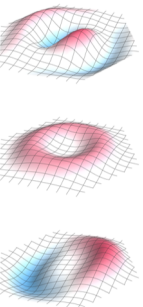
$$\begin{aligned} A(\mathbf{k}, \mathbf{k}', \omega) &= -\frac{1}{\pi} \text{Im} \sum_{\alpha} \lim_{\eta \searrow 0} \frac{1}{\omega + i\eta - \varepsilon_{\alpha}} \left[\mathbf{w}_{\alpha} \mathbf{w}_{\alpha}^{\dagger} \left(i\gamma(\widetilde{\mathbf{M}^{\text{mf}} \times}) \right) \right] \\ &= -\frac{1}{\pi} \text{Im} \sum_{\alpha} \left(-i\pi\delta(\omega - \varepsilon_{\alpha})[\dots] + \mathcal{P}\left(\frac{1}{\omega - \varepsilon_{\alpha}}\right)[\dots] \right) \\ &= \sum_{\alpha} \left[\mathbf{w}_{\alpha} \mathbf{w}_{\alpha}^{\dagger} \left(i\gamma(\widetilde{\mathbf{M}^{\text{mf}} \times}) \right) \right] \delta(\omega - \varepsilon_{\alpha}). \end{aligned} \quad (6.39)$$

Important for relative weights corresponding to a specific energy $\varepsilon_{\alpha'}$ is then the pre-factor of the delta function evaluated at $\alpha = \alpha'$, i.e., the matrix

$$\left[\mathbf{w}_{\alpha'} \mathbf{w}_{\alpha'}^{\dagger} \left(i\gamma(\widetilde{\mathbf{M}^{\text{mf}} \times}) \right) \right] (\mathbf{k}, \mathbf{k}') = \left[\mathbf{w}_{\alpha'} \mathbf{w}_{\alpha'}^{\dagger} \left(i\gamma(\widetilde{\mathbf{M}^{\text{mf}} \times}) \right) \right]_{\mathbf{Q}, \mathbf{Q}'} (\mathbf{q}) \quad (6.40)$$

where the explicit momentum dependence differs as before only up to reciprocal lattice vectors. While the spectrum follows Bloch's theorem, spectral weights given by (6.25) depend on the actual magnitude of \mathbf{k} , i.e., the weight differs between Brillouin zones. This is because the external neutron does not obey Bloch's theorem. One now has two options in this construction. The first is to adjust \mathbf{Q} accordingly and hence jump between sub-blocks within the matrix to select the right contribution which then depends on $\mathbf{q} \in 1$. BZ. The second and easier option is to select the $\mathbf{Q} = 0$ sub-block and increase \mathbf{q} beyond the first Brillouin zone until one arrives at the desired \mathbf{k} . Therefore, the relative weights for inelastic neutron scattering can be written as

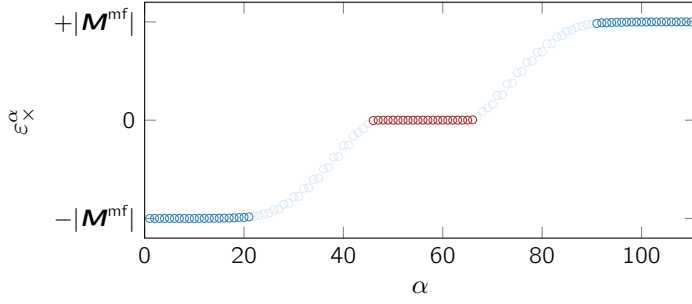
$$\begin{aligned} \Gamma(\mathbf{k}, \omega_{\alpha'}) &= \text{Im} \left(\text{Tr} \left[\left[\mathbf{w}_{\alpha} \mathbf{w}_{\alpha}^{\dagger} \left(i\gamma(\widetilde{\mathbf{M}^{\text{mf}} \times}) \right) \right]_{0,0} (\mathbf{k}) \right] \right. \\ &\quad \left. - \hat{\mathbf{Q}} \left[\left[\mathbf{w}_{\alpha} \mathbf{w}_{\alpha}^{\dagger} \left(i\gamma(\widetilde{\mathbf{M}^{\text{mf}} \times}) \right) \right]_{0,0} (\mathbf{k}) \right] \hat{\mathbf{Q}} \right). \end{aligned} \quad (6.41)$$



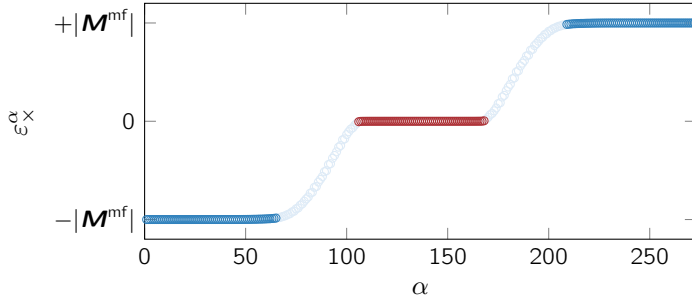
6. Linear Response Dynamics

To be precise, the Bose function $[1 + n_B(\omega)]$ as stated in [equation \(6.25\)](#) is additionally required for a quantitative agreement with experiments.

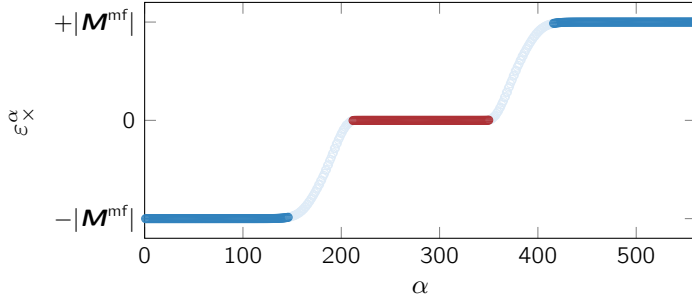
Recognizing, that [\(6.37\)](#) does not depend on the inverse of the $(\mathbf{M}\times)$ matrix, one could argue that it may not be necessary to use the projection onto the non-zero and non-volatile subspaces of $(\mathbf{M}\times)$, as its inverse is neither used to calculate weights nor resonance frequencies. However, these subspaces, whose eigenvalues are indicated by red and light blue colors in [figure 6.3](#), lead to false contributions in the spectrum and weight distribution. The ones in red correspond to zero modes that may become finite due to numerics. Modes corresponding to the light blue eigenvalues stem mostly from the momentum space boundaries due to the Fourier mode cutoff Λ and may lead to misleading or plainly wrong resonances traversing the entire spectrum. This is especially challenging in the skyrmion phase and discussed further in [chapter 12](#).



(a) Reciprocal skyrmion lattice size up to 3 Rings.

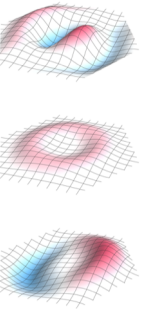


(b) Reciprocal skyrmion lattice size up to 5 Rings.



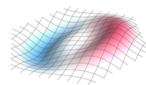
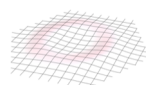
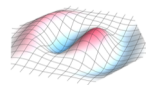
(c) Reciprocal skyrmion lattice size up to 7 Rings.

Figure 6.3: Eigenvalues ε_x^α of the $(\mathbf{m}^{\text{mf}} \times)$ matrix for three different cutoffs. The eigenvalues are sorted in increasing order and labeled by α . Eigenvalues with values close to $|\mathbf{M}|$ are colored in dark blue, those close to zero in red, and the eigenvalues in between those three plateaus in a light blue color. It can be seen that an increase in system size leads to a relatively steeper slope between the three plateaus.



PART III.

HELIMAGNONS



7

— RESONANCE AT THE Γ -POINT —

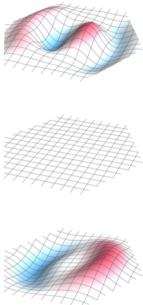
In momentum space, the Γ -point labels the center of the Brillouin zone. This chapter focuses on magnon excitations at such a point of zero momentum. We state an analytical formula for said excitations and discuss the nature of the modes. In the second part, we focus in particular on the ellipticity of the mean magnetization of each mode.

7.1. EXCITATION MODES

This section serves as a summary on excitation modes in the helical and conical phases. More extensive details can be found in [93, 37]. Three specific samples of MnSi, Fe_{0.8}Co_{0.2}Si and Cu₂OSeO₃ were excited in multiple phases via coplanar waveguides, i.e., with wavelengths much larger than intrinsic length scales, cf. [section 5.1](#). The most relevant differences between the samples are their shape and internal conical susceptibility. These values are listed in [table 7.1](#). Resonance frequencies are obtained with respect to an applied static magnetic field strength H_0^{ext} . For an increasing magnetic field, starting in a prepared one-domain state, one traces first through the conical phase and reaches a field polarized phase beyond a critical field H_{c2} . Resonances in the field polarized phase are given by the Kittel mode ([4.26](#)). Because the magnetic susceptibility in the conical phase χ_{con} is constant and the magnetization above the critical field H_{c2} can be considered as saturated, one may approximate the saturation magnetization by $M_s = \chi_{\text{con}} H_{c2}$. This lets us write the Kittel mode in a form that is normalized to

Sample	Material	N_x	N_y	N_z	$\chi_{\text{con}}^{\text{int}}$	χ_{con}	Shape
#1	MnSi	0.175	0.175	0.65	0.34	0.28	disc
#2	Fe _{0.8} Co _{0.2} Si	0.074	0.463	0.463	0.65	0.5	rod
#3	Cu ₂ OSeO ₃	0.39	0.27	0.34	1.76	1.1	spherical

Table 7.1: Sample properties of the three samples discussed in the main text and [37].



7. Resonance at the Γ -Point

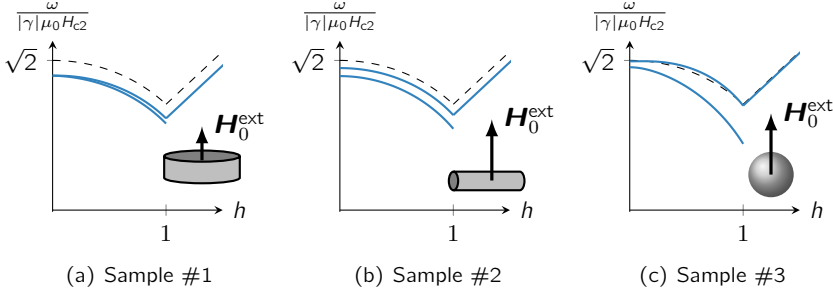


Figure 7.1: Calculated resonances of samples #1, #2 and #3 as a function of the externally applied magnetic field $h = H_0^{\text{ext}}/H_{c2}$. The dashed lines represent resonances without dipolar interactions, i.e., $\chi_{\text{con}}^{\text{int}} = 0$. In the field polarized phase this results in the familiar Larmor frequencies.

H_{c2} as well

$$\frac{\omega_{\text{Kittel}}}{|\gamma|\mu_0 H_{c2}} = \sqrt{(h + (N_x - N_z)\chi_{\text{con}})(h + (N_y - N_z)\chi_{\text{con}})}. \quad (7.1)$$

Whereas in the spin-polarized phase only a single resonance exists, two modes, labeled $+Q$ and $-Q$ for reasons that will become clear later in this section, can be magnetically excited in the conical and helical phases [121]. Their frequencies can be calculated analytically and amount to [91, 37]

$$\begin{aligned} \frac{\omega_{\pm Q}^2}{(\gamma\mu_0 H_{c2})^2} = & \frac{1}{4} \left(8 + 2(2 + N_x + N_y - 8N_z)\chi_{\text{con}} - (N_x + N_y - 4N_z)(-1 + 2N_z)\chi_{\text{con}}^2 \right. \\ & \left. + h^2(-4 - \chi_{\text{con}}(4 + (N_x + N_y - 2N_x N_y)\chi_{\text{con}} + 4N_z(-2 + (-1 + N_z)\chi_{\text{con}}))) \right) \\ & \pm \chi_{\text{con}} \left[N_x^2 \left(2 + (1 + h^2(-1 + 2N_y) - 2N_z)\chi_{\text{con}} \right)^2 + N_y^2 \left(-2 + (-1 + h^2 + 2N_z)\chi_{\text{con}} \right)^2 \right. \\ & \left. + 2N_x N_y \left(-(2 + \chi_{\text{con}} - 2N_z\chi_{\text{con}})^2 - 2h^2(4 + (1 + N_y - 4N_z)\chi_{\text{con}})(-2 + (-1 + 2N_z)\chi_{\text{con}}) \right. \right. \\ & \left. \left. - h^4(8 + \chi_{\text{con}}(8 + \chi_{\text{con}} + 2N_y\chi_{\text{con}} + 8N_z(-2 + (-1 + N_z)\chi_{\text{con}}))) \right) \right]^{\frac{1}{2}}. \quad (7.2) \end{aligned}$$

Here, the magnetic field $h = H_0^{\text{ext}}/H_{c2}$ is normalized to the critical field and $\mathbf{H}_0^{\text{ext}}$ is defined to point along $\hat{\mathbf{e}}_z$. χ_{con} may be rewritten in terms of $\chi_{\text{con}}^{\text{int}}$ via (1.6). Also $\omega_{+Q} > \omega_{-Q}$. A thorough derivation is given in section 8.4. Graphs that illustrate (7.2) and (7.1) for the three samples are shown in figure 7.1.

A couple of points are especially noteworthy. The first thing to notice is that $\chi_{\text{con}}^{\text{int}}$ is a measure that describes the general distance between the two modes in the conical phase. It is also a measure for the strength of dipolar interactions. If set to zero, then the two modes are degenerate. This frequency is shown as the dashed lines in figure 7.1. Therefore, dipolar interaction is the reason for mode

splitting in the conical phase. Additionally, the splitting $s = \frac{(\omega_{+Q}) - (\omega_{-Q})}{|\gamma|\mu_0 H_{c2}}$ is also shape dependent, which is natural considering that dipolar interactions are shape dependent. In the extremal case of a static field applied perpendicular to the surface of an infinite disk with $N_z = 1$, the two modes are degenerate again and that degeneracy is independent of $\chi_{\text{con}}^{\text{int}}$. Taking a closer look at the splitting for $H_0^{\text{ext}} = H_{c2}$ or $h = 1$, one arrives at the following formulas for either rotationally symmetric shapes with $N_x = N_y$ or maximally asymmetric shapes with $N_x = 0$

$$s_{h=1}(N_x = N_y) = \frac{1}{2} \frac{1 - N_z}{(\chi_{\text{con}}^{\text{int}})^{-1} + N_z} \quad (7.3)$$

$$s_{h=1}(N_x = 0) = \frac{\sqrt{1 + (1 - N_z)\chi_{\text{con}}^{\text{int}}} - 1}{1 + N_z\chi_{\text{con}}^{\text{int}}}. \quad (7.4)$$

Especially in the first expression it is evident, that the splitting increases for increasing $\chi_{\text{con}}^{\text{int}}$ but decreases with increasing N_z . Rewritten in terms of χ_{con} it is even more obvious

$$s_{h=1}(N_x = N_y) = \frac{1 - N_z}{2} \chi_{\text{con}}. \quad (7.5)$$

Furthermore, the splitting of these two modes at zero field depends crucially on whether the sample is rotationally invariant around the field axis or not. If it is, as is the case for sample #1, then the two modes are degenerate in this point. A slight deviation already leads to a small gap at $H_0^{\text{ext}} = 0$ as is observed for the almost spherical cuboid sample #3. The largest splitting is observed when N_x and N_y are maximally different as is the case for example for a rod like sample like sample #2. As above the formulas for these two extremal cases are given by

$$s_{h=0}(N_x = N_y) = 0 \quad (7.6)$$

$$s_{h=0}(N_x = 0) = \frac{\sqrt{2 + \chi_{\text{con}}^{\text{int}}} \left(\sqrt{1 + \frac{1 - N_z}{4} \chi_{\text{con}}^{\text{int}}} - 1 \right)}{1 + N_z \chi_{\text{con}}^{\text{int}}}. \quad (7.7)$$

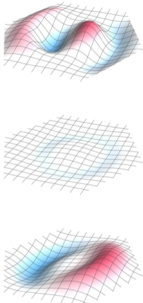
Indeed, also experimentally two modes have been observed in microwave or early electron spin resonance experiments [122, 123] for excitation fields perpendicular to an applied static field. Signatures of the conical modes were also observed in recent pump-probe measurements in $\text{Fe}_{1-x}\text{Co}_x\text{Si}$ [124]. Before circling back in [section 7.2](#) and elucidating what more besides a large distance between the two modes is needed to measure and resolve them individually and efficiently, we briefly focus on their nature and characteristics as already discussed in [93, 37].

Of course, the modes are characterized by different \mathbf{k} -dependent contributions $\delta\mathbf{M}_{\mathbf{k}}(\omega)$. Starting with the higher frequency ω_{+Q} , numerical calculations provide the corresponding eigenvector in momentum space which has the form

$$\delta\mathbf{M}_{\mathbf{k}}(\omega_{+Q}) = \{v_0, \mathbf{0}, v_{+Q}, \mathbf{0}, v_{+2Q}\}$$

with

$$\mathbf{v}_{+Q} = \begin{pmatrix} 0 \\ 0 \\ v_{+Q}^z \end{pmatrix} \quad \text{and} \quad \mathbf{v}_{+2Q} = \begin{pmatrix} v_{+Q}^x \\ v_{+Q}^y \\ 0 \end{pmatrix}$$



7. Resonance at the Γ -Point

The eigenvector of the lower frequency mode ω_{-Q} has components of the form

$$\delta \mathbf{M}_{\mathbf{k}}(\omega_{-Q}) = \{\mathbf{v}_0^*, \mathbf{v}_{-Q}^*, \mathbf{0}, \mathbf{v}_{-2Q}^*, \mathbf{0}\}$$

with

$$\mathbf{v}_{-Q}^* = \begin{pmatrix} 0 \\ 0 \\ (v_{-Q}^z)^* \end{pmatrix} \quad \text{and} \quad \mathbf{v}_{-2Q}^* = \begin{pmatrix} (v_{-Q}^x)^* \\ (v_{-Q}^y)^* \\ 0 \end{pmatrix}$$

The vectors \mathbf{v}_{-2Q} and \mathbf{v}_{+2Q} possess the chiral character in the xy-plane for $\mathbf{v}_{-2Q} \cdot \mathbf{v}_{-2Q} = 0$ and $\mathbf{v}_{+2Q} \cdot \mathbf{v}_{+2Q} = 0$, cf. properties of the basis vectors $\hat{\mathbf{e}}_{\pm}$ of a chiral basis in [appendix D.2](#). More importantly, for the higher frequency mode ω_{+Q} the z-component of the magnetization ($\hat{\mathbf{e}}_z$ -direction is the helix pitch direction in the conical phase) oscillates with $v_{+Q}^z e^{i(Qz - (\omega_{+Q})t)}$.

While locally, the magnetic moments all precess in the same way as determined by the Landé factor g and indicated by the red arrow in [figure 7.2](#), the collective character of the excitations is reflected in periodic compressions of spins within the helix. These compressions move, similar to an Archimedean screw, with a finite phase vector either parallel or anti-parallel to the helix pitch vector \mathbf{Q} , i.e., either *up* ($+\mathbf{Q}$) or *down* ($-\mathbf{Q}$) the helical staircase. The movement is illustrated in [figure 7.2](#).

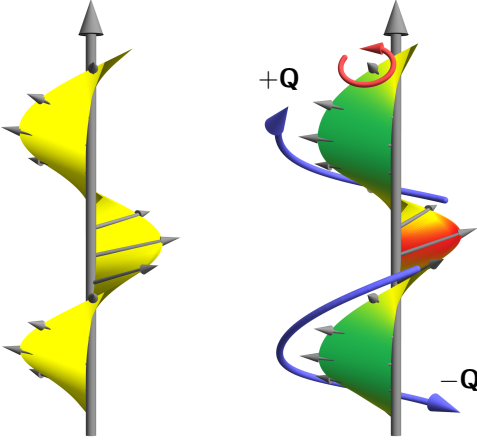


Figure 7.2: Illustration of the excitations in the conical phase.

Left: Equilibrium state in which the tips of all neighboring magnetic moments have the same distance from each other.

Right: The equilibrium state is distorted in such a way, that the tips of neighboring magnetic moments are either closer together (green) or farther away (red). This distortion propagates either *up* or *down* the spiral staircase where *up* is the direction of the helix pitch vector.

If we would not consider demagnetization fields or only excitations at zero-field for a rotationally symmetric shape, the two resonance frequencies would be equal and two-fold degenerate. The calculated eigenvectors that span the degenerate eigenspace would then contain mixed components of both $\delta \mathbf{M}_{+Q}$ and $\delta \mathbf{M}_{-Q}$ which can be decomposed into two eigenvectors that carry pure $+\mathbf{Q}$ and $-\mathbf{Q}$ contributions.

Note, that the numerical calculations have been performed by employing a negative gyromagnetic ratio $\gamma < 0$ in the precession equation (4.7), as is the case

for electrons. It fixes the sense of the local precession of individual moments. As the conical helix state continuously resembles more and more a field polarized state with increasing magnetic field, at least one of the resonances needs to have a continuous transition between the two phases. The orientation of the precession in the field polarized phase is fixed by the gyromagnetic ratio, i.e., right-handed or counter-clockwise around the static field in the case of electrons. As local moments precess the same way in the conical phase, it is the mode in which also the mean magnetization precesses counter-clockwise around the field, that continuously transitions into the Kittel mode of the field-polarized phase. For a right handed helix, this is the $+Q$ mode, cf. [figure 7.2](#). When the chirality is reversed by changing the sign of D in (1.4) or (3.36), the local moments still precess in the same direction. Now however, a counter-clockwisely rotating mean magnetization means that the compression moves anti-parallel to the helix pitch, i.e., now the $-Q$ mode connects with the Kittel mode. A summary is shown in [table 7.2](#).






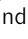


γ	D	FP	Helix	
			high	low
+	+		$-Q$	$+Q$
+	-		$+Q$	$-Q$
-	+		$+Q$	$-Q$
-	-		$-Q$	$+Q$

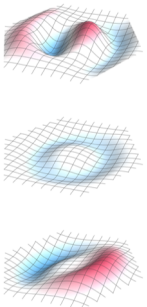
Table 7.2: Summarized relationship between chirality, the gyromagnetic ratio γ and the $\pm Q$ modes. The table lists the signs of γ and D . While local precession and precession in the field-polarized (FP) phase are only influenced by the former, their combination determines in whether the conical mode with higher energy, which is the one continuously connected to the Kittel mode, propagates parallel ($+Q$) or anti-parallel ($-Q$) to the helix pitch vector \mathbf{Q} .

Convention:  and  show a top view of the collective rotations with the magnetic field pointing towards the viewer:  $\hat{=}$ .

7.2. ELLIPTICITY & MAGNETIC LINEAR DICHROISM

To visualize the mode splitting experimentally most efficiently, the first step is to think about choosing a material with high internal conical susceptibility like Cu_2OSeO_3 and a maximally asymmetrical shape and, in the best case, $N_z = 0$ for $\mathbf{H}_0^{\text{ext}} \parallel \hat{\mathbf{e}}_z$. This corresponds to a disc-like sample with the static magnetic field applied parallel to the surface.

While such a setup leads to modes that are maximally apart from each other, the question remains whether they can be seen in experiment. At this point, the calculation of their spectral weights enters. They can be calculated via [equations \(6.8\) and \(6.24\)](#). The results are quite astonishing as the weight



7. Resonance at the Γ -Point

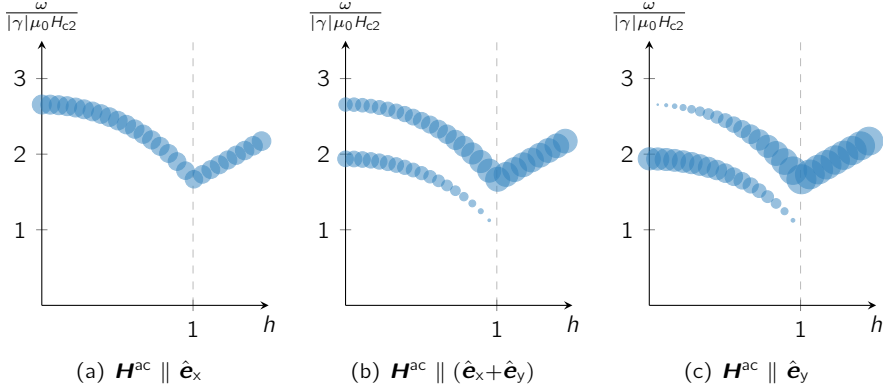


Figure 7.3: Weight distribution in conical phase for a “standing” disc with demagnetization factors $N_x = 1$ and $N_y = N_z = 0$, $\mathbf{H}_0^{\text{ext}} \parallel \hat{\mathbf{e}}_z$ and a varying excitation direction $\mathbf{H}^{\text{ac}} \perp \mathbf{H}_0^{\text{ext}}$.

distribution depends significantly on the excitation direction within the plane perpendicular to the static field. **Figure 7.3** shows such resonances for three different ac-field directions. Most noticeable is the region for small magnetic fields, where the spectral weight is shifted almost entirely from one mode to the other by rotating \mathbf{H}^{ac} by 90° .

Experimentally, this effect has been explicitly measured [125] on three different Cu_2OSeO_3 samples using two different sizes of coplanar waveguides. The samples were rod shaped, as such a geometry makes it easier to mount the sample on a CPW, compared with a “standing” disc, and serve the same purpose. **Figure 7.4** shows data of these experiments. In panels (a) and (b) and (e), also corresponding to **figure 7.3(a)**, one can easily trace out a single mode in the conical/helical phase. In particular, a single resonance is measured at $\mathbf{H}_0^{\text{ext}} = 0$. Upon rotation around $\hat{\mathbf{e}}_z$ a second mode appears whose weight becomes maximal after a 90° rotation, as seen in panels (c) and (f) of **figure 7.4** and **figure 7.3(c)**. Again, only one resonance appears at $\mathbf{H}_0^{\text{ext}} = 0$ but now at a different frequency. Resonances shown in **figure 7.4** that occur in the skyrmion lattice phase are discussed in **section 11.1**. There, resonances not only occur when for $\mathbf{H}^{\text{ac}} \perp \mathbf{H}_0^{\text{ext}}$ but also for $\mathbf{H}^{\text{ac}} \parallel \mathbf{H}_0^{\text{ext}}$.

The observation, that it is possible to select complementary modes at small fields by rotating excitation field or alternatively the sample by 90° , which can be seen as interchanging the demagnetization factors N_x and N_y , suggests an existing cross-polarization between the linearly polarized field \mathbf{H}^{ac} and either mode $+Q$ and $-Q$, respectively. The corresponding linear polarization of the $\pm Q$ modes occurring near 2 GHz has not been considered before. To explain this occurrence or absence of modes we consider the ellipticity of magnetization precession in the

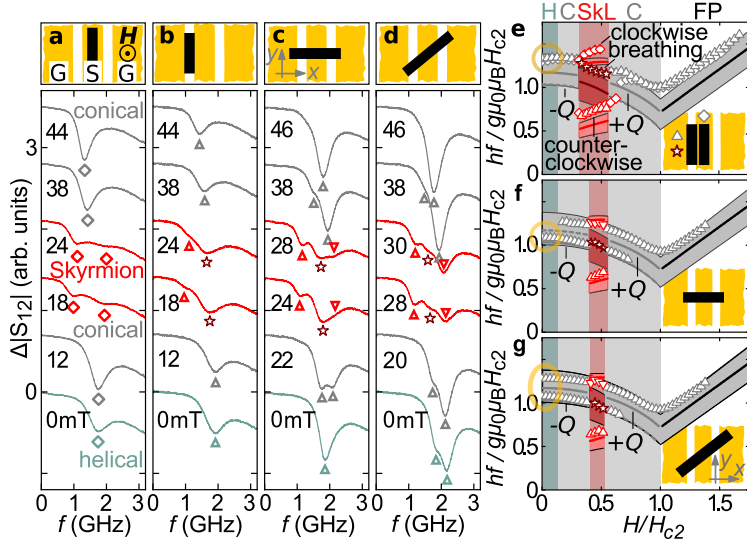


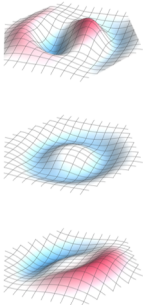
Figure 7.4: Spin resonance data and comparison with theory.

(a)-(d): Typical resonance spectra measured at temperatures around 57 K on three different samples positioned differently on the CPW as sketched at the top of each panel. Data are shown for different applied field values in the helical, conical, and skyrmion lattice phases and are offset for clarity. The static field is applied $\langle 100 \rangle$ and the symbols are guides for the eye and indicate resonance frequencies.

(e)-(g): Comparison between experiment and theory. Lines correspond to calculations at $\mathbf{k} = 0$ and shaded bands to potential deviations due to finite wave vectors that arise from the construction of a CPW, cf. [section 5.1](#). Dashed lines indicate modes with small spectral weight. Circles highlight the modes resolved at small \mathbf{H} . Figure taken from [\[125\]](#).

spin helix phase. We introduce the homogeneous dynamic magnetization $\delta \mathbf{M}_{0,\sigma}$ averaged along a helix period, where $\sigma = \pm$ respectively corresponds to the $\pm Q$ modes. For a helix at zero field, the local magnetization is perpendicular to \mathbf{Q} , cf. [figure 1.3\(a\)](#), and if $\mathbf{Q} \parallel \hat{e}_z$, then it is easy to see that $\delta \mathbf{M}_{0,\sigma}$ lies and oscillates in the xy -plane, since longitudinal deviations cancel each other out. This statement is also true in the conical phase, as the additional contribution parallel to \mathbf{Q} is static. This mean magnetization oscillates counterclockwise for the $+Q$ and clockwise for the $-Q$ mode. While their frequencies are given by [equation \(7.2\)](#), we obtain

$$\frac{\delta \mathbf{M}_{0,\sigma}^x}{\delta \mathbf{M}_{0,\sigma}^y} = \frac{2h^2 N_x N_y \chi_{\text{con}}^{\text{int}} + \sigma W_1 - (N_x - N_y)(2 + (1 - h^2)\chi_{\text{con}}^{\text{int}}) - 2N_x h W_{\sigma,2}}{2h^2 N_x N_y \chi_{\text{con}}^{\text{int}} + \sigma W_1 + (N_x - N_y)(2 + (1 - h^2)\chi_{\text{con}}^{\text{int}}) - 2N_y h W_{\sigma,2}} \quad (7.8)$$



7. Resonance at the Γ -Point

for the ratio of their amplitudes. The abbreviations $W_1, W_{\sigma,2} > 0$ are given by

$$W_1^2 = (N_x - N_y)^2 (2 + (1 - h^2) \chi_{\text{con}}^{\text{int}})^2 + 4h^2 N_x N_y \left((2 + \chi_{\text{con}}^{\text{int}}) (4 + \chi_{\text{con}}^{\text{int}} (N_x + N_y)) - h^2 (4 + \chi_{\text{con}}^{\text{int}} (4 + \chi_{\text{con}}^{\text{int}} (N_x + N_y) - \chi_{\text{con}}^{\text{int}} N_x N_y)) \right) \quad (7.9)$$

$$W_{\sigma,2}^2 = \sigma W_1 \chi_{\text{con}}^{\text{int}} + (2 + \chi_{\text{con}}^{\text{int}}) (4 + \chi_{\text{con}}^{\text{int}} (N_x + N_y)) - h^2 (4 + \chi_{\text{con}}^{\text{int}} (4 + \chi_{\text{con}}^{\text{int}} (N_x + N_y) - 2 \chi_{\text{con}}^{\text{int}} N_x N_y)) \quad (7.10)$$

where $h = H_0^{\text{ext}}/H_{c2}$ is again in units of H_{c2} . For a derivation see [section 8.4](#). This lets us use [equations \(4.43\) and \(4.44\)](#) as the definitions for ellipticity ε_σ and sign σ , respectively, to obtain a set of curves for the ellipticity plotted against one of the demagnetization factor. Here, we take the exemplary specification of one of the samples used in the previously described experiments conducted in [\[125\]](#). They read $N_x = 0.07$, $N_y = 0.4$ and $N_z = 0.53$ for a rod in \hat{e}_x -direction. N_z is kept steady while N_x and N_y are varied continuously between 0 and 0.47 while fulfilling $N_x + N_y + N_z = 1$. In the experiment this was achieved by rotating the sample around \hat{e}_z and the resulting graphs can be seen in panels (b) and (c) of [figure 7.5](#), showing the ellipticity and weight distribution in dependence of n_x , respectively.

In a rotationally symmetric sample with $N_x = N_y$ like a circular disk, the ellipticity vanishes $\varepsilon_\sigma = 0$ for symmetry reasons. This leads to circular polarization of the $\pm Q$ modes as shown in [figure 7.5\(a\)](#) for a small but finite field. As soon as a sample is of slightly elliptical shape within the xy -plane, i.e., $N_x \neq N_y$, the polarization becomes elliptical, too, and ε_σ finite.

The most interesting effect takes place at zero field $\mathbf{H}_0^{\text{ext}} = 0$ which is depicted as black lines in panels (b) and (c) of [figure 7.5](#). For a disc with $N_x = N_y$ the screw symmetry of the helix ensures that the two excitation modes are degenerate and any polarization can be achieved. When this degeneracy is lifted, $N_x \neq N_y$, the two modes become strictly linearly polarized. This can be explained by the π -rotation symmetry of a helix at $\mathbf{H}_0^{\text{ext}} = 0$ around one of its spins pointing along one of the principal axes of the ellipsoid, i.e., along \hat{e}_x or \hat{e}_y . Because of these symmetries, one can always find pairs of spins whose precessional motion conspires to yield a linear polarization along one of the principal axes. A similar effect can be observed in easy-plane anti-ferromagnets where magnetization on the two sub-lattices, labeled up and down, precesses in opposite direction. While their components along one direction cancel each other, they add up in the direction perpendicular to it resulting in a linear oscillation [\[126\]](#). As a consequence of this crossover polarization the ellipticities of modes $+Q$ (solid line) and $-Q$ (dashed line) follow step functions

$$\varepsilon_\sigma |_{\mathbf{H}_0^{\text{ext}}=0} = \text{sgn}[\sigma \cdot (N_x - N_y)]. \quad (7.11)$$

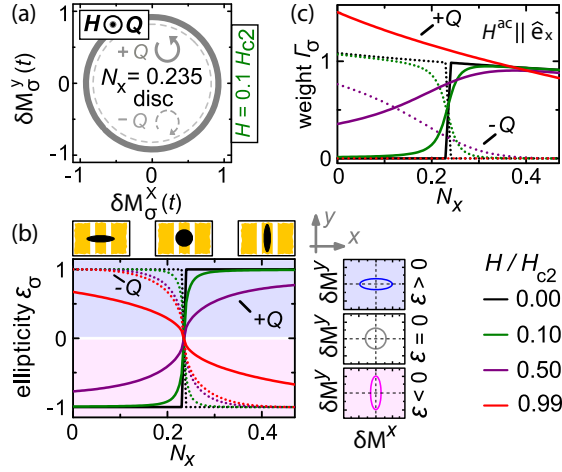


Figure 7.5: Ellipticity and spectral weights for excitations in the conical phase. Solid (dotted) lines correspond to the +Q(−Q) modes. Figure taken from [125].

(a): Special case of a rotationally symmetric disc. Shown are the circularly polarized $\delta \mathbf{M}_\pm$ for $N_x = N_y = 0.235$ and $N_z = 0.53$ for a field $\mathbf{H}_0^{\text{ext}} = 0.1 H_{c2}$.

(b): Ellipticity plotted for different shapes and different field. Most notable is the black curve for $\mathbf{H}_0^{\text{ext}}/H_{c2} = 0$ which is singular for rotationally symmetric samples, here at $N_y = 0.235$. The opposite extreme, the solid red curve of the +Q mode, coincides with the expected ellipticity in the field-polarized phase.

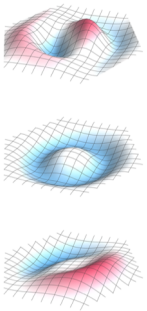
(c): Spectral weights in dependence on N_x . Again, the black curve at zero field has a singular feature for a rotationally symmetric shape.

This singular shape dependence impacts the spectral weights Γ_σ in an equally singular fashion, cf. black lines in figure 7.5(c). For an ac field $\mathbf{H}^{\text{ac}} \parallel \hat{\mathbf{e}}_x$ we find

$$\Gamma_\sigma(N_x, N_y)|_{\mathbf{H}_0^{\text{ext}}=0} \propto \frac{\Theta[\sigma \cdot (N_x - N_y)]}{1 + \frac{2+N_x}{6} \chi_{\text{con}}^{\text{int}}} \quad (7.12)$$

with the Heaviside step function $\Theta[s] = 1$ for $s > 0$ and zero otherwise. Hence, the $\pm Q$ modes can be individually excited, because the weights can be shifted in a way, so that all weight accumulates in one mode or the other. Taking the rod in $\hat{\mathbf{e}}_x$ -direction as an example with $N_x < N_y$, then the +Q mode is linearly polarized along $\hat{\mathbf{e}}_y$ ($\epsilon_+ = -1$). Therefore, $\mathbf{H}^{\text{ac}} \parallel \hat{\mathbf{e}}_x$ does not couple to it which returns zero for the spectral weight Γ_+ represented by the solid black line in figure 7.5(c) for $N_x < 0.235$. This effect is called *magnetic linear dichroism*, see below.

When increasing the magnetic field, one notices that ellipticities and weights of the +Q and −Q modes are not symmetrical with respect to the perfect disc shape at $N_x = 0.235$. Considering the −Q mode (dotted lines) for $N_x \ll N_y$ it is evident, that its ellipticity persists over a wide field range. We extract $\epsilon_- = 0.999$ at $\mathbf{H}_0^{\text{ext}} = 0.5 H_{c2}$ for $N_x = 0.07$, which is the specification of the sample used in [125]. On the contrary, −Q loses spectral weight significantly earlier. This is



7. Resonance at the Γ -Point

due to the mismatch of handedness with the Kittel mode in the field-polarized phase. The spectral weight Γ_+ , on the other hand, increases strongly while $+Q$ gets elliptically polarized.

Upon a further increase, one notices that the $+Q$ mode changes the polarization axis at some intermediate field h_+^{circ} . The $+Q$ mode is then circularly polarized independently of demagnetization factors N_x and N_y , i.e., $\varepsilon_+(h_+^{\text{circ}}) = 0$ for all N_x . For this field we obtain the expression

$$h_+^{\text{circ}} = \frac{2 + \chi_{\text{con}}^{\text{int}}}{\sqrt{(2 + \chi_{\text{con}}^{\text{int}})(2 + (2 - N_z)\chi_{\text{con}}^{\text{int}}) + \sqrt{(1 - N_z)\chi_{\text{con}}^{\text{int}}(2 + \chi_{\text{con}}^{\text{int}})^2(4 + (1 - N_z)\chi_{\text{con}}^{\text{int}})}}}. \quad (7.13)$$

For the Cu_2OSeO_3 sample from [125] with $\chi_{\text{con}}^{\text{int}} = 1.76$ and $N_z = 0.53$ we get $h_+^{\text{circ}} \approx 0.76$.

In the limit $H_0^{\text{ext}} \rightarrow H_{c2}$, the spectral weight of the $-Q$ mode vanishes completely while weights of the $+Q$ mode connect seamlessly to the Kittel mode which is also reflected in the ellipticity of the $+Q$ mode. The latter takes on the same values of the ellipticity in the field-polarized or ferromagnetic phase, which is generally given by [89]

$$\varepsilon_{\text{fm}} = \sqrt{\frac{N_x - N_y}{N_x - N_z + H_0^{\text{ext}}/M_0}} \quad (7.14)$$

or explicitly at H_{c2} with $H_0^{\text{ext}} = h H_{c2}$ and $M_0 = \chi_{\text{con}} H_{c2}$ we get

$$\varepsilon_{\text{fm}}|_{h=1} = \sqrt{\frac{N_x - N_y}{N_x - N_z + \chi_{\text{con}}^{-1}}} = \sqrt{\frac{(N_x - N_y)\chi_{\text{con}}^{\text{int}}}{1 + N_x\chi_{\text{con}}^{\text{int}}}}. \quad (7.15)$$

LINEAR DICHROISM

Linear dichroism in general is the phenomenon of polarization dependent absorption of electromagnetic waves. It plays a prominent role in polarization filters in optical technology and in structure determination or the study of the functionality of bio-molecules. Magnetic linear dichroism comes into play when studying magneto-optical effects. Experiments are most often conducted by using X-rays to examine element-specific magnetic characterizations. Their frequencies are much higher, though, than the few gigahertz regime that is key in communication technologies. There, linear dichroism is not known, because magnetic precession within this frequency range has been argued to be circularly or elliptically polarized. The features described in this section lie at approximately 2 GHz, which is within the operating frequency range of modern telecommunication networks. The previously mentioned similar features occurring in anti-ferromagnets also lie above that frequency in the terrahertz regime. Therefore, our findings offer new prospects in designing new applications in this technologically important frequency range.

8

NON-LINEAR σ MODEL

In this chapter we introduce the non-linear σ model as a way to not only calculate the resonance frequencies in the conical phase analytically, but also the consequential expressions used in the previous section for the discussion about ellipticity. Furthermore, we use it to get a more intuitive insight into the remainder of the spectrum, which will be discussed in the next chapter.

The σ model goes back to work Gell-Mann and Lévi in 1960 [127] which was, similar to the work of Skyrme, a contribution to particle physics. The sigma notation comes from the field they introduced describing a new scalar meson σ with isotopic spin zero. *Linear σ models*, which generally boil down to linear wave equations, are well implementable in numerics and were therefore used in this thesis up to now. For analytical calculations, it is sometimes easier to use a *non-linear σ model* as it is a mode with a decreased number of degrees of freedom. In the original paper, the σ field was made into a function of pion fields already present in the theory, instead of being a field of a new particle. Translated to solid state physics, this means that we could make an ansatz for the magnetization with a fixed length or amplitude M and a normalized field $\hat{\mathbf{n}}(\mathbf{r})$, effectively reducing the degrees of freedom by one

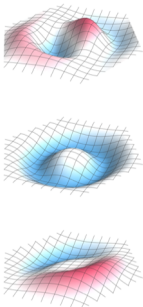
$$\mathbf{M}(\mathbf{r}) = M \hat{\mathbf{n}}(\mathbf{r}). \quad (8.1)$$

Because the target manifold of $\hat{\mathbf{n}}(\mathbf{r})$ is the non-linear surface of a sphere, instead of \mathbb{R}^3 of $\mathbf{M}(\mathbf{r})$, it is referred to as a non-linear σ model [128]. σ models are described by a Lagrangian density \mathcal{L} . Since the $\hat{\mathbf{n}}$ field is forced to have length one, there is no need for quartic terms like in the Ginzburg-Landau theory to stabilize the energy. The Lagrangian density therefore only consist of terms which are directly linked to physical effects. For our model we consider

$$\mathcal{L} = \mathcal{L}_{\text{dyn}} - \mathcal{F} \quad (8.2)$$

with

$$\mathcal{F} = \mathcal{F}_{\text{ex}} + \mathcal{F}_{\text{dip}} \quad (8.3)$$



8. Non-Linear σ Model

where \mathcal{F}_{ex} contains Heisenberg exchange, Dzyaloshinskii-Moriya and Zeeman interaction

$$\mathcal{F}_{\text{ex}} = \frac{\rho_s}{2} \left[(\nabla_i \hat{n}_j)^2 + 2Q \hat{n} \cdot (\nabla \times \hat{n}) \right] - \mu_0 M \hat{n} \cdot \mathbf{H}_0^{\text{ext}} \quad (8.4)$$

with *spin stiffness density*¹ $\rho_s = 2JM^2$ and $Q = D/J$. The spin stiffness is a measure of the strength of the exchange interaction. The static external magnetic field is denoted by $\mathbf{H}_0^{\text{ext}}$. The dipolar interaction is given by

$$\mathcal{F}_{\text{dip}} = \frac{1}{2} \hat{n}_i \chi_{\text{dip}ij}^{-1} \hat{n}_j \quad (8.5)$$

with

$$\chi_{\text{dip},ij}^{-1} = \mu_0 M^2 \begin{cases} \frac{\mathbf{k}_i \mathbf{k}_j}{|\mathbf{k}|^2} & \text{for } |\mathbf{k}| \gg 1/L \\ N_{ij} & \text{for } |\mathbf{k}| \ll 1/L \end{cases} \quad (8.6)$$

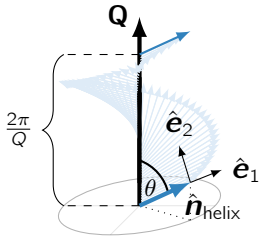
for a sample size L , cf. (3.26).

The equation of motion describing the system is the Landau-Lifshitz equation (4.7). This equation should hence also be retrieved when evaluating the Euler-Lagrange equations from (8.2). This dynamics is encoded in the last term given by

$$\mathcal{L}_{\text{dyn}} = -\frac{M}{\gamma} \mathbf{A}(\hat{n}) \partial_t \hat{n} \quad (8.7)$$

where the gyromagnetic ratio γ is defined as in (4.6) with $\gamma < 0$ for electrons. The gauge field obeys $\epsilon_{ijk} \frac{\partial A_j}{\partial \hat{n}_i} = \hat{n}_k \Leftrightarrow \frac{\partial A_j}{\partial \hat{n}_i} = \frac{1}{2} \epsilon_{ijk} \hat{n}_k + \text{sym}_{ij}$, where the symmetric part sym_{ij} cancels out in the here performed calculations. A derivation can be found in [appendix D.1](#).

8.1. MEAN-FIELD AND PARAMETERIZATION



Let the external field be along the z-axis. Neglecting cubic anisotropies and assuming an ellipsoidal sample shape leads to an alignment of the helix pitch vector with that field, $\mathbf{H}_0^{\text{ext}} = H_0^{\text{ext}} \hat{e}_z \parallel \mathbf{Q}$. This lets us parameterize an arbitrary equilibrated helix in that direction as

$$\hat{n}_{\text{helix}} = \begin{pmatrix} \sin \theta \cos(Qz) \\ \sin \theta \sin(Qz) \\ \cos \theta \end{pmatrix}. \quad (8.8)$$

Figure 8.1: Parameterization of magnetization $\mathbf{M} = M \hat{n}$.

The angle θ is the angle between helix pitch \mathbf{Q} and \hat{n}_{helix} , cf. [figure 8.1](#). Plugging this ansatz for \hat{n}_{helix}

¹Note, that a pre-factor of $1/2$ canonical to field theories has been introduced in \mathcal{F}_{ex} , compared with the theories before. It gives, for example, a cleaner version of the conical susceptibility without the unnecessary factor of two, cf. [equations \(B.10\) and \(8.15\)](#)

into (8.2) and evaluating the derivatives while assuming that $\chi_{\text{dip},ij}^{-1}$ is diagonal, leads to the free energy density

$$f(\theta) = -\frac{\rho_s Q^2}{2} \sin^2 \theta - M \mu_0 H_0^{\text{ext}} \cos \theta + \frac{\mu_0 M^2}{2} N_z \cos^2 \theta. \quad (8.9)$$

Because $\mathbf{Q} \parallel \hat{\mathbf{e}}_z$ there is only a homogeneous component in z -direction in the dipolar contribution and is obtained by using and evaluating $\chi_{\text{dip},ij}^{-1}$ in the limit $\mathbf{k} = 0$. Within the xy -plane, however, $\hat{\mathbf{n}}_{\text{helix}}$ modulates with respect to $Q \gg 1/L$ and the full dipole-dipole interaction, i.e., $\chi_{\text{dip},ij}^{-1}$ in the limit $\mathbf{k} \gg 0$, should be evaluated. Since $\mathbf{Q} \parallel \hat{\mathbf{e}}_z$, these terms are zero. A more physical picture is, that these oscillations average out and cancel each other. To find the minimum of $f(\theta)$ with respect to θ , we differentiate $f(\theta)$ set it to zero yielding the equation of state

$$0 = -\rho_s Q^2 \cos \theta + M \mu_0 H_0^{\text{ext}} - \mu_0 M^2 N_z \cos \theta \quad (8.10)$$

$$= -\rho_s Q^2 \cos \theta + M \mu_0 \left(H_0^{\text{ext}} - \underbrace{M \cos \theta}_{|\mathbf{M}_0|} N_z \right) \quad (8.11)$$

$$= -\rho_s Q^2 \cos \theta + M \mu_0 H_0^{\text{int}} \quad (8.12)$$

The internal magnetic field in the last line is given via equations (3.6) and (3.21) as

$$H_0^{\text{int}} = H_0^{\text{ext}} - N_z M_0 = H_0^{\text{ext}} - N_z M \cos \theta \quad (8.13)$$

for $\mathbf{M}_0 \parallel \hat{\mathbf{e}}_z$. Equation (8.10) lets us derive an expression for the homogeneous net magnetization, i.e., the part parallel to \mathbf{Q} :

$$|\mathbf{M}_0| = M \cos \theta = \frac{\mu_0 M^2 H_0^{\text{ext}}}{\rho_s Q^2 + \mu_0 M^2 N_z}. \quad (8.14)$$

We saw earlier that the susceptibility in the conical phase χ_{con} is approximately constant and here given by $M \cos \theta = \chi_{\text{con}} H_0^{\text{ext}}$ with

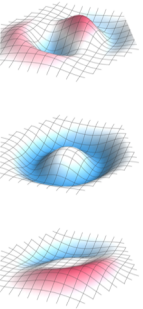
$$\chi_{\text{con}} = \frac{\mu_0 M^2}{\rho_s Q^2 + \mu_0 M^2 N_z} = \frac{\chi_{\text{con}}^{\text{int}}}{1 + N_z \chi_{\text{con}}^{\text{int}}} \quad (8.15)$$

where the internal conical susceptibility is given by $\chi_{\text{con}}^{\text{int}} = \frac{\mu_0 M^2}{\rho_s Q^2}$ and defined via $\chi_{\text{con}} H_0^{\text{ext}} = \chi_{\text{con}}^{\text{int}} H_0^{\text{int}}$. Particularly at the critical field between conical and field-polarized phase at $\theta = 0$ we get

$$M = \chi_{\text{con}} H_{c2} = \chi_{\text{con}}^{\text{int}} H_{c2}^{\text{int}}. \quad (8.16)$$

8.2. FLUCTUATIONS

To study excitations in the conical phase, we add a small fluctuating field $\boldsymbol{\pi}$ on top of the equilibrium state $\hat{\mathbf{n}}_{\text{helix}}$. Since length fluctuations of $\hat{\mathbf{n}}_{\text{helix}}$ are neglected



8. Non-Linear σ Model

by construction, $\boldsymbol{\pi}^\top = (\pi_1, \pi_2)$ is effectively two dimensional and lies in the plane perpendicular to $\hat{\mathbf{n}}_{\text{helix}}$. To this end, we introduce an orthogonal frame

$$\hat{\mathbf{e}}_1 = \begin{pmatrix} -\sin(Qz) \\ \cos(Qz) \\ 0 \end{pmatrix} \quad \hat{\mathbf{e}}_2 = \begin{pmatrix} -\cos\theta \cos(Qz) \\ -\cos\theta \sin(Qz) \\ \sin\theta \end{pmatrix} \quad \hat{\mathbf{e}}_3 = \hat{\mathbf{n}}_{\text{helix}} \quad (8.17)$$

where $\boldsymbol{\pi}$ lies in the plane spanned by $\hat{\mathbf{e}}_1$ and $\hat{\mathbf{e}}_2$. The latter are depicted in [figure 8.1](#). Due to the chiral nature of the equation of motion, it is useful to also introduce a chiral basis $\hat{\mathbf{e}}_+$ and $\hat{\mathbf{e}}_-$ that accommodates the twisted structure:

$$\hat{\mathbf{e}}_\pm = \frac{1}{\sqrt{2}}(\hat{\mathbf{e}}_1 \pm i\hat{\mathbf{e}}_2) \quad \Rightarrow \quad \hat{\mathbf{e}}_1 = \frac{1}{\sqrt{2}}(\hat{\mathbf{e}}_+ + \hat{\mathbf{e}}_-) \quad \hat{\mathbf{e}}_2 = \frac{1}{\sqrt{2}}i(-\hat{\mathbf{e}}_+ + \hat{\mathbf{e}}_-) \quad (8.18)$$

$$\hat{\mathbf{e}}_\pm = \frac{1}{\sqrt{2}} \begin{pmatrix} -\sin(Qz) \mp i \cos(Qz) \cos\theta \\ + \cos(Qz) \mp i \sin(Qz) \cos\theta \\ \pm i \sin\theta \end{pmatrix}. \quad (8.19)$$

Additionally, we denote the projections of $\hat{\mathbf{n}}_{\text{helix}}$ onto the pitch vector \mathbf{Q} and the plane perpendicular it by \mathbf{n}_\parallel and \mathbf{n}_\perp , respectively. They are given by

$$\mathbf{n}_\parallel = \cos\theta \begin{pmatrix} 0 \\ 0 \\ 1 \end{pmatrix} \quad \mathbf{n}_\perp = \sin\theta \begin{pmatrix} \cos(Qz) \\ \sin(Qz) \\ 0 \end{pmatrix}. \quad (8.20)$$

Identities for calculations with these vectors are listed in [appendix D.2](#). The fluctuating field can now be parameterized as

$$\hat{\mathbf{n}} = \hat{\mathbf{n}}_{\text{helix}} \sqrt{1 - \boldsymbol{\pi}^2} + \hat{\mathbf{e}}_1 \pi_1 + \hat{\mathbf{e}}_2 \pi_2 \quad (8.21)$$

$$\approx \hat{\mathbf{n}}_{\text{helix}} \left(1 - \frac{\boldsymbol{\pi}^2}{2}\right) + \hat{\mathbf{e}}_1 \pi_1 + \hat{\mathbf{e}}_2 \pi_2 \quad (8.22)$$

where the square root ensures that $\hat{\mathbf{n}}$ stays normalized and in the second line we expanded the square root to second order. To make use of the chiral basis, we can change from the real $\boldsymbol{\pi}$ field to a complex spinor $\boldsymbol{\psi}^\top = (\psi, \psi^*)$ with $\sqrt{\frac{g\mu_B}{M}}\psi = \frac{1}{\sqrt{2}}(\pi_1 - i\pi_2)$ and obtain

$$\hat{\mathbf{n}} = \hat{\mathbf{n}}_{\text{helix}} \sqrt{1 - 2\frac{g\mu_B}{M}|\psi|^2} + \sqrt{\frac{g\mu_B}{M}}(\psi\hat{\mathbf{e}}_+ + \psi^*\hat{\mathbf{e}}_-) \quad (8.23)$$

$$\approx \hat{\mathbf{n}}_{\text{helix}} \left(1 - \frac{g\mu_B}{M}|\psi|^2\right) + \sqrt{\frac{g\mu_B}{M}}(\psi\hat{\mathbf{e}}_+ + \psi^*\hat{\mathbf{e}}_-) \quad (8.24)$$

The factor $\frac{g\mu_B}{M}$ with units of volume ν has been introduced for later convenience. That makes $\boldsymbol{\psi}$ of unit $1/\sqrt{\nu}$ and the Fourier transformed $\boldsymbol{\psi}(\mathbf{k})$ of unit $\sqrt{\nu}$, cf. [equation \(3.8\)](#). The transformation from one description into the other is achieved by $R \cdot \boldsymbol{\pi} = \boldsymbol{\psi}$ where R is given by the matrix

$$R = \frac{1}{\sqrt{2}} \sqrt{\frac{g\mu_B}{M}} \begin{pmatrix} 1 & -i \\ 1 & i \end{pmatrix} \quad (8.25)$$

which is unitary when normalized and also yields the identities

$$R \cdot \tau^{x,y,z} \cdot R^{-1} = \tau^{y,z,x} \quad (8.26)$$

for Pauli matrices τ^i .

With this preparatory work at hand, we can now derive an effective action \mathcal{S} in lowest order of ψ . The recipe is to plug (8.24) into \mathcal{L} , expand all other quantities around $\psi = 0$ as well and collect all second order terms. Terms of zeroth order only contribute a constant energy offset and first order terms only yield surface terms, which are not considered here. Expansion of \mathcal{F}_{ex} even up to fourth order can be found in [appendix D.3](#). There, we derive the second order term to be

$$\frac{1}{2} \psi^\dagger \mathcal{H}_{\text{ex}} \psi := \mathcal{F}_{\text{ex}}^{(2)'} = \frac{1}{2} \frac{\mathcal{E}_0}{Q^2} \psi^\dagger \left[-1 \nabla^2 + \frac{Q^2 \sin^2 \theta}{2} (1 - \tau^x) - i 2 Q \tau^z \mathbf{n}_\perp(\mathbf{r}) \cdot \nabla \right] \psi \quad (8.27)$$

with $\mathcal{E}_0 = g \mu_B Q^2 \rho_s / M = g \mu_B \mu_0 H_{c2}^{\text{int}}$, cf. definitions in (8.16). The factor $\frac{\mathcal{E}_0}{Q^2} =: \mathcal{D}$ is often referred to as the spin stiffness.

The second order contribution of the dynamic part \mathcal{L}_{dyn} is also obtained straightforward to be

$$\mathcal{L}_{\text{dyn}}^{(2)} = -\frac{1}{2} i \frac{g \mu_B}{\gamma} \psi^\dagger \partial_t \tau^z \psi = -\text{sgn}(q) \frac{1}{2} i \hbar \psi^\dagger \partial_t \tau^z \psi \quad (8.28)$$

for charge q . For clarity and brevity, we will assume electrons as spin carriers and hence $\text{sgn}(q) = -1$ and $\gamma < 0$. The goal is to obtain an effective action of the form

$$\mathcal{S} = \frac{1}{2} \int d\mathbf{r} \psi^\dagger (i \hbar \tau^z \partial_t - \mathcal{H}) \psi. \quad (8.29)$$

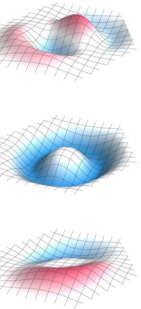
where $\mathcal{H} = \mathcal{H}_{\text{ex}} + \mathcal{H}_{\text{dip}}$ contains all second order contributions of \mathcal{F} . The only thing left is the treatment of the dipolar contributions. Here, things get slightly more complex. Since we consider χ_{dip}^{-1} in Fourier space, we also need to Fourier transform the action

$$\mathcal{S}_{\text{dip}} = \frac{1}{2} \int d\mathbf{r} \psi^\dagger (-\mathcal{H}_{\text{dip}}) \psi \quad (8.30)$$

$$= -\frac{1}{2\nu} \sum_{\mathbf{k}} (\psi^\dagger(\mathbf{k} + \mathbf{Q}), \psi^\dagger(\mathbf{k}), \psi^\dagger(\mathbf{k} - \mathbf{Q})) V_{\text{dip}}(\mathbf{k}) \begin{pmatrix} \psi(\mathbf{k} + \mathbf{Q}) \\ \psi(\mathbf{k}) \\ \psi(\mathbf{k} - \mathbf{Q}) \end{pmatrix}. \quad (8.31)$$

This structure arises, because $\hat{\mathbf{n}}$ and $\hat{\mathbf{e}}_i$ with $i \in \{1, 2, +, -\}$ have, beyond homogeneous ones, only Fourier components with $\mathbf{k} = \pm \mathbf{Q}$, cf. [appendix D.4](#). The matrix $V_{\text{dip}}(\mathbf{k})$ is a block-matrix with nine 2×2 blocks and can be constructed by introducing momentum indices α and β via

$$\mathcal{S}_{\text{dip}} = -\frac{1}{2\nu} \sum_{\mathbf{k}} \sum_{\alpha, \beta=1,0,-1} \psi^\dagger(\mathbf{k} + \alpha \mathbf{Q}) V_{\text{dip}}^{\alpha\beta}(\mathbf{k}) \psi(\mathbf{k} + \beta \mathbf{Q}) \quad (8.32)$$



8. Non-Linear σ Model

which makes

$$V_{\text{dip}}(\mathbf{k}) = \frac{\mathcal{E}_0 \chi_{\text{con}}^{\text{int}}}{2} \begin{pmatrix} V_{\text{dip}}^{1,1}(\mathbf{k}) & V_{\text{dip}}^{1,0}(\mathbf{k}) & V_{\text{dip}}^{1,-1}(\mathbf{k}) \\ V_{\text{dip}}^{0,1}(\mathbf{k}) & V_{\text{dip}}^{0,0}(\mathbf{k}) & V_{\text{dip}}^{0,-1}(\mathbf{k}) \\ V_{\text{dip}}^{-1,1}(\mathbf{k}) & V_{\text{dip}}^{-1,0}(\mathbf{k}) & V_{\text{dip}}^{-1,-1}(\mathbf{k}) \end{pmatrix}. \quad (8.33)$$

Such as before, χ_{dip}^{-1} is divided into two cases with momentum much smaller respectively larger than one over sample size. In the former case of basically zero momentum, χ_{dip}^{-1} consist of the demagnetization factor description. Assuming a diagonal form with N_x , N_y and N_z on the diagonal, we obtain

$$V_{\text{dip}}(\mathbf{0}) = \frac{\mathcal{E}_0 \chi_{\text{con}}^{\text{int}}}{2} \times \begin{pmatrix} \frac{N_x + N_y}{2} \left(\frac{1 + \cos^2 \theta}{2} 1 + \frac{\sin^2 \theta}{2} \tau^x + \cos \theta \tau^z \right) & 0 & \frac{N_x - N_y}{2} \left(-\frac{\sin^2 \theta}{2} 1 - i \cos \theta \tau^y - \frac{1 + \cos^2 \theta}{2} \tau^x \right) \\ 0 & N_z \sin^2 \theta (1 - \tau^x) & 0 \\ \frac{N_x - N_y}{2} \left(-\frac{\sin^2 \theta}{2} 1 + i \cos \theta \tau^y - \frac{1 + \cos^2 \theta}{2} \tau^x \right) & 0 & \frac{N_x + N_y}{2} \left(\frac{1 + \cos^2 \theta}{2} 1 + \frac{\sin^2 \theta}{2} \tau^x - \cos \theta \tau^z \right) \end{pmatrix}. \quad (8.34)$$

plus the additional term

$$- \frac{1}{2} \mathcal{E}_0 \chi_{\text{con}}^{\text{int}} N_z \cos^2 \theta \sum_{\mathbf{k}} \psi^\dagger(\mathbf{k}) \psi(\mathbf{k}). \quad (8.35)$$

This term can be absorbed in the calculation to obtain \mathcal{H}_{ex} in (8.27). Effectively, the external magnetic field as in (D.16) is replaced by the internal magnetic field. For the case of finite momentum \mathbf{k} it is handy to introduce abbreviations for the components of $\hat{\mathbf{k}}$, i.e., $\hat{k}^z = \hat{\mathbf{k}} \cdot \hat{\mathbf{e}}_z$ and $\hat{k}^\pm = \frac{1}{\sqrt{2}} \hat{\mathbf{k}} \cdot (\hat{\mathbf{e}}_x \pm i \hat{\mathbf{e}}_y)$. Using them lets us write the potential as

$$V_{\text{dip}}(\mathbf{k}) = \frac{\mathcal{E}_0 \chi_{\text{con}}^{\text{int}}}{2} \times \begin{pmatrix} \hat{k}^- \hat{k}^+ \left(\frac{1+c^2}{2} 1 + \frac{s^2}{2} \tau^x + c \tau^z \right) & \hat{k}^- \hat{k}^z \left(\frac{-cs}{\sqrt{2}} (1 - \tau^x) + \frac{is}{\sqrt{2}} (\tau^y + i \tau^z) \right) & \hat{k}^- \hat{k}^- \left(-\frac{s^2}{2} 1 - i c \tau^y - \frac{1+c^2}{2} \tau^x \right) \\ \hat{k}^z \hat{k}^+ \left(\frac{-cs}{\sqrt{2}} (1 - \tau^x) - \frac{is}{\sqrt{2}} (\tau^y - i \tau^z) \right) & \hat{k}^z \hat{k}^z s^2 (1 - \tau^x) & \hat{k}^z \hat{k}^- \left(\frac{-cs}{\sqrt{2}} (1 - \tau^x) + \frac{is}{\sqrt{2}} (\tau^y - i \tau^z) \right) \\ \hat{k}^+ \hat{k}^+ \left(-\frac{s^2}{2} 1 + i c \tau^y - \frac{1+c^2}{2} \tau^x \right) & \hat{k}^+ \hat{k}^z \left(\frac{-cs}{\sqrt{2}} (1 - \tau^x) - \frac{is}{\sqrt{2}} (\tau^y + i \tau^z) \right) & \hat{k}^+ \hat{k}^- \left(\frac{1+c^2}{2} 1 + \frac{s^2}{2} \tau^x - c \tau^z \right) \end{pmatrix} \quad (8.36)$$

where $s = \sin \theta$ and $c = \cos \theta$ are abbreviated due to lack of space. Note, that only the center element remains finite when $\mathbf{k} \parallel \hat{\mathbf{e}}_z \parallel \mathbf{Q}$, so in particular if $\mathbf{k} = n\mathbf{Q}$ for $n \in \mathbb{Z}$ and $n \neq 0$. A thorough derivation of $V_{\text{dip}}(\mathbf{0})$ and $V_{\text{dip}}(\mathbf{k})$ is given in [appendix D.5](#).

8.3. EIGENMODES

Minimization of the action \mathcal{S} (8.29) leads to a bosonic version of the *Bogoliubov-deGennes equation*²

$$i\hbar\tau^z\partial_t\psi = \mathcal{H}\psi. \quad (8.37)$$

We define the Fourier transformed free Green's function as

$$g_0^{-1}(\omega, \mathbf{k}) = \hbar\omega\tau^z + \mathcal{D} \left(\mathbf{k}^2 + \frac{Q^2 \sin^2 \theta}{2} (1 - \tau^x) \right). \quad (8.38)$$

The wave equation is obtained by setting the functional derivative of \mathcal{S} with respect to ψ to zero and is given by

$$0 = g_0^{-1}(\omega, \mathbf{k})\psi_\omega(\mathbf{k}) + V(\mathbf{k})\psi_\omega(\mathbf{k} + \mathbf{Q}) + V^*(\mathbf{k})\psi_\omega(\mathbf{k} - \mathbf{Q}) \\ + \sum_{\alpha, \beta} V_{\text{dip}}^{\alpha\beta}(\mathbf{k} - \alpha\mathbf{Q})\psi(\mathbf{k} - (\alpha - \beta)\mathbf{Q}). \quad (8.39)$$

The last term was derived in the previous section and the shift $\mathbf{k} \rightarrow \mathbf{k} - \alpha\mathbf{Q}$ was necessary to obtain the correct derivative. The potential $V(\mathbf{k})$ comes from the remaining term already present in \mathcal{H}_{ex} . Its Fourier transformed form is given by

$$V(\mathbf{k}) = \mathcal{D}Q \sin \theta (k_x + ik_y) \tau^z = \mathcal{D}Q \sin \theta k_\perp e^{i\varphi} \tau^z \quad (8.40)$$

with $\mathbf{k} = (k_\perp \cos \varphi, k_\perp \sin \varphi, k_\parallel)$ for the angle $\varphi = \angle(\mathbf{k}, \hat{e}_x)$.

Combining the diagonal elements of the dipolar contribution and the free Green function to

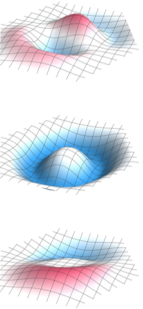
$$g^{-1}(\omega, \mathbf{k}) = g_0^{-1}(\omega, \mathbf{k}) + \sum_{\alpha} V_{\text{dip}}^{\alpha\alpha}(\mathbf{k} - \alpha\mathbf{Q}) \quad (8.41)$$

lets us collect corresponding Fourier components and rewrite the wave equation as

$$0 = g^{-1}(\omega, \mathbf{k})\psi_\omega(\mathbf{k}) + V^*(\mathbf{k})\psi_\omega(\mathbf{k} - \mathbf{Q}) + V(\mathbf{k})\psi_\omega(\mathbf{k} + \mathbf{Q}) \\ + \sum_{\alpha \neq \beta} V_{\text{dip}}^{\alpha\beta}(\mathbf{k} - \alpha\mathbf{Q})\psi_\omega(\mathbf{k} - (\alpha - \beta)\mathbf{Q}) \quad (8.42)$$

$$= g^{-1}(\omega, \mathbf{k})\psi_\omega(\mathbf{k}) + \left[V^*(\mathbf{k}) + V_{\text{dip}}^{1,0}(\mathbf{k} - \mathbf{Q}) + V_{\text{dip}}^{0,-1}(\mathbf{k}) \right] \psi_\omega(\mathbf{k} - \mathbf{Q}) \\ + \left[V(\mathbf{k}) + V_{\text{dip}}^{0,1}(\mathbf{k}) + V_{\text{dip}}^{-1,0}(\mathbf{k} + \mathbf{Q}) \right] \psi_\omega(\mathbf{k} + \mathbf{Q}) \\ + V_{\text{dip}}^{1,-1}(\mathbf{k} - \mathbf{Q})\psi_\omega(\mathbf{k} - 2\mathbf{Q}) \\ + V_{\text{dip}}^{-1,1}(\mathbf{k} + \mathbf{Q})\psi_\omega(\mathbf{k} + 2\mathbf{Q}). \quad (8.43)$$

²Bogoliubov-deGennes equations known from the BCS-theory are fermionic and have the general form $\begin{pmatrix} H_0 & \Delta(\mathbf{r}) \\ \Delta^*(\mathbf{r}) & -H_0^* \end{pmatrix} \psi = E\psi$.



8.4. UNIFORM CHIRAL MAGNETIC RESONANCES

The derivation of the resonances in the conical phase, i.e., of the formula already stated in the beginning of [chapter 7](#), is now obtainable in just a few steps. Sought after are fluctuations at zero momentum \mathbf{k} and with a finite frequency ω . The latter argument restricts the modes to just $\psi(\pm\mathbf{Q})$. Evaluating (8.43) for different values of $\mathbf{k} \in \{\dots, -\mathbf{Q}, \mathbf{0}, \mathbf{Q}, \dots\}$ results in a set of equations. The only finite contributions come from equations for $\mathbf{k} = \pm\mathbf{Q}$. They can be rewritten as

$$\begin{pmatrix} g^{-1}(\omega, \mathbf{Q}) & V_{\text{dip}}^{1,-1}(\mathbf{0}) \\ V_{\text{dip}}^{-1,1}(\mathbf{0}) & g^{-1}(\omega, -\mathbf{Q}) \end{pmatrix} \begin{pmatrix} \psi(\mathbf{Q}) \\ \psi(-\mathbf{Q}) \end{pmatrix} = \mathbf{0}. \quad (8.44)$$

Since V only depends on k_{\perp} rendering $V(n\mathbf{Q}) = 0$ for $n \in \mathbb{Z}$ and $n \neq 0$, combined with properties of $V_{\text{dip}}(\mathbf{k})$ for $\mathbf{Q} \parallel \hat{\mathbf{e}}_z$, there is no coupling to higher order Fourier modes. The Green's function results in

$$\begin{aligned} g^{-1}(\omega, \pm\mathbf{Q}) &= g_0^{-1}(\omega, \pm\mathbf{Q}) + V_{\text{dip}}^{0,0}(\pm\mathbf{Q}) + V_{\text{dip}}^{\pm 1, \pm 1}(\mathbf{0}) \\ &= \hbar\omega\tau^z + \mathcal{E}_0 \left(1 + \frac{(1 + \chi_{\text{con}}^{\text{int}}) \sin^2 \theta}{2} (1 - \tau^x) \right) + V_{\text{dip}}^{\pm 1, \pm 1}(\mathbf{0}) \end{aligned} \quad (8.45)$$

As a solution of the secular equation³ (8.44) we obtain

$$\begin{aligned} \frac{(\hbar\omega_{\pm\mathbf{Q}})^2}{\mathcal{E}_0^2} &= \frac{\omega_{\pm\mathbf{Q}}^2}{(\gamma\mu_0 H_{c2}^{\text{int}})^2} = \\ \frac{1}{4} &\left((2 + \chi_{\text{con}}^{\text{int}}) (4 + (N_x + N_y)\chi_{\text{con}}^{\text{int}}) + h^2 \left(-4 + \chi_{\text{con}}^{\text{int}} (-4 - N_y\chi_{\text{con}}^{\text{int}} + N_x(-1 + 2N_y)\chi_{\text{con}}^{\text{int}}) \right) \right. \\ &\pm \chi_{\text{con}}^{\text{int}} \left[N_y^2 (2 + \chi_{\text{con}}^{\text{int}} - h^2\chi_{\text{con}}^{\text{int}})^2 + N_x^2 (2 + (1 + h^2(-1 + 2N_y))\chi_{\text{con}}^{\text{int}})^2 - 2N_x N_y (2 + \chi_{\text{con}}^{\text{int}})^2 \right. \\ &\left. \left. - 2h^2 (2 + \chi_{\text{con}}^{\text{int}}) (4 + \chi_{\text{con}}^{\text{int}} + N_y\chi_{\text{con}}^{\text{int}}) + h^4 (8 + \chi_{\text{con}}^{\text{int}} (8 + \chi_{\text{con}}^{\text{int}} + 2N_y\chi_{\text{con}}^{\text{int}})) \right] \right]^{1/2} \end{aligned} \quad (8.46)$$

with $\cos \theta = h$ which is the projection of $\hat{\mathbf{n}}$ onto \mathbf{Q} . It is a measure of the magnetic field between zero and H_{c2} respectively H_{c2}^{int} [37]. The former was used in the previous expression (7.2) while the latter was used for this one leading to a description in terms of $\chi_{\text{con}}^{\text{int}}$ instead of χ_{con} . Since $h = H^{\text{ext}}/H_{c2} = H^{\text{int}}/H_{c2}^{\text{int}}$, substituting $H_{c2}^{\text{int}} = (1 - N_z\chi_{\text{con}})H_{c2}$ on the left and $(\chi_{\text{con}}^{\text{int}})^{-1} = (\chi_{\text{con}})^{-1} - N_z$ on the right hand side of equation (8.46) gives equation (7.2).

Plugging the two positive eigenvalues $w_{\pm\mathbf{Q}}$ into (8.44) lets us obtain two corresponding eigenvectors. They are needed, for example, to calculate the ellipticity in [section 7.2](#). To calculate the ellipticity one requires the change of the mean magnetization which is in this formalism given by

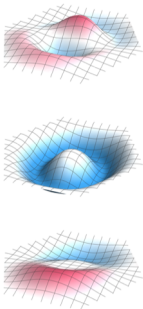
$$\delta M_0 = \int d\mathbf{r} \, \hat{\mathbf{n}} - \hat{\mathbf{n}}_{\text{helix}}. \quad (8.47)$$

³also called characteristic equation

The difference $\hat{\mathbf{n}} - \hat{\mathbf{n}}_{\text{helix}} = \delta\mathbf{M}$ is the local deviation from the equilibrium configuration of the helix. This deviation is then averaged over a helix to obtain the change in the mean magnetization. Using (8.24) for $\hat{\mathbf{n}}$ leaves three terms and the integral basically results in a Fourier transformation. The first term then vanishes because only $\psi(\pm\mathbf{Q})$ are finite and only the two terms proportional to $\hat{\mathbf{e}}_+$ and $\hat{\mathbf{e}}_-$ remain. One is ultimately left with the vector

$$\delta\mathbf{M}_0 \propto \begin{pmatrix} -i [(1+h)(\psi(+\mathbf{Q}) - \psi^*(-\mathbf{Q})) + (1-h)(\psi^*(+\mathbf{Q}) - \psi(-\mathbf{Q}))] \\ (1+h)(\psi(+\mathbf{Q}) + \psi^*(-\mathbf{Q})) + (1-h)(\psi^*(+\mathbf{Q}) + \psi(-\mathbf{Q})) \\ 0 \end{pmatrix}. \quad (8.48)$$

Whether it is an elliptical or linear rotation or polarization is encoded in the eigenvectors ψ . Note, that now ψ and ψ^* only label the components of ψ and are not necessarily the complex conjugate of each other anymore. This expression then naturally leads to the ratio $\frac{\delta\mathbf{M}_{0,\sigma}^x}{\delta\mathbf{M}_{0,\sigma}^y}$ stated in (7.8), with σ labeling the plus or minus Q mode, respectively, as well as to the subsequent abbreviations and results.



9

— FINITE MOMENTUM SPIN WAVES —

We start this chapter by analytically analyzing first aspects of spin waves with finite momentum on the basis of the non-linear σ model described in the previous chapter. We then continue the investigation revisiting and using the numerical approach to obtain flat helimagnon bands, discuss neutron scattering weights and take a look at the magnetic field dependence of the spectrum.

9.1. ANALYSIS VIA THE NON-LINEAR σ MODEL

When dealing with finite momenta we can distinguish between two different cases discussed in the following.

LONGITUDINAL MOMENTA

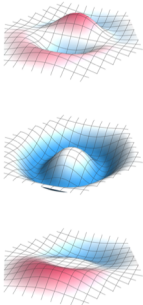
This first one considers momenta $\mathbf{k}_{\parallel} \parallel \mathbf{Q}$ parallel to the helix pitch. In this case, the dipolar contribution simplifies and the wave equation reads [94]

$$i\hbar\tau^z\partial_t\psi(\mathbf{k}_{\parallel}) = \mathcal{D}\left(\mathbf{k}_{\parallel}^2 + Q^2\frac{(1 + \chi_{\text{con}}^{\text{int}})\sin^2\theta}{2}(1 - \tau^x)\right)\psi(\mathbf{k}_{\parallel}). \quad (9.1)$$

The eigenfrequencies are given by

$$\hbar\omega = \mathcal{D}|\mathbf{k}_{\parallel}|\sqrt{\mathbf{k}_{\parallel}^2 + Q^2(1 + \chi_{\text{con}}^{\text{int}})\sin^2\theta} \quad (9.2)$$

and shown in [figure 9.1](#). The spectrum for a helix in zero field corresponding to $\theta = \pi/2$ is shown in solid dark blue. Note the linear behavior around $k_{\parallel} = 0$. When the field increases, this behavior softens and becomes quadratic at $H_0^{\text{ext}} = H_{c2}$, i.e., $\theta = 0$, shown in solid light blue. This corresponds to a ferromagnetic or field-polarized state which is achieved for $H_0^{\text{ext}} \geq H_{c2}$. A gap opens for fields truly larger than H_{c2} and the parabola is shifted upwards. Dashed lines in the background depict the zero-field spectrum in the repeated zone-scheme. Of course, a repeated zone scheme is also applicable for the spectrum at H_{c2} and actually necessary because the only parabola with remaining weight has its apex at $k_{\parallel} = +Q$ for positive and at $k_{\parallel} = -Q$ for negative chirality.



9. Finite Momentum Spin Waves

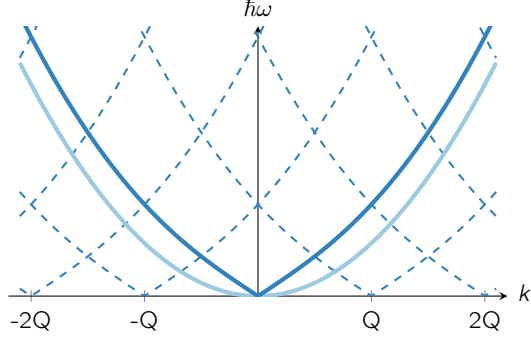


Figure 9.1: Helimagnon spectrum for longitudinal momenta $\mathbf{k}_{\parallel} \parallel \mathbf{Q}$ parallel to the helix pitch as given by (9.2). The spectrum for a helix in zero field, i.e., $\theta = \pi/2$, is shown in solid dark blue. Note the linear behavior around $k_{\parallel} = 0$. When the field increases, this behavior softens and becomes quadratic at $H_0^{\text{ext}} = H_{c2}$, i.e., $\theta = 0$, shown in solid light blue. The dashed lines in the background indicate this spectrum in the repeated zone scheme of the former case.

LARGE PERPENDICULAR MOMENTA

For momenta $\mathbf{k}_{\perp} \perp \mathbf{Q}$ the last term in \mathcal{H}_{ex} becomes finite, cf. equation (8.27). For large momenta $k_{\perp} \gg Q$ dipolar interactions may be neglected as well as the term proportional to $\sin^2 \theta$ in \mathcal{H}_{ex} . The remaining effective Schrödinger equation for the first component of the spinor ψ reads

$$\begin{aligned} i\hbar\partial_t\psi(\mathbf{k}_{\perp}, z) &= \mathcal{D} [k_{\perp}^2 - \partial_z^2 + 2Q\mathbf{n}_{\perp} \cdot \mathbf{k}_{\perp}] \psi(\mathbf{k}_{\perp}, z) \\ &= \mathcal{D} [k_{\perp}^2 - \partial_z^2 + 2Qk_{\perp} \sin \theta \cos(Qz - \varphi)] \psi(\mathbf{k}_{\perp}, z) \end{aligned} \quad (9.3)$$

for $\mathbf{k}_{\perp}^{\text{T}} = (k_{\perp} \cos \varphi, k_{\perp} \sin \varphi, 0)$. It effectively describes a particle in a cosine potential along the $\hat{\mathbf{e}}_z$ -direction. Equation (9.3) is generally called *Mathieu equation*. The strength of the cosine potential can be controlled by the size of k_{\perp} . Finite \mathbf{k}_{\perp} activates Bragg reflections at Bragg planes which open gaps in the longitudinal spectrum. Because the cosine only has two Fourier components, the size of these gaps decreases quickly with increasing band index $n = 0, 1, 2, \dots$ [129]. When k_{\perp} is large, the magnons will become localized along the $\hat{\mathbf{e}}_z$ -direction around the minima of the cosine:

$$\cos(Qz - \varphi) \approx -1 + \frac{1}{2}Q^2 \left(z - \frac{\varphi + \pi}{Q} \right)^2 - \frac{1}{24}Q^4 \left(z - \frac{\varphi + \pi}{Q} \right)^4. \quad (9.4)$$

Shifting $z \rightarrow z + \frac{\varphi + \pi}{Q}$ lets us obtain

$$\begin{aligned} i\hbar\partial_t\psi(\mathbf{k}_{\perp}, z) &\approx \\ \mathcal{D} \left[k_{\perp}^2 - 2Qk_{\perp} \sin \theta - \partial_z^2 + Q^3k_{\perp} \sin \theta z^2 - \frac{1}{12}Q^5k_{\perp} \sin \theta z^4 \right] \psi(\mathbf{k}_{\perp}, z) \end{aligned} \quad (9.5)$$

This expression now contains the harmonic oscillator with a quartic higher order perturbation. The eigenenergies are given by [130, 131]

$$\hbar\omega_n(\mathbf{k}) \approx \mathcal{D} \left[k_{\perp}^2 - 2Qk_{\perp} \sin \theta + 2Q\sqrt{Qk_{\perp} \sin \theta} \left(n + \frac{1}{2} \right) - \frac{Q^2}{8} \left(n^2 + n + \frac{1}{2} \right) \right] \quad (9.6)$$

where the second and third term derive from the harmonic oscillator potential and the last term is attributed to the anharmonicity. The last summand $-\frac{Q^2}{16}$ may be neglected as has been done in [94]. Equation (9.6) is plotted at zero field, i.e., $\theta = \pi/2$, for different n in figure 9.2. Due to the cosine approximation valid for $k_{\perp} \gg Q$, formula (9.6) is only valid for such momenta. Additionally, this entire theory is a low energy theory. That means that although the cosine expansion might be valid in that regime, high energy corrections to the free energy are necessary for high momenta. Size and form are discussed in chapter 10.

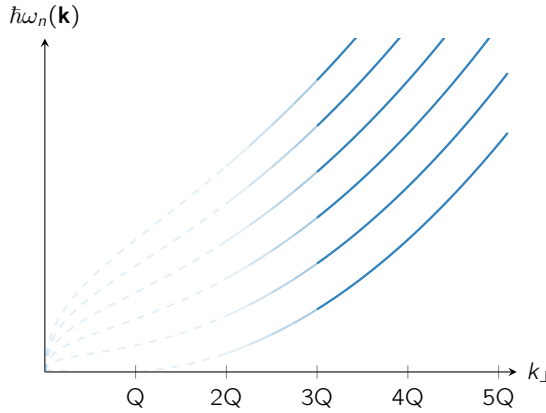
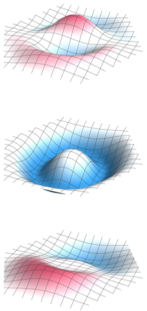


Figure 9.2: Helimagnon spectrum for large perpendicular momenta $\mathbf{k}_{\perp} \perp \mathbf{Q}$ perpendicular to the helix pitch as given by (9.6) for a helix in zero field, i.e., $\theta = \pi/2$. Different curves correspond to different band indices n starting with $n = 0$ being the lowest and $n = 5$ the highest curve in this figure. Due to the cosine approximation valid for $k_{\perp} \gg Q$, formula (9.6) is only valid for such momenta. Experimental comparison gives already good agreement for k_{\perp} being simply larger than Q , cf. chapter 10.

9.2. EXTENDED ANALYSIS WITH NUMERICAL INPUT

As mentioned before, a finite \mathbf{k}_{\perp} opens gaps in the longitudinal spectrum. By selecting a finite but fixed \mathbf{k}_{\perp} it is possible to calculate the longitudinal spectrum for that given perpendicular momentum. Since the spectrum for an arbitrary momentum is more elaborate, we employ the numerical method outlined in chapter 6. Results are shown in figure 9.3. While figure 9.3(a) shows again the longitudinal helimagnon spectrum at $k_{\perp} = 0$, one can see that already a



9. Finite Momentum Spin Waves

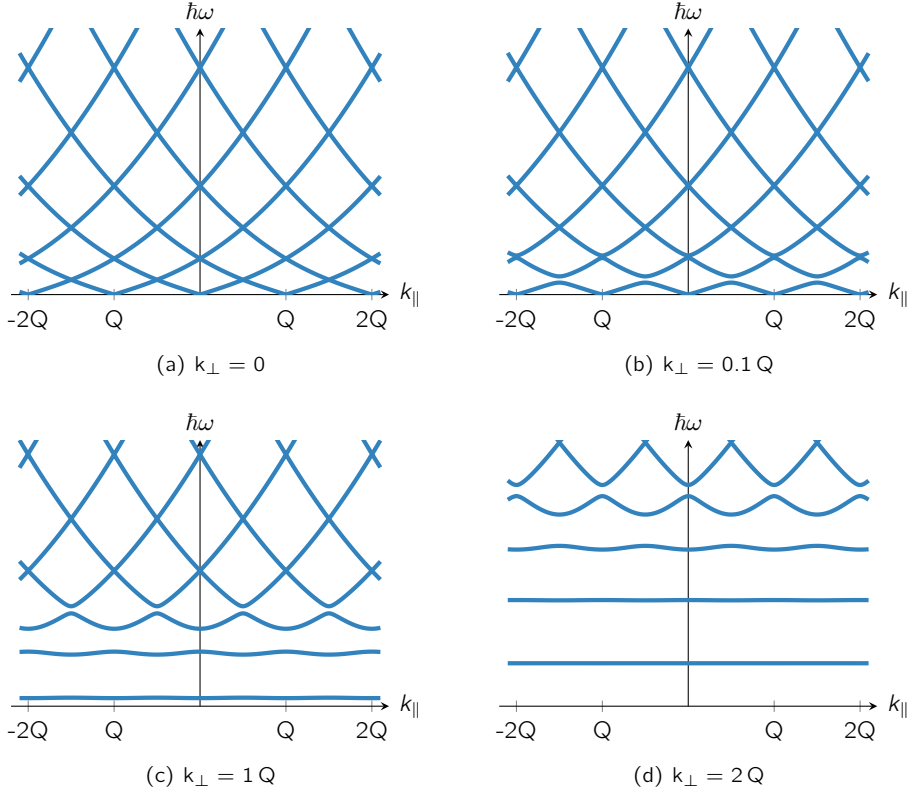


Figure 9.3: Helimagnon spectra for longitudinal momenta at various perpendicular momenta. Already a small finite perpendicular momentum opens visible gaps in the lower part of the spectrum, compare (a) and (b). Large perpendicular momenta lead to an increasing number of flat bands in the spectrum, compare (c) and (d).

small finite perpendicular momentum opens visible gaps in the lower part of the spectrum, [figure 9.3\(b\)](#). For a significantly larger k_{\perp} , several flat bands arise due to Bragg scattering.

Another interesting aspect is the influence of dipolar interaction on the spectrum. [Figure 9.4](#) compares the spectra with and without dipolar interactions. The strength has been assumed to be that of Cu_2OSeO_3 with $\chi_{\text{con}}^{\text{int}} = 1.76$ to have a strong effect. The observation with regard to the longitudinal spectrum depicted in light blue is stretched along the $\hbar\omega$ -axis increasing its stiffness. A similar effect is seen in the overall perpendicular spectrum as well. The most interesting effect happens in the region around energies corresponding to ferromagnetic resonance highlighted by the red circle and ellipse. Without dipolar interactions the two $\pm Q$ modes with $k \ll 1/L$ for sample size L are degenerate. Let their energy be

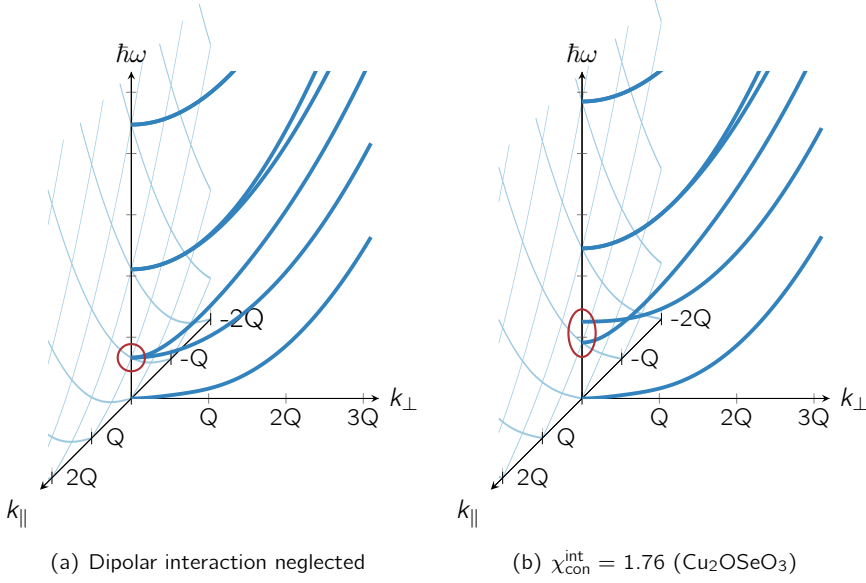
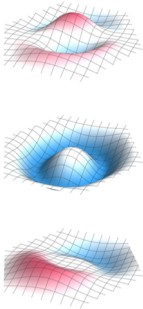


Figure 9.4: Helimagnon spectra plotted for both longitudinal and perpendicular \mathbf{k} -directions for $k \gg 1/L$ with sample size L . Sub-figures (a) and (b) compare present and non-present dipolar interactions. Highlighted by the red circle is the energy range of chiral magnetic resonances. Especially noteworthy is the non-unique and directionally dependent limit $\mathbf{k} \rightarrow 0$ in the presence of dipolar interactions.

$\hbar\omega_0$. The helimagnon spectra are calculated in the regime of $k \gg 1/L$, which means there is a momentum range in between which is not controlled by neither of those theories. One can, however, take the limit of $\mathbf{k} \rightarrow 0$ considering finite momentum. This is shown in figure 9.4 around $k = 0$. When dipolar interactions are not present, figure 9.4(a), one can see that this limit converges to a single point which also coincides with $\hbar\omega_0$. Switching on dipolar interactions leads to mode splitting in the ferromagnetic resonance regime and to energies $\hbar\omega_{\pm Q}$. The magnon spectrum for finite \mathbf{k} reacts in a singular way. The longitudinal spectrum gets stiffer but most importantly the limit $\hbar\omega(\mathbf{k}_{\parallel} \rightarrow 0)$ for $k_{\perp} = 0$ still converges to a single value instead of two. The limit $\hbar\omega(\mathbf{k}_{\perp} \rightarrow 0)$ for $k_{\parallel} = 0$, on the other hand, changes from two bands sharing a degenerate point to two distinct values. There is still a band crossing of those two modes but it is now located at a larger value of k_{\perp} . Most interestingly, the limit $\lim_{\mathbf{k} \rightarrow 0} \hbar\omega(\mathbf{k})$ is therefore highly dependent on the direction of \mathbf{k} . It also does not coincide with the resonances at $\mathbf{k} = 0$ anymore.

This effect has a profound consequence for experimental measurements, in particular with coplanar waveguides. Figure 5.1(b) on page 58 already indicates that the oscillating magnetic field has a momentum distribution with a dominant



9. Finite Momentum Spin Waves

but not exclusive direction. This leads to a potential frequency range for expected resonances instead of only two distinct modes at $k = 0$, which ultimately smears out the measured absorption. This smearing out is indicated in [figures 7.4](#) and [10.2](#) in the form of the extended dark gray bands around the resonances in the conical and field-polarized phases. For most shapes and setups, the resonances at $\mathbf{k} = 0$ lie within that range. The exception is a rod-like sample, with the static field along its rotation axis. Then also the Kittel mode lies above the possible resonance values in the limit of $k \gg 1/L$ [\[109\]](#).

Still regarding [figure 9.4](#) we can move the focus to the low energy regime, i.e., to the goldstone mode of the spectrum. Goldstone modes are soft modes due to residual fluctuations on top of a symmetry broken ground state [\[68\]](#), for example the ordered state in a ferromagnet. In [section 4.4](#) we have seen that they have a quadratic dispersion for the ferromagnet in the low energy limit. Belitz et al. [\[132\]](#) found that the helimagnonic ones are highly anisotropic. The mode is softer in the direction perpendicular to the pitch vector than in the longitudinal direction,

$$\omega \propto \sqrt{c_{\parallel} k_{\parallel}^2 + c_{\perp} k_{\perp}^4}. \quad (9.7)$$

This formula was derived for zero applied field and the behavior it describes is also nicely visible in [figure 9.4](#). There and maybe even better in [figure 9.1](#), one can see that the mode is linear in the longitudinal direction while in the perpendicular direction the behavior is quadratic. Added dipole-dipole interactions does not change that. Also note in that context that while dipolar interactions induce a gap in the ferromagnetic spectrum [\[133\]](#), they do not affect the degree of the mode dispersion in the helical/conical phases. The external magnetic field, on the other hand, does have an effect. We have already seen in [figure 9.1](#) that the mode becomes softer with an increasing magnetic field until reaching a quadratic dispersion at the critical field H_{c2} . As the state at H_{c2} is already field-polarized, we expect a quadratic dispersion in all directions. Since the dispersion in perpendicular direction is already quadratic one could expect, that it will stay that way. Upon an increase in the magnetic field, the dispersion changes to a linear behavior around $k = 0$ and then settles to be quadratic again [\[93\]](#).

SPECTRAL WEIGHTS

In [section 10.2](#) we present inelastic neutron scattering data obtained by collaborators in the group of Prof. Böni. At this point we want to investigate which results can be expected. Which part of the helimagnon spectrum can actually be observed depends on the spectral weights which are given by the previously mentioned scattering cross section [\(6.25\)](#) on page [70](#) that is proportional to

$$[1 + n_B(\omega)] \text{Im} \left(\text{Tr} [\chi(\mathbf{k}, \omega + i0)] - \hat{\mathbf{Q}} \chi(\mathbf{k}, \omega + i0) \hat{\mathbf{Q}} \right). \quad (9.8)$$

The spectral weights of the susceptibility were given in [\(6.39\)](#) and the only thing left to do is to apply the appropriate projection. The measurements take place

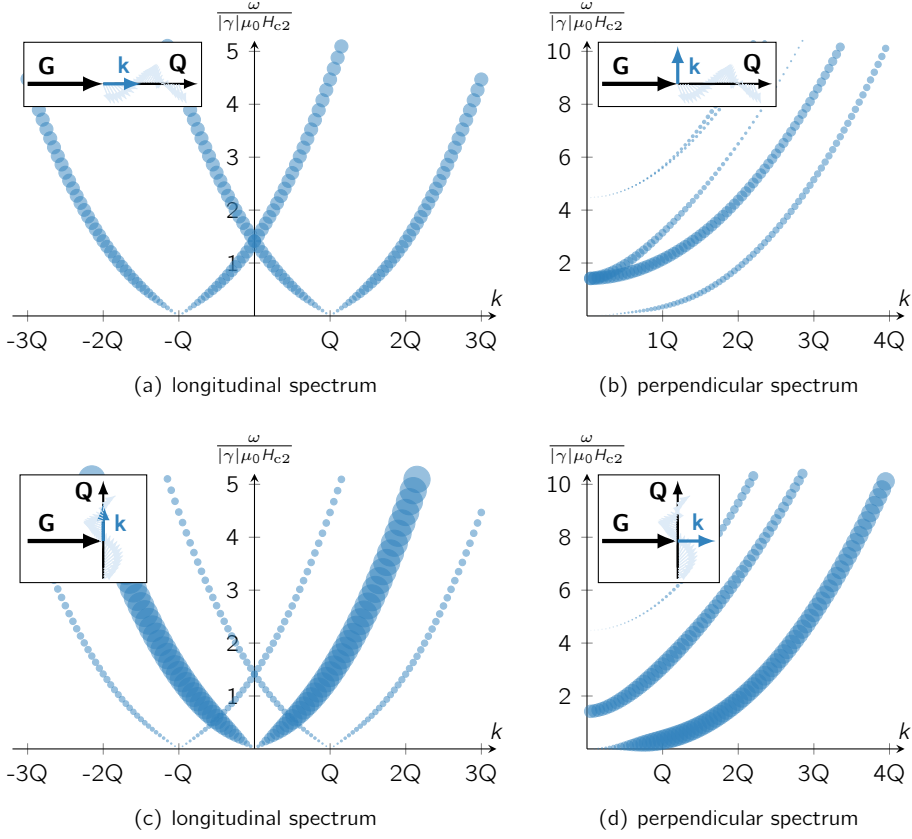
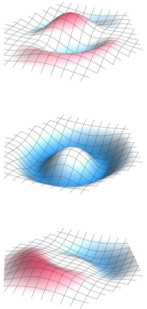


Figure 9.5: Spectral weight distributions are shown for different inelastic neutron scattering setups without dipolar interaction and at zero field. The weights are proportional to the area of the circles. Panels (a)-(d) show the four extremal cases in the weight distribution when considering either \mathbf{k}_{\parallel} or \mathbf{k}_{\perp} to be finite while the other remains zero. The insets illustrate the relationships between the direction of the nuclear Bragg peak $\mathbf{G} \approx \mathbf{Q}$, the helix pitch direction \mathbf{Q} and momentum \mathbf{k} . The most noticeable effect is lack of otherwise detectable modes when $\mathbf{k} \parallel \mathbf{G}$.

very close to a nuclear Bragg peak \mathbf{G} and since the wavelength of the studied helices is much larger than the atomic lattice spacing, we can approximate $\mathbf{Q} \approx \mathbf{G}$ and hence $\hat{\mathbf{Q}} \approx \mathbf{G}/|\mathbf{G}|$ to simplify the calculation. This leaves us with several geometric arrangements of \mathbf{G} , \mathbf{Q} and \mathbf{k} . When considering either finite \mathbf{k}_{\parallel} or \mathbf{k}_{\perp} while the other remains zero, it turns out that only four extremal cases in the weight distribution exist with two corresponding to the longitudinal and two to the perpendicular spectrum. They are shown in figure 9.5. The most prominent effect is that some modes do not carry finite weights when $\mathbf{k} \parallel \mathbf{G}$, figures 9.5(a) and 9.5(d), which do otherwise. This can be attributed to the type of scattering



9. Finite Momentum Spin Waves

processes. The outer two and remaining branches of the longitudinal spectrum are due to spin-flip scattering, while the middle one is not. When all momentum and spin is and remains along \mathbf{G} and \mathbf{Q} , then there is no reason for a detection in the plane perpendicular to it and the middle branch is not detected. During spin-flip scattering the perpendicular spin components are part of the flipping process which leads to the detectable outer branches. When $\mathbf{Q} \perp \mathbf{G}$, then the non-spin-flip process is also in the plane perpendicular to \mathbf{G} and its corresponding branch can be detected. The outer spin-flip branches, however, lose weight because the plane perpendicular to \mathbf{Q} does not equal the scattering plane any more, but merely intersects it. Ultimately, all three branches are also individually detectable by polarized neutron scattering.

For completion one should also mention the case where $\mathbf{k} \perp \mathbf{Q} \perp \mathbf{G}$. This case yield a perpendicular spectrum and the weight distribution is such that the weights are as equally distributed as possible. For examples modes two and three in [figure 9.5\(b\)](#), the lower of which vanishes in the case shown in [figure 9.5\(d\)](#), obtain equal weights. So do modes five and six.

9.3. RESONANCES CLOSE TO H_{c2}

Instead of preparing the system at a fixed point in the field-temperature phase diagram and subsequently measuring the spectrum by performing momentum scans in different directions, we can also fix the momentum and study the field-dependence of the helimagnon dispersion. To do this, we select a finite \mathbf{k}_\perp and $\mathbf{k}_\parallel = 0$ so then be able to follow the positions of the obtained flat bands with increasing field. Such a setup, with two different cases of orientations between helix pitch \mathbf{Q} and nuclear Bragg peak \mathbf{G} , has also been measured by our collaborators, in particular Tobias Weber of the group of Prof. Böni in Munich [\[134\]](#). His results are presented in [section 10.2](#). Because of these measurements, we choose to present the theory graphs corresponding to two of their exact setups. What both described setups have in common is the direction of the nuclear Bragg peak given by $[1\ 1\ 0]$ and that $k_\perp = 2.52 H_{c2}$. What differs is the orientation of the magnetic field and hence the pitch vector of the helix. In the first case $\mathbf{Q} \parallel [0\ 0\ 1] \perp \mathbf{G}$ and in the second $\mathbf{Q} \parallel [1\ 1\ 0] \parallel \mathbf{G}$. The direction of \mathbf{k}_\perp changes from $[1\ \bar{1}\ 0]$ to $[\bar{1}\ 1\ 0]$ for cases one and two, respectively, but this is tantamount for the theory as both directions are perpendicular to \mathbf{Q} and \mathbf{G} .

The spectra of those two cases are shown in [figure 9.6](#). In the background and colored light blue are spectra without including dipolar interactions. The dark blue lines are calculations for the dipole-dipole strength of MnSi, which is the material studied in [\[134\]](#). It is interesting to see, that all modes bend towards the point of resonance in the field polarized phase at H_{c2} . Ultimately only one mode remains with weight while all others loose their spectral weight before reaching H_{c2} . Although to be fair, this loss of weight happens rather very close to the phase transition. It is also nice to see, that the property of relatively equal weights between the modes, as was mentioned at the end of the previous section

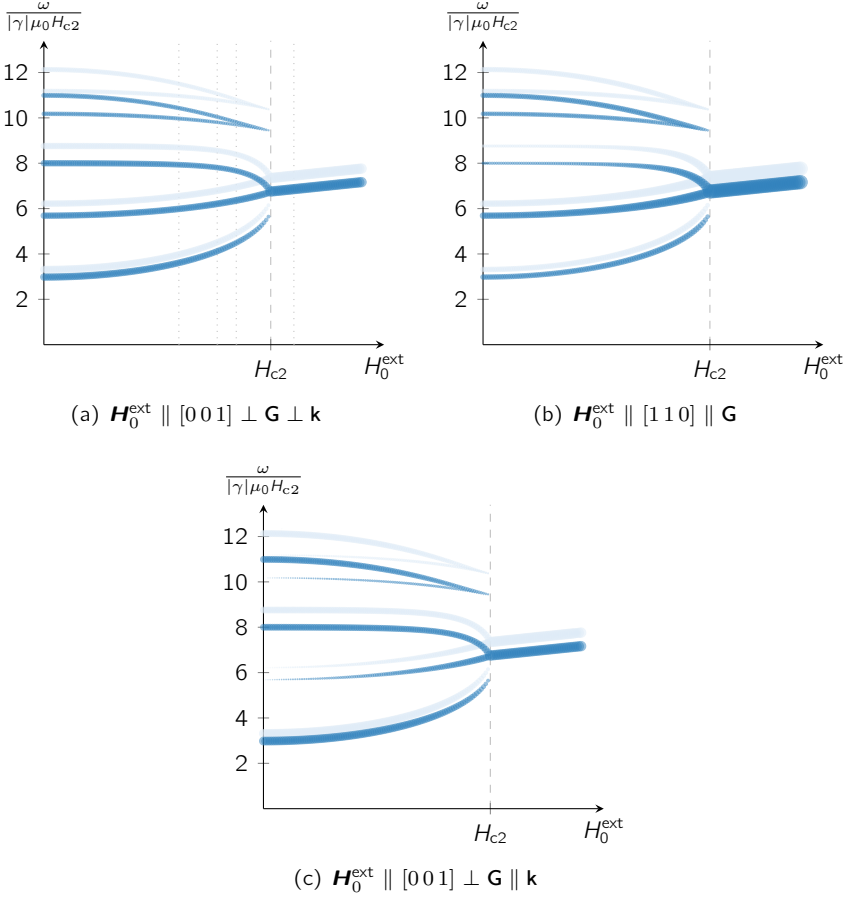
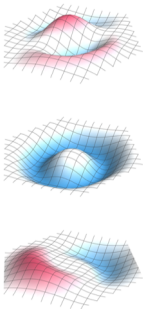


Figure 9.6: Field dependence of the helimagnon spectrum for different orientations of magnetic field $\mathbf{H}_0^{\text{ext}}$, nuclear Bragg peak $\mathbf{G} \parallel [1\ 1\ 0]$ and fixed but finite momentum $\mathbf{k} = \mathbf{k}_\perp$. In cases (a) and (b) \mathbf{k}_\perp points along a $\langle \bar{1}\ 1\ 0 \rangle$ direction perpendicular to the \mathbf{G} , while it is parallel to \mathbf{G} in panel (c). Its value is chosen to be fixed and given by $k_\perp = 2.52$. The magnetic field and hence pitch vector $\mathbf{Q} \parallel \mathbf{H}_0^{\text{ext}}$ direction changes as described in the corresponding sub-captions. Light blue spectral lines correspond to the spectrum without dipolar interaction while the dark blue lines represent the spectrum as it is for MnSi which was used in the corresponding experiments [134]. The dotted lines in (a) represent the there used values for the magnetic field and correspond successively to panels (a)-(d) of figure 10.5 on page 114.

corresponding to the setup $\mathbf{k} \perp \mathbf{Q} \perp \mathbf{G}$, i.e., figure 9.6(a) in the current context, stays that way over almost the entire field range.

Of theoretical interest is also the configuration where \mathbf{k}_\perp is chosen corresponding to figure 9.5(d), where some of the modes are not excited at all. Their development



9. Finite Momentum Spin Waves

with increasing field is shown in [figure 9.6\(c\)](#). The true non-excitability is only given at zero field. However, the increase in weight happens only slowly. Significant value is only taken on above around $\mathbf{H}_0^{\text{ext}} \approx 1/3 H_{c2}$.

10

— COMPARISON TO EXPERIMENTS —

In [chapter 7](#) we presented a field dependent formula for helimagnonic resonances at zero momentum, i.e., at the Γ -point of momentum space. Measurements of these excitations have been performed numerous times, for example by [[124](#), [122](#), [123](#)]. Our collaborators in the groups of Prof. Pfeleiderer and Prof. Grunder in Munich respectively Lausanne use coplanar waveguides for their experiments [[37](#), [125](#)], cf. [section 5.1](#). In this chapter we first briefly review these ferromagnetic resonance experiments and then focus on neutron scattering experiments also performed by collaborators from Munich in the group of Prof. Böni. Neutrons can be used to probe the helimagnon spectrum for a broader range of energies and momenta.

10.1. FERROMAGNETIC RESONANCES

The experiments in [[37](#)], producing absorption data similar to those shown in [figure 10.1](#), focus on ferromagnetic resonances which correspond to excitations at $\mathbf{k} \approx 0$. The typical ac field distribution generated by their CPW setup is around $k_{\text{CPW}} = 9.4 \times 10^{-6} \text{ \AA}^{-1}$ which is much smaller than intrinsic momentum scale Q of the magnetic structure but still finite. For this reason, it is sufficient to confine the discussion to the small momentum limit of the magnetic resonances, $\lim_{\mathbf{k} \rightarrow 0} \lim_{L \rightarrow \infty} \omega(\mathbf{k})$ where L is the length of the sample. However, bear in mind that we have seen, at the end of [section 9.2](#), that the limit $\mathbf{k} \rightarrow 0$ is not unique.

[Figure 10.2](#) compares theory and experimental data. The resonances at $\mathbf{k} = 0$ in the helical and conical phases, given by [equations \(7.2\)](#) and [\(8.46\)](#), are shown as thin lines. As previously discussed, depending on the momentum distribution of $\mathbf{H}^{\text{ac}}(\mathbf{k}, \omega)$, the non-uniqueness of the limit $\mathbf{k} \rightarrow 0$ leads to a superposition of resonances located within the dark gray bands provoking an increased line width.

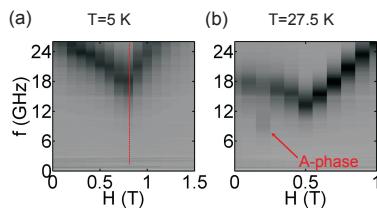
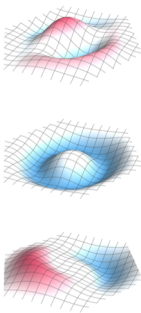


Figure 10.1: Grayscale plots of absorbed microwave intensity in bulk MnSi. The scale of darkness corresponds to the absorption strength. Figure from Andreas Bauer [[52](#)].



10. Comparison to Experiments

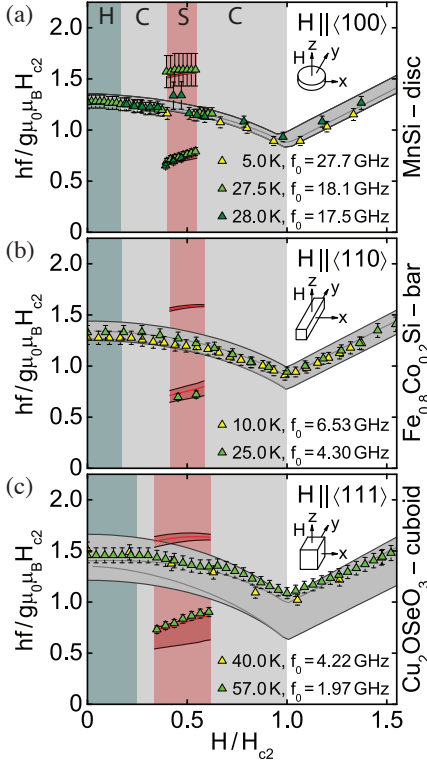


Figure 10.2: Comparison between experimental data (triangles) and theory (lines and shaded bands) as found in [37]. Magnetic resonances at the Γ -point are shown for different materials and shapes in dependence on the magnetic field. Tracing along the magnetic field covers different phases indicated by the colored background. Helical (H) and conical (C) phases are the focus in this section while the skyrmion lattice phase (S) is discussed later. The panels not only include resonances at $\mathbf{k} = 0$ (light gray lines) but also theoretical results for the zero momentum limit of the resonance frequencies, $\lim_{\mathbf{k} \rightarrow 0} \lim_{L \rightarrow \infty} \omega(\mathbf{k})$, which depends on the orientation of \mathbf{k} . The resulting bands of possible resonances is shown as light gray shaded bands for H, C and the field polarized phase, and as red shaded bands in S. Due to the differences in conical susceptibility and shape, the broadness of these bands can vary significantly.

This phenomenon is also present in the skyrmion lattice phase which is indicated in red. These modes are discussed in [section 11.1](#).

Corresponding spectra are in agreement with this analysis as shown in [figure 10.1](#). However, to obtain a defined double peak structure in the conical phase, as it is expected at $\mathbf{k} = 0$, the momentum distribution needs to decrease, which can be achieved by selecting a larger CPW. This has been done in [125]. There, the authors mostly used a CPW with a signal line width of 1000 μm , additionally to a CPW with a 20 μm wide signal line, which is the same size as the one used by [37]. Their obtained data was already shown in [figure 7.4](#) on page 85 where one is able to observe a well defined double peak structure in the conical phase.

10.2. NEUTRON SCATTERING

In order to verify the helimagnon theory presented in [chapter 8](#), our collaborators, in particular Maximilian Kugler from the group of Prof. Böni at the TU Munich, conducted inelastic neutron scattering experiments (see [section 5.2](#)) on MnSi at the cold neutron triple-axis spectrometer MIRA-2 in Garching [94]. They used neutrons with incident energies between 3.18–5.04 meV and most experiments

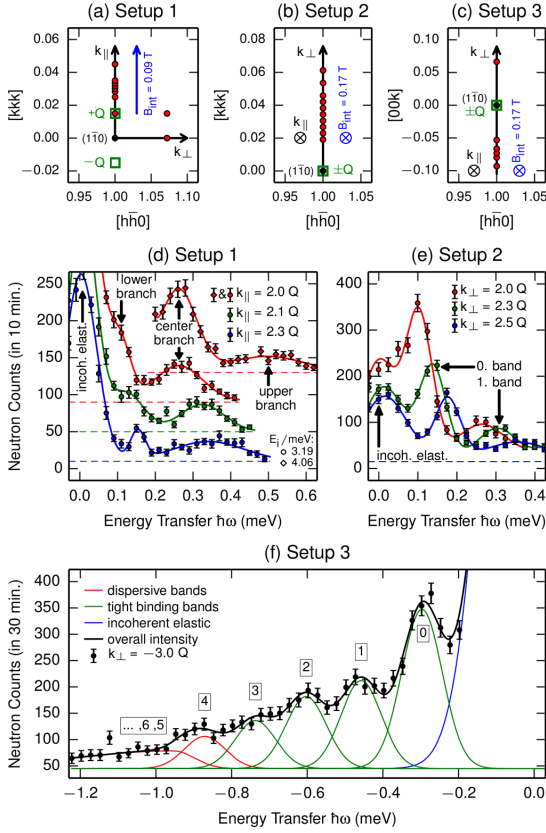
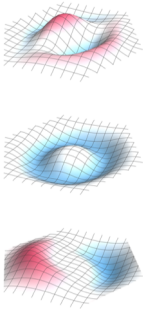


Figure 10.3: Inelastic neutron scattering data of [94]. (a)-(c) show the scattering planes for three setups described in the text. The magnetic field indicated by blue arrows and \otimes symbols defines the direction of \mathbf{Q} forming satellite peaks indicated by green squares. In (b) and (c) they are located above and below the scattering plane. Red circles mark positions where constant Q scans were performed. (d)-(f) show example scans of setups 1 to 3. Full lines are fits of multi-Gaussian profiles. (d) Three helimagnon branches are measured and set apart by 40 counts for clarity. Setups 2 and 3 clearly resolve the first two and five bands, respectively. The elastic peak appears due to the Q -independent incoherent scattering.

were performed at around 20 K. Three different setups, labeled 1, 2 and 3, were chosen to measure various parts of the spectrum. They are shown in figure 10.3 (a)-(c). In all three cases, measurements were conducted around the nuclear Bragg peak $[1\bar{1}0]$ for various fixed incident energies E_i and with the magnetic field pointing in various crystal directions. The latter turned out to not have noticeable influence on the spectrum. Earlier experiments conducted by Janoschek et al. [120] used similar setups. Their measurements, however, were performed in a helical multi-domain state at zero field. Although their data are very well described by the theory as well, the average over the multiple domains does not enable a distinction between individual modes. Therefore, the magnetic field was increased to a value just above H_{c1} in the experiments discussed here. This, most importantly, prepares a single domain state while still being close to a truly helical state with $\mathbf{M}_{\text{helix}}(\mathbf{r})$ still almost perpendicular to the helix pitch vector. The pitch direction \mathbf{Q} then also conveniently aligns with the field direction.

The measurement points of setup 1 can be arranged to trace the longitudinal spectrum along \mathbf{k}_{\parallel} for $\mathbf{k}_{\perp} = 0$. Combining results from setups 2 and 3 traces out the perpendicular spectrum. This is plotted in figure 10.4 (a) and (b), respectively.



10. Comparison to Experiments

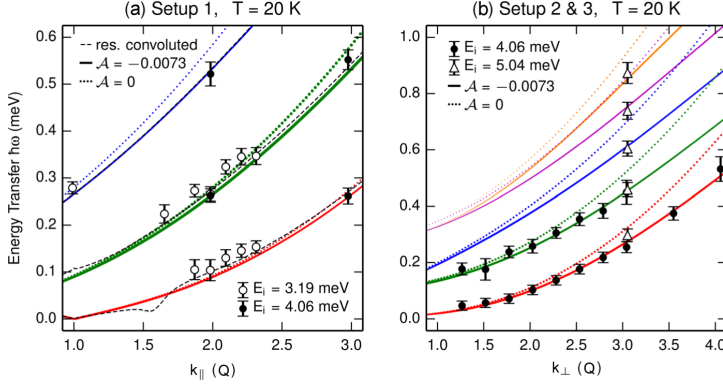


Figure 10.4: Comparison between helimagnon theory and experiment. Panel (a) shows data and theory of the longitudinal spectrum while (b) combines data from setups 2 and 3 to trace the perpendicular spectrum. The helimagnon theory described in [chapter 8](#) is shown by dotted lines. The solid lines include an additional high energy correction to that theory, which is necessary to achieve quantitative agreement at higher energies. The black dashed lines in (a) account for the instrumental resolution slightly shifting the lower and center branches upwards. Figure taken from [94] and relabeled.

The expected theory is shown as dotted lines. There is evidently great agreement at low energies. At higher energies the quantitative agreement is less pronounced. These deviations can be attributed to corrections to the low energy theory, caused by higher-order contributions in the gradient expansion, arising, for example, from cubic anisotropies like (3.31) or (3.32). For an estimate, we consider here a simpler and isotropic term of the form

$$\delta\mathcal{F}_{\text{mag}} = \frac{\rho_s}{2} \frac{\mathcal{A}}{Q^2} (\nabla^2 \hat{n})^2, \quad (10.1)$$

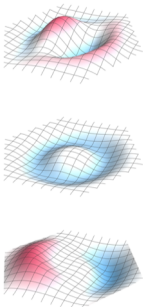
where \mathcal{A} is an expectedly small number of order $\mathcal{A} \sim \mathcal{O}((aQ)^2)$ with atomic lattice spacing a . For MnSi we have $V_{\text{f.u.}} = a^3 \approx 24 \text{ \AA}^3$ for the volume per formula unit and a helix pitch of $Q \approx 0.035 \text{ \AA}^{-1}$, cf. [table 1.1](#). For momenta of $k \approx 3Q$, for example, such a correction amounts to $(a3Q)^2 \sim 10\%$ when comparing (10.1) with the first term in \mathcal{F}_{ex} (8.4). This discrepancy is comparable to the size of the observed deviation. The energy correction (10.1) was therefore taken into account providing us with a single fit-parameter \mathcal{A} for the entire investigated energy range. The best fit was obtained for a value of $\mathcal{A}_{\text{fit}} = -0.0073 \pm 0.0004$. This fit is shown as solid lines in [figure 10.4](#).

Another effect that influences the quantitative alignment between measured data and theory is the instrument resolution. The bands in [figure 10.4](#) (b) are the flat bands in the tight binding limit and are therefore nearly independent of \mathbf{k}_{\parallel} . This makes them rather insensitive to the vertical, i.e., longitudinal, momentum

resolution. The dispersive bands in [figure 10.4 \(a\)](#), on the other hand, have a significant \mathbf{k}_\perp dependence. Considering all contributions of the resolution ellipsoid by convolving the spectral weights, including points in the spectrum with finite \mathbf{k}_\perp , into the nominal $\mathbf{k}_\perp = 0$ spectrum, as was done by Maximilian Kugler and Tobias Weber, leads to a slight upward shift. The result of this process is indicated by the black dashed lines in [figure 10.4 \(a\)](#).

The continuation to much higher energies was measured by Tucker et al. [\[135\]](#). They also performed inelastic neutron scattering on a helimagnet, this time Cu_2OSeO_3 , to measure spin excitations. Their focus was the atomic Brillouin zone which is much larger than the magnetic one. In their setup, they were not able to resolve the fine structure of the modes and their results resembles only a single mode that originates at zero at the Γ -point. Considering the resolution and the much larger energy scales this fits well to the observation that, in [figure 9.5](#) and corresponding measurements shown in [figure 10.4](#), not all branches obtain weights and are excited in a broad fashion. Extrapolated and from afar, they give the impression being one big mode as seen by [\[135\]](#) which hence fits well together.

Last but not least we show, in [figure 10.5](#), measurements at a fixed momentum for four different magnetic field strengths. These measurement were obtained by Tobias Weber [\[134\]](#) of the group of Prof. Böni at the TU Munich, and correspond to the theoretically calculated spectrum shown in [figure 9.6\(a\)](#). The setup was such that the three relevant directions \mathbf{Q} , \mathbf{k} and \mathbf{G} form an orthogonal set. It is also the setup with the best possibility to resolve all modes, because of the most regular weight distribution. Additionally to the helimagnon model used in [section 9.3](#) it was again necessary to incorporate the higher order correction term [\(10.1\)](#) to obtain this excellent quantitative agreement. Hereby we used the same fitting value $\mathcal{A}_{\text{fit}} = -0.0073 \pm 0.0004$ as for the previous helimagnon bands.



10. Comparison to Experiments

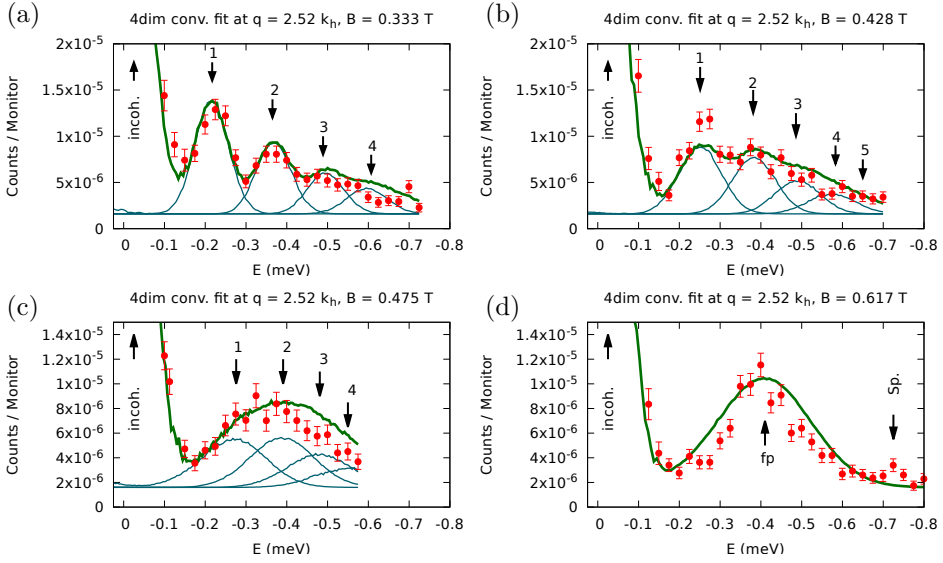
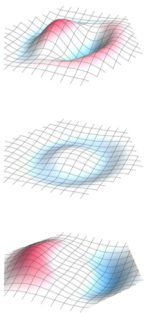


Figure 10.5: Constant k -scans performed using the cold triple-axis spectrometer MIRA at temperature $T = 20$ K, for different values of the magnetic field strength B . The critical field is given by $B_{c2} = 0.56$ T which makes (a) $0.595 B_{c2}$, (b) $0.764 B_{c2}$, (c) $0.848 B_{c2}$ and (d) $1.102 B_{c2}$. These relative positions are marked in figure 9.6(a) by successive dotted lines. The helix pitch Q is denoted by k_h and the momentum k by q . Arrows mark the positions of the energies of the individual helimagnon bands. The blue lines show the convoluted contributions of individual helimagnon bands which form the total convolution indicated by the green lines. The figure is taken from [134].

PART IV.

MAGNONS IN THE SKYRMION LATTICE



11

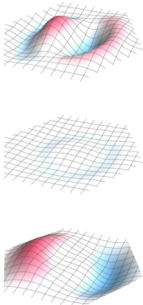
— RESONANCES AT THE Γ -POINT —

Coming from the one dimensional magnetic crystal structure present in the helical phases, we now make our way to the two dimensional skyrmion lattice phase. Here, we focus on uniform excitations at the Γ -point, i.e., the regime that can be probed by ferromagnetic resonance experiments. The first section serves as a reminder of the type of resonances and modes that are present at zero momentum while the second section complements [section 7.2](#) by briefly revisiting the ellipticity of the mean magnetization.

11.1. EXCITATION MODES

Studies of Cu_2OSeO_3 using stripline waveguides provided first experimental evidence of the excitations in the skyrmion phase [[122](#), [136](#)]. Then existing theories were, however, not able to account for these modes in different materials or for different sample shapes. Schwarze et al. [[37](#)] filled this gap with a universal theory achieving good quantitative agreement, in particular on the three samples and materials already listed in [table 7.1](#).

These calculations are the ones presented in [chapter 6](#). Since they are much more elaborate for the skyrmion phase, analytical calculations in a closed form, like for the helical phase, have not been achieved so far. In [figures 7.4](#) and [10.2](#) results of these numerical calculations were already shown alongside results for the conical and field polarized phases and compared to experimental data. These graphs show fixed temperature scans through a phase diagram as, or similar to, [figure 1.2](#). Following such a scan one may enter up to four different magnetically ordered phases, the helical, conical, skyrmion lattice and field polarized phases. Since the numerics are based on a mean-field calculation, the corresponding theoretical phase diagram does not correspond to the experimental one, cf. [section 3.6](#). One can, however, enforce the desired phase by fixing the \mathbf{Q} -directions to be, up to numerical errors, either parallel or perpendicular to the applied magnetic field to achieve a conical or skyrmion lattice state, respectively. Since the here presented formalism is based on equivalent parameters for all phases, just applied for different fields and initial configurations, one merely needs to manually selection which



11. Resonances at the Γ -Point

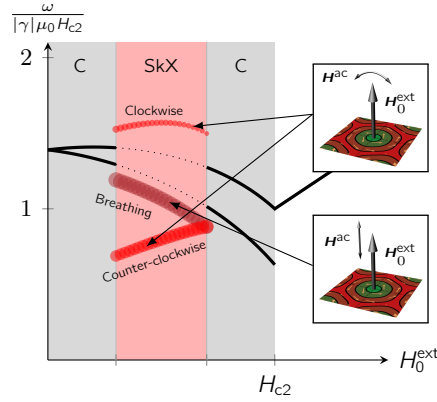


Figure 11.1: Potential resonance frequencies and weights of the skyrmion lattice for perpendicular (light blue) and longitudinal (dark blue) excitations if the skyrmion phase would be stable over a more extended area in the phase diagram. The plotted values correspond to a spherical sample of Cu_2OSeO_3 , chosen for its relatively strong dipole-dipole interaction. Dashed lines in the background correspond to resonances in the conical and field polarized phase as if they were present in the same parameter range. They serve as a guide to the eye.

region of the phase diagram is of interest and apply the appropriate code. Of course, not only resonances at $\mathbf{k} = 0$ follow that rule, but so do those in the finite momentum regime, which is mainly responsible for the peak broadening indicated by the broad gray and red shaded bands in figures 7.4 and 10.2. The phase pocket where the skyrmion lattice phase is stable occurs in the vicinity of $H_0^{\text{ext}} \approx 0.5 H_{c2}$. Figure 11.1 shows the potential resonance frequencies calculated by our method for a much more extended phase pocket than is experimentally realized in bulk chiral magnets. The assumed sample shape is a sphere and the dipolar interaction strength has been chosen to be that of Cu_2OSeO_3 . While we have seen in the helical and conical phases that geometry, excitation direction and dipolar interactions play a pronounced role for the peak positions and mode degeneracies, the skyrmion lattice phase behaves more stable to changes in these parameters. The relative peak positions between the three skyrmion modes and the Kittel mode are almost not influenced by dipole-dipole interaction. Depending on the shape, the Kittel mode takes on values in a broad range and the energies of the three skyrmion modes change accordingly. The effect of a change in shape on the spectral weight distribution is discussed in section 11.2, but it can already be said that also regarding the weights, the modes in the skyrmion phase are much less susceptible to the change than the $\pm Q$ modes in the conical phase.

In the conical phase, the excitation perpendicular to the applied field at $\mathbf{k} = 0$ resulted in the excitation of the $+Q$ and $-Q$ modes, which took only distinct values due to dipole-dipole interaction, while longitudinal excitation yielded no response. In the skyrmion lattice phase, this is different. First, perpendicular excitation

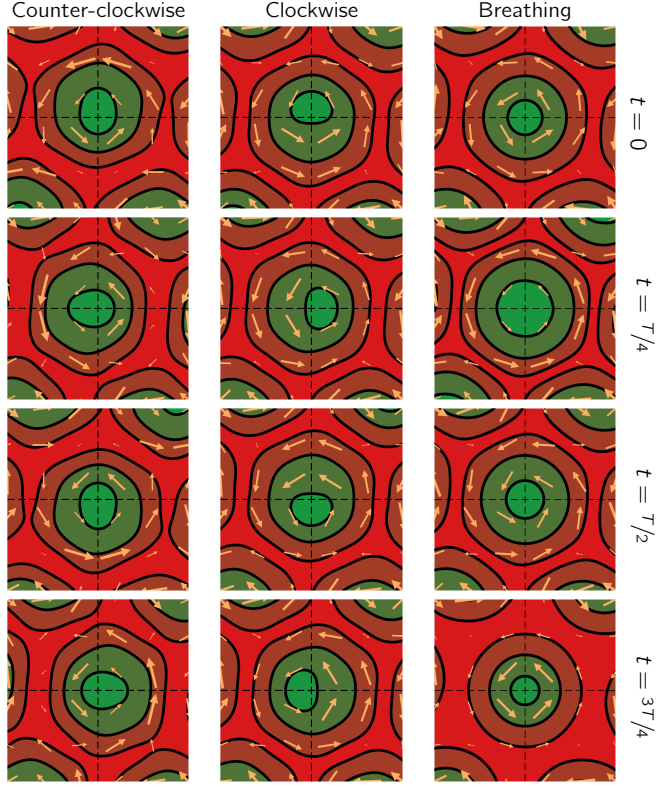
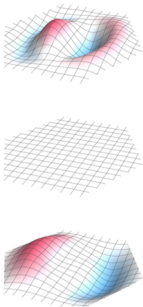


Figure 11.2: Visualization of resonance modes in the skyrmion lattice phase in real space at different times t during a period T . The external magnetic field points out of the image plane. The in-plane components of the magnetization are shown by amber colored arrows while the out-of-plane component is represented by a contour plot where green corresponds to the magnetization pointing anti-parallel to the external field, i.e., into the plane, and red indicates magnetization pointing out of plane. The three different modes are sorted in columns as indicated with a downward time evolution.

also excites two distinct modes, but they are already non-degenerate even without dipolar interaction. The latter only leads to a quantitative change but does not have a qualitative influence. Contrary to the conical phase, longitudinal excitation also excites a mode. The nature of the modes present in the skyrmion lattice phase, and excitable via FMR experiments, have already been simulated and identified by Mochizuki [137] in qualitative terms. They consist of a clockwise and a counter-clockwise precession of the skyrmion cores for perpendicular excitations, and a breathing mode in the longitudinal case. In the latter, the size of the skyrmion core in- and decreases, if seen as being embedded in a ferromagnetic background, without changing the distance between cores. Their motion is



11. Resonances at the Γ -Point

illustrated in [figure 11.2](#). Additional uniform modes that do not carry a finite weight are presented and discussed in [section 12.1](#).

Just like in the helical case, the direction of gyration does not depend on the chirality D , but on the sign of the gyromagnetic γ which is defined negative for electrons. In [table 11.1](#) we list those relations in the skyrmion case compared to the helical one. We remember that the combination of the signs of γ and D determines whether the $+Q$ or $-Q$ has the higher frequency. In the skyrmion case, it is just the sign of γ that determines whether the clockwise or counter-clockwise mode has a higher frequency.


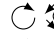










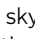
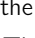


γ	D	Skyrmion		Helix		FM
		high	low	high	low	
+	+	 +C	 -C	-Q	+Q	
+	-	 -C	 +C	+Q	-Q	
-	+	 -C	 +C	+Q	-Q	
-	-	 +C	 -C	-Q	+Q	

Table 11.1: Summarized relationship between chirality, the gyromagnetic ratio γ and the chiral magnetic resonances in the helical/conical phase, i.e., the $\pm Q$ modes, and the gyration modes of the skyrmion phase. The table lists the signs of γ and D .  and  show a top view of the collective rotations with the magnetic field pointing towards the viewer: $\text{Clockwise} \cong \text{Right-handed}$. The handedness of the skyrmion chirality is illustrated by  (right handed) and  (left handed). +C and -C respectively indicate whether the rotation direction of that modes coincides with the chirality or not.

11.2. ELLIPTICITY AND WEIGHT DISTRIBUTION

In [section 7.2](#) we studied the ellipticity of the mean magnetization $\delta \mathbf{M}_0$ in the conical phase and discovered a sensitive relationship towards the shape of the sample. We now study the same in the skyrmion lattice phase. Hereby, we disregard the breathing mode since the magnetic structure is rotationally symmetric and the mean magnetization oscillates linearly along $\mathbf{H}_0^{\text{ext}}$. The mean magnetization of the other two modes oscillates counter-clockwise and clockwise within the plane perpendicular to the applied magnetic field. Analyzing the ellipticity and weight distributions of their mean magnetization leads to results shown in [figure 11.3](#). For these plots we used the same setup as for [figure 7.5](#) with the demagnetization factor along $\mathbf{H}_0^{\text{ext}}$ fixed to $N_z = 0.53$ and varying N_x and N_y between zero and 0.47 while fulfilling $\sum_i N_i = 1$. Furthermore, only field values around $0.5 H_{c2}$ are of interest to us, because this is the region in which the skyrmion lattice phase is stable in bulk crystals.

Contrary to the conical phase, the ellipticity is not a step-function and we also do not observe linear polarization in the skyrmion phase since the ellipticity never

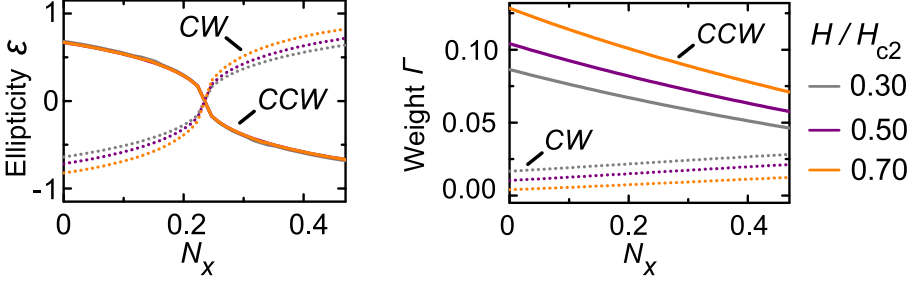
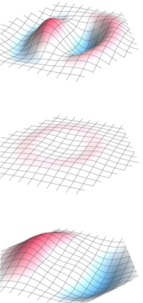


Figure 11.3: Shape and field dependence of the ellipticity ε of the mean magnetization of the clockwise (CW) and counter-clockwise (CCW) gyration modes in the skyrmion lattice is shown on the left. The right panel shows the shape and field dependence of their spectral weights. As in figure 7.5, the demagnetization factor along $\mathbf{H}_0^{\text{ext}}$ is fixed to $N_z = 0.53$ while N_x and N_y are varied between zero and 0.47 fulfilling $\sum_i N_i = 1$. Here, we concentrate on field values around $0.5 H_{c2}$ because the skyrmion lattice is only stable in that regime. The figure is taken from [125].

becomes unity. Most interestingly, the ellipticity of the counter-clockwise mode is independent with respect to a change in magnetic field strength. To be precise, its ellipticity already equals the ellipticity in the field-polarized phase at $H_0^{\text{ext}} = H_{c2}$ given by (7.15). This behavior corresponds to that of a paramagnet in a finite field. Coming from high fields and crossing the threshold above which the magnetization is saturated, there is a linear relationship between external field and magnetization. Since the counter-clockwise motion matches the handedness of the rotation of the mean magnetization in the field-polarized phase, one could say that the system behaves like an ordinary paramagnet just without a disordered redistribution of spins pointing in all directions, but with an ordered one by forming skyrmions in a ferromagnetic background. With decreasing field strength, the skyrmion core radius becomes larger. Because many of the magnetic moments within a skyrmion point opposite to the magnetic field, their contributions add and the average static magnetization consequently decreases like the magnetic field strength does. The ellipticity, however, is still dominated by the ferromagnetic background.

Since there is a mismatch between the handedness of the Kittel mode in the field-polarized phase and the clockwise mode, this argument does not apply for this mode. This mismatch is ultimately the reason why the clockwise mode always has a smaller spectral weight than the counter-clockwise mode. It is similar to the mismatch between the handedness between the Kittel and $-Q$ modes. There, as well as in the skyrmion case, the mode with the mismatched handedness loses weight with increasing magnetic field while the other gains weight. The latter can be easily understood because the magnetic structure becomes more and more ferromagnetic with increasing field.



12

SPECTRUM

In the previous chapter we focused on the regime where $k \ll 1/L$ for sample size L . Here, we focus on the opposite regime of the magnon spectrum in the skyrmion lattice phase. To obtain the spectrum, we use again the formalism and method described in [chapter 6](#). The numerical refinements described in [section 6.2](#) gain particular importance in this context.

In the conical phase, we identified the directions $\mathbf{k}_{\parallel} \parallel \mathbf{Q}$ and $\mathbf{k}_{\perp} \perp \mathbf{Q}$ as the two conceptionally different momentum directions. In the skyrmion phase, we can distinguish between in-plane and out-of-plane momenta. The former is discussed in the first two sections and the out-of-plane case in [section 12.3](#). In that context, we also define $\mathbf{k}_{\parallel} \parallel \mathbf{Q}$ to be in plane along one of the \mathbf{Q} vectors and $\mathbf{k}_{\perp} \perp \mathbf{Q}$ perpendicular to all \mathbf{Q} vectors, i.e., perpendicular to the skyrmion lattice plane. These direction are illustrated in [figure 12.1](#).

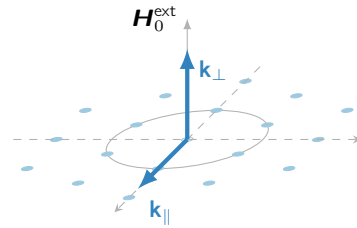
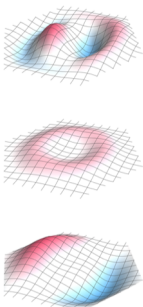


Figure 12.1: Directions of \mathbf{k}_{\parallel} and \mathbf{k}_{\perp} with respect to the reciprocal skyrmion lattice.

12.1. SPECTRUM WITHIN THE 1. BRILLIION ZONE

In this section we present magnon spectra in the first Brillouin zone. [Figure 12.2](#) shows three spectra to demonstrate the influence of dipolar interaction on the spectrum. The figures show in each case the first 16 bands in a stable configuration for which a momentum space cutoff of 7 rings, cf. [figure 6.1](#), is sufficient. The aspect of stability and reliability of the obtained modes is not trivial and will be addressed further in [section 12.2](#). Also, here and in the remaining sections, the magnetic field strength has been chosen to be $H_0^{\text{ext}} = 0.5 H_{c2}$, because this value brings us within the skyrmion lattice phase pocket of typical bulk chiral magnets.

The energy bands shown in [figure 12.2](#) correspond to momenta that trace a path through the first Brillouin zone connecting high symmetry points. The first part, i.e., $\overline{\Gamma\text{M}}$, of said path follows the direction of one of the six \mathbf{Q} -vectors



12. Spectrum

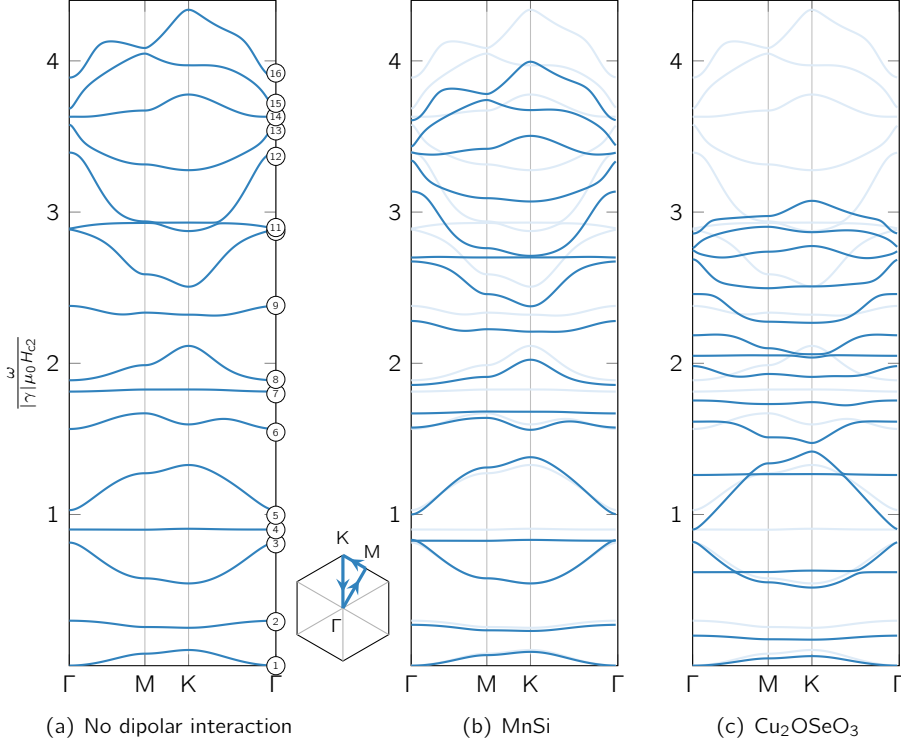


Figure 12.2: Shown are the lowest 16 bands of three magnon spectra in the skyrmion lattice phase within the first Brillouin zone. The x-axis traces a path through the 1. BZ as shown in the small inset. One of the \mathbf{Q} -vectors lies along the ΓM direction. Calculations were performed with a reciprocal lattice size containing 7 rings, cf. figure 6.1, and for different dipolar interaction strengths. Panel (a) shows the spectrum without dipole-dipole interaction. It is, for comparison, also shown in light blue colors in the backgrounds of panels (b) and (c) which, respectively, show the magnon spectrum with small (MnSi, $\chi_{\text{con}}^{\text{int}} = 0.34$) and large dipolar interaction (Cu₂OSeO₃, $\chi_{\text{con}}^{\text{int}} = 1.76$).

connecting neighboring Γ -points. The path then turns perpendicular, extends until it reaches the corner K of the Brillouin zone and returns to the Γ -point. Figure 12.2(a) shows the magnon spectrum without dipolar interaction and the modes are labeled by small encircled numbers on the right hand side. A three-dimensional illustration of the first 12 bands of this spectrum provides figure 12.3. When comparing this spectrum to previous calculations at the Γ -point we notice, that modes 3, 5 and 6 connect with the counter-clockwise, breathing and clockwise modes, respectively. This connection becomes even clearer when spectral weights are considered, as we do in section 12.4, and those three modes are the only ones that remain with finite spectral weight in the

limit $\mathbf{k} \rightarrow 0$. Also, upon inspection of the Goldstone mode marked by 1 in [figure 12.2\(a\)](#), its quadratic dispersion in the long wavelength limit is evident. There, a Berry phase contribution to the Lagrangian dominates over the kinetic term and renders an otherwise linear dispersion, for waves propagating within the skyrmion lattice plane, quadratic [\[138\]](#).

[Figures 12.2\(b\) and 12.2\(c\)](#) then move on to elucidate the effect of dipole-dipole interaction. Continuing with regard to the Goldstone mode, one can see that its long wavelength behavior is practically not influenced and still quadratic, see also [\[93\]](#). Furthermore, [figure 12.2\(b\)](#) corresponds to the dipolar interaction strength in MnSi with $\chi_{\text{con}}^{\text{int}} = 0.34$, which is comparably weak, but from there it is already evident that higher energy modes are generally influenced more strongly by dipole-dipole interaction than low energy modes. It becomes even clearer in panel (c), that its influence results in a general decrease in energy of each mode. Besides that, there are more things to observe. First, while most bands show a decrease in energy, in particular modes 3, 5 and 6, corresponding to the gyration and breathing modes, remain at a relatively constant frequency and mostly only get distorted in shape. Another peculiarity are three (almost) flat modes 4, 7 and 11. Besides being flat, they are also the only ones that cross into other modes. At these crossing points hybridization is present. They also move at different speeds, compared to the other modes, when the strength of the dipolar interaction changes. This phenomenon is not completely understood yet, but the occurrence of flat bands in a spectrum reminds us of the flat Helimagnon bands and motivates the explanation of the magnon spectrum in the skyrmion phase by a superposition of helimagnon spectra. Further supporting arguments of an analogy are given on [page 137](#) as part of [section 12.4](#).

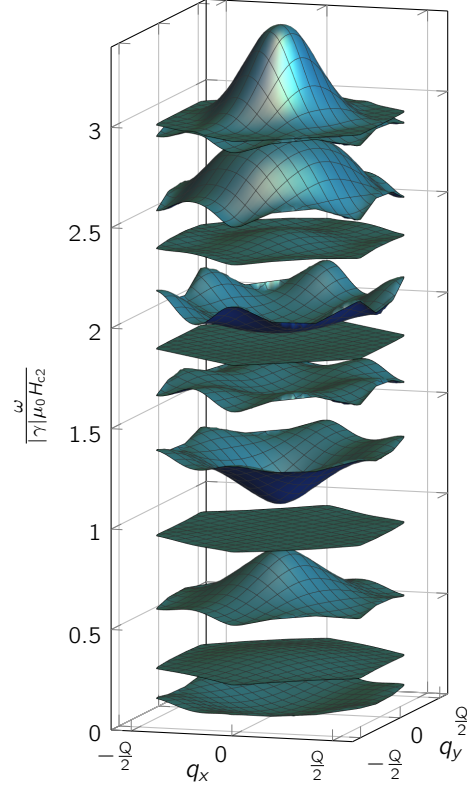
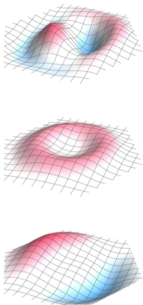


Figure 12.3: 3D representation of the first twelve modes in the magnon spectrum in the skyrmion phase.

Seeing this large number of bands, one may ask the question what those modes actually look like and how they behave. Since a finite momentum vector distorts the mode behavior over space, we take again a look at the corresponding



12. Spectrum

uniform modes. In [section 11.1](#) we already saw three of those modes. There, we considered those modes excitable via FMR experiments and incorporated the corresponding weights into their motion and the distortion of their shape. Doing that, only three modes remained, the counter-clockwise (mode 3), breathing (mode 5) and clockwise mode (mode 6). In a more general approach we can consider the eigenvectors of all modes and plot them. [Figure 12.4](#) shows the real space magnetization of the first 16 modes, all at a fixed time, analogously to [figure 11.2](#). The color red corresponds to magnetization pointing parallel and green anti-parallel to the applied magnetic field. Said field points out of the shown planes. The first thing one notices is a number of different shapes beyond the round ones seen in the three previously studied modes. There are rod, triangle, cross and pentagon shapes, among others. Their motion can be even more intricate. Let us take the counter-clockwise and clockwise modes as examples, i.e., modes 3 and 6. A more detailed observation lets us notice that, besides the obviously different sense of gyration, cf. [figure 11.2](#), there is a second difference. In the still picture of mode 3 one can see that the entire skyrmion is “pushed” towards one direction out of its equilibrium state. This pushed-away state then starts to rotate counter-clockwise. Looking more closely at mode 6 on the other hand, one notices, that while the center is “pushed” towards one direction, the outer part of the skyrmion is “pushed” towards the opposite direction creating something like an additional node in its structure. This new distorted state then rotates clockwise. This difference can be seen more clearly when plotting the change $\delta\mathbf{M}$ in magnetization away from equilibrium instead of the full real space magnetization $\mathbf{M} = \mathbf{M}^{\text{mf}} + \delta\mathbf{M}$. This is illustrated in [figure 12.5](#) which shows $\delta\mathbf{M}$ for the first 16 modes at the same time frames as those snapshots in [figure 12.4](#). Note, that the first mode is the Goldstone mode and hence has an excitation frequency zero leading to no distortion. In [figure 12.5](#), one can clearly see the difference in node structure between modes three and six manifested in a different number of rings which we will count and label by the letter m . Such a labeling is also common in the classification of linearly polarized optical waveguide modes (LP-modes) of optical fibers. They have radially symmetric index profiles in the approximation of weak guidance, which resemble those patterns shown in [figure 12.5](#) very much, cf. section about multimode fibers in [\[139\]](#). That means, that $m = 1$ for the counter-clockwise and $m = 2$ for the clockwise mode. The color-code is such that red stands again for magnetization pointing parallel to the external magnetic field. The anti-parallel direction on the other hand is encoded by blue. The change in color has been made to emphasize the difference between \mathbf{M} and $\delta\mathbf{M}$. Although resemblance to the aforementioned LP-modes or to vibrations of a circular membrane is remarkable, the skyrmion modes (SM) show clear differences. The first is, that the change in magnetization at the center of the Brillouin zone is zero, i.e., meaning no intensity at the center. This is the case for many LP-modes, too, but in particular for those that can be compared to the skyrmion breathing modes, i.e., modes 5 and 13, it is not. Complexity does not stop there. The rotation direction of the resulting structure does not necessarily need to be uniform. Let us take mode 9 for example. There, we also

12.1. Spectrum within the 1. Brillouin Zone

have $m = 2$ but this time the inner and outer ring rotate in opposite directions! And even without this opposite sense of rotation, mode 9 falls already into a different category because of additional splicings within a ring, that lead to the triangular shape. Looking at the real space picture using the full magnetization in [figure 12.4](#) of modes three, two and four, in that order, the mode shape changes from round, to rod, to triangle. This difference is labeled by the letter $l = 1, 2, 3$ for modes three, two and four, respectively. This labeling is more evident when looking at the density plots of the change of the magnetization $\delta\mathbf{M}$, [figure 12.5](#), where l counts the splicings across the Brillouin zone.

Additionally, we can also introduce a labeling for observed rotation directions or breathing properties. The letter b labels a breathing mode tantamount to a standing wave property. More delicate distinctions can be made for the rotation directions. The most obvious is a continuous process where a fixed intensity moves around a circle. For these types of rotations we will use c for a clockwise and \bar{c} for a counter-clockwise rotation. But a rotation can also take a more discrete form, where intensity is lost at a point A and gained at a neighboring point B, but with a finite distance between A and B. These types of rotations will be indicated by c^* and \bar{c}^* for such clockwise and counter-clockwise rotations, respectively. Skyrmion mode 9 can therefore be labeled via $\text{SM}_{l,m}^{\text{rot. dirs}} = \text{SM}_{32}^{c\bar{c}}$, where the rotation directions are ordered from the center to the rim.

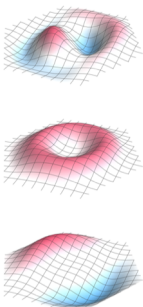
There are, however, slight exceptions or anomalies to these descriptive classifications. Those cases are:

modes 8, 10, 15 $l_{\text{inner ring}} = 2$, $l_{\text{outer ring}} = 3$. We labeled these modes with $l = 2_3$ to indicate this anomaly. However, although it is evident, that there are 6 spots on the outer part, i.e., corresponding to $l = 3$, and only 4 in the inner part, the intensity or color accumulates only in 4 joint areas on the outer ring. So in terms of global intensity, the characteristics of $l = 2$ dominates.

mode 11 On first sight, it seems like a clockwise rotating mode, because the red and blue structure stays as it is and continuously rotates clockwise, which would justify an index c . However, the intensities change in a way, that they shift weight from one adjacent zone to the next in a counter clockwise direction, and that faster than the node structure rotates. This, in turn, would mean a rotation corresponding to the label \bar{c}^* .

mode 12 There is again not a normal “color to l ”-correspondence as $l = 3$ but there are only 2 pits (blue) and 2 hills (red) instead of 3 each. At the same time, same colors neighbor each other which resembles, on average, a splitting according to $l = 1$.

At this point we also want to mention and list in [table 12.1](#) the change of the homogeneous magnetization $\delta\mathbf{M}_0$ of each mode obtained from normalized eigenvectors $\delta\mathbf{M}$. Expected non-zero values for the known and measured counter-clockwise, clockwise and breathing modes are recovered nicely. Furthermore, there



12. Spectrum

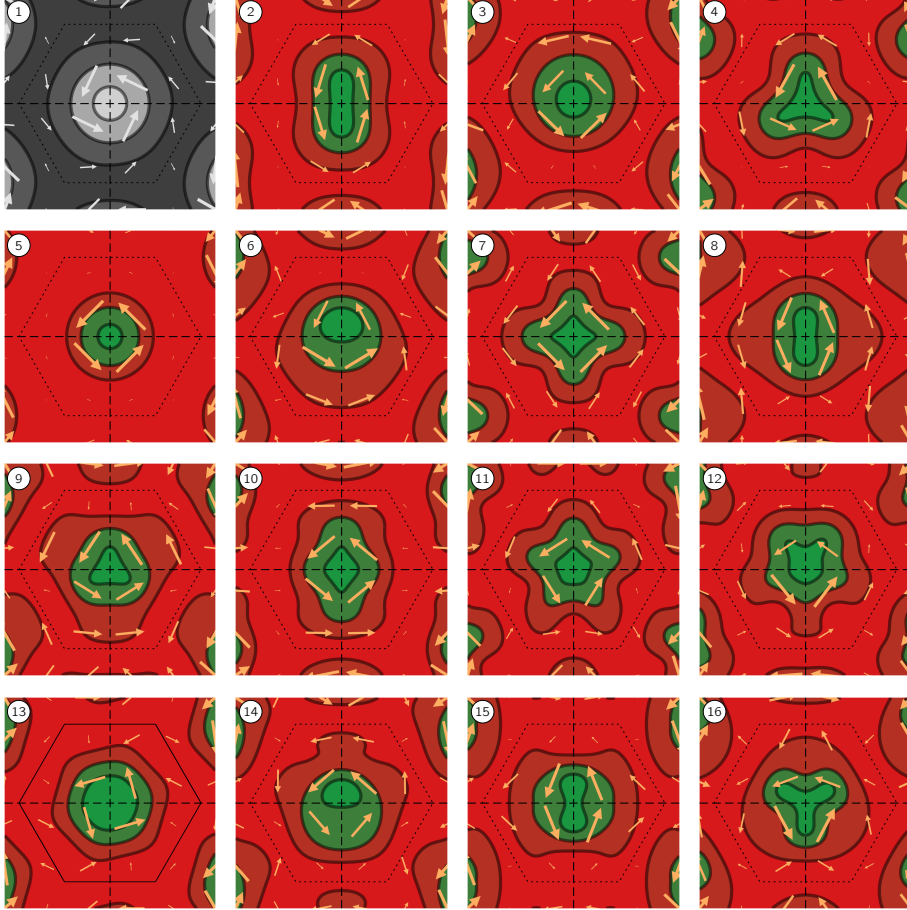


Figure 12.4: Snapshots at a fixed time t of the real space magnetization $\mathbf{M} = \mathbf{M}^{\text{mf}} + \delta\mathbf{M}$ of the first 16 uniform modes. The applied magnetic field points out of the shown planes. Red (green) color indicates magnetization pointing parallel (anti-parallel) to that field. The arrows illustrate the in-plane component. Dashed lines are a guide to the eye and their crossing point marks the center of the Wigner Seitz cell. The latter is indicated by the dotted line. Modes 3, 5 and 6 are the counter-clockwise, breathing and clockwise modes accessible via FMR. Note, that the other modes exhibit a variety of different shapes. The motion of the remaining modes can be quite complex and can be explained via their node structure shown in [figure 12.5](#), see text.

12.1. Spectrum within the 1. Brillion Zone

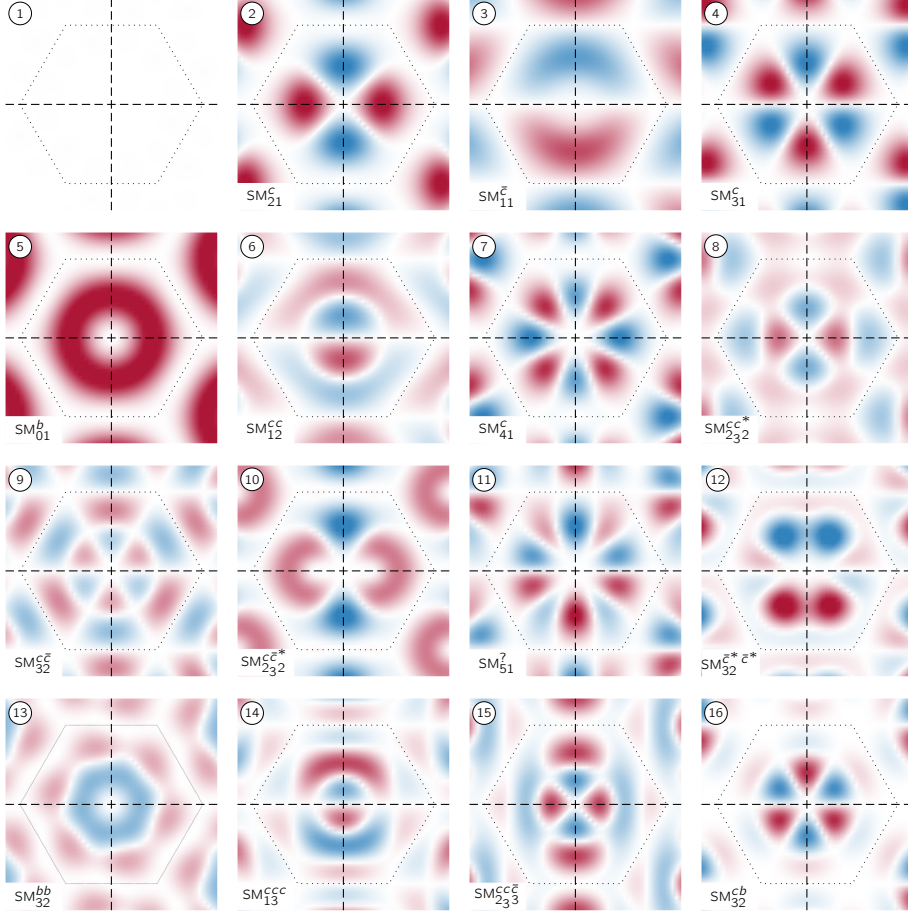
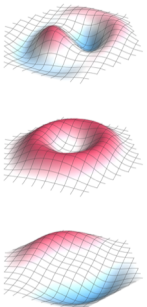


Figure 12.5: Snapshots at a fixed time t of the change in magnetization $\delta \mathbf{M}$ of the first 16 uniform modes to illustrate the node structure of the modes. The applied magnetic field points out of the shown planes. Red (blue) color indicates $\delta \mathbf{M}$ pointing parallel (anti-parallel) to that field. Dashed lines are a guide to the eye and their crossing point marks the center of the Wiegner Seitz cell. The latter is indicated by the dotted line. Modes 3, 5 and 6 are the counter-clockwise, breathing and clockwise modes accessible via FMR. Each skyrmion mode (SM) is labeled by the expression in the lower left corner of each panel. See the main text for a description.



12. Spectrum

Mode	$\max_{0 < t \leq T} \delta \mathbf{M}_0(t) $	Motion
1	0	
2	0	
3	4.40	CCW
4	0	
5	5.55	breathing
6	2.11	CW
7	0	
8	0	
9	0	
10	0	
11	0.07	CCW
12	0.18	CCW
13	0.42	breathing
14	0.14	CW
15	0	
16	0	

Table 12.1: List of the absolute values and motions of the change of the homogeneous or mean magnetization $\delta \mathbf{M}_0(t)$ over the period T of the first 16 modes. Motion types are counter-clockwise (CCW), clockwise (CW) and breathing types.

are further homogeneous motions of that type evident. However, the maximal absolute values of $\delta \mathbf{M}_0$ of those modes are less than a tenth than that of the already barely measurable clockwise mode, which makes them extremely difficult to observe in experiments. The restriction to the maximal value is only necessary for the breathing modes as all others are constant. The likeliest of the higher modes to see in experiment is mode 13, which is a second breathing mode. Interesting to see is also that the sequence of the motion of the higher modes is the same as that of the lower modes, i.e., CCW \rightarrow breathing \rightarrow CW. It would be interesting to see whether this is a general trend up to higher energies, since the pattern “relatively flat band enclosed by convex bands below and concave band above” repeats itself.

The Goldstone mode, mode 1, of course has zero frequency and is hence not excited. It is listed here to complete the picture and shown as a black and white equilibrium configuration in [figures 12.4](#) and [12.5](#).

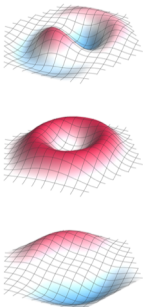
12.2. SPECTRUM BEYOND THE 1. BRILLION ZONE

In this section we discuss two major aspects. The first is the effect of the finite size of the reciprocal skyrmion lattice on the spectrum while simply following the recipe leading to [equation \(6.9\)](#). The second step concerns mode stability and mode selection, which is not trivial as was indicated in the previous section.

It is our goal to obtain a reliable spectrum for momenta and energies as large as possible. This is particularly the case with the foresight to compare experimental data, of inelastic neutron scattering experiments, similar to those discussed in [section 10.2](#), to the theoretically obtained spectrum. Such experiments are generally performed in a momentum range of $k \sim 1\text{--}4\text{Q}$ and beyond. [Figure 12.6](#) illustrates how the spectrum evolves in terms of the momentum space system size. While it is already enough to consider a system size containing three to four rings when interested in the modes at the Γ -point relevant for FMR experiments, since their values only change marginally above 3 rings, this is not enough when examining higher energies. Here, we are particularly interested in obtaining reliable values for the spectrum in the red shaded area highlighted in [figure 12.6\(c\)](#). The reason is that while the spectrum itself may obey Bloch's theorem, the distribution with weights attributed to neutron scattering does not, because of the momentum transfer that is potentially larger than the extent of the first Brillouin zone. In principle, one could increase the system size until reaching a stable spectrum in the energy and momentum range of interest. As numerical effort grows at least quadratically with system size, we rather focus on obtaining a reliable spectrum for the first Brillouin zone first, reaching up to the overall desired energies. We do this with the intention to use these results to construct the extended zone scheme and deal with the weights later.

We consider the spectrum as *stable* when it does not change noticeably upon an increase in system size. When taking a look at the evolution with system size illustrated in [figure 12.6](#), we notice a plethora of flat bands that cross the entire spectrum that seem to be far from any convergence. It is hence crucial to understand whether these modes are relevant or maybe numerical artifacts. They actually change their relative positions and numbers not only when varying the system size, but also when varying the parameter t introduced in the rescaled free energy functional ([3.37](#)). It is a measure of the distance to the phase transition and one may think that increasing that distance would give better results. This is generally true, but does not improve the situation regarding these flat bands.

It turns out, that they are due to finite size effects and numerical inaccuracies. Their origin is elucidated in [figure 12.7](#). In this figure we show 4 different plots on top of each other. The gray one in the background is the one obtained by a straightforward application of [equation \(6.9\)](#) for a system containing 7 rings as was also the case in [figure 12.6\(c\)](#). At the end of [section 6.3](#) we already mentioned that the $(\mathbf{M}^{\text{mf}} \times)$ matrix plays a non-trivial role in the construction of the spectrum and that its eigenvalues in momentum space do not form clean plateaus. Instead, they could be classified into three regions as illustrated in [figure 6.3](#) on page 75, namely those with values of approximately $\pm|\mathbf{M}^{\text{mf}}|$, approximately zero, and those in between. We can then project not only the $(\mathbf{M}^{\text{mf}} \times)$ but also χ_0^{-1} onto the corresponding subspaces and obtain the modes that, for example, should be zero-modes per construction, and see where they actually end up. In [figure 12.7](#) these zero modes are indicated by red colors as are the corresponding eigenvalues in [figure 6.3\(c\)](#). Dark blue in both figures corresponds to the subspace with



12. Spectrum

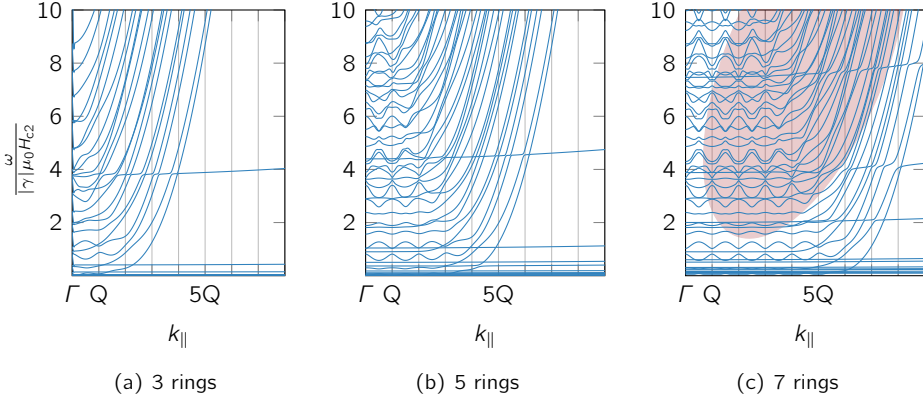


Figure 12.6: Evolution of the resulting magnon spectrum in the skyrmion lattice phase with increasing the momentum space system size from left to right. Notice in particular arbitrarily crossing flat bands. The red shaded area in panel (c) roughly indicates the region accessible with inelastic neutron scattering experiments.

eigenvalues of $\pm |\mathbf{M}^{\text{mf}}|$. The subspace with intermediate eigenvalues is indicated by black lines in [figure 12.7](#) instead of light blue as in [figure 6.3\(c\)](#), for better distinguishability. [Figure 12.7](#) lets us draw the following conclusions. First of all, alleged zero-modes can take on quite sizable finite values which explains the lower lying flat bands in the initial spectrum. Second, the intermediate subspace is responsible for the flat bands that cross through the entire spectrum without diverging at the sides. Furthermore, they stem from the outer Fourier components and are hence somewhat of a boundary or finite size effect. It can be concluded from the parabolas that appear when this subspace is treated on its own without the context of the rest of the spectrum. This has been double checked by applying the same concept in the conical phase. There, numerics are much less volatile, so that this identification is even more evident. Last but not least, the subspace corresponding to eigenvalues of $\pm |\mathbf{M}^{\text{mf}}|$ is the relevant one needed to construct a clean magnon spectrum in the skyrmion phase.

To conclude a converged and clean spectrum in the first Brillouin zone, we must hence check that there is not only marginal to no discrepancy between two spectra constructed using consecutive system sizes, but also between the initial spectrum and the spectrum restricted to the $\pm |\mathbf{M}^{\text{mf}}|$ subspace. The light blue shaded area in [figure 12.7](#) indicates the area for pretty much exact agreement of those terms for a system containing 7 rings. In practice, even higher energies may be considered, depending on the area of application, since the discrepancies are still very small for most modes. These differences do not play a decisive role when interested in the comparison to inelastic neutron scattering data, since the resolution ellipsoid, over which the weights of the spectrum are averaged, is often even larger than the inter mode spacing itself. Numerical inaccuracies,

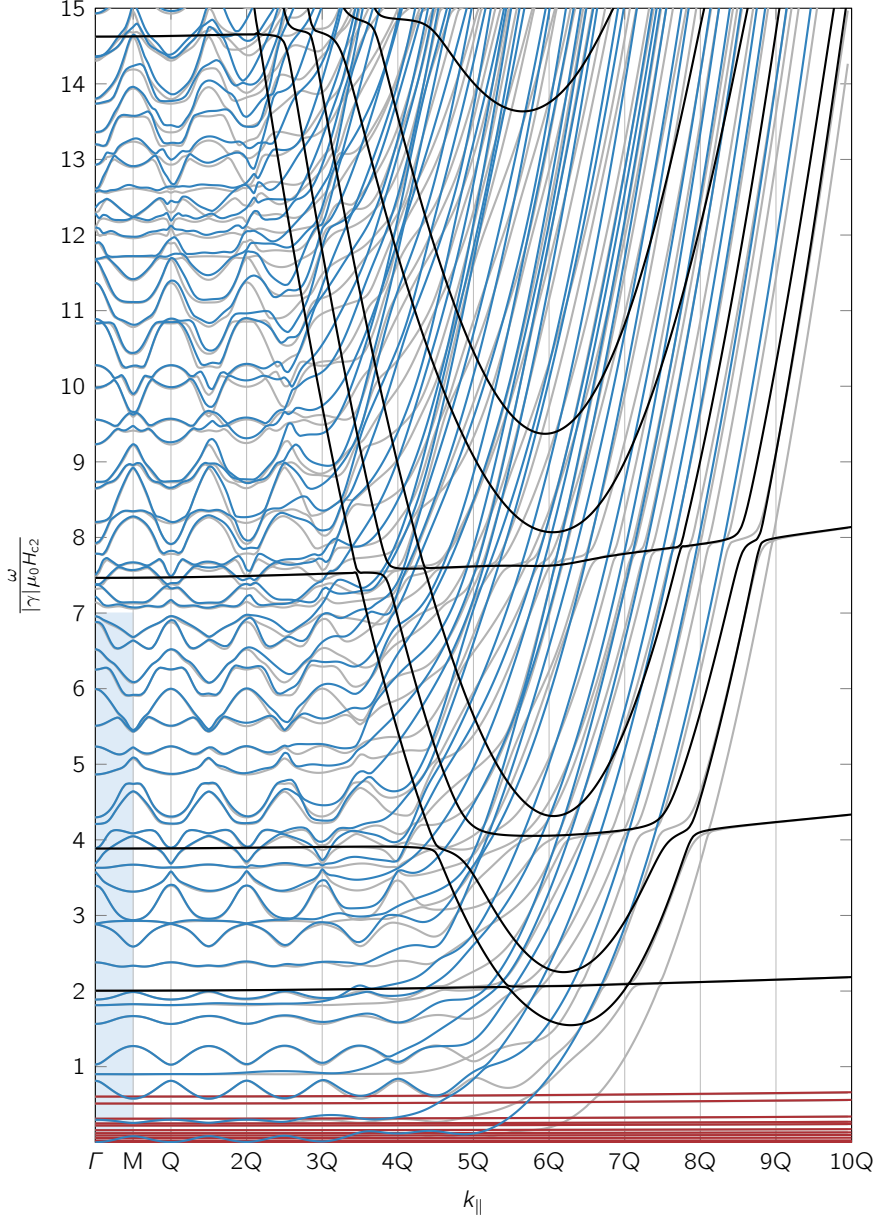
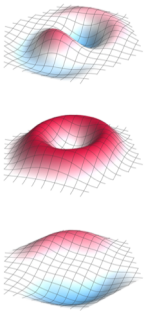


Figure 12.7: Comparison between magnon spectrum, with $\mathbf{k}_{||}$ along one of the \mathbf{Q} vectors, between the general scheme of calculation (gray) and when one restricts the calculation to different subspaces of the $(\mathbf{M}^{mf} \times)$ matrix. Details are described in the main text.



12. Spectrum

however, play a non negligible role when calculating ideally analytic quantities like Chern numbers corresponding to individual bands. For those calculations see [section 13.1](#). The spectrum in the extended zone scheme representation can now be obtained by simply folding and copying the modes of the first Brillouin zone.

12.3. \mathbf{k} PERPENDICULAR TO THE 1. BRILLION ZONE

After discussing the spectrum for momenta within the skyrmion lattice plane, we now focus on momenta \mathbf{k}_\perp perpendicular to it, as illustrated in [figure 12.1](#). In the helical and conical phases, the spectrum with respect to \mathbf{k}_\perp was independent on the direction of \mathbf{k}_\perp as long as it was perpendicular to \mathbf{Q} and $\mathbf{H}_0^{\text{ext}}$. This changes in the skyrmion case. Besides being perpendicular to the lattice, \mathbf{k}_\perp can now be parallel or anti-parallel to the external field $\mathbf{H}_0^{\text{ext}}$. The spectrum $\omega(k_\perp)$ at $\mathbf{H}_0^{\text{ext}} = 0.5 H_{c2}$ and without considering dipolar interaction, i.e., $\chi_{\text{con}}^{\text{int}} = 0$, is shown in [figure 12.8](#) (a). It is evident, that this spectrum is not symmetric with respect to $k_\perp = 0$. This is due to the skyrmion chirality. When it is reversed, i.e., $D \rightarrow -D$, then the spectrum is mirrored at the y -axis. The corresponding weights calculated in [section 12.4](#) are mirrored accordingly, too. Additionally, the Goldstone mode is observed to also have a quadratic behavior in perpendicular direction. The part in positive \mathbf{k}_\perp direction, however, is stiffer and has small tendencies to be of cubic nature.

[Figure 12.8](#) (b) shows a magnified part of the spectrum for lower energies that are of the relevant magnitude of the FMR modes, i.e., the gyration and breathing modes. The latter occur at $k = 0$ and are indicated by red and yellow dots, respectively. Remember, that those modes occur in the regime where $k \ll 1/L$ for sample size L , where as the modes of the spectrum indicated in blue correspond to the $k \gg 1/L$ limit. Without dipolar interactions, these three FMR modes form the unique limit of individual ($k \gg 1/L$)-modes.

Including dipolar interaction, as was done in [figure 12.8](#) (c), the uniqueness of the limit $\mathbf{k} \rightarrow 0$ is not given anymore for every mode, in particular not for the three FMR modes. Like in the helical/conical phase, we arrive at a situation where $\omega(\mathbf{k}_\parallel \rightarrow 0) \neq \omega(\mathbf{k}_\perp \rightarrow 0)$. This is illustrated in [figure 12.8](#) (c) by the added, appropriately colored, vertical lines connecting those two limits. They form hence a broad band in which the expected FMR modes may lie, depending on shape. The values without dipolar interactions are again indicated by the red and yellow dots. To be precise, this non-analytic limit is actually only observed for the three FMR-modes as far as we can tell from the investigation of the first 50 bands. An assumption, that this phenomenon is only valid for bands with a certain Chern number seems plausible when only considering the lowest six bands, but gets disproved for higher bands, see [chapter 13](#). Furthermore, this singular behavior also appears in the topologically trivial helical phase, and there also only for the corresponding FMR-modes, which makes it unlikely to have a topological origin. It is hence most likely a consequence of the chirality due to

12.3. \mathbf{k} perpendicular to the 1. Brillion Zone

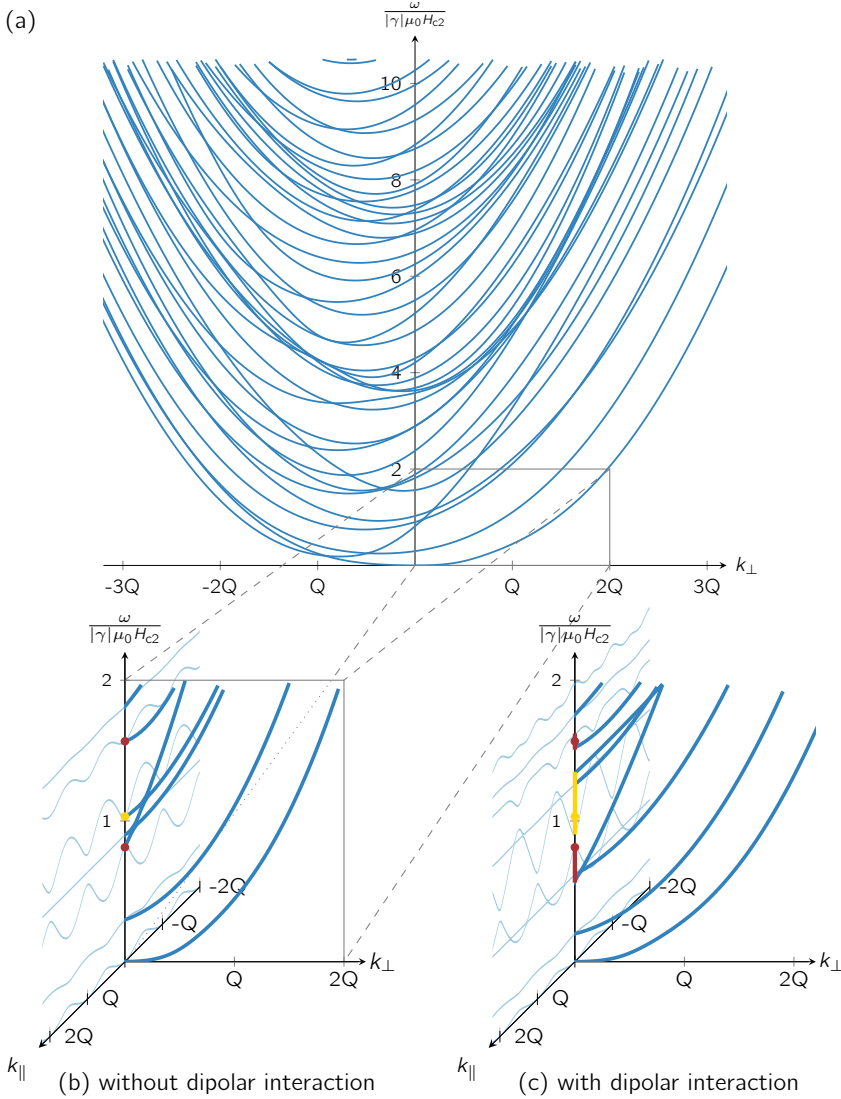
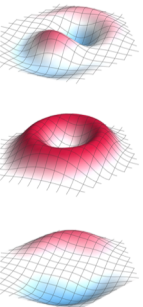


Figure 12.8: (a) Magnon spectrum for \mathbf{k} perpendicular to the skyrmion lattice plane without present dipolar interaction. The positive (negative) direction corresponds to the direction parallel (anti-parallel) to the applied magnetic field. (b) shows a magnified portion of that spectrum with energies of the order of magnitude of FMR resonances. The gyration (breathing) modes are indicated by the additional red (yellow) dots. (c) illustrates the effect of dipolar interactions on that part of the spectrum. As in the helical case, the limit $\mathbf{k} \rightarrow 0$ is not unique for all modes, in particular the three modes accessible via FMR. Their discrepancies and resulting bands are illustrated by the vertical correspondingly colored lines. Note that $\omega_{\parallel}^{\text{gyr.}}(\mathbf{k} \rightarrow 0) > \omega_{\perp}^{\text{gyr.}}(\mathbf{k} \rightarrow 0)$ but $\omega_{\parallel}^{\text{breathing}}(\mathbf{k} \rightarrow 0) < \omega_{\perp}^{\text{breathing}}(\mathbf{k} \rightarrow 0)$. The colored dots still mark their mode position for $\chi_{\text{con}}^{\text{int}} = 0$.



12. Spectrum

the Dzyaloshinskii-Moriya interaction, but a definite answer cannot be given at the moment and leaves room for exploration.

12.4. WEIGHTS FOR NEUTRON SCATTERING

For inelastic neutron scattering experiments in the skyrmion lattice phase, similar conditions apply as for experiments in the helical phases. Merely the magnetic field strength is now relatively fixed to about $0.5 H_{c2}$ to obtain a skyrmion lattice state in the bulk chiral magnets that we study here. Also as before, the weights given by (6.41) do not follow Bloch's law, which brings us again to a point where we have to weigh effort versus benefit. We would like to avoid using many Fourier modes in the mean field minimization. We have seen in section 12.2 that one needs at least a minimal amount of Fourier modes to achieve accuracy up to the desired energies already within the first Brillouin zone. To natively achieve the same amount of accuracy in other Brillouin zones would require many more Fourier modes as was illustrated in figure 12.6. To avoid this and also use said minimum number of rings for the minimization, we employ the following trick.

If \mathbf{k} is so large that one ends up beyond the 1. BZ, then one would like to have the information of the 1. BZ at that point in the concerning matrix including all the possible coupling to other Fourier components, i.e., the off-diagonal terms. To this end, we define the initial data and matrix structure as the *initial system* which we embed in an *extended system* consisting out of zeros. Figure 12.9 visualizes this arrangement, and the process explained in the following, in a schematic way. Brillouin zones are indicated by drawn honeycombs and each honeycomb leads to an additional block dimension in the momentum matrix. Those considered by the initial system are marked by the light blue dots and the remaining empty ones, disregarding the dark blue rings at the moment, get added and filled up with zeros to form the extended system. The center Brillouin zone is the 1. BZ. If one now wishes to calculate the spectrum and weights in a Brillouin zone that is not the first one, for example in the one indicated by the tip of the red arrow in figure 12.9, then we rearrange the matrix in a way, that the 1. BZ information is centered around that Brillouin zone of interest. The matrix then consists of entries at positions indicated by the dark blue rings in figure 12.9 and zeros otherwise. This provides us with the most accurate spectrum information at this point, while the weights are calculated via (6.41) with respect to the center Brillouin zone of the extended system and the larger-than-BZ-dimension large \mathbf{k} vector. Moving the matrix elements without the embedding in an extended system leads to loss of information since some of the initial matrix elements are moved beyond the scope of that smaller matrix.

Having created this new matrix lets us employ (6.41) again to calculate the spectrum with the expected relative weight distribution for inelastic neutron scattering. Figure 12.10 shows these results for different relative orientations between nuclear Bragg peak \mathbf{G} , external magnetic field $\mathbf{H}_0^{\text{ext}}$ and probing momentum transfer \mathbf{k} . Whenever \mathbf{k} is in plane with the skyrmion lattice, then $\mathbf{k} \parallel \mathbf{Q}$.

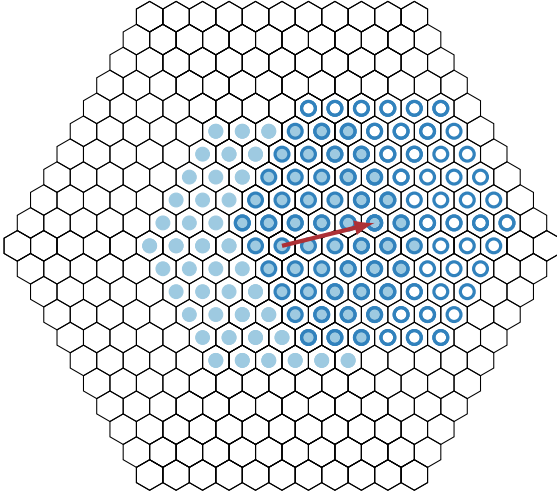
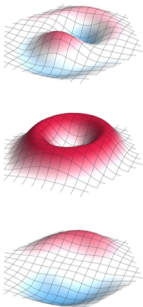


Figure 12.9: Schematic view of the momentum space matrix structure in the *extended system* whose elements are drawn as hexagonal shapes. Fourier modes of the *initial system* are centered around the 1. BZ. They are indicated by the light blue dots. When interested in the spectrum with neutron scattering weights it is necessary to move (red arrow) those entries to the BZ in focus. This new arrangement is indicated by the dark blue rings. For more information see text.

Panels (a) and (b) show the in-plane spectrum perpendicular to the external field. These two can be seen analogously to panels (a) and (c) of [figure 9.5](#), describing the helical phase, in terms of the relation between \mathbf{k} and \mathbf{G} . In the first, $\mathbf{k} \parallel \mathbf{G}$ and the middle helimagnon branch is not resolved and in the second the middle branch is measured and actually carries most of the weight. A similar trend is also observed in the skyrmion spectrum. There, one does not have three individual branches or modes that get excited but a large and dense amount of them. However, the weight distribution follows a similar pattern. Weights in [figure 12.10](#) (a) accumulate most dominantly on two curves similar to those two of the longitudinal helimagnon spectrum while, on the other hand, weights in [figure 12.10](#) (b) rather form more dominantly in the space in between, just like they do in [figure 9.5](#) (c). The weights in the spectrum for \mathbf{k} perpendicular to the \mathbf{Q} plane, panels (c) and (d) of [figure 12.10](#), also follow the trend evident in the corresponding helimagnon spectra.

The explanation for this is, at this point, a feature tracking argument. Starting with the magnon spectrum in the skyrmion phase along a \mathbf{Q} vector, [figures 12.7](#) and [12.10](#) (a) and (b), one notices flat bands that remind us of the flat bands observed in the longitudinal helimagnon spectrum for finite \mathbf{k}_\perp . Indeed, measuring along a \mathbf{Q} vector in the skyrmion plane leaves us with a multitude of parallel \mathbf{Q} vectors at different distances. It seems natural, that the skyrmion spectrum comprises hence of the superposition of a multitude of helimagnon spectra. One must, however, not only consider contributions of parallel helices but also those angled by 120° which then also add partial contributions of the perpendicular spectrum to the picture. Furthermore, all helices are distorted due to the finite magnetic field perpendicular to the helix pitches, a setup not considered in this



12. Spectrum

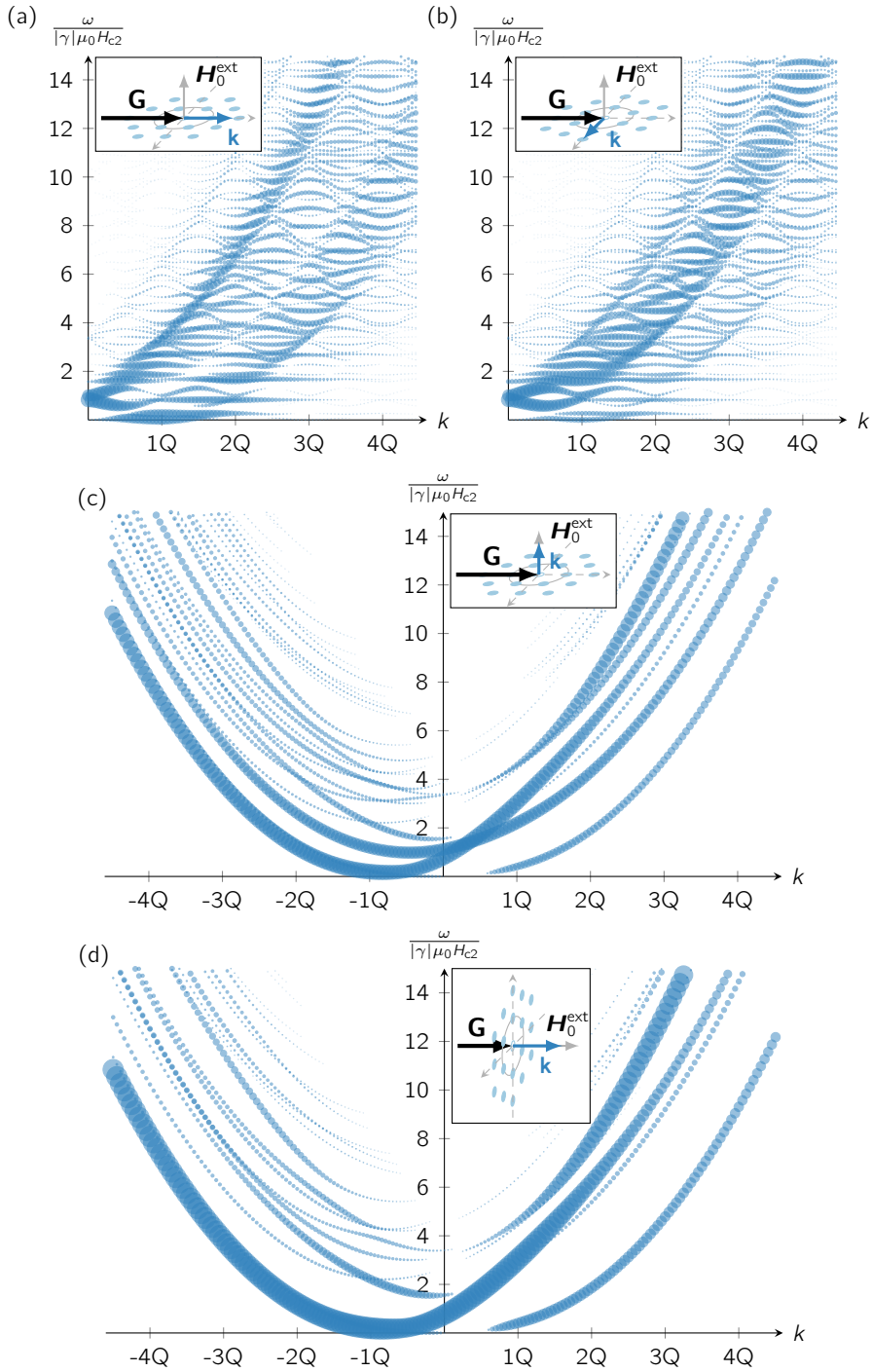


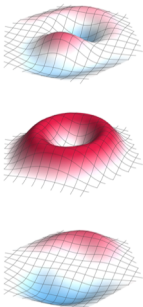
Figure 12.10: (*Caption to figure on previous page*) Magnon spectra in the skyrmion lattice phase for different orientations of nuclear Bragg peak \mathbf{G} , external magnetic field $\mathbf{H}_0^{\text{ext}}$ and probing momentum transfer \mathbf{k} . Whenever \mathbf{k} is in plane with the skyrmion lattice, then $\mathbf{k} \parallel \mathbf{Q}$. Panels (a) and (b) show the in-plane spectrum perpendicular to the external field. Additionally, these graphs are analogs to panels (a) and (c) of [figure 9.5](#) in terms of the relation between \mathbf{k} and \mathbf{G} , as well as panels (c) and (d) of this figure are analogs to panels (b) and (d) of [figure 9.5](#), respectively.

thesis. Because of this not yet controlled distortion it was not possible to achieve quantitative agreement but the uncanny resemblance motivates the drawn analogy.

EXPERIMENTS

There have already been inelastic neutron scattering experiments conducted to measure the magnon spectrum of the skyrmion lattice by our collaborators [140]. Their data are shown in [figure 12.11](#). Their setup was such as illustrated in the inset of [figure 12.10](#) (a). Qualitatively speaking, one can nicely see a two peak structure as we now would expect with the theory at hand and the given resolution.

In course of our collaborations, further experiments have been conducted by Marc Janoschek and David Fobes from the Los Alamos National Laboratory, as well as Maximilian Kugler from the TU Munich, with the goal to bring experiment and theory even closer together. As mentioned before, the theoretically predicted modes are very densely stacked and are unlikely to be resolved individually. This is the reason why the convolution with the resolution ellipsoid needs to be very precise to also obtain good quantitative agreement, which is current work in progress.



12. Spectrum

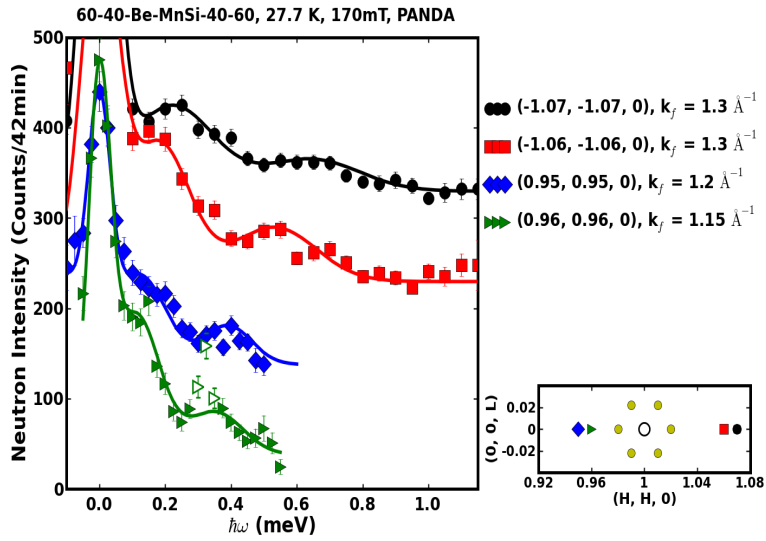


Figure 12.11: Magnon spectrum in the skyrmion lattice phase probed by inelastic neutron scattering [140].

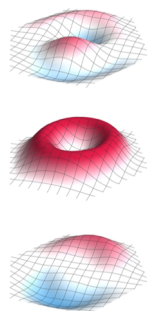
13

CHERN NUMBERS

In [section 2.2](#) we learned that skyrmions are topologically non-trivial objects. We also saw, that it is therefore possible to associate a winding number W given by [\(2.19\)](#) with their individual magnetic structure. This, of course, still remains when several of them are arranged in a lattice like they appear in chiral magnets. Since the lattice is trigonal, the shape of the first Brillouin zone is hexagonal. The winding number is then obtained by integration over this hexagonal shape where magnetization points parallel to the magnetic field on the rim and anti-parallel in the center.

It has also been shown, that the magnetic structure of skyrmions gives rise to an emergent electrodynamics whose derivation can be found in [\[80\]](#) and uses a technique outlined in [\[141\]](#). The intriguing insight is that each skyrmion carries a quantized amount of emergent flux, where the quantization is directly linked to the finite integer winding number. It is hence a consequence of the topology of the skyrmion and manifests itself, for example, in the topological Hall effect [\[142–144\]](#). Recent studies on single skyrmions have additionally shown, that magnons scatter off these emergent fields in a non-obvious way [\[145, 146\]](#). In particular, they skew scatter always either towards the left or right direction independent of the scattering parameter. The reason behind this is an effective Lorentz force due to the emergent flux of a skyrmion. A densely packed arrangement of many skyrmions, as is the hexagonal lattice, then suggests the prospect of a cyclotron motion. This and the already found topological ramifications motivate the search for non-zero Chern numbers for certain bands in the spectrum, in the former case similar to Landau levels for charged particles in a magnetic field.

This is the objective for this chapter and we start by following mostly [\[147\]](#) and [\[148\]](#) in the following section to provide a definition and some background for Chern numbers and their relation to Berry's phase, which we later use to compute Chern numbers for the energy bands.



13.1. DEFINITION AND MEANS OF CALCULATION

In recent decades, topology has become an undeniably important tool to understand many concepts in physics, that could otherwise not be explained, even providing the notion of topological order as a new classification of matter. Examples of topologically ordered states are 3D s-wave superconductors or integer quantum hall states. The latter occurs when electrons are confined to two dimensions and placed in a strong and perpendicular magnetic field. Quantization of the circular orbits of electrons with cyclotron frequency ω_c leads to so-called *Landau levels* [149], which are quantized to energies $E_n = \hbar\omega_c (n + \frac{1}{2})$. When the Fermi surface lies in a gap between these Landau levels then the state is similar to that of an insulator. But unlike in an ordinary insulator, an applied electric field causes the cyclotron orbits to drift leading to a Hall current which is characterized by a quantized Hall conductivity [150] $\sigma_H = \frac{e^2}{h}\nu$, where ν is known as the filling factor and our first example of a Chern number. In the context of Bloch band structures, it is also referred to as the TKNN invariant named after [150].

Mathematically, the concept of Chern numbers is rooted in the theory of fiber bundles. To be precise, Chern numbers are the result of a special case when studying more general topological invariants, Chern classes, associated with vector bundles on a smooth manifold. When considering an oriented two-dimensional manifold, then products of Chern classes can be integrated over that manifold to produce a number, the *Chern number*. Rigorous mathematical definitions, context and treatments can be found in [70]. Here, we want to focus on physical applications.

In topological band theory, a rather recent extension to the field of band theory that has existed since the foundation of quantum mechanics, a method has been developed to calculate Chern numbers of energy bands via the quantum mechanical *Berry phase*, also known as geometric or twist phase. The Berry phase is an additional phase factor, that a quantum system in an eigenstate acquires (next to the usual dynamical phase factor) when adiabatically transported along a path \mathcal{C} by varying parameters \mathbf{R} in its Hamiltonian $\mathcal{H}(\mathbf{R})$ [151]. A time dependent state $|\psi(t)\rangle$ of the system, evolving according to the Schrödinger equation

$$\mathcal{H}(\mathbf{R}(t))|\psi(t)\rangle = i\hbar\dot{|\psi(t)\rangle}, \quad (13.1)$$

is then given by

$$|\psi(t)\rangle = \exp\left(\frac{-i}{\hbar} \int_0^t E_n(\mathbf{R}(t')) dt'\right) \exp(i\gamma_n(t)) |n(\mathbf{R}(t))\rangle, \quad (13.2)$$

where $|n(\mathbf{R}(t))\rangle$ is an eigenstate of the Hamiltonian the system is prepared in. The first exponential is the dynamical phase factor and the second one contains Berry's phase γ_n . Using (13.1) one obtains the expression

$$\dot{\gamma}_n(t) = i\langle n(\mathbf{R}(t)) | \nabla_{\mathbf{R}} | n(\mathbf{R}(t)) \rangle \cdot \dot{\mathbf{R}}(t). \quad (13.3)$$

The explicit time dependence can be removed for closed loops \mathcal{C} after which the only thing needed is the dependence of the eigenstates on the parameters R_i :

$$\gamma_n(\mathcal{C}) = i \oint_{\mathcal{C}} \langle n(\mathbf{R}) | \nabla_{\mathbf{R}} | n(\mathbf{R}) \rangle d\mathbf{R} =: \oint_{\mathcal{C}} \mathbf{A}_n(\mathbf{R}) d\mathbf{R}, \quad (13.4)$$

where the last step defines the integrand as a Berry vector potential called *Berry connection* with components

$$\mathbf{A}_n^j(\mathbf{R}) = i \langle n(\mathbf{R}) | \nabla_{R_j} | n(\mathbf{R}) \rangle. \quad (13.5)$$

Note, that normalization of $|n(\mathbf{R})\rangle$ ensures that γ_n is real. Also, for closed loops, the Berry phase is gauge invariant¹ and independent of the specific form of how \mathbf{R} varies in time. It is, however, gauge dependent in general, but we will not consider this case here. For more details see [151, 148, 152]. The parameter space we are interested in is the three dimensional momentum space ($\mathbf{R} = \mathbf{q} = (q_1, q_2, q_3)$). One can apply Stokes Theorem to transform the closed line into a surface integral which gives

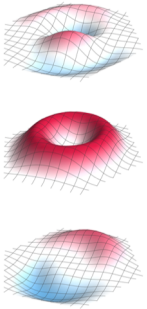
$$\begin{aligned} \gamma_n(\mathcal{C}) &= i \int d\mathbf{S} \cdot (\nabla_{\mathbf{R}} \times \langle n(\mathbf{R}) | \nabla_{\mathbf{R}} | n(\mathbf{R}) \rangle) \\ &= i \int d\mathbf{S} \cdot (\langle \nabla_{\mathbf{R}} n(\mathbf{R}) | \times | \nabla_{\mathbf{R}} n(\mathbf{R}) \rangle) \\ &= i \int dS_i \epsilon_{ijk} (\partial_j \langle n(\mathbf{R}) | \partial_k | n(\mathbf{R}) \rangle), \end{aligned} \quad (13.6)$$

where $d\mathbf{S}$ denotes an area element in \mathbf{R} space. We are interested in the integral over a two-dimensional Brillouin zone in the xy-plane implying $\mathbf{S} \parallel \hat{\mathbf{e}}_z$ leading to

$$\gamma_n(\mathcal{C}) = \int dq_x dq_y (\partial_{q_x} A_n^y(\mathbf{q}) - \partial_{q_y} A_n^x(\mathbf{q})). \quad (13.7)$$

The quantity $b_n^z(\mathbf{q}) := (\partial_{q_x} A_n^y(\mathbf{q}) - \partial_{q_y} A_n^x(\mathbf{q}))$ is called the *Berry curvature*. A two-dimensional Brillouin zone is topologically a torus. Integration over it corresponds to an integration over a closed surface also corresponding to a loop that is a point at which Stokes theorem is not automatically applicable anymore. A path that is a point describes a non-moving particle implying a vanishing Berry phase, which is tantamount to it being an integer multiple of 2π leading to the second phase factor in (13.2) to be unity. Which integer that is, is defined by the topology of the band and can be calculated. Barry Simon [153] provided the more rigorous mathematical interpretation of Berry's phase in terms of holonomy where (13.6) emerged naturally as the curvature of a Hermitean line bundle which

¹A gauge transformation $|n(\mathbf{R})\rangle \rightarrow e^{i\zeta(\mathbf{R})} |n(\mathbf{R})\rangle$ leads to a change of the Berry phase γ_n of $\zeta(\mathbf{R}(0)) - \zeta(\mathbf{R}(T))$, for a closed loop \mathcal{C} and where T is the time needed to cover it once. Because the basis state is then necessarily the same, this phase factor and change of the Berry phase needs to be a multiple of 2π .



13. Chern Numbers

equals to the first Chern class and is a topological invariant. The corresponding integer is given by

$$c_n = \frac{1}{2\pi} \int_{1. \text{ BZ}} dq_x dq_y b_n^z(\mathbf{q}) \in \mathbb{Z} \quad (13.8)$$

and is called the *Chern number*.

NUMERICAL IMPLEMENTATION

The recipe to calculate the Chern numbers for the magnon spectrum bands in the skyrmion phase are, in principle, straight forward: the eigenstates of the n^{th} band with energy ε_n are obtained by using (6.33), they give means to calculate the Berry connection needed to calculate the Berry curvature $b_n^z(\mathbf{q})$ which then needs to be integrated over the first Brillouin zone.

The first numerical challenge is to obtain an expression for the occurring derivatives. To achieve this, we discretized the first Brillouin zone by a square lattice with a lattice constant of $a = 0.01$ Q. Local derivatives of the eigenstates were then calculated at all points (q_x, q_y) for two directions in the xy-plane via

$$\nabla_{q_x} \mathbf{w}_n(q_x, q_y) = \frac{\mathbf{w}_n(q_x + \frac{a}{2}, q_y) - \mathbf{w}_n(q_x - \frac{a}{2}, q_y)}{a} \quad (13.9a)$$

$$\nabla_{q_y} \mathbf{w}_n(q_x, q_y) = \frac{\mathbf{w}_n(q_x, q_y + \frac{a}{2}) - \mathbf{w}_n(q_x, q_y - \frac{a}{2})}{a}. \quad (13.9b)$$

This brings us to the two expressions for the Berry connection

$$\mathcal{A}_n^x(q_x, q_y) = i \mathbf{w}_n(q_x, q_y) \cdot (\nabla_{q_x} \mathbf{w}_n(q_x, q_y)) \quad (13.10a)$$

$$\mathcal{A}_n^y(q_x, q_y) = i \mathbf{w}_n(q_x, q_y) \cdot (\nabla_{q_y} \mathbf{w}_n(q_x, q_y)) \quad (13.10b)$$

which we then interpolated to obtain a smooth function within the used Mathematica framework. This made the evaluation of the next derivatives, that are part of the Berry curvature $b_n^z(\mathbf{q})$, easier than an additional discretization. The function $b_n^z(\mathbf{q})$ can then, in principle, be plugged into (13.8) and integrated over the first Brillouin zone to obtain the Chern number for the n th band.

If one is lucky, then this readily works. But for most of the bands, one runs into unwanted singularities in $b_n^z(\mathbf{q})$. They are due to the fact, that the eigenstates are only determined up to a complex phase factor and this one does not behave in a smooth way because it is a degree of freedom that the computer may choose arbitrarily. In our case, the phase has finite sized jumps when following a path through the first Brillouin zone. This is shown for two typical components of an eigenstate \mathbf{w}_n in figure 13.1. The derivatives and discretizations then lead to uncontrolled points or even neighborhoods of points of $b_n^z(\mathbf{q})$ within the first Brillouin zone. To avoid this, it is common to employ a gauge-independent formula

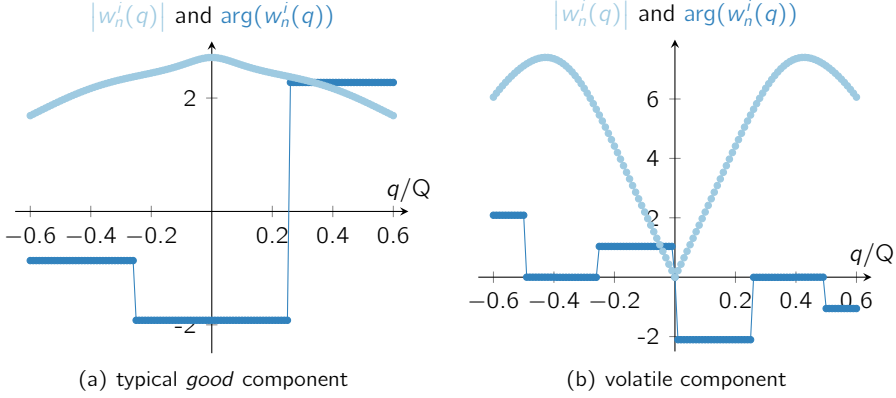


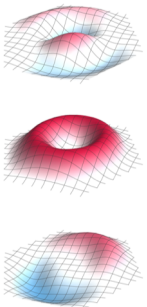
Figure 13.1: Typical absolute values and phase arguments of the i th component of the eigenstate $\mathbf{w}_n(\mathbf{q})$ of band n plotted on a path through the first Brillouin zone. It illustrates the discontinuous behavior of the phase argument. It is responsible for the singular behavior of the derivatives. For the smooth-gauging process it is also important be aware of the zero points of the absolute value. Panel (a) shows a typically directly usable behavior, while panel (b) does is not, as the absolute value becomes zero. For our chosen gauge process we need a partner component, that has zero points anywhere but in the center.

of the Berry phase given by [151]

$$\gamma_n = i \int_{\mathcal{C}} d\mathbf{S} \cdot \sum_{m \neq n} \frac{\langle n(\mathbf{R}) | (\nabla_{\mathbf{R}} \mathcal{H}(\mathbf{R})) | m(\mathbf{R}) \rangle \times \langle m(\mathbf{R}) | (\nabla_{\mathbf{R}} \mathcal{H}(\mathbf{R})) | n(\mathbf{R}) \rangle}{(E_m(\mathbf{R}) - E_n(\mathbf{R}))^2}. \quad (13.11)$$

This, however, comes at the price of evaluating an additional sum over potentially all bands, but at least those in a certain distance from each other since their contribution decreases with one over energy difference squared. For systems with just a few bands, this is very useful. In our case, the bands are relatively tightly packed and there are infinitely many. The latter makes this formula a constant approximation for our problem and the former introduces a significant amount of needed computation power.

We therefore smooth-gauge the resulting eigenstates \mathbf{w}_n semi-manually. The idea is to select one component of the eigenvectors and locally gauge it to be real and therefore smooth. The manual step is to find that i^{th} component $w_n^i(\mathbf{q})$. This can be done by tracing across the entire Brillouin zone and through the Γ -point, and search for components that do not reach an absolute value of zero. Allowing those points, too, would require to check whether it is a zero point of odd or even order, hence implying a sign change in the gauged real part or not. In either case one would then need to decide whether to implement a phase change of π at these points or not. To circumvent this problem, we do one of the two following things.



13. Chern Numbers

The first thing one can try is to search until one finds a component, that does not have a zero absolute value anywhere in the first Brillouin zone like the one shown in [figure 13.1\(a\)](#). Then we can modify the eigenstates locally so that the i^{th} component will be always real by multiplying the opposite phase of this component to it, i.e.,

$$\mathbf{w}_n(q_x, q_y) \rightarrow \mathbf{w}_n(q_x, q_y) e^{-i \arg(\mathbf{w}_n^i(q_x, q_y))}. \quad (13.12)$$

After that, the derivatives [\(13.9a\)](#) and [\(13.9b\)](#) will be smooth over the extent of the Brillouin zone. In case we do not find such a component, we consider two components, that have zero points, or rather zero point regions, at different positions. Usually, we can find one component with a zero point at the Γ -point, like the one shown in [figure 13.1\(b\)](#), and one with zeros at a distance of around $0.4Q$ from the Γ -point. This gives us two Berry curvatures that have singularities at different points in the Brillouin zone. Those can be patched together by only selecting the non singular sub-parts of each one, giving ultimately one smooth Berry curvature. This patch process gets more elaborate the higher the energy bands lie, then involving also a high number of patches. But once obtained, integration of the Berry curvature over the first Brillouin zone to calculate the Chern numbers is straight forward.

13.2. RESULTS

For the following discussion we refer to the spectrum in the first Brillouin zone with different dipolar interaction strengths shown in [figure 12.2](#), calculated Berry curvatures shown in [figures 13.2](#) and [13.3](#), and the Chern numbers resulting from the integration of the Berry curvatures from the previously mentioned figures shown in [figure 13.4](#) alongside the corresponding energy bands. We succeeded to obtain Chern numbers that are reliable from our current viewpoint for the first 14 bands with an increasing sequence that reads

$$\text{Chern number sequence} = 0 \ 0 \ 1 \ 0 \ 1 \ 1 \ 0 \ 1 \ 1 \ 1 \ 1 \ 1 \ 1 \ 1. \quad (13.13)$$

Challenges and problems before obtaining these results are explained in the following.

[Figure 13.2](#) shows Berry curvatures calculated for the first 14 bands of the magnon spectrum in the skyrmion lattice phase. One of the \mathbf{Q} -vectors is aligned with the x -direction. We mostly considered no dipolar interactions which worked fine for most of the bands. The same results are obtained with dipolar interaction included, as long as bands do not cut and hybridize, or change places hence changing the Chern number sequence. Problems first arise with bands 11 and 12. Without dipolar interaction, one can argue for a level crossing between these two bands seeing [figure 12.2\(a\)](#), although they do hybridize on a small scale. The result were uncontrolled poles ultimately leading non-integer and random Chern numbers. Random, for instance, upon a change in the discretization. To

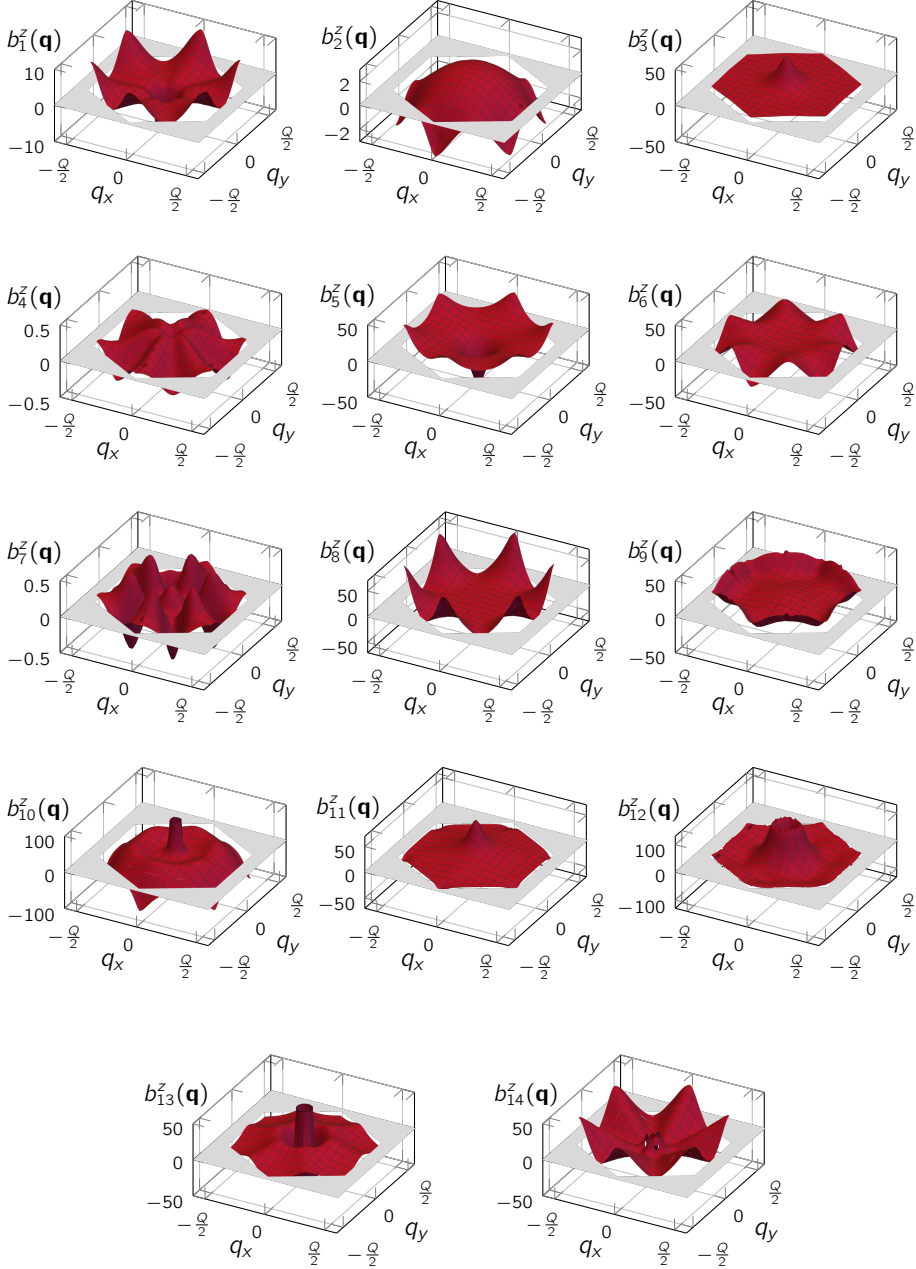
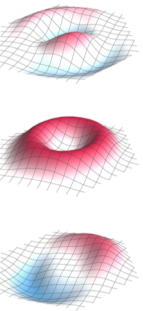


Figure 13.2: Berry curvatures of the first 14 bands of the skyrmion magnon spectrum without dipolar interaction as seen in figures 12.2(a) and 12.3. Note the individually different overall magnitudes. The feature at the center of b_{14}^z is the suppression of unwanted singularities that could not be cleaned up.



13. Chern Numbers

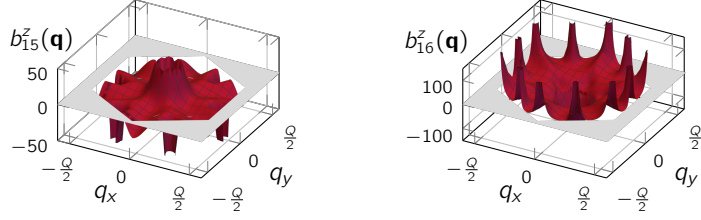


Figure 13.3: Berry curvatures of bands 15 and 16 of the skyrmion magnon spectrum without dipolar interaction as seen in figures 12.2(a) and 12.3. At this point reliability may not be given anymore. For further discussion, see the main text.

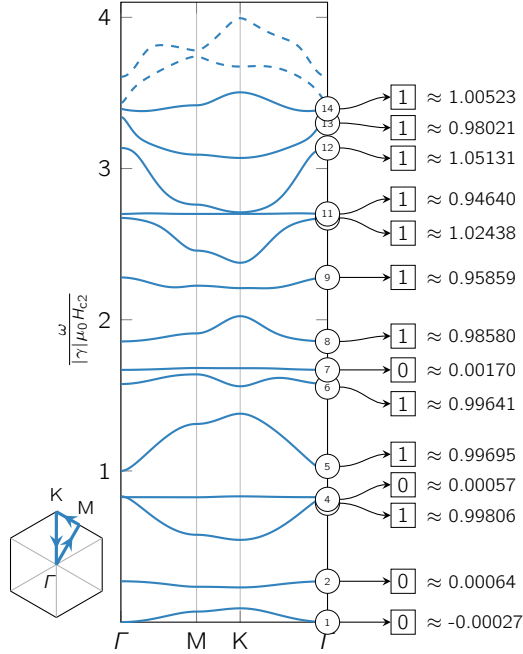


Figure 13.4: Shown is again the magnon band structure in the skyrmion lattice phase with dipolar interaction strength present in MnSi to inhibit crossings between the first 14 bands. The bands are successively numbered as indicated by encircled numbers. Chern numbers are listed in correspondence to each band and enclosed by squares. The approximate values are also given to their right hand side. Bands 15 and 16 are only shown by dashed lines to complement the spectrum. For them we failed to acquire reliable Chern numbers, see text.

circumvent this problem we included dipolar interaction of the strength present in MnSi, because that moves them apart just far enough so that they do not cross into other bands, cf. [figure 12.2\(b\)](#). Up to a little but benign inaccuracy in the center of $b_{14}^z(\mathbf{q})$ this gives us a quite large and reliable set of Berry curvatures.

Beyond the 14th band, the situation becomes more difficult because, for one, our numerical accuracy decreases. The two next bands in particular also seem to be arguably crossing when following their general slope, which makes an abrupt turn at the M-point of the Brillouin zone. This is reflected by poles at those points in the Berry curvatures, see [figure 13.3](#). Integrating them nevertheless results in an unusually large deviation from an integer number for the 15th band, namely $c_{15} \approx -2.2862$. These reasons lead to a word of caution regarding its reliability. A summary of the calculated Chern numbers together with their corresponding bands is given in [figure 13.4](#). There, we plotted the spectrum with the dipolar interaction strength of MnSi to separate bands 11 and 12.

The here calculated Chern numbers mostly agree with those found by Roldán-Molina et al. [154]. Their given sequence of the lowest Chern numbers reads 0,0,1,0,1,-2,3,1, see [figure 13.5](#). The first five are the same as ours. There are several reasons for the discrepancies of the remaining three. First of all, the studied systems are not exactly the same. The most noticeable difference is their use of a Dzyaloshinskii-Moriya interaction compatible with interfacial inversion symmetry breaking, which leads to the formation of Néel-skyrmions instead of the Bloch-type skyrmions that we considered. More subtle differences are the use of a discrete model with a finite and relatively small number of spins per unit cell opposed to the continuum theory we applied. They also employ a finite uniaxial anisotropy of the same order of magnitude as are the ferromagnetic exchange J and Dzyaloshinskii-Moriya interaction D . These reasons are most likely the reason for the discrepancies in the shape of

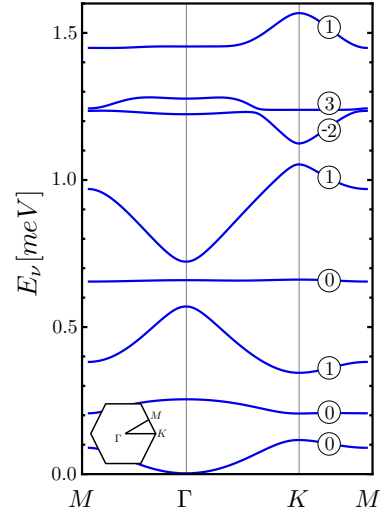
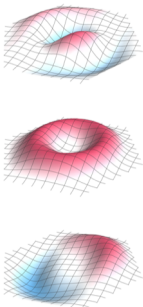


Figure 13.5: Spectrum and Chern numbers by Roldán-Molina et al. [154]

the bands between our two calculations, although the first 5 modes have very agreeable tendencies in terms of positions of maxima and minima. In our analysis of the effect of dipolar interactions on the spectrum in [figure 12.2](#) on page 124 we have seen that some modes are stronger influenced than others. It is hence very plausible that this is the case with the additional uniaxial anisotropy as well, which may have lead to a rearrangement of the modes. We also learned in our calculations, that the flat and dispersive modes 11 and 12 gave mixed results for the Chern numbers when they seemed to have been cutting through each



13. Chern Numbers

other, while giving integer values when separated, implying a “violation” of the adiabatic theorem or a much higher computation accuracy at and around these poles. Considering Roldán-Molina’s results in [figure 13.5](#), it can be argued that a similar effect takes place for bands 6 and 7 as they also get very close together and their slopes indicate that parts of the one mode may belong to the other and vice versa. With this in mind, one can argue that the sum of the Chern numbers of Roldán-Molina’s bands 6 and 7, which is one, only belongs to one of the bands while the other band carries zero Chern number. If that is indeed the case, then the Chern number sequences would agree perfectly. We also agree with chirality, i.e., the sign of D , not having an effect on the calculated Chern numbers.

Another noteworthy work that calculated Chern numbers in the context of a skyrmion lattice is [\[155\]](#). But there are two considerable differences to our setup. First, they do not consider a hexagonal but a quadratic skyrmion lattice hence changing the shape of the Brillouin zone. The biggest difference is that they calculate the electron band structure of a free-electron system coupled adiabatically to the background spin texture of a skyrmion. They find, that each band has a Chern number of -1 , which they argue is the same as that of Landau levels. They also state, that one can adiabatically pass from uniform magnetic field to the space-dependent magnetic field induced by skyrmion lattice without a singularity in this deformation

TRAJECTORIES

The presence of finite Chern numbers in the magnon and electron spectra form a promising basis in the search of closed orbits in the movement of electrons in the emergent magnetic field induced by the skyrmion lattice. With that in mind we considered the simplest model of a skyrmion lattice, namely the superposition of three helices with equal wavelength arranged to form a tripod with 120° angles between its legs, cf./ [figure 3.5](#). Choosing

$$\begin{aligned}\mathbf{Q}_1 &= (1, 0, 0)^\top \\ \mathbf{Q}_2 &= \left(-\frac{1}{2}, \frac{\sqrt{3}}{2}, 0\right)^\top \\ \mathbf{Q}_3 &= \left(-\frac{1}{2}, -\frac{\sqrt{3}}{2}, 0\right)^\top\end{aligned}$$

lets us obtain a relatively simple expression for the magnetization of the skyrmion

$$\mathbf{M}_{\text{sky}}(x, y) = \begin{pmatrix} -\frac{1}{\sqrt{3}} \cos\left(\frac{x}{2}\right) \sin\left(\frac{\sqrt{3}y}{2}\right) \\ \frac{1}{3} \sin\left(\frac{x}{2}\right) \left(2 \cos\left(\frac{x}{2}\right) + \cos\left(\frac{\sqrt{3}y}{2}\right)\right) \\ \frac{1}{12} \left(-8 \cos\left(\frac{x}{2}\right) \cos\left(\frac{\sqrt{3}y}{2}\right) - 4 \cos(x) + 3\right) \end{pmatrix}. \quad (13.14)$$

In the search for closed loops for electrons confined to two dimensions, we are interested in the local z -component of the emergent magnetic field $\mathbf{B}_z^e(x, y)$ which

is proportional to the integrand of the winding number W given by (2.19) [80, 144]. For a path-parameterization $\mathbf{r}(t) = (x(t), y(t))$ with $t \geq 0$ we obtain

$$\begin{aligned} \mathbf{B}_z^e(x(s), y(s)) &\propto \hat{\mathbf{M}}_{\text{sky}}(\mathbf{r}(s)) \cdot \left(\partial_x \hat{\mathbf{M}}_{\text{sky}}(\mathbf{r}(s)) \times \partial_y \hat{\mathbf{M}}_{\text{sky}}(\mathbf{r}(s)) \right) \propto \\ &\frac{\left(\frac{3}{2} - 2 \cos x \right) \cos(\sqrt{3}y) + 2 \cos \frac{x}{2} (3 \cos x - 8) \cos\left(\frac{\sqrt{3}y}{2}\right) - \frac{13}{2} \cos x - (\cos 2x + 9)}{\left(16 \cos\left(\frac{3x}{2}\right) \cos\left(\frac{1}{2}\sqrt{3}y\right) + 8 \cos(\sqrt{3}y) + 57 \right)^{3/2}} \end{aligned} \quad (13.15)$$

as an expression proportional to the emergent magnetic field, where we omitted the t dependence in the last line due to lack of space. The velocity \mathbf{v} dependent Lorentz force \mathbf{F} is given by

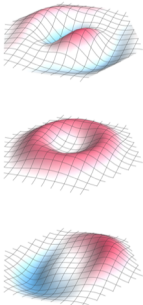
$$\mathbf{F} = q \mathbf{E}^e + q \mathbf{v} \times \mathbf{B}^e \quad (13.16)$$

$$\ddot{\mathbf{r}}(t) = -\dot{\mathbf{r}}(t) \times \mathbf{B}^e(\mathbf{r}(t)). \quad (13.17)$$

In the last line we have set $q = -1$ and the mass to unity. Since the magnetization is considered to be static, there is also no emergent electric field. We then solved this equation of motion numerically and simulated trajectories as shown in figure 13.6. There, we plot three electron trajectories with different initial conditions traversing a real space lattice of skyrmion which are represented by gray circles. The initial velocity is the same for all three, but the scattering parameter is different. The first one (dark blue) starts from the center of the central skyrmion, while the second (red) starts at a small distance away from the skyrmion center and the third one (light blue) two times that distance away from the center.

One can see, that a circular motion is in principle possible, but also that it is vulnerable to small changes in the initial conditions. That means, that a real skyrmion lattice makes it much harder to achieve perfectly closed loops due to further distortions, defects, possible domain formations etc. This issue becomes better when going to higher energies, i.e., higher initial speed, but the issue of rare and unstable, perfectly close loops remains. A more thorough analysis, also regarding relevant energy scales and therefore realized, initial velocities is still work in progress.

All this, however, offers a starting point for interesting future studies. Next steps could be to make a statistical analysis trying to find a general rule for the occurrence of closed loops. In the high energy regime, which can be treated classically, too, one could try to correlate the density of states of the classical problem to the quantum density of states of the spectrum like in the studies of Gutzwiller who found that the density of states for bound states only depends on such closed, classical orbits [156, 157].



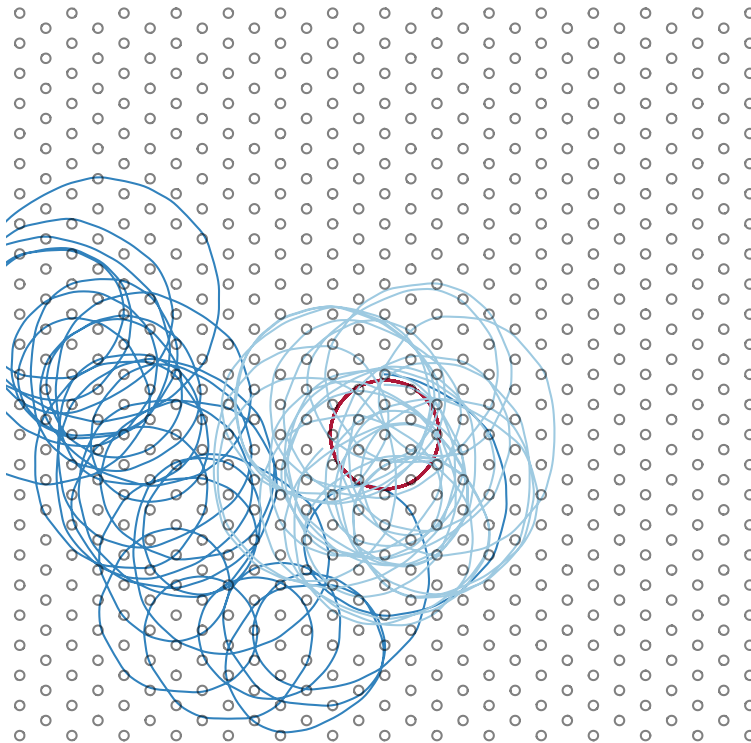


Figure 13.6: Possible trajectories of an electron in the effective magnetic field of a simple model skyrmion lattice. The basis is a skyrmion lattice constructed via the superposition of three helices of equal pitch forming a tripod with 120° angles and their real space positions are marked by gray circles. Shown are three different paths of particles that have the same initial velocity but slightly different scattering parameters. One can see that it is principally possible to obtain closed loops (red), although they might not be true circles. In any case, however, finding those closed loops can be hard as small variations in the initial can lead immediately to almost chaotic behavior (light and dark blue).

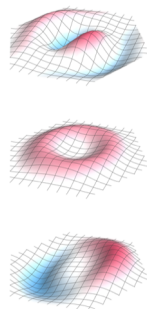
14

— CONCLUSIONS AND OUTLOOK —

Magnetically ordered structures in bulk chiral magnets played the leading role in our studies. We treated these phases on a mean-field level including Gaussian fluctuations and especially dipolar interaction with the aim to study their spin wave excitations. After introducing properties of chiral magnets and spin waves in general, we focused on two of these phases in more detail in [parts III](#) and [IV](#), respectively.

In [part III](#) we analyzed spin waves in a phase of spin spirals. Without an external magnetic field the spins form screws or helices where the spins are perpendicular to the pitch vector \mathbf{Q} . That pitch vector is aligned to certain high symmetry directions of the crystal. Which directions are chosen depends on the material. Applying a magnetic field eventually favors an alignment of those helices with the field. Also, the individual spins tilt in field direction forming a cone shape once the helix pitch is aligned with the magnetic field. In our models we usually assumed to be in that conical phase immediately once there is an applied field.

In our study of spin waves we differentiated between different regimes. First, we examined uniform excitations at the Γ -point and found two resonance modes called $+\mathbf{Q}$ and $-\mathbf{Q}$ that are degenerate when dipolar interactions are not considered. If they are considered, then the two modes split, unless in the special case when the static external field is applied perpendicular to an (infinite) disc. An interesting discovery was the truly linear polarization of those two modes at zero field, especially in a frequency range of a few GHz. The resonances could also be obtained analytically by using a non-linear σ model approach. The latter also gave us a clearer insights into the specifics of the remaining spectrum. Of the full spectrum $\omega(\mathbf{k})$ we particularly studied four sections. First the longitudinal spectrum $\omega(\mathbf{k}_{\parallel})$ with $\mathbf{k}_{\parallel} \parallel \mathbf{Q}$ and $0 = \mathbf{k}_{\perp} \perp \mathbf{Q}$ and second the perpendicular spectra $\omega(\mathbf{k}_{\perp})$ with $\mathbf{k}_{\perp} \perp \mathbf{Q}$. Both of them could also be understood analytically. The logical next step is to study a mixture of both which we did by considering the longitudinal spectrum after fixing \mathbf{k}_{\perp} to a finite value. There we discussed the formation of flat bands that are consequences of Bragg scattering. While these analyses all took place at zero, or at least a small magnetic field, we lastly also studied the influence of the magnetic field on the spectrum. Collaborators from different



14. Conclusions and Outlook

groups provided FMR and inelastic neutron scattering data, corresponding to the described cases, that agree very well with the theory.

Part IV concerns spin wave excitations in the skyrmion lattice phase. Skyrmions are topologically stable magnetic whirls that form perpendicular to an applied magnetic field and arrange themselves in a trigonal lattice. It can also be seen in first order as a superposition of three helices whose pitch vectors form a tripod with angles of 120° between them. Unlike the conical phase, they only occur in a small phase pocked at around $0.5 H_{c2}$ and close to T_c . H_{c2} is the critical field strength between the conical and the field polarized phase and T_c the critical temperature below which magnetic order sets in.

We first studied resonances at the Γ -point, too, where three modes can be excited by FMR experiments. They are two gyration modes whose cores precess clockwise and counter-clockwise around the applied field, and a breathing mode whose core grows and shrinks over time. The magnon spectrum in the skyrmion phase exhibits a plethora of modes, some flat and some dispersive. We studied the effect of dipolar interaction on the spectrum in the first Brillouin zone. The result was that dipolar interaction not only leads to a general decrease in the resonance energies, but also affects some modes more than others. We also re-analyzed the resonances at the Γ -point and presented and discussed some of the other modes, that were not excitable by FMR measurements. We also calculated spectral weights that correspond to inelastic neutron scattering experiments in the case of $\mathbf{k} \parallel \mathbf{Q}_i \perp \mathbf{H}_0^{\text{ext}}$, where \mathbf{Q}_i stands for one of the pitch vectors with which the skyrmion lattice can be constructed via a superposition, and for $\mathbf{k} \parallel \mathbf{H}_0^{\text{ext}} \perp \mathbf{Q}_i$. Despite the plethora of modes, we observed similar features as we did in the conical phase. Like in the conical case, collaborators performed successful experiments to measure the magnon spectrum in the skyrmion phase. Because the skyrmion case is much more elaborate conclusive quantitative agreement between neutron scattering data and theory is still work in progress. Finally, the topological nature of skyrmions and the fact that they carry finite flux quanta motivated us to calculate Chern numbers for the bands of the spectrum. We achieved to calculate the first 14 which took on values of zero or one.

OUTLOOK AND OPEN QUESTIONS

The helimagnon spectra and modes discussed in this thesis are already quite well understood. In terms of dipolar interaction, we considered only two approximative limits. The first was that of uniform excitation, i.e., $k \ll 1/L$ with sample size L , meaning that the exciting wavelength was basically infinite in regard to intrinsic length scales. Those were the modes accessible by FMR measurements. The second limit were local excitations, i.e., $k \gg 1/L$, accessible via inelastic neutron scattering. The next logical step is to study the intermediate regime where Damon Eshbach physics and surface modes come into play. This region is particularly interesting at the point of the first two finite resonances. Without dipolar interactions, it is merely a crossing point of the $+Q$ and $-Q$ branches. Including dipolar interactions opens up a gap at this point and the limit $\mathbf{k} \rightarrow 0$ is

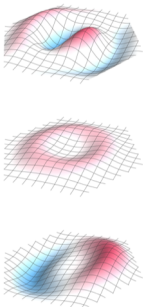
highly anisotropic. It also does not necessarily coincide with the corresponding resonance values of the limit of $k \ll 1/L$.

In the skyrmion case, there are even more unanswered questions and interesting possibilities for future studies. One of the natural questions is the question of theory verification. It would be nice to not only be able to see the average of the weight distribution of the modes, as is currently possible with neutron scattering, but also to resolve individual modes. Maybe further analysis of the modes that were not accessible via FMR reveals other possibilities, maybe excitation via a specially constructed, inhomogeneous magnetic field. Electrical excitation has been proposed, too, by coupling to the potentially finite polarization of the skyrmion [158, 93, 48]. However, because an oscillating electric field is accompanied by an oscillating magnetic one and since the resonances of electrical excitation are much weaker than the magnetic ones, it was so far not possible to resolve electrically excited modes without being overshadowed by the magnetic resonances.

Another big open question is the exact origin of the Chern numbers and why some bands have Chern number zero and others Chern number one. Besides asking for their origin, it is also still an open problem to determine the exact consequences that non-zero Chern numbers have for the skyrmion lattice. Analogously to topological insulators, where finite Chern numbers lead to edge states, one can take a look at boundary and surface modes. This also brings us back to a follow-up question already asked in the conical phase, i.e., what happens when the limit $\mathbf{k} \rightarrow 0$ is not unique? This questions applies to the gyration and breathing modes, like it did for the $+Q$ and $-Q$ modes in the conical phase.

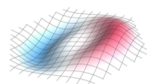
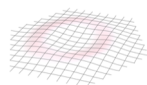
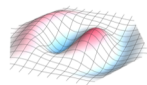
The next step into the future consists of device constructions. An optimistic projection would be to exploit the magnetic linear dichroism found in the helical phase to construct polarization filters, or to save energy since such a system is easier to excite.

All these points show that helices and skyrmions have many exciting aspects, but also that a number of interesting questions remain to be answered.



PART V.

APPENDIX





DERIVATION OF DIPOLE-DIPOLE INTERACTION

This derivation is mostly taken from [93]. The major difference is the definition of the Fourier transform, which introduces additional factors of $\frac{1}{\nu}$ (cf. (3.8)).

Since its origin are the microscopic magnetic moments, the magnetic field \mathbf{H}_s due to the spins themselves depends on the distribution of the magnetization \mathbf{M} . The magnetic induction is $\mathbf{B} = \mu_0(\alpha\mathbf{H}_s + \mathbf{M})$, which suggest the application of Maxwell's equations to establish a relation between the two entities \mathbf{M} and \mathbf{H}_s .

$$\nabla \cdot \mathbf{B} = \mu_0 \nabla \cdot (\alpha \mathbf{H}_s + \mathbf{M}) \stackrel{!}{=} 0 \quad \text{and} \quad \nabla \times \mathbf{H}_s = 0 \quad (\text{A.1})$$

The uncommon factor α is a remnant of unit rescaling as introduced in section 3.5. One can toggle between the physical and rescaled units in the following calculation by setting $\alpha = 1$ for physical units and $\alpha = JQ^2$ in the rescaled case. The Fourier representations of magnetization $\mathbf{M}(\mathbf{r})$ and $\mathbf{H}_s(\mathbf{r})$ are

$$\mathbf{M}(\mathbf{r}) = \frac{1}{\nu} \sum_{\mathbf{k}} \mathbf{m}_{\mathbf{k}} e^{i\mathbf{k} \cdot \mathbf{r}} \quad \text{and} \quad \mathbf{H}_s(\mathbf{r}) = \frac{1}{\nu} \sum_{\mathbf{k}} \mathbf{h}_{s,\mathbf{k}} e^{i\mathbf{k} \cdot \mathbf{r}}$$

Fourier transforming the second equation of (A.1) fixes the direction of $\mathbf{h}_{s,\mathbf{k}}$.

$$\begin{aligned} \nabla \times \mathbf{H}_s &= \frac{1}{\nu} \sum_{\mathbf{k}} (i\mathbf{k} \times \mathbf{h}_{s,\mathbf{k}}) e^{i\mathbf{k} \cdot \mathbf{r}} \stackrel{!}{=} 0 \\ \hookrightarrow \mathbf{k} &\parallel \mathbf{h}_{s,\mathbf{k}} \end{aligned} \quad (\text{A.2})$$

The Fourier transformed spin field $\mathbf{h}_{s,\mathbf{k}}$ is hence, up to a complex phase $\phi_{\mathbf{k}}$ with $|\phi_{\mathbf{k}}| = 1$, parallel to \mathbf{k} ¹. This means that one can write

$$\mathbf{h}_{s,\mathbf{k}} = |\mathbf{h}_{s,\mathbf{k}}| \phi_{\mathbf{k}} \hat{\mathbf{k}} \quad (\text{A.3})$$

¹The fact, that the requirement of a global phase is enough is not completely trivial but can be seen by proving the statement: $0 = \epsilon_{\alpha\beta\gamma} k_{\beta} h_{\mathbf{k},\gamma} \Leftrightarrow \exists c_{\mathbf{k}} \in \mathbb{C} : k_{\alpha} = c_{\mathbf{k}} h_{\mathbf{k},\alpha} \forall \alpha$.

A. Derivation of Dipole-Dipole Interaction

with $\hat{\mathbf{k}} = \frac{\mathbf{k}}{|\mathbf{k}|}$. Continuing with the first equation of (A.1) gives

$$\nabla \cdot \mathbf{M}(\mathbf{r}) = \frac{1}{\nu} \sum_{\mathbf{k}} (\mathbf{m}_{\mathbf{k}} \cdot i\mathbf{k}) e^{i\mathbf{k} \cdot \mathbf{r}} \stackrel{!}{=} -\alpha \nabla \cdot \mathbf{H}_s = -\frac{\alpha}{\nu} \sum_{\mathbf{k}} (\mathbf{h}_{s,\mathbf{k}} \cdot i\mathbf{k}) e^{i\mathbf{k} \cdot \mathbf{r}}. \quad (\text{A.4})$$

Comparing coefficients leads to

$$\begin{aligned} \mathbf{m}_{\mathbf{k}} \cdot \mathbf{k} &= -\alpha \mathbf{h}_{s,\mathbf{k}} \cdot \mathbf{k} \stackrel{(\text{A.2})}{=} -\phi_{\mathbf{k}} \alpha |\mathbf{h}_{s,\mathbf{k}}| |\mathbf{k}| \\ \curvearrowright |\mathbf{h}_{s,\mathbf{k}}| &= -\frac{1}{\alpha \phi_{\mathbf{k}}} \frac{(\mathbf{m}_{\mathbf{k}} \cdot \mathbf{k})}{|\mathbf{k}|} \\ \stackrel{(\text{A.3})}{\curvearrowright} \mathbf{h}_{s,\mathbf{k}} &= -\frac{1}{\alpha} \frac{(\mathbf{m}_{\mathbf{k}} \cdot \mathbf{k})}{|\mathbf{k}|} \hat{\mathbf{k}} \\ \curvearrowright \mathbf{H}_s(\mathbf{r}) &= -\frac{1}{\alpha} \frac{1}{\nu} \sum_{\mathbf{k}} \frac{(\mathbf{m}_{\mathbf{k}} \cdot \mathbf{k})}{|\mathbf{k}|} \hat{\mathbf{k}} e^{i\mathbf{k} \cdot \mathbf{r}} \end{aligned} \quad (\text{A.5})$$

Because \mathbf{H}_s is an additional component to the internal magnetic field, an additional term F_{DD} in the free energy needs to arise with the property $\frac{\delta F_{\text{DD}}}{\delta \mathbf{M}} = -\mu_0 \mathbf{H}_s$ or, in Fourier representation, $\frac{\delta F_{\text{DD}}}{\delta \mathbf{m}} = -\mu_0 \mathbf{h}_s$. A first guess is

$$\begin{aligned} -\mu_0 \int d^3r \mathbf{M} \cdot \mathbf{H}_s &= -\frac{\mu_0}{\alpha} \int d^3r \left(\frac{1}{\nu} \sum_{\mathbf{k}} \mathbf{m}_{\mathbf{k}} e^{i\mathbf{k} \cdot \mathbf{r}} \right) \cdot \left(\frac{1}{\nu} \sum_{\mathbf{k}'} \mathbf{h}_{s,\mathbf{k}'} e^{i\mathbf{k}' \cdot \mathbf{r}} \right) \\ &= \frac{\mu_0}{\alpha} \frac{1}{\nu} \sum_{\mathbf{k} \mathbf{k}'} \mathbf{m}_{\mathbf{k}} \cdot \frac{(\mathbf{m}_{\mathbf{k}'} \cdot \mathbf{k}')}{|\mathbf{k}|^2} \mathbf{k}' \underbrace{\frac{1}{\nu} \int d^3r e^{i(\mathbf{k}+\mathbf{k}') \cdot \mathbf{r}}}_{\delta_{\mathbf{k}', -\mathbf{k}}} \\ &= \frac{\mu_0}{\alpha} \frac{1}{\nu} \sum_{\mathbf{k}} \frac{(\mathbf{m}_{\mathbf{k}} \cdot \mathbf{k})(\mathbf{m}_{-\mathbf{k}} \cdot \mathbf{k})}{|\mathbf{k}|^2} \end{aligned} \quad (\text{A.6})$$

To substantiate this guess, it is good to differentiate (A.6) with respect to the i th component of $\mathbf{m}_{-\mathbf{k}}$.

$$\begin{aligned} -\mu_0 \frac{\partial \int d^3r \mathbf{M} \cdot \mathbf{H}_s}{\partial m_{-\mathbf{k}}^i} &= \frac{\mu_0}{\alpha} \frac{1}{\nu} \frac{\partial}{\partial m_{-\mathbf{k}}^i} \sum_{\mathbf{k}'} \frac{(\mathbf{m}_{\mathbf{k}'} \cdot \mathbf{k}')(\mathbf{m}_{-\mathbf{k}'} \cdot \mathbf{k}')}{|\mathbf{k}'|^2} \\ &= \frac{\mu_0}{\alpha} \frac{1}{\nu} \left[\frac{\partial}{\partial m_{-\mathbf{k}}^i} \left(\frac{(\mathbf{m}_{\mathbf{k}} \cdot \mathbf{k})(\mathbf{m}_{-\mathbf{k}} \cdot \mathbf{k})}{|\mathbf{k}|^2} \right) \right. \\ &\quad \left. + \frac{\partial}{\partial m_{-\mathbf{k}}^i} \left(\frac{(\mathbf{m}_{-\mathbf{k}} \cdot (-\mathbf{k})(\mathbf{m}_{\mathbf{k}} \cdot (-\mathbf{k}))}{|-\mathbf{k}|^2} \right) \right] \\ &= \frac{\mu_0}{\alpha} \frac{1}{\nu} \frac{\mathbf{m}_{\mathbf{k}} \cdot \mathbf{k}}{|\mathbf{k}|^2} q^i = \mu_0 \frac{2}{\alpha} h_{s,\mathbf{k}}^i \end{aligned} \quad (\text{A.7})$$

To obtain the right contribution to the free energy, we just need to compensate the additional factor of 2 in our initial formula leading to

$$F_{\text{DD}, \mathbf{k} \gg 1/L}[\mathbf{m}] = \frac{1}{2} \frac{\mu_0}{\alpha} \frac{1}{\nu} \sum_{\mathbf{k}} \frac{(\mathbf{m}_{\mathbf{k}} \cdot \mathbf{k})(\mathbf{m}_{-\mathbf{k}} \cdot \mathbf{k})}{|\mathbf{k}|^2}$$

B

GROUND STATE ON MEAN-FIELD LEVEL

This extract is almost an exact copy of subsection 1.4.1 of [93] and serves to complement the argument that the helical phase minimizes the free energy $F_0[\mathbf{M}]$ (cf. (3.36) and (3.37)) on a mean-field level. Here, the rescaled units of section 3.5 are used and the tildes omitted.

To prove, that the helical/conical phase represents the global minimum, let us consider the Fourier transformation of $\mathbf{M}(\mathbf{r})$ defined by (3.8), which is allowed due to translation invariance of $F_0[\mathbf{M}]$ [80]. Plugging this transformation into the free energy, (3.37) can be written as a sum of a constant term plus several quadratic terms [7]:

$$\begin{aligned} \frac{F_0}{\kappa} = & -\frac{1}{\nu} \frac{t^2 - \mu_0^2 (\mathbf{H}^{\text{ext}})^2}{4} + \frac{1}{\nu} \sum_{\mathbf{k} \neq 0} \mathbf{m}_{-\mathbf{k}}^\alpha [r^{\alpha\beta}(\mathbf{k}) - t \delta^{\alpha\beta}] \mathbf{m}_{\mathbf{k}}^\beta \\ & + \int \left(\mathbf{M}^2 + \frac{t}{2} \right)^2 d\mathbf{r} + \frac{1}{\nu} \left(M_0 - \frac{\mu_0 \mathbf{H}^{\text{ext}}}{2} \right)^2 \end{aligned} \quad (\text{B.1})$$

The system volume is given by ν and $r^{\alpha\beta} = (1 + t + k^2)\delta^{\alpha\beta} - 2i\epsilon^{\alpha\beta\gamma}k^\gamma$. The two terms on the far right in (B.1) are obviously greater or equal to zero. The eigenvalues of the matrix $[r^{\alpha\beta}(\mathbf{k}) - t\delta^{\alpha\beta}]$ are $\{1 + k^2, (1 - k)^2, (1 + k)^2\}$, which makes it positive semi-definite. As a result, the free energy is bounded from below by the constant $-\frac{\kappa}{\nu}(t^2 - \mu_0^2(\mathbf{H}^{\text{ext}})^2)/4$.

To get a first, simple idea of the representation of the structure and parameter relations, let us consider a helical ansatz for the magnetization in the mean-field limit.

$$\mathbf{M}_{\text{hel}}(\mathbf{r}) = \begin{pmatrix} A \cos(\mathbf{Q} \cdot \mathbf{r}) \\ A \sin(\mathbf{Q} \cdot \mathbf{r}) \\ M_0 \end{pmatrix} = \begin{pmatrix} A \cos(Qz) \\ A \sin(Qz) \\ M_0 \end{pmatrix} \quad (\text{B.2})$$

We choose here, as a simplification, the propagation direction of the helix $\mathbf{Q} = Q\hat{\mathbf{e}}_z$ to be parallel to $\hat{\mathbf{e}}_z$, which in turn is also the direction of a static external magnetic

B. Ground State on Mean-Field Level

field $\mathbf{H}^{\text{ext}} = \{0, 0, H_z\}$. Plugging (B.2) into (3.37) and minimizing with respect to Q , A and M_0 yields the solution:

$$Q = 1 \quad A^2 = -M_0^2 - \frac{t}{2} \quad M_0 = \frac{1}{2}\mu_0 H_z \quad (\text{B.3})$$

One can see, that this solution effectively minimizes the free energy as it puts all quadratic terms of (B.1) simultaneously to zero.

Through a combination of the equations in (B.3) and setting A to zero, one obtains the boundary of the phase transition between the conical and the field polarized phase as

$$H_{c2} = \sqrt{-2t}.$$

Notably, the zero-field phase transition is at $t = 0$.

Before we go into more detail and study the effect of demagnetization factors in the mean-field limit, it is worthwhile to elaborate on the previous calculation in a new basis, that accommodates the twist in the magnetic structure. While \hat{e}_x , \hat{e}_y and \hat{e}_z are the ordinary Cartesian unit vectors, the new basis has the form

$$\hat{e}_z = \hat{e}_z, \quad \hat{e}^{\pm} = \frac{\hat{e}_x \pm i\hat{e}_y}{\sqrt{2}} \quad \text{or} \quad \hat{e}_x = \frac{\hat{e}^+ + \hat{e}^-}{\sqrt{2}}, \quad \hat{e}_y = \frac{\hat{e}^+ - \hat{e}^-}{i\sqrt{2}} \quad (\text{B.4})$$

We further assumed that the pitch of the helix, as well as the magnetic field, point in \hat{e}_z -direction. In this new basis, we can formulate an ansatz for the magnetization in the mean-field limit as follows.

$$\mathbf{M}_{\text{hel}}(\mathbf{r}) = M_0 \hat{e}_z + A \hat{e}^- e^{i\mathbf{Q}\mathbf{r}} + A^* \hat{e}^+ e^{-i\mathbf{Q}\mathbf{r}} \quad (\text{B.5})$$

Here, A is a complex amplitude of the helix and M_0 the homogeneous component in direction of the applied magnetic field. One may note, that this ansatz is still valid even while considering dipole-dipole interaction. Since $\mathbf{k} \perp \mathbf{M}_{\mathbf{k}}$, no dipole fields arise. Using this ansatz in the free energy (3.35), which now only consists of the contributions F_0 and F_{DD} , which are respectively defined by (3.37) and (3.26), we obtain an expression for the energy density $f = f_0 + f_{\text{DD}}$, i.e., the integrand of the free energy functional, in terms of the new basis and the rescaled units:

$$f = (t+1) \left(M_0^2 + 2|A|^2 \right) + 2Q^2|A|^2 - 4Q|A|^2 + \left(M_0^2 + 2|A|^2 \right)^2 - \mu_0 H_z M_0 + \frac{1}{2} \frac{\mu_0}{\alpha} \bar{N} M_0^2 \quad (\text{B.6})$$

We have introduced \bar{N} as the demagnetization factor “pointing along” the magnetic field direction $\bar{N} = \hat{\mathbf{H}}^{\text{ext}} \cdot \underline{\bar{N}} \cdot \hat{\mathbf{H}}^{\text{ext}}$. A field $\mathbf{H}^{\text{ext}} \parallel \hat{e}_z$ would mean $\bar{N} = N_z$. Differentiation with respect to Q leads to $Q = 1$, which concurs with the rescaling

of units. Minimizing (B.6) with respect to M_0 and A^* gives two equations of states.

$$\left(2(t+1) + \frac{\mu_0}{\alpha} \bar{N}\right) M_0 + 4 \left(M_0^2 + 2|A|^2\right) M_0 = \mu_0 H_z \quad (\text{B.7a})$$

$$2tA + 4 \left(M_0^2 + 2|A|^2\right) A = 0 \quad (\text{B.7b})$$

Being in the conical/helical phase implies a finite helix amplitude. Assuming hence a finite A and combining both equations of (B.7) yields an expression for the homogeneous component of the magnetization. To avoid confusion in the following, we have reintroduced the tilde to indicate rescaled quantities.

$$\tilde{M}_0 = \frac{\mu_0 \tilde{H}_z}{2 + \frac{\mu_0}{\alpha} \bar{N}} \quad (\text{B.8})$$

It is noteworthy, that \tilde{M}_0 does not depend on temperature to first order, which leads to an also temperature independent susceptibility ($\tilde{\chi}_{\text{con}} = \tilde{M}_0 / \tilde{H}_z$) in the conical phase

$$\tilde{\chi}_{\text{con}} = \frac{\mu_0}{2 + \frac{\mu_0}{\alpha} \bar{N}} \quad (\text{B.9})$$

This makes the susceptibility indeed nearly constant in the conical phase, as has been measured by Bauer *et al.* [21]. The measured susceptibility however is expressed by the susceptibility χ_{con} calculated analogously in the not rescaled units used of (3.35). The relation amongst each other is given by

$$\chi_{\text{con}} = \frac{1}{\alpha} \tilde{\chi}_{\text{con}} = \frac{\mu_0}{2JQ^2 + \mu_0 \bar{N}} \quad (\text{B.10})$$

Combining this relation and (B.9) provides us with a concrete value for the thus far unfixed pre-factor α in terms of measurable quantities.

$$\frac{\mu_0}{\alpha} = \frac{2}{\chi_{\text{con}}^{-1} - \bar{N}} \quad (\text{B.11})$$

For the helix amplitude we obtain via (B.7b) and (B.8) the expression

$$|A|^2 = -\frac{t}{4} - \frac{1}{2} \left(\frac{\mu_0 \tilde{H}_z}{2 + \frac{\mu_0}{\alpha} \bar{N}} \right)^2 \quad (\text{B.12})$$

A finite helix amplitude is given as long as \tilde{H}_z is smaller than a critical field \tilde{H}_{c2} , for which the relation

$$0 = -\frac{t}{2} - \left(\frac{\mu_0 \tilde{H}_{c2}}{2 + \frac{\mu_0}{\alpha} \bar{N}} \right)^2 \quad (\text{B.13})$$

holds. The helix amplitude can then also be expressed in terms of the critical field H_{c2}

$$|A|^2 = \frac{\tilde{\chi}_{\text{con}}^2}{2} (\tilde{H}_{c2}^2 - \tilde{H}_z^2) \quad (\text{B.14})$$



FMR WITH DAMPING

This is a calculation that describes magnetic resonance of a ferromagnet in a magnetic field $\mathbf{B}_0^{\text{ext}} = \mu_0 \mathbf{H}_0^{\text{ext}}$ with shape and cubic anisotropies and including damping via the Landau-Lifshitz-Gilbert equation. An energy density is given by

$$\mathcal{H} = \frac{\mu_0}{2} \mathbf{M} \cdot \underline{N} \cdot \mathbf{M} + \frac{K}{M_s^4} (M_x^4 + M_y^4 + M_z^4) - \mathbf{B}_0^{\text{ext}} \cdot \mathbf{M}. \quad (\text{C.1})$$

Note that $K = K'_1 = \frac{K_1}{2}$ in terms of Gurevich's notation [89]. M_s is the saturation magnetization making the anisotropy constant of units J/m³. The equation of motion is given by

$$\frac{d\mathbf{M}}{dt} = \gamma \mathbf{M} \times \mathbf{B}^{\text{eff}} + \frac{\alpha}{M_s} \mathbf{M} \times \frac{d\mathbf{M}}{dt}. \quad (\text{C.2})$$

Two coordinate systems are used, namely $\hat{\mathbf{e}}_x, \hat{\mathbf{e}}_y, \hat{\mathbf{e}}_z$ represent axes aligned with the principal axes of the sample and $\hat{\mathbf{e}}_x^a, \hat{\mathbf{e}}_y^a, \hat{\mathbf{e}}_z^a$ represent the crystallographic axes.

Setup: External magnetic field always points along the same (principal) axis $\hat{\mathbf{e}}_z$ of the sample so that the demagnetization tensor is diagonal. However, two cases arise due to cubic anisotropies. In the first one $\mathbf{B}_0^{\text{ext}} \parallel [001]$ and in the second $\mathbf{B}_0^{\text{ext}} \parallel [111]$.

FIRST CASE: $\mathbf{B} \parallel [001]$

The $\hat{\mathbf{e}}_x$ -axis and the $\hat{\mathbf{e}}_x^a$ -axis differ from each other by a $\pi/4$ rotation around $\hat{\mathbf{e}}_z = \hat{\mathbf{e}}_z^a$. We hence rotate the (diagonal) demagnetization tensor \underline{N} around the $\hat{\mathbf{e}}_z$ -axis by $\pi/4$ and obtain

$$\underline{N}_{\text{rot}} = \begin{pmatrix} \frac{N_1}{2} + \frac{N_y}{2} & -\frac{N_1}{2} + \frac{N_y}{2} & 0 \\ -\frac{N_1}{2} + \frac{N_y}{2} & \frac{N_1}{2} + \frac{N_y}{2} & 0 \\ 0 & 0 & N_z \end{pmatrix} \quad (\text{C.3})$$

C. Complex Resonances in the Ferromagnet

The effective magnetic field is given by

$$\mathbf{B}^{\text{eff}} = -\frac{\partial \mathcal{H}}{\partial \mathbf{M}} = \begin{pmatrix} 0 \\ 0 \\ B_0^{\text{ext}} \end{pmatrix} - \mu_0 \underline{N}_{\text{rot}} \cdot \mathbf{M} - 4 \frac{K}{M_s^4} \begin{pmatrix} M_x^3 \\ M_y^3 \\ M_z^3 \end{pmatrix} \quad (\text{C.4})$$

Plugging this into the equation of motion, and expanding up to first order with $\mathbf{M} = \mathbf{M}_s + \delta \mathbf{M}(t)$ leads to $\mathbf{B}^{\text{eff}} = \mathbf{B}' + \mathbf{B}'' + \mathcal{O}(\delta \mathbf{M}^2)$ with

$$\mathbf{B}' = \begin{pmatrix} 0 \\ 0 \\ B_0^{\text{ext}} \end{pmatrix} - \mu_0 \underline{N}_{\text{rot}} \cdot \begin{pmatrix} 0 \\ 0 \\ M_s \end{pmatrix} - \frac{4K}{M_s^4} \begin{pmatrix} 0 \\ 0 \\ M_s^3 \end{pmatrix} \quad (\text{C.5})$$

$$\mathbf{B}'' = -\mu_0 \underline{N}_{\text{rot}} \cdot \begin{pmatrix} \delta M_x \\ \delta M_y \\ \delta M_z \end{pmatrix} - \frac{4K}{M_s^4} \begin{pmatrix} 0 \\ 0 \\ 3M_s^2 \delta M_z \end{pmatrix} \quad (\text{C.6})$$

Plugging this expansion into the Fourier transformed equation of motion (C.2), keeping only terms up to first order and collecting all terms on one side yields

$$\begin{aligned} \mathbf{v}_0 := i\omega \begin{pmatrix} \delta M_x \\ \delta M_y \\ \delta M_z \end{pmatrix} + \gamma \left[\begin{pmatrix} \delta M_x \\ \delta M_y \\ \delta M_z \end{pmatrix} \times \mathbf{B}' + \begin{pmatrix} 0 \\ 0 \\ M_s \end{pmatrix} \times \mathbf{B}'' - \frac{\alpha i\omega}{\gamma M_s} \begin{pmatrix} 0 \\ 0 \\ M_s \end{pmatrix} \times \begin{pmatrix} \delta M_x \\ \delta M_y \\ \delta M_z \end{pmatrix} \right] \\ = 0 \end{aligned} \quad (\text{C.7})$$

$$(\text{C.8})$$

For \mathbf{v}_0 to be zero, the determinant of \mathcal{W} , given by

$$\mathcal{W} = \begin{pmatrix} \partial_{\delta M_x} \mathbf{v}_{0,x} & \partial_{\delta M_y} \mathbf{v}_{0,x} & \partial_{\delta M_z} \mathbf{v}_{0,x} \\ \partial_{\delta M_x} \mathbf{v}_{0,y} & \partial_{\delta M_y} \mathbf{v}_{0,y} & \partial_{\delta M_z} \mathbf{v}_{0,y} \\ \partial_{\delta M_x} \mathbf{v}_{0,z} & \partial_{\delta M_y} \mathbf{v}_{0,z} & \partial_{\delta M_z} \mathbf{v}_{0,z} \end{pmatrix}, \quad (\text{C.9})$$

needs to be zero since $\mathcal{W} \cdot \delta \mathbf{M} = 0$ has to hold for all $\delta \mathbf{M}$. Solving $\det \mathcal{W} = 0$ for ω and only keeping terms up to first order in α leads to three solutions with one being $\omega = 0$ and the other two are equal up to a sign change of the ω_{res} part. The positive solution is given by

$$\begin{aligned} \omega_1 = \omega_{\text{res},1} + i\Gamma \\ = |\gamma| \sqrt{\left(4 \frac{K}{M_s} - (B_0^{\text{ext}} + \mu_0 M_s (N_x - N_z)) \right) \left(4 \frac{K}{M_s} - (B_0^{\text{ext}} + \mu_0 M_s (N_y - N_z)) \right)} \\ - i\gamma \left(4 \frac{K}{M_s} - \left(B_0^{\text{ext}} + \frac{\mu_0 M_s}{2} (N_x + N_y - 2N_z) \right) \right) \alpha. \end{aligned} \quad (\text{C.10})$$

SECOND CASE: $\mathbf{B} \parallel [1\ 1\ 1]$

Again, we need to rotate the demagnetization tensor in a way, that it concurs with the crystallographic direction. This is achieved by rotating the shape coordinate system away from the crystal system, first with a rotation of $\arccos \frac{1}{\sqrt{3}}$ around the $\hat{\mathbf{e}}_x^a$ -axis, followed by a $\pi/4$ rotation around the $\hat{\mathbf{e}}_z^a$ -axis, i.e. the former $\hat{\mathbf{e}}_z$ -axis. Then, the crystallographic $[1\ 1\ 1]$ direction points along the $\hat{\mathbf{e}}_z$ -direction of the sample and the oscillating field component of the corresponding experiment, cf. [figure 4.4](#), along the $\hat{\mathbf{e}}_x$ -axis points along the crystallographic $[\bar{1}\ \bar{1}\ 0]$ direction. The rotated demagnetization tensor takes the form

$$\underline{N}_{\text{rot}} = \begin{pmatrix} \frac{1}{6}(3N_x + N_y + 2N_z) & \frac{1}{6}(-3N_x + N_y + 2N_z) & \frac{1}{3}(-N_y + N_z) \\ \frac{1}{6}(-3N_x + N_y + 2N_z) & \frac{1}{6}(3N_x + N_y + 2N_z) & \frac{1}{3}(-N_y + N_z) \\ \frac{1}{3}(-N_y + N_z) & \frac{1}{3}(-N_y + N_z) & \frac{1}{3}(2N_y + N_z) \end{pmatrix} \quad (\text{C.11})$$

after a rotation via

$$\mathcal{M}_{\text{rot}} = \begin{pmatrix} \frac{1}{\sqrt{2}} & \frac{1}{\sqrt{6}} & \frac{1}{\sqrt{3}} \\ -\frac{1}{\sqrt{2}} & \frac{1}{\sqrt{6}} & \frac{1}{\sqrt{3}} \\ 0 & -\sqrt{\frac{2}{3}} & \frac{1}{\sqrt{3}} \end{pmatrix}. \quad (\text{C.12})$$

Employing the same scheme as above leads to

$$\mathbf{B}' = \frac{1}{\sqrt{3}} \begin{pmatrix} B^{\text{ext}} \\ B^{\text{ext}} \\ B^{\text{ext}} \end{pmatrix} - \mu_0 \underline{N}_{\text{rot}} \cdot \begin{pmatrix} M_s \\ M_s \\ M_s \end{pmatrix} \frac{1}{\sqrt{3}} - \frac{4K}{(\sqrt{3})^3 M_s^4} \begin{pmatrix} M_s^3 \\ M_s^3 \\ M_s^3 \end{pmatrix} \quad (\text{C.13})$$

$$\mathbf{B}'' = -\mu_0 \underline{N}_{\text{rot}} \cdot \begin{pmatrix} m_x \\ m_y \\ m_z \end{pmatrix} - \frac{4K}{(\sqrt{3})^2 M_s^4} \begin{pmatrix} 3M_s^2 m_x \\ 3M_s^2 m_y \\ 3M_s^2 m_z \end{pmatrix} \quad (\text{C.14})$$

$$\mathbf{v}_0 := i\omega \begin{pmatrix} \delta M_x \\ \delta M_y \\ \delta M_z \end{pmatrix} + \gamma \left[\begin{pmatrix} \delta M_x \\ \delta M_y \\ \delta M_z \end{pmatrix} \times \mathbf{B}' + \frac{1}{\sqrt{3}} \begin{pmatrix} M_s \\ M_s \\ M_s \end{pmatrix} \times \mathbf{B}'' - \frac{\alpha}{\gamma M_s \sqrt{3}} \begin{pmatrix} M_s \\ M_s \\ M_s \end{pmatrix} \times \begin{pmatrix} \delta M_x \\ \delta M_y \\ \delta M_z \end{pmatrix} \right] \quad (\text{C.15})$$

Rand ultimately to the resonance formula for $\mathbf{B}^{\text{ext}} \parallel [1\ 1\ 1]$

$$\begin{aligned} \omega_2 &= \omega_{\text{res},2} + i\Gamma \\ &= |\gamma| \sqrt{\left(\frac{8}{3} \frac{K}{M_s} + (B^{\text{ext}} + \mu_0 M_s (N_x - N_z)) \right) \left(\frac{8}{3} \frac{K}{M_s} + (B^{\text{ext}} + \mu_0 M_s (N_y - N_z)) \right)} \\ &\quad + i\gamma \left(\frac{8}{3} \frac{K}{M_s} + \left(B^{\text{ext}} + \frac{\mu_0 M_s}{2} (N_x + N_y - 2N_z) \right) \right) \alpha \end{aligned} \quad (\text{C.16})$$

D

AUXILIARY CALCULATIONS IN THE NON-LINEAR σ MODEL

D.1. DERIVATION OF EQUATION (8.7)

The goal is to obtain the Landau-Lifshitz equation $\partial_t \mathbf{M} = \gamma \mathbf{M} \times \mathbf{B}^{\text{eff}}$ as a result of the Euler-Lagrange equations

$$\frac{\partial \mathcal{L}}{\partial \hat{n}_i} - \partial_t \frac{\partial \mathcal{L}}{\partial (\partial_t \hat{n}_i)} = 0 \quad (\text{D.1})$$

with \mathcal{L} as defined by (8.2) in the main text. To make things clearer, we directly collect the contributions of \mathcal{F}_{ex} and \mathcal{F}_{dip} in a single term with an effective magnetic field $-M \hat{\mathbf{n}} \cdot (\mu_0 \mathbf{H}^{\text{eff}})$. This makes

$$\mathcal{L} = -\frac{M}{\gamma} \mathbf{A}(\hat{\mathbf{n}}) \partial_t \hat{\mathbf{n}} + M \hat{\mathbf{n}} \cdot \mathbf{B}^{\text{eff}}. \quad (\text{D.2})$$

Plugging (D.2) into $\hat{\mathbf{n}} \times (\text{D.1})$ and using the Einstein summation convention gives

$$0 = \frac{M}{\gamma} \left(\epsilon_{ijk} \hat{n}_j \frac{\partial A_l}{\partial \hat{n}_i} (\partial_t \hat{n}_l) - \epsilon_{ijk} \hat{n}_j (\partial_t A_j) \right) - M \epsilon_{ijk} \hat{n}_j B_k^{\text{eff}}. \quad (\text{D.3})$$

Requiring $\epsilon_{ijk} \frac{\partial A_j}{\partial \hat{n}_i} = \hat{n}_k \Leftrightarrow \frac{\partial A_j}{\partial \hat{n}_i} = \frac{1}{2} \epsilon_{ijk} \hat{n}_k + \text{sym}_{ij}$ for the gauge potential \mathbf{A} , where sym_{ij} is a general symmetric part, lets us rewrite

$$\begin{aligned} \frac{\partial A_l}{\partial \hat{n}_k} &= \frac{1}{2} \epsilon_{klm} \hat{n}_m + \text{sym}_{kl} \quad \text{and} \\ \frac{\partial A_j}{\partial t} &= \frac{\partial A_j}{\partial \hat{n}_\alpha} \frac{\partial \hat{n}_\alpha}{\partial t} = \frac{1}{2} \epsilon_{\alpha k \beta} \hat{n}_\beta \frac{\partial \hat{n}_\alpha}{\partial t} + \text{sym}_{\alpha j} \frac{\partial \hat{n}_\alpha}{\partial t} \end{aligned}$$

D. Auxiliary Calculations in the non-linear σ model

of the first and second term in the large parentheses, respectively, and we obtain

$$\begin{aligned}
0 &= \frac{M}{\gamma} \left(\frac{1}{2} \epsilon_{kij} \epsilon_{klm} \hat{n}_j \hat{n}_m (\partial_t \hat{n}_l) - \frac{1}{2} \epsilon_{kij} \epsilon_{k\beta\alpha} \hat{n}_j \hat{n}_\beta (\partial_t \hat{n}_\alpha) \right) - M \epsilon_{ijk} \hat{n}_j B_k^{\text{eff}} \\
&\quad + \frac{M}{\gamma} \left(\epsilon_{kij} \hat{n}_j \text{sym}_{kl} (\partial_t \hat{n}_l) - \epsilon_{kij} \hat{n}_j \text{sym}_{\alpha j} (\partial_t \hat{n}_\alpha) \right) \\
&= \frac{M}{\gamma} (\epsilon_{kij} \epsilon_{klm} \hat{n}_j \hat{n}_m \partial_t \hat{n}_l) - M \epsilon_{ijk} \hat{n}_j B_k^{\text{eff}}
\end{aligned} \tag{D.4}$$

To get to the last line we renamed $\alpha \rightarrow l$ and $\beta \rightarrow m$ making the two terms in the first parentheses equal so they can be added. The terms in the second parentheses cancel each other because $\text{sym}_{ij} = \text{sym}_{ji}$. Using $\epsilon_{kij} \epsilon_{klm} = \delta_{il} \delta_{jm} - \delta_{im} \delta_{jl}$ we arrive at

$$0 = \frac{M}{\gamma} \left((\partial_t \hat{n}_i) \underbrace{\hat{n}^2}_{=1} - \hat{n}_i \underbrace{(\hat{n}_m \partial_t \hat{n}_m)}_{=0, \text{ since } \partial_t \hat{\mathbf{n}} \perp \hat{\mathbf{n}}} \right) - M \epsilon_{ijk} \hat{n}_j B_k^{\text{eff}} \tag{D.5}$$

Rewritten in vector notation gives

$$\curvearrowright \partial_t (M \hat{\mathbf{n}}) = \gamma (M \hat{\mathbf{n}}) \times \mathbf{B}^{\text{eff}} \tag{D.6}$$

$$\partial_t \mathbf{M} = \gamma \mathbf{M} \times \mathbf{B}^{\text{eff}} \tag{D.7}$$

D.2. IDENTITIES FOR CHIRAL BASIS VECTORS

A list of identities and relations between vectors defined in [section 8.2](#).

$$\hat{n}_{\text{helix}}^2 = \hat{e}_1^2 = \hat{e}_2^2 = 1 \quad \hat{n}_{\text{helix}} \cdot \hat{e}_1 = \hat{n}_{\text{helix}} \cdot \hat{e}_2 = \hat{e}_1 \cdot \hat{e}_2 = 0$$

$$\hat{e}_+^2 = \hat{e}_-^2 = 0 \quad \hat{e}_+ \cdot \hat{e}_- = 1 \quad \hat{n}_{\text{helix}} \cdot \hat{e}_\pm = 0$$

$$\begin{aligned}
\hat{e}_1 \times \hat{e}_2 &= \hat{n}_{\text{helix}} & \nabla \times \hat{e}_1 &= -Q \hat{e}_1 \\
\hat{e}_+ \times \hat{e}_- &= -i \hat{n}_{\text{helix}} & \nabla \times \hat{e}_2 &= \frac{Q}{\tan \theta} \mathbf{n}_\perp \\
\hat{e}_\pm \times \hat{e}_\pm &= 0 & \nabla \times \hat{n}_{\text{helix}} &= -Q \mathbf{n}_\perp \\
\hat{n}_{\text{helix}} \times \hat{e}_+ &= -i \hat{e}_+ & \nabla \times \hat{e}_+ &= -Q \hat{e}_+ + i \frac{Q \tan \theta}{\sqrt{2}} \mathbf{n}_\parallel \\
\hat{n}_{\text{helix}} \times \hat{e}_- &= i \hat{e}_- & \nabla \times \hat{e}_- &= -Q \hat{e}_- - i \frac{Q \tan \theta}{\sqrt{2}} \mathbf{n}_\parallel \\
\mathbf{n}_\perp \cdot \hat{e}_\pm &= \mp \frac{i \cos \theta}{\sqrt{2}} & & \\
\mathbf{n}_\parallel \cdot \hat{e}_\pm &= \pm \frac{i \sin \theta}{\sqrt{2}} & &
\end{aligned}$$

$$\begin{aligned}
 (\partial_z \hat{\mathbf{n}}_{\text{helix}}) \cdot \hat{\mathbf{n}}_{\text{helix}} &= 0 & \nabla^2 \hat{\mathbf{n}}_{\text{helix}} &= -Q^2 \mathbf{n}_{\perp} \\
 (\partial_z \hat{\mathbf{e}}_{\pm}) \cdot \hat{\mathbf{e}}_{\pm} &= 0 & \nabla^2 \hat{\mathbf{e}}_1 &= -Q^2 \hat{\mathbf{e}}_1 \\
 (\partial_z \hat{\mathbf{e}}_{\pm}) \cdot \hat{\mathbf{e}}_{\mp} &= \mp iQ \cos \theta & \nabla^2 \hat{\mathbf{e}}_2 &= \frac{Q^2}{\tan \theta} \mathbf{n}_{\perp} \\
 (\partial_z \hat{\mathbf{e}}_{\pm}) \cdot \hat{\mathbf{n}}_{\text{helix}} &= -\frac{Q \sin \theta}{\sqrt{2}} & \nabla^2 \hat{\mathbf{e}}_{\pm} &= -Q^2 \hat{\mathbf{e}}_{\pm} \pm iQ^2 \frac{\tan \theta}{\sqrt{2}} \mathbf{n}_{\parallel}
 \end{aligned}$$

D.3. \mathcal{F}_{EX} EXPANSION TO 4TH ORDER

The part of the Lagrangian density in the discussed non-linear σ model was given by (8.4) in the main text as

$$\mathcal{F}_{\text{ex}} = \frac{\rho_s}{2} [\hat{\mathbf{n}} (-\nabla^2) \hat{\mathbf{n}} + 2Q \hat{\mathbf{n}} \cdot (\nabla \times \hat{\mathbf{n}})] - \mu_0 M \hat{\mathbf{n}} \cdot \mathbf{H}^{\text{ext}}. \quad (\text{D.8})$$

Here, we go a step further and state all expansion terms of \mathcal{F}_{ex} up to first order. Further expansion of $\hat{\mathbf{n}}$ in terms of $\boldsymbol{\pi}$ or $\boldsymbol{\psi}$ are needed

$$\hat{\mathbf{n}} \approx \hat{\mathbf{n}}_{\text{helix}} \left(1 - \frac{\boldsymbol{\pi}^2}{2} - \frac{(\boldsymbol{\pi}^2)^2}{8} \right) + \hat{\mathbf{e}}_1 \pi_1 + \hat{\mathbf{e}}_2 \pi_2 \quad (\text{D.9})$$

$$\approx \hat{\mathbf{n}}_{\text{helix}} \left(1 - \frac{g\mu_B}{M} |\psi|^2 - \frac{\left(\frac{g\mu_B}{M} |\psi|^2 \right)^2}{2} \right) + \sqrt{\frac{g\mu_B}{M}} (\psi \hat{\mathbf{e}}_+ + \psi^* \hat{\mathbf{e}}_-). \quad (\text{D.10})$$

Plugging these expansions into (D.8) and keeping terms up to fourth order yields the following contributions.

ZEROth ORDER

The static part is given by

$$\mathcal{F}_{\text{ex}}^{(0)} = -\frac{\rho_s Q^2}{2} \sin^2 \theta - M \mu_0 H_0^{\text{ext}} \cos \theta. \quad (\text{D.11})$$

LINEAR ORDER

Although one might expect a completely vanishing term due to a mean-field calculation, a finite term is obtained

$$\begin{aligned}
 \mathcal{F}_{\text{ex}}^{(1)} &= \underbrace{(+\rho_s Q^2 \cos \theta - M \mu_0 H_0^{\text{ext}})}_{\rightarrow 0} \sin \theta \\
 &\quad + \rho_s Q \left[(\partial_x, \partial_y) \cdot \begin{pmatrix} \cos(Qz) & -\sin(Qz) \\ \sin(Qz) & \cos(Qz) \end{pmatrix} \cdot \begin{pmatrix} \pi_1 \cos \theta \\ \pi_2 \end{pmatrix} \right]
 \end{aligned} \quad (\text{D.12})$$

$$\mathcal{F}_{\text{ex}}^{(1)'} = \rho_s Q \left[(\partial_x, \partial_y) \cdot (\cos(Qz) 1 - i \sin(Qz) \tau^y) \cdot \begin{pmatrix} \pi_1 \cos \theta \\ \pi_2 \end{pmatrix} \right]. \quad (\text{D.13})$$

D. Auxiliary Calculations in the non-linear σ model

The first term vanished due to the mean-field equation of state when combining with the remaining term of the dipolar contribution. The second term remains but only generates surface term of the corresponding action, which can be rewritten in terms of Pauli matrices τ^i to allow an easier conversion to the formulation in terms of ψ :

$$\mathcal{F}_{\text{ex}}^{(1)'} = \rho_s Q \sqrt{\frac{g\mu_B}{M}} \left[\left(R \cdot \begin{pmatrix} \partial_x \\ \partial_y \end{pmatrix} \right)^\dagger \cdot (\cos(Qz)1 + i \sin(Qz)\tau^z) \cdot \left(\frac{1 + \tau^x}{2} \cos \theta + \frac{1 - \tau^x}{2} \right) \cdot \begin{pmatrix} \psi \\ \psi^* \end{pmatrix} \right]. \quad (\text{D.14})$$

QUADRATIC ORDER

$$\mathcal{F}_{\text{ex}}^{(2)} = \pi_\alpha \left[\left(\frac{M}{2} \mu_0 H_0^{\text{ext}} \cos \theta - \frac{\rho_s}{2} \nabla^2 \right) 1_{\alpha\beta} - \frac{\rho_s Q^2}{2} \begin{pmatrix} \cos^2 \theta & 0 \\ 0 & \cos(2\theta) \end{pmatrix}_{\alpha\beta} - i \rho_s Q \sin \theta \left(\cos(Qz) \partial_x + \sin(Qz) \partial_y \right) \tau_{\alpha\beta}^y \right] \pi_\beta \quad (\text{D.15})$$

where τ^y is the second Pauli-matrix and Einstein summation convention has been used. Using again the identities for the Pauli matrices (8.26) let us obtain the ψ representation.

$$\mathcal{F}_{\text{ex}}^{(2)} = \frac{1}{2} \frac{g\mu_B}{M} \psi^\dagger \left[(M \mu_0 H_0^{\text{ext}} \cos \theta - \rho_s \nabla^2) 1 - \frac{\rho_s Q^2}{2} ((1 + \tau^x) \cos^2 \theta + (1 - \tau^x) \cos(2\theta)) + i 2 \rho_s Q \sin \theta \left(\cos(Qz) \partial_x + \sin(Qz) \partial_y \right) \tau^z \right] \psi \quad (\text{D.16})$$

This expression can be simplified further by rewriting $\cos(2\theta) = \cos^2 \theta - \sin^2 \theta$ and using the equation of state to eliminate the terms proportional to $\cos \theta$ and $\cos^2 \theta$. Again, to use the equation of state, one also includes the “left over term” of the dipolar contribution, i.e., (8.35) at this point.

With \mathbf{n}_\perp as defined in (8.20) we get

$$\mathcal{F}_{\text{ex}}^{(2)'} = \frac{\rho_s}{2} \frac{g\mu_B}{M} \psi^\dagger \left[-1 \nabla^2 + \frac{Q^2 \sin^2 \theta}{2} (1 - \tau^x) + i 2 Q \tau^z \mathbf{n}_\perp(\mathbf{r}) \cdot \nabla \right] \psi. \quad (\text{D.17})$$

By defining $\mathcal{E}_0 = g\mu_B Q^2 \rho_s / M = g\mu_B \mu_0 H_{c2}^{\text{int}}$ using definitions in (8.16), the pre-factor can be summarized to $\frac{\rho_s}{2} \frac{g\mu_B}{M} = \frac{1}{2} \frac{\mathcal{E}_0}{Q^2}$.

CUBIC ORDER

$$\begin{aligned}
 \mathcal{F}_{\text{ex}}^{(3)} = & -\frac{1}{4}\rho_s Q^2 \sin(2\theta) \boldsymbol{\pi}^2 \pi_2 \\
 & + \frac{1}{4}\rho_s Q \left[\pi_1^2 \left(-2 \cos(Qz) [\partial_y \pi_2 - \cos \theta \partial_x \pi_1] + 2 \sin(Qz) [\cos \theta \partial_y \pi_1 + \partial_x \pi_2] \right) \right. \\
 & \quad \left. + \pi_2^2 \left(+2 \cos(Qz) [\partial_y \pi_2 - \cos \theta \partial_x \pi_1] - 2 \sin(Qz) [\cos \theta \partial_y \pi_1 + \partial_x \pi_2] \right) \right. \\
 & \quad \left. + 2\pi_1 \pi_2 \left(2 \sin(Qz) [\cos \theta \partial_y \pi_2 - \partial_x \pi_1] + 2 \cos(Qz) [\partial_y \pi_1 + \cos \theta \partial_x \pi_2] \right) \right] \\
 & \hspace{15em} \text{(D.18)}
 \end{aligned}$$

$$\begin{aligned}
 = & -\frac{1}{4}\rho_s Q^2 \sin(2\theta) \boldsymbol{\pi}^2 \pi_2 \\
 & + \frac{1}{2}\rho_s Q \left[\pi_1^2 \left(-\cos(Qz) [\partial_y \pi_2 - \cos \theta \partial_x \pi_1] + \sin(Qz) [\cos \theta \partial_y \pi_1 + \partial_x \pi_2] \right) \right. \\
 & \quad \left. + \pi_2^2 \left(+\cos(Qz) [\partial_y \pi_2 - \cos \theta \partial_x \pi_1] - \sin(Qz) [\cos \theta \partial_y \pi_1 + \partial_x \pi_2] \right) \right. \\
 & \quad \left. + \pi_1 \pi_2 \left(\sin(Qz) [2 \cos \theta \partial_y \pi_2 - 2 \partial_x \pi_1] + \cos(Qz) [2 \partial_y \pi_1 + 2 \cos \theta \partial_x \pi_2] \right) \right] \\
 & \hspace{15em} \text{(D.19)}
 \end{aligned}$$

Partial integration, i.e. $\pi_1^2(\partial_i \pi_2) \rightarrow -(\partial_i \pi_1^2) \pi_2 = -2\pi_1 \pi_2 (\partial_i \pi_1)$ leads to

$$\begin{aligned}
 \mathcal{F}_{\text{ex}}^{(3)} = & -\frac{1}{4}\rho_s Q^2 \sin(2\theta) \boldsymbol{\pi}^2 \pi_2 \\
 & + \frac{1}{2}\rho_s Q \left[\cos(Qz) \cos \theta [\pi_1^2 \partial_x \pi_1 + \pi_2^2 \partial_y \pi_2] + \sin(Qz) \cos \theta [\pi_1^2 \partial_y \pi_1 - \pi_2^2 \partial_x \pi_2] \right. \\
 & \quad \left. + 4 \sin(Qz) [\cos \theta \pi_1 \pi_2 \partial_y \pi_2 - \pi_1 \pi_2 \partial_x \pi_1] + 4 \cos(Qz) [\pi_1 \pi_2 \partial_y \pi_1 + \cos \theta \pi_1 \pi_2 \partial_x \pi_2] \right] \\
 & \hspace{15em} \text{(D.20)}
 \end{aligned}$$

In the case of a pure helix, i.e. $\hat{\mathbf{n}}_{\text{helix}} \perp \mathbf{Q}_{\text{helix}}$ the angle $\theta = \frac{\pi}{2} \Rightarrow \cos \theta = 0$. Hence, the above expression simplifies significantly to

$$\begin{aligned}
 \mathcal{L}_0^{(3)}(\theta = \frac{\pi}{2}) = & -\frac{1}{4}\rho_s Q^2 \sin(2\theta) \boldsymbol{\pi}^2 \pi_2 - 2\rho_s Q \pi_1 \pi_2 [\sin(Qz) \partial_x - \cos(Qz) \partial_y] \pi_1 \\
 = & \frac{1}{4}\rho_s Q^2 \sin(2\theta) \boldsymbol{\pi}^2 \pi_2 - 2\rho_s Q \pi_1 \pi_2 (\hat{\mathbf{e}}_1 \cdot \nabla) \pi_1 \\
 & \hspace{15em} \text{(D.21)}
 \end{aligned}$$

D. Auxiliary Calculations in the non-linear σ model

QUARTIC ORDER

$$\begin{aligned} \mathcal{F}_{\text{ex}}^{(4)} = & \frac{1}{8} \left[(-2\rho_s Q^2 \sin^2 \theta - M\mu_0 H_0^{\text{ext}} \cos \theta) (\boldsymbol{\pi}^2)^2 \right. \\ & - 4\rho_s \left(2\pi_1^2 ((\partial_x \pi_1)^2 + (\partial_y \pi_1)^2 + (\partial_z \pi_1)^2) + \pi_1^2 ((\partial_x \pi_2)^2 + (\partial_y \pi_2)^2 + (\partial_z \pi_2)^2) \right. \\ & + 2\pi_2^2 ((\partial_x \pi_2)^2 + (\partial_y \pi_2)^2 + (\partial_z \pi_2)^2) + \pi_2^2 ((\partial_x \pi_1)^2 + (\partial_y \pi_1)^2 + (\partial_z \pi_1)^2) \\ & + 2\pi_1 \pi_2 \pi_1^2 ((\partial_x \pi_1)(\partial_x \pi_2) + (\partial_y \pi_1)(\partial_y \pi_2) + (\partial_z \pi_1)(\partial_z \pi_2)) \\ & + \pi_1^2 \pi_2 (\partial_x^2 \pi_2 + \partial_y^2 \pi_2 + \partial_z^2 \pi_2) + \pi_1 \pi_2^2 (\partial_x^2 \pi_1 + \partial_y^2 \pi_1 + \partial_z^2 \pi_1) \\ & \left. \left. + \pi_1^3 (\partial_x^2 \pi_1 + \partial_y^2 \pi_1 + \partial_z^2 \pi_1) + \pi_2^3 (\partial_x^2 \pi_2 + \partial_y^2 \pi_2 + \partial_z^2 \pi_2) \right) \right] \quad (\text{D.22}) \end{aligned}$$

A first partial integration i.e. $\pi_1^2(\partial_i \pi_2)(\partial_i \pi_2) \rightarrow -2\pi_1 \pi_2 (\partial_i \pi_1)(\partial_i \pi_2) - \pi_1^2 \pi_2 (\partial_i^2 \pi_2)$ yields

$$\begin{aligned} \mathcal{F}_{\text{ex}}^{(4)} = & \frac{1}{8} \left[(-2\rho_s Q^2 \sin^2 \theta - M\mu_0 H_0^{\text{ext}} \cos \theta) (\boldsymbol{\pi}^2)^2 \right. \\ & - 4\rho_s \left(2\pi_1^2 ((\partial_x \pi_1)^2 + (\partial_y \pi_1)^2 + (\partial_z \pi_1)^2) \right. \\ & + 2\pi_2^2 ((\partial_x \pi_2)^2 + (\partial_y \pi_2)^2 + (\partial_z \pi_2)^2) + \pi_2^2 ((\partial_x \pi_1)^2 + (\partial_y \pi_1)^2 + (\partial_z \pi_1)^2) \\ & + \pi_1 \pi_2^2 (\partial_x^2 \pi_1 + \partial_y^2 \pi_1 + \partial_z^2 \pi_1) \\ & \left. \left. + \pi_1^3 (\partial_x^2 \pi_1 + \partial_y^2 \pi_1 + \partial_z^2 \pi_1) + \pi_2^3 (\partial_x^2 \pi_2 + \partial_y^2 \pi_2 + \partial_z^2 \pi_2) \right) \right] \quad (\text{D.23}) \end{aligned}$$

A second partial integration $\pi_2^2(\partial_i \pi_1)(\partial_i \pi_2) \rightarrow -2\pi_1 \pi_2 (\partial_i \pi_1)(\partial_i \pi_2) - \pi_1 \pi_2^2 (\partial_i^2 \pi_1)$ leads to

$$\begin{aligned} \mathcal{F}_{\text{ex}}^{(4)} = & \frac{1}{8} \left[(-2\rho_s Q^2 \sin^2 \theta - M\mu_0 H_0^{\text{ext}} \cos \theta) (\boldsymbol{\pi}^2)^2 \right. \\ & - 4\rho_s \left(2\pi_1^2 ((\partial_x \pi_1)^2 + (\partial_y \pi_1)^2 + (\partial_z \pi_1)^2) + 2\pi_2^2 ((\partial_x \pi_2)^2 + (\partial_y \pi_2)^2 + (\partial_z \pi_2)^2) \right. \\ & - 2\pi_1 \pi_2 ((\partial_x \pi_1)(\partial_x \pi_2) + (\partial_y \pi_1)(\partial_y \pi_2) + (\partial_z \pi_1)(\partial_z \pi_2)) \\ & \left. \left. + \pi_1^3 (\partial_x^2 \pi_1 + \partial_y^2 \pi_1 + \partial_z^2 \pi_1) + \pi_2^3 (\partial_x^2 \pi_2 + \partial_y^2 \pi_2 + \partial_z^2 \pi_2) \right) \right] \quad (\text{D.24}) \end{aligned}$$

Collecting all the terms by summing over all $\boldsymbol{\pi}$ components α and spacial components i gives the following compacted expression.

$$\begin{aligned} \mathcal{F}_{\text{ex}}^{(4)} = & -\frac{1}{8} (2\rho_s Q^2 \sin^2 \theta + M\mu_0 H_0^{\text{ext}} \cos \theta) (\boldsymbol{\pi}^2)^2 \\ & - \frac{\rho_s}{2} \sum_{\alpha, i} \left(2\pi_\alpha^2 (\partial_i \pi_\alpha)^2 - 2\pi_1 \pi_2 (\partial_i \pi_1)(\partial_i \pi_2) + \pi_\alpha^3 (\partial_i^2 \pi_\alpha) \right) \quad (\text{D.25}) \end{aligned}$$

D.4. FOURIER TRANSFORMATION OF $\hat{n}(r)$

$$\begin{aligned}\hat{n}_{\text{helix}}(\mathbf{k}) &= \int d\mathbf{r} \hat{n}_{\text{helix}}(\mathbf{r}) e^{-i\mathbf{k}\cdot\mathbf{r}} = \int d\mathbf{r} [\mathbf{n}_{\parallel} + \mathbf{n}_{\perp}(\mathbf{r})] e^{-i\mathbf{k}\cdot\mathbf{r}} = \int d\mathbf{r} \left[\mathbf{n}_{\parallel} + \frac{\sin\theta}{2} \begin{pmatrix} e^{i\mathbf{Q}\cdot\mathbf{r}} + e^{-i\mathbf{Q}\cdot\mathbf{r}} \\ -ie^{i\mathbf{Q}\cdot\mathbf{r}} + ie^{-i\mathbf{Q}\cdot\mathbf{r}} \\ 0 \end{pmatrix} \right] e^{-i\mathbf{k}\cdot\mathbf{r}} \\ &= \nu \left[\mathbf{n}_{\parallel} \delta(\mathbf{k}) + \frac{\sin\theta}{2} \begin{pmatrix} \delta(\mathbf{k} + \mathbf{Q}) + \delta(\mathbf{k} - \mathbf{Q}) \\ i\delta(\mathbf{k} + \mathbf{Q}) - i\delta(\mathbf{k} - \mathbf{Q}) \\ 0 \end{pmatrix} \right]\end{aligned}\quad (\text{D.26})$$

$$\hat{e}_1(\mathbf{k}) = \int d\mathbf{r} \hat{e}_1(\mathbf{r}) e^{-i\mathbf{k}\cdot\mathbf{r}} = \int d\mathbf{r} \begin{pmatrix} -\frac{1}{2i}(e^{i\mathbf{Q}\cdot\mathbf{r}} - e^{-i\mathbf{Q}\cdot\mathbf{r}}) \\ \frac{1}{2}(e^{i\mathbf{Q}\cdot\mathbf{r}} + e^{-i\mathbf{Q}\cdot\mathbf{r}}) \\ 0 \end{pmatrix} e^{-i\mathbf{k}\cdot\mathbf{r}} = \frac{\nu}{2} \begin{pmatrix} -i\delta(\mathbf{k} + \mathbf{Q}) + i\delta(\mathbf{k} - \mathbf{Q}) \\ \delta(\mathbf{k} + \mathbf{Q}) + \delta(\mathbf{k} - \mathbf{Q}) \\ 0 \end{pmatrix}\quad (\text{D.27})$$

$$\hat{e}_2(\mathbf{k}) = \int d\mathbf{r} \hat{e}_2(\mathbf{r}) e^{-i\mathbf{k}\cdot\mathbf{r}} = \int d\mathbf{r} \left[\tan\theta \mathbf{n}_{\parallel} - \frac{1}{\tan\theta} \mathbf{n}_{\perp}(\mathbf{r}) \right] e^{-i\mathbf{k}\cdot\mathbf{r}} = \nu \left[\tan\theta \mathbf{n}_{\parallel} \delta(\mathbf{k}) - \frac{\cos\theta}{2} \begin{pmatrix} \delta(\mathbf{k} + \mathbf{Q}) + \delta(\mathbf{k} - \mathbf{Q}) \\ i\delta(\mathbf{k} + \mathbf{Q}) - i\delta(\mathbf{k} - \mathbf{Q}) \\ 0 \end{pmatrix} \right]\quad (\text{D.28})$$

$$\hat{e}_+(\mathbf{k}) = \int d\mathbf{r} \hat{e}_+(\mathbf{r}) e^{-i\mathbf{k}\cdot\mathbf{r}} = \frac{\nu}{\sqrt{2}} \left[i \tan\theta \mathbf{n}_{\parallel} \delta(\mathbf{k}) + \begin{pmatrix} -i \cos^2\left(\frac{\theta}{2}\right) \delta(\mathbf{k} + \mathbf{Q}) + i \sin^2\left(\frac{\theta}{2}\right) \delta(\mathbf{k} - \mathbf{Q}) \\ \cos^2\left(\frac{\theta}{2}\right) \delta(\mathbf{k} + \mathbf{Q}) + \sin^2\left(\frac{\theta}{2}\right) \delta(\mathbf{k} - \mathbf{Q}) \\ 0 \end{pmatrix} \right]\quad (\text{D.29})$$

$$\hat{e}_-(\mathbf{k}) = \int d\mathbf{r} \hat{e}_-(\mathbf{r}) e^{-i\mathbf{k}\cdot\mathbf{r}} = \frac{\nu}{\sqrt{2}} \left[-i \tan\theta \mathbf{n}_{\parallel} \delta(\mathbf{k}) + \begin{pmatrix} -i \sin^2\left(\frac{\theta}{2}\right) \delta(\mathbf{k} + \mathbf{Q}) + i \cos^2\left(\frac{\theta}{2}\right) \delta(\mathbf{k} - \mathbf{Q}) \\ \sin^2\left(\frac{\theta}{2}\right) \delta(\mathbf{k} + \mathbf{Q}) + \cos^2\left(\frac{\theta}{2}\right) \delta(\mathbf{k} - \mathbf{Q}) \\ 0 \end{pmatrix} \right]\quad (\text{D.30})$$

Collecting all those terms yields

$$\begin{aligned}\hat{\mathbf{n}}(\mathbf{k}) &= \int d\mathbf{r} \hat{\mathbf{n}}(\mathbf{r}) e^{-i\mathbf{k}\cdot\mathbf{r}} \\ &= \hat{\mathbf{n}}_{\text{helix}}(\mathbf{k}) - \frac{1}{2\nu^2} \sum_{\mathbf{k}'\mathbf{k}''} \hat{\mathbf{n}}_{\text{helix}}(\mathbf{k} - \mathbf{k}' - \mathbf{k}'') (\boldsymbol{\pi}(\mathbf{k}') \cdot \boldsymbol{\pi}(\mathbf{k}'')) + \frac{1}{\nu} \sum_{\mathbf{k}',i} \pi_i(\mathbf{k}') \hat{e}_i(\mathbf{k} - \mathbf{k}')\end{aligned}\quad (\text{D.31})$$

$$= \hat{\mathbf{n}}_{\text{helix}}(\mathbf{k}) - \frac{g\mu_B}{\mu\phi} \frac{1}{\nu^2} \sum_{\mathbf{k}'\mathbf{k}''} \hat{\mathbf{n}}_{\text{helix}}(\mathbf{k} - \mathbf{k}' - \mathbf{k}'') (\boldsymbol{\psi}(\mathbf{k}') \cdot \boldsymbol{\psi}^*(\mathbf{k}'')) + \sqrt{\frac{g\mu_B}{\mu\phi}} \frac{1}{\nu} \sum_{\mathbf{k}'} [\hat{e}_+(\mathbf{k} - \mathbf{k}') \boldsymbol{\psi}(\mathbf{k}') + \hat{e}_-(\mathbf{k} - \mathbf{k}') \boldsymbol{\psi}^*(\mathbf{k}')] \quad (\text{D.32})$$

D.5. QUADRATIC ORDER OF \mathcal{S}_{DIP} IN π

To derive the matrices $V_{\text{dip}}(\mathbf{0})$ and $V_{\text{dip}}(\mathbf{k})$, cf. [equations \(8.34\) and \(8.36\)](#), we first consider $\hat{\mathbf{n}}$ dependent on the real fields $\boldsymbol{\pi}$ instead of the complex fields $\boldsymbol{\psi}$. This makes the derivation of \mathcal{S}_{dip} easier. To obtain the representation in terms of the natural $\boldsymbol{\psi}$ fields is finally obtained by a rotation via R , [\(8.25\)](#).

The first step is to plug [\(D.29\)](#) into the Fourier transform of \mathcal{S}_{dip} and only keep terms quadratic in π_i to give the effective action $\mathcal{S}_{\text{dip}}^{(2)}$.

$$\begin{aligned} \mathcal{S}_{\text{dip}} &= \frac{1}{2\nu} \sum_{\mathbf{k}} \hat{\mathbf{n}}(\mathbf{k}) \chi_{\text{dip}}^{-1}(\mathbf{k}) \hat{\mathbf{n}}(-\mathbf{k}) \\ &= \frac{1}{2\nu} \sum_{\mathbf{k}} \left[\hat{\mathbf{n}}_{\text{h}}(\mathbf{k}) - \frac{1}{2\nu^2} \sum_{\mathbf{q}'\mathbf{q}''} \hat{\mathbf{n}}_{\text{h}}(\mathbf{k}-\mathbf{q}'-\mathbf{q}'') (\boldsymbol{\pi}(\mathbf{q}') \cdot \boldsymbol{\pi}(\mathbf{q}'')) + \frac{1}{\nu} \sum_{\mathbf{q}'} \pi_i(\mathbf{k}-\mathbf{q}') \hat{e}_i(\mathbf{q}') \right] \chi_{\text{dip}}^{-1}(\mathbf{k}) \left[\hat{\mathbf{n}}_{\text{h}}(-\mathbf{k}) - \frac{1}{2\nu^2} \sum_{\mathbf{q}'\mathbf{q}''} \hat{\mathbf{n}}_{\text{h}}(-\mathbf{k}-\mathbf{q}'-\mathbf{q}'') (\boldsymbol{\pi}(\mathbf{q}') \cdot \boldsymbol{\pi}(\mathbf{q}'')) + \frac{1}{\nu} \sum_{\mathbf{q}'} \pi_i(-\mathbf{k}-\mathbf{q}') \hat{e}_i(\mathbf{q}') \right] \end{aligned} \quad (\text{D.33})$$

$$\begin{aligned} \mathcal{S}_{\text{dip}}^{(2)} &= \frac{1}{2\nu^3} \sum_{\mathbf{k}} \left[-\hat{\mathbf{n}}_{\text{h}}(\mathbf{k}) \chi_{\text{dip}}^{-1}(\mathbf{k}) \frac{1}{2} \sum_{\mathbf{q}'\mathbf{q}''} \hat{\mathbf{n}}_{\text{h}}(-\mathbf{k}-\mathbf{q}'-\mathbf{q}'') (\boldsymbol{\pi}(\mathbf{q}') \cdot \boldsymbol{\pi}(\mathbf{q}'')) - \frac{1}{2} \sum_{\mathbf{q}'\mathbf{q}''} \hat{\mathbf{n}}_{\text{h}}(\mathbf{k}-\mathbf{q}'-\mathbf{q}'') (\boldsymbol{\pi}(\mathbf{q}') \cdot \boldsymbol{\pi}(\mathbf{q}'')) \chi_{\text{dip}}^{-1}(\mathbf{k}) \hat{\mathbf{n}}_{\text{h}}(-\mathbf{k}) + \sum_{\mathbf{q}} \pi_i(\mathbf{k}-\mathbf{q}) \hat{e}_i(\mathbf{q}) \chi_{\text{dip}}^{-1}(\mathbf{k}) \sum_{\mathbf{q}'} \pi_j(-\mathbf{k}-\mathbf{q}') \hat{e}_j(\mathbf{q}') \right] \\ &= \frac{1}{2\nu} \sum_{\mathbf{k}} \left[-\hat{\mathbf{n}}_{\text{h}}(\mathbf{k}) \chi_{\text{dip}}^{-1}(\mathbf{k}) \frac{1}{2\nu^2} \sum_{\mathbf{q}'\mathbf{q}''} \hat{\mathbf{n}}_{\text{h}}(-\mathbf{k}-\mathbf{q}'-\mathbf{q}'') (\boldsymbol{\pi}(\mathbf{q}') \cdot \boldsymbol{\pi}(\mathbf{q}'')) - \frac{1}{2\nu^2} \sum_{\mathbf{q}'\mathbf{q}''} \hat{\mathbf{n}}_{\text{h}}(\mathbf{k}-\mathbf{q}'-\mathbf{q}'') (\boldsymbol{\pi}(\mathbf{q}') \cdot \boldsymbol{\pi}(\mathbf{q}'')) \chi_{\text{dip}}^{-1}(\mathbf{k}) \hat{\mathbf{n}}_{\text{h}}(-\mathbf{k}) + \frac{1}{\nu^2} \sum_{\mathbf{q}\mathbf{q}',ij} \hat{e}_i(\mathbf{q}) \chi_{\text{dip}}^{-1}(\mathbf{k}) \hat{e}_j(\mathbf{q}') \pi_i(\mathbf{k}-\mathbf{q}) \pi_j(-\mathbf{k}-\mathbf{q}') \right] \end{aligned} \quad (\text{D.34})$$

with abbreviation $\hat{\mathbf{n}}_{\text{h}} = \hat{\mathbf{n}}_{\text{helix}}$. In the following, we examine each term individually and separate between the two cases of $k \ll 1/L$ (case 1) and $k \gg 1/L$ (case 2), respectively. In those two cases the dipolar tensors take are

$$\begin{aligned} \text{case 1: } \chi_{\text{dip}}^{-1}(\mathbf{0}) &= \mu_0 M^2 \begin{pmatrix} N_x & 0 & 0 \\ 0 & N_y & 0 \\ 0 & 0 & N_z \end{pmatrix} & \text{case 2: } \chi_{\text{dip}}^{-1}(\mathbf{k}) &= \mu_0 M^2 \begin{pmatrix} \hat{k}^x \hat{k}^x & \hat{k}^x \hat{k}^y & \hat{k}^x \hat{k}^z \\ \hat{k}^y \hat{k}^x & \hat{k}^y \hat{k}^y & \hat{k}^y \hat{k}^z \\ \hat{k}^z \hat{k}^x & \hat{k}^z \hat{k}^y & \hat{k}^z \hat{k}^z \end{pmatrix}. \end{aligned} \quad (\text{D.35})$$

FIRST TERM

$$\begin{aligned}
 & - \sum_{\mathbf{k}} \hat{n}_{\text{helix}}(\mathbf{k}) \chi_{\text{dip}}^{-1}(\mathbf{k}) \frac{1}{2\nu^2} \sum_{\mathbf{q}'\mathbf{q}''} \hat{n}_{\text{helix}}(-\mathbf{k} - \mathbf{q}' - \mathbf{q}'') \left(\pi(\mathbf{q}') \cdot \pi(\mathbf{q}'') \right) \\
 = & - \frac{1}{2} \sum_{\mathbf{k}\mathbf{q}'\mathbf{q}''} \left[\delta(\mathbf{k}) \delta(-\mathbf{k} - \mathbf{q}' - \mathbf{q}'') n_{\parallel} \chi_{\text{dip}}^{-1}(\mathbf{k}) n_{\parallel} + \frac{\sin \theta}{2} n_{\parallel} \chi_{\text{dip}}^{-1}(\mathbf{k}) \left(\frac{\delta(-\mathbf{k} - \mathbf{q}' - \mathbf{q}'' + \mathbf{Q}) + \delta(-\mathbf{k} - \mathbf{q}' - \mathbf{q}'' - \mathbf{Q})}{i\delta(-\mathbf{k} - \mathbf{q}' - \mathbf{q}'' + \mathbf{Q}) - i\delta(-\mathbf{k} - \mathbf{q}' - \mathbf{q}'' - \mathbf{Q})} \right) \delta(\mathbf{k}) \right. \\
 & \left. + \frac{\sin \theta}{2} \left(\frac{\delta(\mathbf{k} + \mathbf{Q}) + \delta(\mathbf{k} - \mathbf{Q})}{i\delta(\mathbf{k} + \mathbf{Q}) - i\delta(\mathbf{k} - \mathbf{Q})} \right) \chi_{\text{dip}}^{-1}(\mathbf{k}) n_{\parallel} \delta(-\mathbf{k} - \mathbf{q}' - \mathbf{q}'') + \frac{\sin^2 \theta}{4} \left(\frac{\delta(\mathbf{k} + \mathbf{Q}) + \delta(\mathbf{k} - \mathbf{Q})}{i\delta(\mathbf{k} + \mathbf{Q}) - i\delta(\mathbf{k} - \mathbf{Q})} \right) \chi_{\text{dip}}^{-1}(\mathbf{k}) \left(\frac{\delta(-\mathbf{k} - \mathbf{q}' - \mathbf{q}'' + \mathbf{Q}) + \delta(-\mathbf{k} - \mathbf{q}' - \mathbf{q}'' - \mathbf{Q})}{i\delta(-\mathbf{k} - \mathbf{q}' - \mathbf{q}'' + \mathbf{Q}) - i\delta(-\mathbf{k} - \mathbf{q}' - \mathbf{q}'' - \mathbf{Q})} \right) \right] \left(\pi(\mathbf{q}') \cdot \pi(\mathbf{q}'') \right) \\
 = & - \frac{1}{2} \sum_{\mathbf{k}\mathbf{q}'} \left[\delta(\mathbf{k}) n_{\parallel} \chi_{\text{dip}}^{-1}(\mathbf{k}) n_{\parallel} \left(\pi(\mathbf{q}') \cdot \pi(-\mathbf{k} - \mathbf{q}') \right) + \frac{\sin \theta}{2} n_{\parallel} \chi_{\text{dip}}^{-1}(\mathbf{k}) \left(i \left(\frac{\pi(\mathbf{q}') \cdot \pi(-\mathbf{k} - \mathbf{q}' + \mathbf{Q})}{\pi(\mathbf{q}') \cdot \pi(-\mathbf{k} - \mathbf{q}' + \mathbf{Q})} \right) + \left(\frac{\pi(\mathbf{q}') \cdot \pi(-\mathbf{k} - \mathbf{q}' - \mathbf{Q})}{\pi(\mathbf{q}') \cdot \pi(-\mathbf{k} - \mathbf{q}' - \mathbf{Q})} \right) \right) \delta(\mathbf{k}) \right. \\
 & \left. + \frac{\sin \theta}{2} \left(\frac{\delta(\mathbf{k} + \mathbf{Q}) + \delta(\mathbf{k} - \mathbf{Q})}{i\delta(\mathbf{k} + \mathbf{Q}) - i\delta(\mathbf{k} - \mathbf{Q})} \right) \chi_{\text{dip}}^{-1}(\mathbf{k}) n_{\parallel} \left(\pi(\mathbf{q}') \cdot \pi(-\mathbf{k} - \mathbf{q}') \right) + \frac{\sin^2 \theta}{4} \left(\frac{\delta(\mathbf{k} + \mathbf{Q}) + \delta(\mathbf{k} - \mathbf{Q})}{i\delta(\mathbf{k} + \mathbf{Q}) - i\delta(\mathbf{k} - \mathbf{Q})} \right) \chi_{\text{dip}}^{-1}(\mathbf{k}) \left(i \left(\frac{\pi(\mathbf{q}') \cdot \pi(-\mathbf{k} - \mathbf{q}' + \mathbf{Q})}{\pi(\mathbf{q}') \cdot \pi(-\mathbf{k} - \mathbf{q}' + \mathbf{Q})} \right) + \left(\frac{\pi(\mathbf{q}') \cdot \pi(-\mathbf{k} - \mathbf{q}' - \mathbf{Q})}{\pi(\mathbf{q}') \cdot \pi(-\mathbf{k} - \mathbf{q}' - \mathbf{Q})} \right) \right) \right]
 \end{aligned}$$

Case 1:

$$= - \frac{\mu_0 M^2}{2} \sum_{\mathbf{q}'} \left[\cos^2 \theta N_z \left(\pi(\mathbf{q}') \cdot \pi(-\mathbf{q}') \right) + \text{vanishing term due to sample on principal axes} + \text{two vanishing terms due to } k \ll Q \right]$$

Case 2:

$$\begin{aligned}
 = & - \frac{\mu_0 M^2}{2} \sum_{\mathbf{q}'} \left[\text{two vanishing terms due to } k \gg \frac{1}{L} \right. \\
 & + \frac{1}{2} \sin \theta \cos \theta \left(\hat{k}^z (\hat{k}^x - i\hat{k}^y) \pi(\mathbf{q}') \cdot \pi(-\mathbf{q}' - \mathbf{Q}) + \hat{k}^z (\hat{k}^x + i\hat{k}^y) \left(\pi(\mathbf{q}') \cdot \pi(-\mathbf{q}' + \mathbf{Q}) \right) \right) \\
 & \left. + \frac{1}{4} \sin^2 \theta \left((\hat{k}^x - i\hat{k}^y)^2 \underbrace{\pi(\mathbf{q}') \cdot \pi(-\mathbf{q}' - 2\mathbf{Q})}_{\mathbf{q}' \rightarrow \mathbf{q}' - \mathbf{Q} \pi(\mathbf{q}' - \mathbf{Q}) \cdot \pi(-\mathbf{q}' - \mathbf{Q})} + 2(\hat{k}^x \hat{k}^x + \hat{k}^y \hat{k}^y) \pi(\mathbf{q}') \cdot \pi(-\mathbf{q}') + (\hat{k}^x + i\hat{k}^y)^2 \underbrace{\pi(\mathbf{q}') \cdot \pi(-\mathbf{q}' + 2\mathbf{Q})}_{\mathbf{q}' \rightarrow \mathbf{q}' + \mathbf{Q} \pi(\mathbf{q}' + \mathbf{Q}) \cdot \pi(-\mathbf{q}' + \mathbf{Q})} \right) \right]
 \end{aligned}$$

SECOND TERM

$$\begin{aligned}
& - \sum_{\mathbf{k}} \frac{1}{2\nu^2} \sum_{\mathbf{q}'\mathbf{q}''} \hat{n}_{\text{helix}}(\mathbf{k} - \mathbf{q}' - \mathbf{q}'') \left(\boldsymbol{\pi}(\mathbf{q}') \cdot \boldsymbol{\pi}(\mathbf{q}'') \right) \chi_{\text{dip}}^{-1}(\mathbf{k}) \hat{n}_{\text{helix}}(-\mathbf{k}) \\
& = -\frac{1}{2} \sum_{\mathbf{k}\mathbf{q}'} \left[\mathbf{n}_{\parallel} \chi_{\text{dip}}^{-1}(\mathbf{k}) \mathbf{n}_{\parallel} \delta(-\mathbf{k}) \left(\boldsymbol{\pi}(\mathbf{q}') \cdot \boldsymbol{\pi}(\mathbf{k} - \mathbf{q}') \right) + \frac{\sin \theta}{2} \mathbf{n}_{\parallel} \chi_{\text{dip}}^{-1}(\mathbf{k}) \left(\begin{smallmatrix} \delta(-\mathbf{k} + \mathbf{Q}) + \delta(-\mathbf{k} - \mathbf{Q}) \\ i\delta(-\mathbf{k} + \mathbf{Q}) - i\delta(-\mathbf{k} - \mathbf{Q}) \end{smallmatrix} \right) \left(\boldsymbol{\pi}(\mathbf{q}') \cdot \boldsymbol{\pi}(\mathbf{k} - \mathbf{q}') \right) \right. \\
& \quad \left. + \frac{\sin \theta}{2} \left(\begin{smallmatrix} \left(\boldsymbol{\pi}(\mathbf{q}') \cdot \boldsymbol{\pi}(\mathbf{k} - \mathbf{q}' + \mathbf{Q}) \right) + \left(\boldsymbol{\pi}(\mathbf{q}') \cdot \boldsymbol{\pi}(\mathbf{k} - \mathbf{q}' - \mathbf{Q}) \right) \\ i \left(\boldsymbol{\pi}(\mathbf{q}') \cdot \boldsymbol{\pi}(\mathbf{k} - \mathbf{q}' + \mathbf{Q}) \right) - i \left(\boldsymbol{\pi}(\mathbf{q}') \cdot \boldsymbol{\pi}(\mathbf{k} - \mathbf{q}' - \mathbf{Q}) \right) \end{smallmatrix} \right) \chi_{\text{dip}}^{-1}(\mathbf{k}) \mathbf{n}_{\parallel} \delta(-\mathbf{k}) + \frac{\sin^2 \theta}{4} \left(\begin{smallmatrix} \left(\boldsymbol{\pi}(\mathbf{q}') \cdot \boldsymbol{\pi}(\mathbf{k} - \mathbf{q}' + \mathbf{Q}) \right) + \left(\boldsymbol{\pi}(\mathbf{q}') \cdot \boldsymbol{\pi}(\mathbf{k} - \mathbf{q}' - \mathbf{Q}) \right) \\ i \left(\boldsymbol{\pi}(\mathbf{q}') \cdot \boldsymbol{\pi}(\mathbf{k} - \mathbf{q}' + \mathbf{Q}) \right) - i \left(\boldsymbol{\pi}(\mathbf{q}') \cdot \boldsymbol{\pi}(\mathbf{k} - \mathbf{q}' - \mathbf{Q}) \right) \end{smallmatrix} \right) \chi_{\text{dip}}^{-1}(\mathbf{k}) \left(\begin{smallmatrix} \delta(-\mathbf{k} + \mathbf{Q}) + \delta(-\mathbf{k} - \mathbf{Q}) \\ i\delta(-\mathbf{k} + \mathbf{Q}) - i\delta(-\mathbf{k} - \mathbf{Q}) \end{smallmatrix} \right) \right]
\end{aligned}$$

Case 1:

$$\begin{aligned}
& = -\frac{\mu_0 M^2}{2} \sum_{\mathbf{q}'} \left[\cos^2 \theta N_z \left(\boldsymbol{\pi}(\mathbf{q}') \cdot \boldsymbol{\pi}(-\mathbf{q}') \right) + \text{vanishing term due to } k \ll Q \right. \\
& \quad \left. + \text{vanishing term due to sample on principal axes} + \text{vanishing term due to } k \ll Q \right]
\end{aligned}$$

Case 2:

$$\begin{aligned}
& = -\frac{\mu_0 M^2}{2} \sum_{\mathbf{q}'} \left[\text{vanishing term due to } k \gg \frac{1}{L} \right. \\
& \quad + \frac{1}{2} \sin \theta \cos \theta \left(\hat{k}^z (\hat{k}^x - i\hat{k}^y) \boldsymbol{\pi}(\mathbf{q}') \cdot \boldsymbol{\pi}(-\mathbf{q}' - \mathbf{Q}) + (\hat{k}^z (\hat{k}^x + i\hat{k}^y) \boldsymbol{\pi}(\mathbf{q}') \cdot \boldsymbol{\pi}(-\mathbf{q}' + \mathbf{Q})) \right) + \text{vanishing term due to } k \gg \frac{1}{L} \\
& \quad \left. + \frac{1}{4} \sin^2 \theta \left((\hat{k}^x - i\hat{k}^y)^2 \underbrace{\boldsymbol{\pi}(\mathbf{q}') \cdot \boldsymbol{\pi}(-\mathbf{q}' - 2\mathbf{Q})}_{\mathbf{q}' \xrightarrow{\mathbf{Q}} \boldsymbol{\pi}(\mathbf{q}' - \mathbf{Q}) \cdot \boldsymbol{\pi}(-\mathbf{q}' - \mathbf{Q})} + 2(\hat{k}^x \hat{k}^x + \hat{k}^y \hat{k}^y) \boldsymbol{\pi}(\mathbf{q}') \cdot \boldsymbol{\pi}(-\mathbf{q}') + (\hat{k}^x + i\hat{k}^y)^2 \underbrace{\boldsymbol{\pi}(\mathbf{q}') \cdot \boldsymbol{\pi}(-\mathbf{q}' + 2\mathbf{Q})}_{\mathbf{q}' \xrightarrow{\mathbf{Q}} \boldsymbol{\pi}(\mathbf{q}' + \mathbf{Q}) \cdot \boldsymbol{\pi}(-\mathbf{q}' + \mathbf{Q})} \right) \right]
\end{aligned}$$

THIRD TERMS: $i = j = 1$

$$\begin{aligned} & \frac{1}{\nu^2} \sum_{\mathbf{k}} \sum_{\mathbf{q}\mathbf{q}'} \hat{e}_1(\mathbf{q}) \chi_{\text{dip}}^{-1}(\mathbf{k}) \hat{e}_1(\mathbf{q}') \pi_1(\mathbf{k} - \mathbf{q}) \pi_1(-\mathbf{k} - \mathbf{q}') \\ &= \frac{1}{4} \sum_{\mathbf{k}} \sum_{\mathbf{q}} \begin{pmatrix} -i\delta(\mathbf{q}+\mathbf{Q})+i\delta(\mathbf{q}-\mathbf{Q}) \\ \delta(\mathbf{q}+\mathbf{Q})+\delta(\mathbf{q}-\mathbf{Q}) \\ 0 \end{pmatrix} \chi_{\text{dip}}^{-1}(\mathbf{k}) \begin{pmatrix} -i\pi_1(\mathbf{k}-\mathbf{q})\pi_1(-\mathbf{k}+\mathbf{Q})+i\pi_1(\mathbf{k}-\mathbf{q})\pi_1(-\mathbf{k}-\mathbf{Q}) \\ \pi_1(\mathbf{k}-\mathbf{q})\pi_1(-\mathbf{k}+\mathbf{Q})+\pi_1(\mathbf{k}-\mathbf{q})\pi_1(-\mathbf{k}-\mathbf{Q}) \\ 0 \end{pmatrix} \end{aligned}$$

Case 1:

$$\begin{aligned} &= \frac{\mu_0 M^2}{4} \sum_{\mathbf{k} \ll \frac{1}{L}} \left[N_x \left(-\pi_1(-\mathbf{k} - \mathbf{Q})\pi_1(\mathbf{k} - \mathbf{Q}) + \pi_1(\mathbf{k} - \mathbf{Q})\pi_1(-\mathbf{k} + \mathbf{Q}) + \pi_1(-\mathbf{k} - \mathbf{Q})\pi_1(\mathbf{k} + \mathbf{Q}) - \pi_1(-\mathbf{k} + \mathbf{Q})\pi_1(\mathbf{k} + \mathbf{Q}) \right) \right. \\ &\quad \left. + N_y \left(\pi_1(-\mathbf{k} - \mathbf{Q})\pi_1(\mathbf{k} - \mathbf{Q}) + \pi_1(\mathbf{k} - \mathbf{Q})\pi_1(-\mathbf{k} + \mathbf{Q}) + \pi_1(-\mathbf{k} - \mathbf{Q})\pi_1(\mathbf{k} + \mathbf{Q}) + \pi_1(-\mathbf{k} + \mathbf{Q})\pi_1(\mathbf{k} + \mathbf{Q}) \right) \right] \\ &\stackrel{\mathbf{k} \approx 0}{=} \frac{\mu_0 M^2}{4} \left[-N_x \left(\pi_1(\mathbf{Q}) - \pi_1(-\mathbf{Q}) \right)^2 + N_y \left(\pi_1(\mathbf{Q}) + \pi_1(-\mathbf{Q}) \right)^2 \right] \end{aligned}$$

Case 2:

$$\begin{aligned} &= \frac{\mu_0 M^2}{4} \sum_{\mathbf{k} \gg \frac{1}{L}} \left[(\hat{k}^x \hat{k}^x + \hat{k}^y \hat{k}^y) \pi_1(-\mathbf{k} + \mathbf{Q}) \pi_1(\mathbf{k} - \mathbf{Q}) - (\hat{k}^x + i\hat{k}^y)^2 \pi_1(-\mathbf{k} + \mathbf{Q}) \pi_1(\mathbf{k} + \mathbf{Q}) \right. \\ &\quad \left. - (\hat{k}^x - i\hat{k}^y)^2 \pi_1(-\mathbf{k} - \mathbf{Q}) \pi_1(\mathbf{k} - \mathbf{Q}) + (\hat{k}^x \hat{k}^x + \hat{k}^y \hat{k}^y) \pi_1(-\mathbf{k} - \mathbf{Q}) \pi_1(\mathbf{k} + \mathbf{Q}) \right] \end{aligned}$$

THIRD TERMS: $i = 1, j = 2$

$$\begin{aligned} & \frac{1}{\nu^2} \sum_{\mathbf{k}} \sum_{\mathbf{q}\mathbf{q}'} \hat{e}_1(\mathbf{q}) \chi_{\text{dip}}^{-1}(\mathbf{k}) \hat{e}_2(\mathbf{q}') \pi_1(\mathbf{k} - \mathbf{q}) \pi_2(-\mathbf{k} - \mathbf{q}') \\ &= \frac{1}{2} \sum_{\mathbf{k}} \left[\begin{pmatrix} -i\pi_1(\mathbf{k}+\mathbf{Q})\pi_2(-\mathbf{k}) + i\pi_1(\mathbf{k}-\mathbf{Q})\pi_2(-\mathbf{k}) \\ \pi_1(\mathbf{k}+\mathbf{Q})\pi_2(-\mathbf{k}) + \pi_1(\mathbf{k}-\mathbf{Q})\pi_2(-\mathbf{k}) \\ 0 \end{pmatrix} \chi_{\text{dip}}^{-1}(\mathbf{k}) \tan \theta \mathbf{n}_{\parallel} - \frac{\cos \theta}{2} \sum_{\mathbf{q}} \begin{pmatrix} -i\delta(\mathbf{q}+\mathbf{Q}) + i\delta(\mathbf{q}-\mathbf{Q}) \\ \delta(\mathbf{q}+\mathbf{Q}) + \delta(\mathbf{q}-\mathbf{Q}) \\ 0 \end{pmatrix} \chi_{\text{dip}}^{-1}(\mathbf{k}) \begin{pmatrix} \pi_1(\mathbf{k}-\mathbf{q})\pi_2(-\mathbf{k}+\mathbf{Q}) + \pi_1(\mathbf{k}-\mathbf{q})\pi_2(-\mathbf{k}-\mathbf{Q}) \\ i\pi_1(\mathbf{k}-\mathbf{q})\pi_2(-\mathbf{k}+\mathbf{Q}) - i\pi_1(\mathbf{k}-\mathbf{q})\pi_2(-\mathbf{k}-\mathbf{Q}) \\ 0 \end{pmatrix} \right] \end{aligned}$$

Case 1:

$$\begin{aligned} &= \frac{\mu_0 M^2}{2} \sum_{\mathbf{k} \ll \frac{1}{L}} \left[\text{vanishing term due to sample on principal axes} \right. \\ &\quad \left. - \frac{\cos \theta}{2} i \left((N_x - N_y) \pi_1(\mathbf{k}-\mathbf{Q}) - (N_x + N_y) \pi_1(\mathbf{k}+\mathbf{Q}) \right) \pi_2(-\mathbf{k}-\mathbf{Q}) + \left((N_x + N_y) \pi_1(\mathbf{k}-\mathbf{Q}) + (-N_x + N_y) \pi_1(\mathbf{k}+\mathbf{Q}) \right) \pi_2(-\mathbf{k}+\mathbf{Q}) \right] \\ &\stackrel{\mathbf{k} \approx 0}{=} - \frac{\mu_0 M^2}{2} \frac{\cos \theta}{2} i \left[N_x \left(\pi_1(-\mathbf{Q}) - \pi_1(\mathbf{Q}) \right) \left(\pi_2(-\mathbf{Q}) + \pi_2(+\mathbf{Q}) \right) - N_y \left(\pi_1(-\mathbf{Q}) + \pi_1(\mathbf{Q}) \right) \left(\pi_2(-\mathbf{Q}) - \pi_2(\mathbf{Q}) \right) \right] \end{aligned}$$

Case 2:

$$\begin{aligned} &= \frac{\mu_0 M^2}{2} \sum_{\mathbf{k} \gg \frac{1}{L}} \left[i \sin \theta \left\{ -\hat{k}^z (\hat{k}^x + i\hat{k}^y) \pi_1(\mathbf{k} + \mathbf{Q}) \pi_2(-\mathbf{k}) + \hat{k}^z (\hat{k}^x - i\hat{k}^y) \pi_1(\mathbf{k} - \mathbf{Q}) \pi_2(-\mathbf{k}) \right\} \right. \\ &\quad \left. - i \frac{\cos \theta}{2} \left\{ (\hat{k}^x - i\hat{k}^y)^2 \pi_1(\mathbf{k} - \mathbf{Q}) \pi_2(-\mathbf{k} - \mathbf{Q}) + (\hat{k}^x \hat{k}^x + \hat{k}^y \hat{k}^y) \pi_1(\mathbf{k} - \mathbf{Q}) \pi_2(-\mathbf{k} + \mathbf{Q}) \right. \right. \\ &\quad \left. \left. - (\hat{k}^x \hat{k}^x + \hat{k}^y \hat{k}^y) \pi_1(\mathbf{k} + \mathbf{Q}) \pi_2(-\mathbf{k} - \mathbf{Q}) - (\hat{k}^x + i\hat{k}^y)^2 \pi_1(\mathbf{k} + \mathbf{Q}) \pi_2(-\mathbf{k} + \mathbf{Q}) \right\} \right] \end{aligned}$$

THIRD TERMS: $i = 2, j = 1$

$$\begin{aligned}
 & \frac{1}{\nu^2} \sum_{\mathbf{k}} \sum_{\mathbf{q}\mathbf{q}'} \hat{e}_2(\mathbf{q}) \chi_{\text{dip}}^{-1}(\mathbf{k}) \hat{e}_1(\mathbf{q}') \pi_2(\mathbf{k} - \mathbf{q}) \pi_1(-\mathbf{k} - \mathbf{q}') \\
 &= \frac{1}{2} \sum_{\mathbf{k}} \sum_{\mathbf{q}} \left[\tan \theta n_{\parallel} \delta(\mathbf{q}) - \frac{\cos \theta}{2} \begin{pmatrix} \delta(\mathbf{q} + \mathbf{Q}) + \delta(\mathbf{q} - \mathbf{Q}) \\ i\delta(\mathbf{q} + \mathbf{Q}) - i\delta(\mathbf{q} - \mathbf{Q}) \\ 0 \end{pmatrix} \right] \chi_{\text{dip}}^{-1}(\mathbf{k}) \left[\begin{pmatrix} -i\pi_2(\mathbf{k} - \mathbf{q})\pi_1(-\mathbf{k} + \mathbf{Q}) + i\pi_2(\mathbf{k} - \mathbf{q})\pi_1(-\mathbf{k} - \mathbf{Q}) \\ \pi_2(\mathbf{k} - \mathbf{q})\pi_1(-\mathbf{k} + \mathbf{Q}) + \pi_2(\mathbf{k} - \mathbf{q})\pi_1(-\mathbf{k} - \mathbf{Q}) \\ 0 \end{pmatrix} \right]
 \end{aligned}$$

Case 1:

$$\begin{aligned}
 &= \frac{\mu_0 M^2}{2} \sum_{\mathbf{k} \ll \frac{1}{L}} \left[\text{vanishing term due to sample on principal axes} \right. \\
 &\quad \left. - \frac{\cos \theta}{2} i \left(-\pi_1(-\mathbf{k} + \mathbf{Q}) \left((N_x + N_y) \pi_2(\mathbf{k} - \mathbf{Q}) + (N_x - N_y) \pi_2(\mathbf{k} + \mathbf{Q}) \right) + \pi_1(-\mathbf{k} - \mathbf{Q}) \left((N_x - N_y) \pi_2(\mathbf{k} - \mathbf{Q}) + (N_x + N_y) \pi_2(\mathbf{k} + \mathbf{Q}) \right) \right) \right] \\
 &\stackrel{\mathbf{k} \approx 0}{=} -\frac{\mu_0 M^2}{2} \frac{\cos \theta}{2} i \left[N_x \left(\pi_1(-\mathbf{Q}) - \pi_1(+\mathbf{Q}) \right) \left(\pi_2(-\mathbf{Q}) + \pi_2(+\mathbf{Q}) \right) - N_y \left(\pi_1(-\mathbf{Q}) + \pi_1(+\mathbf{Q}) \right) \left(\pi_2(-\mathbf{Q}) - \pi_2(+\mathbf{Q}) \right) \right]
 \end{aligned}$$

Case 2:

$$\begin{aligned}
 &= \frac{\mu_0 M^2}{2} \sum_{\mathbf{k} \gg \frac{1}{L}} \left[i \sin \theta \left\{ \hat{k}^z (\hat{k}^x - i\hat{k}^y) \pi_1(-\mathbf{k} - \mathbf{Q}) \pi_2(\mathbf{k}) + \hat{k}^z (\hat{k}^x + i\hat{k}^y) \pi_1(-\mathbf{k} + \mathbf{Q}) \pi_2(\mathbf{k}) \right\} \right. \\
 &\quad \left. - i \frac{\cos \theta}{2} \left\{ (\hat{k}^x - i\hat{k}^y)^2 \pi_1(-\mathbf{k} - \mathbf{Q}) \pi_2(\mathbf{k} - \mathbf{Q}) + (\hat{k}^x \hat{k}^x + \hat{k}^y \hat{k}^y) \pi_1(-\mathbf{k} - \mathbf{Q}) \pi_2(\mathbf{k} + \mathbf{Q}) \right. \right. \\
 &\quad \left. \left. - (\hat{k}^x \hat{k}^x + \hat{k}^y \hat{k}^y) \pi_1(-\mathbf{k} + \mathbf{Q}) \pi_2(\mathbf{k} - \mathbf{Q}) - (\hat{k}^x + i\hat{k}^y)^2 \pi_1(-\mathbf{k} + \mathbf{Q}) \pi_2(\mathbf{k} + \mathbf{Q}) \right\} \right]
 \end{aligned}$$

THIRD TERMS: $i = 2, j = 2$

$$\begin{aligned} & \frac{1}{\nu^2} \sum_{\mathbf{k}} \sum_{\mathbf{q}\mathbf{q}'} \hat{e}_2(\mathbf{q}) \chi_{\text{dip}}^{-1}(\mathbf{k}) \hat{e}_2(\mathbf{q}') \pi_2(\mathbf{k} - \mathbf{q}) \pi_2(-\mathbf{k} - \mathbf{q}') \\ &= \sum_{\mathbf{k}} \sum_{\mathbf{q}} \left[\tan \theta \mathbf{n}_{\parallel} \delta(\mathbf{q}) - \frac{\cos \theta}{2} \begin{pmatrix} \delta(\mathbf{q} + \mathbf{Q}) + \delta(\mathbf{q} - \mathbf{Q}) \\ i\delta(\mathbf{q} + \mathbf{Q}) - i\delta(\mathbf{q} - \mathbf{Q}) \\ 0 \end{pmatrix} \right] \chi_{\text{dip}}^{-1}(\mathbf{k}) \left[\tan \theta \mathbf{n}_{\parallel} \pi_2(\mathbf{k} - \mathbf{q}) \pi_2(-\mathbf{k}) - \frac{\cos \theta}{2} \begin{pmatrix} \pi_2(\mathbf{k} - \mathbf{q}) \pi_2(-\mathbf{k} + \mathbf{Q}) + \pi_2(\mathbf{k} - \mathbf{q}) \pi_2(-\mathbf{k} - \mathbf{Q}) \\ i\pi_2(\mathbf{k} - \mathbf{q}) \pi_2(-\mathbf{k} + \mathbf{Q}) - i\pi_2(\mathbf{k} - \mathbf{q}) \pi_2(-\mathbf{k} - \mathbf{Q}) \\ 0 \end{pmatrix} \right] \end{aligned}$$

Case 1:

$$\begin{aligned} &= \mu_0 M^2 \sum_{\mathbf{k} \ll \frac{1}{L}} \left[N_z \sin^2 \theta \pi_2(\mathbf{k}) \pi_2(-\mathbf{k}) + \text{two vanishing terms due to sample on principal axes} \right. \\ &\quad \left. + \frac{\cos^2 \theta}{4} N_x \left(\pi_2(\mathbf{k} + \mathbf{Q}) \pi_2(-\mathbf{k} + \mathbf{Q}) + \pi_2(\mathbf{k} + \mathbf{Q}) \pi_2(-\mathbf{k} - \mathbf{Q}) + \pi_2(\mathbf{k} - \mathbf{Q}) \pi_2(-\mathbf{k} + \mathbf{Q}) + \pi_2(\mathbf{k} - \mathbf{Q}) \pi_2(-\mathbf{k} - \mathbf{Q}) \right) \right. \\ &\quad \left. + \frac{\cos^2 \theta}{4} N_y \left(-\pi_2(\mathbf{k} + \mathbf{Q}) \pi_2(-\mathbf{k} + \mathbf{Q}) + \pi_2(\mathbf{k} + \mathbf{Q}) \pi_2(-\mathbf{k} - \mathbf{Q}) + \pi_2(\mathbf{k} - \mathbf{Q}) \pi_2(-\mathbf{k} + \mathbf{Q}) - \pi_2(\mathbf{k} - \mathbf{Q}) \pi_2(-\mathbf{k} - \mathbf{Q}) \right) \right] \\ &\stackrel{\mathbf{k} \approx 0}{=} \mu_0 M^2 \left[N_z \sin^2 \theta \pi_2(0) \pi_2(0) + \frac{\cos^2 \theta}{4} \left(N_x \left(\pi_2(-\mathbf{Q}) + \pi_2(\mathbf{Q}) \right)^2 - N_y \left(\pi_2(-\mathbf{Q}) - \pi_2(+\mathbf{Q}) \right)^2 \right) \right] \end{aligned}$$

Case 2:

$$\begin{aligned} &= \mu_0 M^2 \sum_{\mathbf{k} \gg \frac{1}{L}} \left[\hat{k}^z \hat{k}^z \sin^2 \theta \pi_2(-\mathbf{k}) \pi_2(\mathbf{k}) \right. \\ &\quad \left. - \frac{1}{2} \sin(\theta) \cos(\theta) \left\{ \hat{k}^z (\hat{k}^x - i\hat{k}^y) \pi_2(\mathbf{k}) \pi_2(-\mathbf{k} - \mathbf{Q}) + \hat{k}^z (\hat{k}^x + i\hat{k}^y) \pi_2(\mathbf{k}) \pi_2(-\mathbf{k} + \mathbf{Q}) \right. \right. \\ &\quad \left. \left. + \hat{k}^z (\hat{k}^x - i\hat{k}^y) \pi_2(-\mathbf{k}) \pi_2(\mathbf{k} - \mathbf{Q}) + \hat{k}^z (\hat{k}^x + i\hat{k}^y) \pi_2(-\mathbf{k}) \pi_2(\mathbf{k} + \mathbf{Q}) \right\} \right. \\ &\quad \left. + \frac{1}{4} \cos^2 \theta \left\{ (\hat{k}^x - i\hat{k}^y)^2 \pi_2(-\mathbf{k} - \mathbf{Q}) \pi_2(\mathbf{k} - \mathbf{Q}) + (\hat{k}^x \hat{k}^x - \hat{k}^y \hat{k}^y) \pi_2(-\mathbf{k} - \mathbf{Q}) \pi_2(\mathbf{k} + \mathbf{Q}) \right. \right. \\ &\quad \left. \left. + (\hat{k}^x \hat{k}^x - \hat{k}^y \hat{k}^y) \pi_2(-\mathbf{k} + \mathbf{Q}) \pi_2(\mathbf{k} - \mathbf{Q}) + (\hat{k}^x + i\hat{k}^y)^2 \pi_2(-\mathbf{k} + \mathbf{Q}) \pi_2(\mathbf{k} + \mathbf{Q}) \right\} \right] \end{aligned}$$

COLLECTION OF TERMS

After evaluating the individual terms, we rearrange them in a matrix notation corresponding to

$$\mathcal{S}_{\text{dip}} = \frac{1}{2\nu} \sum_{\mathbf{k} \gg \frac{1}{L}} (\boldsymbol{\pi}^\top(-\mathbf{k} - \mathbf{Q}), \boldsymbol{\pi}^\top(-\mathbf{k}), \boldsymbol{\pi}^\top(-\mathbf{k} + \mathbf{Q})) \mathcal{M}(\hat{\mathbf{k}}) \begin{pmatrix} \boldsymbol{\pi}(\mathbf{k} - \mathbf{Q}) \\ \boldsymbol{\pi}(\mathbf{k}) \\ \boldsymbol{\pi}(\mathbf{k} + \mathbf{Q}) \end{pmatrix} \quad (\text{D.36})$$

by also renaming the remaining sums over \mathbf{q}' to sums over \mathbf{k} . In the first case, when χ_{dip}^{-1} is the diagonal demagnetization tensor, we obtain

$$\mathcal{M}_{\text{dem}}(\mathbf{0}) = \mu_0 M^2 \begin{pmatrix} \frac{N_x + N_y}{2} \begin{pmatrix} 1 & -i \cos \theta \\ i \cos \theta & \cos^2 \theta \end{pmatrix} & 0 & \frac{N_x - N_y}{2} \begin{pmatrix} -1 & -i \cos \theta \\ -i \cos \theta & \cos^2 \theta \end{pmatrix} \\ 0 & N_z \begin{pmatrix} 0 & 0 \\ 0 & \sin^2 \theta \end{pmatrix} & 0 \\ \frac{N_x - N_y}{2} \begin{pmatrix} -1 & i \cos \theta \\ i \cos \theta & \cos^2 \theta \end{pmatrix} & 0 & \frac{N_x + N_y}{2} \begin{pmatrix} 1 & i \cos \theta \\ -i \cos \theta & \cos^2 \theta \end{pmatrix} \end{pmatrix} \quad (\text{D.37})$$

and for the second case, using the abbreviations $\hat{k}^z = \mathbf{k} \cdot \hat{\mathbf{e}}_z$ and $\hat{k}^\pm = \frac{1}{\sqrt{2}} \mathbf{k} \cdot (\hat{\mathbf{e}}^x \pm i \hat{\mathbf{e}}^y)$, we get

$$\mathcal{M}_{\text{dip}}(\hat{\mathbf{k}}) = \mu_0 M^2 \begin{pmatrix} \frac{\hat{k}^- \hat{k}^+}{2} \begin{pmatrix} 1 & -i \cos \theta \\ i \cos \theta & \cos^2 \theta \end{pmatrix} & \frac{\hat{k}^- \hat{k}^z}{\sqrt{2}} \begin{pmatrix} 0 & i \sin \theta \\ 0 & -\cos \theta \sin \theta \end{pmatrix} & \frac{\hat{k}^- \hat{k}^-}{2} \begin{pmatrix} -1 & -i \cos \theta \\ -i \cos \theta & \cos^2 \theta \end{pmatrix} \\ \frac{\hat{k}^z \hat{k}^+}{\sqrt{2}} \begin{pmatrix} 0 & 0 \\ -i \sin \theta & -\cos \theta \sin \theta \end{pmatrix} & \hat{k}^z \hat{k}^z \begin{pmatrix} 0 & 0 \\ 0 & \sin^2 \theta \end{pmatrix} & \frac{\hat{k}^z \hat{k}^+}{\sqrt{2}} \begin{pmatrix} 0 & 0 \\ i \sin \theta & -\cos \theta \sin \theta \end{pmatrix} \\ \frac{\hat{k}^+ \hat{k}^+}{2} \begin{pmatrix} -1 & i \cos \theta \\ i \cos \theta & \cos^2 \theta \end{pmatrix} & \frac{\hat{k}^+ \hat{k}^z}{\sqrt{2}} \begin{pmatrix} 0 & -i \sin \theta \\ 0 & -\cos \theta \sin \theta \end{pmatrix} & \frac{\hat{k}^+ \hat{k}^-}{2} \begin{pmatrix} 1 & i \cos \theta \\ -i \cos \theta & \cos^2 \theta \end{pmatrix} \end{pmatrix} \quad (\text{D.38})$$

Note that the sign changes between the upper left and lower right block are not obvious in when only collecting term for $\mathbf{k} = 0$ since the relation between \mathbf{k} and $-\mathbf{k}$ is lost. This structure, however, becomes clear when evaluating case 2. To derive the representations (8.34) and (8.36) of the main text, one first rewrites the individual block matrices in terms of Pauli matrices. A followed rotation from the $\boldsymbol{\pi}$ to the $\boldsymbol{\psi}$ fields via (8.25), which ultimately permutes the Pauli matrices and provides an effective conversion of $\mu_0 M^2 \rightarrow \mathcal{E}_0 \chi_{\text{con}}^{\text{int}}/2$, gives the desired result.



BIBLIOGRAPHY

- [1] H. J. Williams, J. H. Wernick, R. C. Sherwood, and G. K. Wertheim, “Magnetic Properties of the Monosilicides of Some 3d Transition Elements”, *Journal of Applied Physics* **37**, 1256 (1966).
- [2] D. Shinoda and S. Asanabe, “Magnetic Properties of Silicides of Iron Group Transition Elements”, *Journal of the Physical Society of Japan* **21**, 555 (1966).
- [3] Y. Ishikawa, K. Tajima, D. Bloch, and M. Roth, “Helical Spin Structure in Manganese Silicide MnSi”, *Solid State Communications* **19**, 525 (1976).
- [4] Y. Ishikawa, T. Komatsubara, and D. Bloch, “Magnetic phase diagram of MnSi”, *Physica B C* **86-88**, 401 (1977).
- [5] Y. Ishikawa, G. Shirane, J. A. Tarvin, and M. Kohgi, “Magnetic excitations in the weak itinerant ferromagnet MnSi”, *Physical Review B* **16**, 4956 (1977).
- [6] C. Pfleiderer, “Non-Fermi liquid puzzle of MnSi at high pressure”, *Physica B-Condensed Matter* **328**, 100 (2003).
- [7] S. Mühlbauer *et al.*, “Skyrmion Lattice in a Chiral Magnet”, *Science* **323**, 915 (2009).
- [8] T. H. R. Skyrme, “A Non-Linear Field Theory”, *Proceedings of the Royal Society A: Mathematical, Physical and Engineering Sciences* **260**, 127 (1961).
- [9] A. Bogdanov and D. A. Yablonskii, “Thermodynamically stable "vortices" in magnetically ordered crystals. The mixed state of magnets”, *Sov. Phys. JETP* **68**, 1 (1989).
- [10] S. S. P. Parkin, M. Hayashi, and L. Thomas, “Magnetic Domain-Wall Racetrack Memory”, *Science* **320**, 190 (2008).
- [11] F. Jonietz *et al.*, “Spin Transfer Torques in MnSi at Ultralow Current Densities”, *Science* **330**, 1648 (2010).

Bibliography

- [12] S. Neusser, “Magnonics: Spin Waves on the Nanoscale”, *Advanced Materials* **21**, 2927 (2009).
- [13] V. V. Kruglyak, S. O. Demokritov, and D. Grundler, “Magnonics”, *Journal of Physics D: Applied Physics* **43**, 264001 (2010).
- [14] W. T. Kelvin, *Baltimore Lectures on Molecular Dynamics and the Wave Theory of Light* (Cambridge University Press, Cambridge, 2010).
- [15] “Bläck Fööss band logo”, <http://www.blaeckfoeoess.de>, with kind permission of the Bläck Fööss band.
- [16] B. Borén, “Röntgenuntersuchung der Legierungen von Silicium mit Chrom, Mangan, Kobalt und Nickel”, *Arkiv för Kemi, Mineralogi och Geologi* **11A**, 1 (1933).
- [17] H. Effenberger and F. Pertlik, “Die Kristallstrukturen der Kupfer(II)-oxoselenite $\text{Cu}_2\text{O}(\text{SeO}_3)$ (kubisch und monoklin) und $\text{Cu}_4\text{O}(\text{SeO}_3)_3$ (monoklin und triklin)”, *Monatshefte für Chemie* **117**, 887 (1986).
- [18] N. Ashcroft and D. Mermin, *Solid State Physics* (Harcourt College Publishers, Orlando, 1976).
- [19] P. M. Chaikin and T. C. Lubensky, *Principles of condensed matter physics*, 3 ed. (Cambridge University Press, Cambridge, 2006).
- [20] T. Moriya, “Anisotropic Superexchange Interaction and Weak Ferromagnetism”, *Physical Review* **120**, 91 (1960).
- [21] A. Bauer *et al.*, “Quantum phase transitions in single-crystal $\text{Mn}_{1-x}\text{Fe}_x\text{Si}$ and $\text{Mn}_{1-x}\text{Co}_x\text{Si}$: Crystal growth, magnetization, ac susceptibility, and specific heat”, *Physical Review B* **82**, 064404 (2010).
- [22] M. Janoschek *et al.*, “Fluctuation-induced first-order phase transition in Dzyaloshinskii-Moriya helimagnets”, *Physical Review B* **87**, 134407 (2013).
- [23] A. Bauer, M. Garst, and C. Pfleiderer, “Specific Heat of the Skyrmion Lattice Phase and Field-Induced Tricritical Point in MnSi”, *Physical Review Letters* **110**, 177207 (2013).
- [24] J. Kindervater *et al.*, “Critical spin-flip scattering at the helimagnetic transition of MnSi”, *Physical Review B* **89**, 180408 (2014).
- [25] O. Nakanishi, A. Yanase, A. Hasegawa, and M. Kataoka, “The origin of the helical spin density wave in MnSi”, *Solid State Communications* **35**, 995 (1980).
- [26] P. Bak and M. H. Jensen, “Theory of helical magnetic structures and phase transitions in MnSi and FeGe”, *Journal of Physics C: Solid State Physics* **13**, L881 (1980).

- [27] H. Arnold *et al.*, in *International Tables for Crystallography*, 5th ed., edited by T. Hahn (Springer, Dordrecht, 2005), Vol. A.
- [28] L. Taillefer, G. G. Lonzarich, and P. Strange, “The band magnetism of MnSi”, *Journal of Magnetism and Magnetic Materials* **54-57**, 957 (1986).
- [29] C. Pfleiderer, G. J. McMullan, S. R. Julian, and G. G. Lonzarich, “Magnetic quantum phase transition in MnSi under hydrostatic pressure”, *Physical Review B (Condensed Matter)* **55**, 8330 (1997).
- [30] C. Pfleiderer, S. R. Julian, and G. Lonzarich, “Non-Fermi-liquid nature of the normal state of itinerant-electron ferromagnets”, *Nature* **414**, 427 (2001).
- [31] N. Doiron-Leyraud *et al.*, “Fermi-liquid breakdown in the paramagnetic phase of a pure metal”, *Nature* **425**, 595 (2003).
- [32] C. Pfleiderer *et al.*, “Partial order in the non-Fermi-liquid phase of MnSi”, *Nature* **427**, 227 (2004).
- [33] C. Pfleiderer *et al.*, “Non-Fermi liquid metal without quantum criticality”, *Science* **316**, 1871 (2007).
- [34] M. L. Plumer and M. B. Walker, “Wavevector and Spin Reorientation in MnSi”, *Journal of Physics C: Solid State Physics* **14**, 4689 (1981).
- [35] M. Tanaka, H. Takayoshi, M. Ishida, and Y. Endoh, “Crystal Chirality and Helicity of the Helical Spin Density Wave in MnSi. I. Convergent-Beam Electron Diffraction”, *Journal of the Physical Society of Japan* **54**, 2970 (2013).
- [36] M. Ishida *et al.*, “Crystal Chirality and Helicity of the Helical Spin Density Wave in MnSi. II. Polarized Neutron Diffraction”, *Journal of the Physical Society of Japan* **54**, 2975 (2013).
- [37] T. Schwarze *et al.*, “Universal helimagnon and skyrmion excitations in metallic, semiconducting and insulating chiral magnets.”, *Nature Materials* **14**, 478 (2015).
- [38] N. Manyala *et al.*, “Large anomalous Hall effect in a silicon-based magnetic semiconductor”, *Nature* **3**, 255 (2004).
- [39] D. Morikawa *et al.*, “Crystal chirality and skyrmion helicity in MnSi and (Fe,Co)Si as determined by transmission electron microscopy”, *Physical Review B* **88**, 024408 (2013).
- [40] S. V. Grigoriev *et al.*, “Principal interactions in the magnetic system $\text{Fe}_{1-x}\text{Co}_x\text{Si}$: Magnetic structure and critical temperature by neutron diffraction and SQUID measurements”, *Physical Review B* **76**, 092407 (2007).

Bibliography

- [41] S. A. Siegfried *et al.*, “Controlling the Dzyaloshinskii-Moriya interaction to alter the chiral link between structure and magnetism for $\text{Fe}_{1-x}\text{Co}_x\text{Si}$ ”, *Physical Review B* **91**, 184406 (2015).
- [42] J. Beille, J. Voiron, and M. Roth, “Long period helimagnetism in the cubic B20 $\text{Fe}_x\text{Co}_{1-x}\text{Si}$ and $\text{Co}_x\text{Mn}_{1-x}\text{Si}$ alloys”, *Solid State Communications* **47**, 399 (1983).
- [43] J. Beille *et al.*, “Helimagnetic structure of the $\text{Fe}_x\text{Co}_{1-x}\text{Si}$ alloys”, *Journal of Physics F: Metal Physics* **11**, 2153 (2000).
- [44] W. Münzer *et al.*, “Skyrmion lattice in the doped semiconductor $\text{Fe}_{1-x}\text{Co}_x\text{Si}$ ”, *Physical Review B* **81**, 041203 (2010).
- [45] K. Kohn, “A New Ferrimagnet Cu_2SeO_4 ”, *Journal of the Physical Society of Japan* **42**, 2065 (1977).
- [46] T. Adams *et al.*, “Long-Wavelength Helimagnetic Order and Skyrmion Lattice Phase in Cu_2OSeO_3 ”, *Physical Review Letters* **108**, 237204 (2012).
- [47] S. Seki, X. Z. Yu, S. Ishiwata, and Y. Tokura, “Observation of Skyrmions in a Multiferroic Material”, *Science* **336**, 198 (2012).
- [48] S. Seki, S. Ishiwata, and Y. Tokura, “Magnetoelectric nature of skyrmions in a chiral magnetic insulator Cu_2OSeO_3 ”, *Physical Review B* **86**, 060403 (2012).
- [49] W. Eerenstein, N. D. Mathur, and J. F. Scott, “Multiferroic and magnetoelectric materials”, *Nature* **442**, 759 (2006).
- [50] E. Ruff *et al.*, “Magnetoelectric effects in the skyrmion host material Cu_2OSeO_3 ”, *Scientific reports* **5**, 15025 (2015).
- [51] Y.-H. Liu, Y.-Q. Li, and J. H. Han, “Skyrmion dynamics in multiferroic insulators”, *Physical Review B* **87**, 100402 (2013).
- [52] A. Bauer “Private Communication”, (unpublished).
- [53] M. Richardson *et al.*, “Crystal Structure Refinements of the B20 and Monoclinic (CoGe-type) Polymorphs of FeGe”, *Acta Chemica Scandinavica* **21**, 753 (1967).
- [54] B. Lebech, J. Bernhard, and T. Freltoft, “Magnetic-Structures of Cubic FeGe Studied by Small-Angle Neutron-Scattering”, *Journal of Physics: Condensed Matter* **1**, 6105 (1989).
- [55] H. Wilhelm *et al.*, “Confinement of chiral magnetic modulations in the precursor region of FeGe”, *Journal of Physics: Condensed Matter* **24**, 294204 (2012).

- [56] I. Stasinopoulos “Private Communication”, (unpublished).
- [57] X. Z. Yu *et al.*, “Near room-temperature formation of a skyrmion crystal in thin-films of the helimagnet FeGe”, *Nature Materials* **10**, 106 (2010).
- [58] N. Kanazawa *et al.*, “Large Topological Hall Effect in a Short-Period Helimagnet MnGe”, *Physical Review Letters* **106**, 156603 (2011).
- [59] O. Meshcheriakova, Ph.D. thesis, University of Mainz, Mainz, 2015.
- [60] S. Heinze *et al.*, “Spontaneous atomic-scale magnetic skyrmion lattice in two dimensions”, *Nature Physics* **7**, 713 (2011).
- [61] S. Seki and M. Mochizuki, *Skyrmions in Magnetic Materials* (Springer, Cham, 2016).
- [62] Y. Tokunaga *et al.*, “A new class of chiral materials hosting magnetic skyrmions beyond room temperature”, *Nature Communications* **6**, 7638 (2015).
- [63] T. H. R. Skyrme, “A Non-Linear Theory of Strong Interactions”, *Proceedings of the Royal Society A: Mathematical, Physical and Engineering Sciences* **247**, 260 (1958).
- [64] T. H. R. Skyrme, “A Unified Model of K- and π - mesons”, *Proceedings of the Royal Society of London. Series A* **252**, 236 (1959).
- [65] T. H. R. Skyrme, “Particle States of a Quantized Meson Field”, *Proceedings of the Royal Society A: Mathematical, Physical and Engineering Sciences* **262**, 237 (1961).
- [66] J. K. Perring and T. H. R. Skyrme, “A model unified field equation”, *Nuclear Physics* **31**, 550 (1962).
- [67] T. H. R. Skyrme, “A unified field theory of mesons and baryons”, *Nuclear Physics* **31**, 556 (1962).
- [68] A. Altland and B. Simons, *Condensed Matter Field Theory*, 2 ed. (Cambridge University Press, Cambridge, 2010).
- [69] N. Manton and P. M. Sutcliffe, *Topological Solitons* (Cambridge University Press, Cambridge, 2004).
- [70] M. Nakahara, *Geometry, Topology and Physics*, 2 ed. (Institute of Physics Publishing, Bristol, 2003).
- [71] G. E. Bredon, *Topology and Geometry* (Springer, New York, 1993).
- [72] A. Bogdanov and A. Hubert, “Thermodynamically stable magnetic vortex states in magnetic crystals”, *Journal of Magnetism and Magnetic Materials* **138**, 255 (1994).

Bibliography

- [73] A. Bogdanov, “New localized solutions of the nonlinear field equations”, *Sov. Phys. JETP* **62**, 247 (1995).
- [74] T. Adams *et al.*, “Long-Range Crystalline Nature of the Skyrmion Lattice in MnSi.”, *Physical Review Letters* **107**, 217206 (2011).
- [75] K. Everschor-Sitte, M. Garst, R. A. Duine, and A. Rosch, “Current-induced rotational torques in the skyrmion lattice phase of chiral magnets”, *Physical Review B* **84**, 064401 (2011).
- [76] A. Fert, V. Cros, and J. Sampaio, “Skyrmions on the track”, *Nature Nanotechnology* **8**, 152 (2013).
- [77] J. Sampaio *et al.*, “Nucleation, stability and current-induced motion of isolated magnetic skyrmions in nanostructures”, *Nature Nanotechnology* **8**, 839 (2013).
- [78] J. W. Negele and H. Orland, *Quantum many-particle systems, Advanced book classics* (Westview, Boulder, CO, 1988).
- [79] S. Blundell, *Magnetism in Condensed Matter* (Oxford University Press, Oxford, 2003).
- [80] K. Everschor-Sitte, Ph.D. thesis, University of Cologne, Cologne, 2012.
- [81] L. Heinen, Master’s thesis, University of Cologne, Cologne, 2015.
- [82] C. Kittel, “Interpretation of Anomalous Larmor Frequencies in Ferromagnetic Resonance Experiment”, *Physical Review* **71**, 270 (1947).
- [83] W. F. Brown, *Magnetostatic Principles in Ferromagnetism, Selected topics in solid state physics* (North-Holland Pub. Co., Amsterdam, 1962).
- [84] P. A. M. Dirac, “Quantised Singularities in the Electromagnetic Field”, *Proceedings of the Royal Society A: Mathematical, Physical and Engineering Sciences* **133**, 60 (1931).
- [85] C. Castelnovo, R. Moessner, and S. L. Sondhi, “Magnetic monopoles in spin ice”, *Nature* **451**, 42 (2008).
- [86] D. J. P. Morris *et al.*, “Dirac Strings and Magnetic Monopoles in the Spin Ice $\text{Dy}_2\text{Ti}_2\text{O}_7$ ”, *Science* **326**, 411 (2009).
- [87] P. Milde *et al.*, “Unwinding of a skyrmion lattice by magnetic monopoles”, *Science* **340**, 1076 (2013).
- [88] N. S. Akulov, “Über ein Gesetz, das verschiedene Eigenschaften ferromagnetischer Kristalle miteinander verknüpft”, *Zeitschrift für Physik* **59**, 254 (1930).

- [89] A. G. Gurevich and G. A. Melkov, *Magnetization Oscillations and Waves* (CRC Press, Boca Raton, 1996).
- [90] R. Becker and W. Döring, *Ferromagnetismus* (Springer, Berlin, 1939).
- [91] M. Garst “Private Communication”, (unpublished).
- [92] A. Bauer *et al.*, “Symmetry breaking, slow relaxation dynamics, and topological defects at the field-induced helix reorientation in MnSi”, *Physical Review B* **95**, 024429 (2017).
- [93] J. Waizner, Master’s thesis, University of Cologne, Cologne, 2013.
- [94] M. Kugler *et al.*, “Band Structure of Helimagnons in MnSi Resolved by Inelastic Neutron Scattering”, *Physical Review Letters* **115**, 097203 (2015).
- [95] S. Buhrandt and L. Fritz, “Skyrmion lattice phase in three-dimensional chiral magnets from Monte Carlo simulations”, *Physical Review B* **88**, 195137 (2013).
- [96] D. D. Stancil and A. Prabhakar, *Spin Waves, Theory and Applications* (Springer US, Boston, MA, 2009).
- [97] F. Bloch, “Zur Theorie des Ferromagnetismus”, *Zeitschrift für Physik* **61**, 206 (1930).
- [98] T. Holstein and H. Primakoff, “Field Dependence of the Intrinsic Domain Magnetization of a Ferromagnet”, *Physical Review* **58**, 1098 (1940).
- [99] F. J. Dyson, “General Theory of Spin-Wave Interactions”, *Physical Review* **102**, 1217 (1956).
- [100] J. H. E. Griffiths, “Anomalous High-frequency Resistance of Ferromagnetic Metals”, *Nature* **158**, 670 (1946).
- [101] P. A. Fleury, S. P. S. Porto, L. E. Cheesman, and H. J. Guggenheim, “Light Scattering by Spin Waves in FeF₂”, *Physical Review Letters* **17**, 84 (1966).
- [102] L. D. Landau and E. Lifshitz, “On the theory of the dispersion of magnetic permeability in ferromagnetic bodies”, *Phys. Z. Sowjet.* **8**, 153 (1935).
- [103] T. L. Gilbert, “A Lagrangian formulation of gyromagnetic equation of the magnetization field”, *Physical Review* **100**, 1243 (1955).
- [104] C. Kittel, “On the Theory of Ferromagnetic Resonance Absorption”, *Physical Review* **73**, 155 (1948).
- [105] J. R. Macdonald, “Ferromagnetic Resonance and the Internal Field in Ferromagnetic Materials”, *Proceedings of the Physical Society. Section A* **64**, 968 (1951).

Bibliography

- [106] I. Stasinopoulos *et al.*, “Low spin wave damping in the insulating chiral magnet Cu_2OSeO_3 ”, *Applied Physics Letters* **111**, 032408 (2017).
- [107] C. Kittel, *Einführung in die Festkörperphysik*, 8 ed. (R. OldenbourgVerlag, München, 1989).
- [108] A. Clogston, “Ferromagnetic resonance line width in insulating materials”, *Journal of Physics and Chemistry of Solids* **1**, 129 (1956).
- [109] C. Herring and C. Kittel, “On the Theory of Spin Waves in Ferromagnetic Media”, *Physical Review* **81**, 869 (1951).
- [110] A. B. Harris, “Effect of Dipolar Interactions on the Spin-Wave Spectrum of a Cubic Antiferromagnet”, *Physical Review* **143**, 353 (1966).
- [111] J. H. Van Vleck, “The Influence of Dipole-Dipole Coupling on the Specific Heat and Susceptibility of a Paramagnetic Salt”, *The Journal of Chemical Physics* **5**, 320 (1937).
- [112] R. Loudon and P. Pincus, “Effect of Dipolar Fields on the Antiferromagnetic Spin-Wave Spectrum”, *Physical Review* **132**, 673 (1963).
- [113] S. O. Demokritov, B. Hillebrands, and A. N. Slavin, “Brillouin light scattering studies of confined spin waves: linear and nonlinear confinement”, *Physics Reports-Review Section of Physics Letters* **348**, 441 (2001).
- [114] J. R. Eshbach and R. W. Damon, “Surface Magnetostatic Modes and Surface Spin Waves”, *Physical Review* **118**, 1208 (1960).
- [115] R. W. Damon and J. R. Eshbach, “Magnetostatic modes of a ferromagnet slab”, *Journal of Physics and Chemistry of Solids* **19**, 308 (1961).
- [116] R. N. Simons, *Coplanar Waveguide Circuits Components and Systems* (Wiley-Interscience, New York, 2001).
- [117] G. Shirane, S. M. Shapiro, and J. M. Tranquada, *Neutron Scattering with a Triple-Axis Spectrometer* (Cambridge University Press, Cambridge, 2004).
- [118] M. Janoschek, Ph.D. thesis, Technische Universität München, München, 2008.
- [119] B. N. Brockhouse, in *Inelastic Scattering of Neutrons in Solids and Liquids* (Vienna, 1961), p. 113.
- [120] M. Janoschek *et al.*, “Helimagnon bands as universal excitations of chiral magnets”, *Physical Review B* **81**, 214436 (2010).
- [121] M. Kataoka, “Spin Waves in Systems with Long Period Helical Spin Density Waves Due to the Antisymmetric and Symmetric Exchange Interactions”, *Journal of the Physical Society of Japan* **56**, 3635 (1987).

- [122] Y. Onose *et al.*, “Observation of Magnetic Excitations of Skyrmion Crystal in a Helimagnetic Insulator Cu_2OSeO_3 ”, *Physical Review Letters* **109**, 037603 (2012).
- [123] M. Date, K. Okuda, and K. Kadowaki, “Electron Spin Resonance in the Itinerant-Electron Helical Magnet MnSi ”, *Journal of the Physical Society of Japan* **42**, 1555 (1977).
- [124] J. D. Koralek *et al.*, “Observation of Coherent Helimagnons and Gilbert Damping in an Itinerant Magnet”, *Physical Review Letters* **109**, 247204 (2012).
- [125] I. Stasinopoulos *et al.*, “Linearly polarized GHz magnetization dynamics of spin helix modes in the ferrimagnetic insulator Cu_2OSeO_3 ”, *Scientific reports* **7**, 153 (2017).
- [126] A. J. Sievers and M. Tinkham, “Far Infrared Antiferromagnetic Resonance in MnO and NiO ”, *Physical Review* **129**, 1566 (1963).
- [127] M. Gell-Mann and M. Lévy, “The axial vector current in beta decay”, *Il Nuovo Cimento* **16**, 705 (1960).
- [128] J. Jost, *Geometry and Physics* (Springer, Berlin, Heidelberg, 2009).
- [129] J. Avron and B. Simon, “The asymptotics of the gap in the Mathieu equation”, *Annals of Physics* **134**, 76 (1981).
- [130] B. R. Holstein, *Topics in advanced quantum mechanics* (Addison-Wesley Publishing Company, Advanced Book Program, Redwood City, CA, Redwood City, 1992).
- [131] G. Auletta, M. Fortunato, and G. Parisi, *Quantum Mechanics* (Cambridge University Press, Cambridge, 2009).
- [132] D. Belitz, T. Kirkpatrick, and A. Rosch, “Theory of helimagnons in itinerant quantum systems”, *Physical Review B* **73**, 054431 (2006).
- [133] T. Wolfram and R. E. De Wames, “Magnetoexchange Branches and Spin-Wave Resonance in Conducting and Insulating Films: Perpendicular Resonance”, *Physical Review B* **4**, 3125 (1971).
- [134] T. Weber *et al.* “Field-dependence of the helimagnon dispersion in the chiral magnet MnSi ”, (unpublished).
- [135] G. S. Tucker *et al.*, “Spin excitations in the skyrmion host Cu_2OSeO_3 ”, *Physical Review B* **93**, 054401 (2016).
- [136] Y. Okamura *et al.*, “Microwave magnetoelectric effect via skyrmion resonance modes in a helimagnetic multiferroic”, *Nature Communications* **4**, 2391 (2013).

Bibliography

- [137] M. Mochizuki, “Spin-Wave Modes and Their Intense Excitation Effects in Skyrmion Crystals”, *Physical Review Letters* **108**, 017601 (2012).
- [138] O. Petrova and O. Tchernyshyov, “Spin waves in a skyrmion crystal”, *Physical Review B* **84**, 214433 (2011).
- [139] R. Paschotta, *Field Guide to Optical Fiber Technology* (Spie Press, Bellingham, Washington, USA, 2010).
- [140] M. Janoschek *et al.*, “Helimagnons in the skyrmion lattice of MnSi”, *Journal of Physics: Conference Series* **200**, 032026 (2010).
- [141] S. Zhang and S. S. L. Zhang, “Generalization of the Landau-Lifshitz-Gilbert Equation for Conducting Ferromagnets”, *Physical Review Letters* **102**, 086601 (2009).
- [142] A. Neubauer *et al.*, “Topological Hall effect in the A phase of MnSi”, *Physical Review Letters* **102**, 186602 (2009).
- [143] M. Lee *et al.*, “Unusual Hall Effect Anomaly in MnSi under Pressure”, *Physical Review Letters* **102**, 186601 (2009).
- [144] T. Schulz *et al.*, “Emergent electrodynamics of skyrmions in a chiral magnet”, *Nature Physics* **8**, 301 (2012).
- [145] C. Schütte and M. Garst, “Magnon-skyrmion scattering in chiral magnets”, *Physical Review B* **90**, 094423 (2014).
- [146] S. Schroeter and M. Garst, “Scattering of high-energy magnons off a magnetic skyrmion”, *Low Temperature Physics* **41**, 817 (2015).
- [147] M. Z. Hasan and C. L. Kane, “Colloquium: Topological insulators”, *Reviews of Modern Physics* **82**, 3045 (2010).
- [148] B. A. Bernevig and T. L. Hughes, *Topological Insulators and Topological Superconductors* (Princeton University Press, Woodstock, 2013).
- [149] L. Landau, “Diamagnetismus der Metalle”, *Zeitschrift für Physik* **64**, 629 (1930).
- [150] D. J. Thouless, M. Kohmoto, M. P. Nightingale, and M. den Nijs, “Quantized Hall Conductance in a Two-Dimensional Periodic Potential”, *Physical Review Letters* **49**, 405 (1982).
- [151] M. V. Berry, “Quantal Phase-Factors Accompanying Adiabatic Changes”, *Proceedings of the Royal Society of London Series a-Mathematical and Physical Sciences* **392**, 45 (1984).
- [152] R. Bamler, Ph.D. thesis, University of Cologne, Cologne, 2016.

- [153] B. Simon, “Holonomy, the Quantum Adiabatic Theorem, and Berry’s Phase”, *Physical Review Letters* **51**, 2167 (1983).
- [154] A. Roldán-Molina, A. S. Nunez, and J. Fernández-Rossier, “Topological spin waves in the atomic-scale magnetic skyrmion crystal”, *New Journal of Physics* **18**, 045015 (2016).
- [155] K. Hamamoto, M. Ezawa, and N. Nagaosa, “Quantized topological Hall effect in skyrmion crystal”, *Physical Review B* **92**, 115417 (2015).
- [156] M. C. Gutzwiller, “Energy Spectrum According to Classical Mechanics”, *Journal of Mathematical Physics* **11**, 1791 (1970).
- [157] M. C. Gutzwiller, “Periodic Orbits and Classical Quantization Conditions”, *Journal of Mathematical Physics* **12**, 343 (1971).
- [158] M. Mochizuki, “Microwave Magnetochiral Effect in Cu_2OSeO_3 ”, *Physical Review Letters* **114**, 197203 (2015).

LIST OF FIGURES

1.1.	<i>Blück Fööss</i> logo as an illustration of chirality	5
1.2.	Typical magnetic phase diagram of chiral magnets	7
1.3.	Magnetically ordered phases in chiral magnets.	7
1.4.	B20 crystal structure and magnetization measurements of MnSi.	9
1.5.	Effects of doping and temperature on $\text{Fe}_{1-x}\text{Mn}_x\text{Si}$ and $\text{Fe}_{1-x}\text{Co}_x\text{Si}$	10
1.6.	Crystal structures and chiralities of B20-alloys	11
1.7.	Crystal structure and electric polarization of Cu_2OSeO_3	12
2.1.	Skyrmion - stereographical projection	19
2.2.	Structure factor of the helical and skyrmion lattice phase	21
3.1.	First and second order phase transitions	25
3.2.	Illustration of the demagnetization field	29
3.3.	Three examples for different demagnetization factors	30
3.4.	Special high symmetry directions	33
3.5.	Tripod of Q-vectors	37
3.6.	Theoretical phase diagrams including fluctuations	38
4.1.	Precession of a magnetization \mathbf{M} around a static magnetic field \mathbf{H}^{eff}	44
4.2.	Examples of Kittel resonances	47
4.3.	Angle definition for cubic anisotropies	49
4.4.	Influence of anisotropies on the Kittel mode	50
4.5.	Ellipse	51
4.6.	Dispersion relations of magnetic chains	52
4.7.	Volume and surface modes of magnetic slab	55
5.1.	Coplanar waveguides	58
5.2.	Elastic and inelastic neutron scattering	60
5.3.	Satellites around nuclear Bragg peak	60
6.1.	Reciprocal helical and skyrmion lattice	65
6.2.	Remaining Fourier components after symmetries	69
6.3.	Eigenvalues of $(\mathbf{m}^{\text{mf}} \times)$	75
7.1.	Resonances in conical phase	80

List of Figures

7.2. Illustration of the excitations in the conical phase	82
7.3. Weight distribution in the conical phase for a “standing” disc. . . .	84
7.4. Spin resonance data and comparison with theory	85
7.5. Ellipticity and spectral weights in conical phase.	87
8.1. Parameterization of magnetization $\mathbf{M} = M \hat{\mathbf{n}}$	90
9.1. Helimagnon spectrum for longitudinal momenta	100
9.2. Helimagnon spectrum for large perpendicular momenta	101
9.3. Magnon spectra for longitudinal at various perpendicular momenta	102
9.4. Helimagnon spectra in both directions	103
9.5. Spectral weight distribution for inelastic neutron scattering	105
9.6. Field dependence of the helimagnon spectrum	107
10.1. Grayscale plots of absorbed microwave intensity	109
10.2. Magnetic resonances of Schwarze et al.	110
10.3. Inelastic neutron scattering data of Kugler et al.	111
10.4. Comparison between helimagnon theory and experiment	112
10.5. Experimental data to field dependence of the helimagnon spectrum	114
11.1. Potential resonance frequencies and weights of the skyrmion lattice	118
11.2. Mode visualization in skyrmion crystal	119
11.3. Shape and field dependence of the skyrmionic ellipticity	121
12.1. Directions of \mathbf{k}_{\parallel} and \mathbf{k}_{\perp} with respect to the skyrmion lattice . . .	123
12.2. Magnon spectra in the skyrmion phase within the 1.BZ	124
12.3. 3D representation of the magnon spectrum in the skyrmion phase .	125
12.4. The first 16 skyrmion modes	128
12.5. Node structure of the first 16 skyrmion modes	129
12.6. Skyrmion magnon spectrum evolution with increasing system size .	132
12.7. Skyrmion magnon spectrum for subspaces of the $(\mathbf{M}^{\text{mf}} \times)$ matrix .	133
12.8. Perpendicular magnon spectrum of the skyrmion lattice.	135
12.9. Schematic view of the extended momentum space matrix structure .	137
12.10 Magnon spectra and weights in the skyrmion phase	139
12.11 Magnon spectrum in the skyrmion phase probed by inelastic neu- tron scattering	140
13.1. Absolute values and phase arguments of an eigenstate component .	145
13.2. Berry curvatures of the first fourteen bands	147
13.3. Berry curvatures of bands 15 and 16	148
13.4. Skyrmion magnon spectrum with corresponding Chern numbers . .	148
13.5. Spectrum and Chern numbers by Roldán-Molina et al.	149
13.6. Trajectories of an electron in the effective magnetic field of a skyrmion lattice.	152

————— LIST OF TABLES —————

- 1.1. Summary of material properties 14
- 5.1. Properties of the neutron 59
- 7.1. Sample data 79
- 7.2. Relationship between chirality, γ and the $\pm Q$ modes. 83
- 11.1. Relationship between chirality, γ and chiral magnetic resonances . 120
- 12.1. List of absolute values and motion of the change of $\delta \mathbf{M}_0(t)$ of the
first 16 modes 130

INDEX

- anisotropy constants, K , c_i , 32, 50
- Berry connection, 143
- Berry curvature, 143
- Berry phase, 142
- Bloch's theorem, 73
- Bogoliubov-deGennes equation, 95
- Bohr magneton, 43
- Chern number, 142
- chirality, 5
- coplanar waveguide, CPW, 50, 57, 103, 109
- Copper(II)-oxo-selenite, Cu_2OSeO_3 , 79
- Copper(II)-oxo-selenite, Cu_2OSeO_3 , 11, 50, 84, 113
- demagnetization factors, N_i , 29
- demagnetization field, 28
- dipolar interaction, 31, 90, 102
- Dzyaloshinskii-Moriya interaction, 6, 11, 34, 90, 149
- eccentricity, 51
- ellipticity, 50
- ferromagnetic resonance, 109, 117
- Fourier transformation, 24
- Γ -point, 69, 79, 117
- Ginzburg-Landau theory, 26, 34, 89
- gyromagnetic ratio, 43, 82
- Hall conductivity, 142
- Heisenberg exchange interaction, 6, 34, 51, 90
- Iron Cobalt Silicide, $\text{Fe}_{1-x}\text{Co}_x\text{Si}$, 79
- Iron Cobalt Silicide, $\text{Fe}_{1-x}\text{Co}_x\text{Si}$, 10
- Kittel formula, 46
- Landé factor, 43, 82
- Landau level, 142
- Landau-Lifshitz equation, 43, 64, 90
- Landau-Lifshitz-Gilbert equation, 44
- Larmor frequency, 27, 45
- linear dichroism, 87, 88
- Lorentz force, 141, 151
- magnetostatic approximation, 53
- magnons, 41
- Manganese Silicide, MnSi , 79
- Manganese Silicide, MnSi , 9
- Mathieu equation, 100
- mode behavior
 - conical phase, 82, 87
 - skyrmion phase, 119, 121, 128, 129
- neutrons
 - cold, 59, 110
 - thermal, 59
- permeability
 - relative μ_r , 24

Index

- vacuum μ_0 , 23, 28
- resonance frequency, 45
- scattering
 - cross section, 70, 104
 - SANS, 61
- σ model, 71, 89
 - non-linear, 89
- skyrmion, 15
 - Bloch-type, 19, 149
 - lattice, 8
 - Néel, 19, 149
- spectral weight, 70, 104
- spin stiffness, 90, 93
- spin-flip scattering, 106
- susceptibility
 - conical, 10, 79, 91, 165
 - internal conical, 10, 91
 - magnetic, 24, 45
- topological degree, 19
- topological Hall effect, 141
- tripple-axis spectrometer, 60, 110
- winding number, 19, 20
- Zeeman interaction, 26, 34, 48, 90

DANKSAGUNG

And every drinker every dancer
lifts a happy face to thank her
the fiddler fiddles something so sublime
All the women tear their blouses off
and the men they dance on the polka-dots
and it's partner found, it's partner lost
and it's hell to pay when the fiddler stops:
it's CLOSING TIME

Leonard Cohen – The Future (album)

Wie am Ende jeder schönen Zeit ist nun der Punkt gekommen Danke zu sagen, Danke an alle, die mir meine Zeit um und während der Dissertation so angenehm, erfahrungsreich und spannend gestaltet haben. Mein größter Dank gebührt meinem Betreuer PD Dr. Markus Garst, der, nicht nur mit seinem fachlichen Wissen, wesentlich zum Erfolg dieser Arbeit beitrug, sondern auch, durch seine lustige und gelassene Art, Motivation und Freude an Physik verbreitete. Besonders bedanken möchte ich mich außerdem bei Prof. Achim Rosch für seine unentwegte Unterstützung und beflügelnden Diskussionen, die immer wieder zu neuen und spannenden Ideen führten.

Weiterer Dank geht an meine Ko-Autoren, insbesondere Ioannis Stasinopoulos, für gute, einfache und enge Zusammenarbeit. Ohne die gute Kommunikation und die tollen Messdaten, von ebenso Maximilian Kugler und Tobias Weber, wäre auch diese Arbeit nur halb so gut.

Bei meinen Arbeitsgruppen- und Bürokollegen, von denen ich dank verschiedener Wechsel von Büroräumen glücklicherweise einige hatte, möchte ich mich für ein tolles Arbeitsklima bedanken. Es hat mir immer wieder Spaß mit euch gemacht, sowohl in der Physik als auch außerhalb. Alle namentlich zu nennen sprengt ein wenig den Rahmen, aber besonders möchte ich mich zumindest bei Lukas, Sarah, Maximilian, Robert, Finn und Sascha bedanken, die ich gerade in der Schlussphase des Schreibens jederzeit, selbst mit Kleinigkeiten, nerven konnte.

Zu guter Letzt möchte ich meiner Familie für ihre Unterstützung, Verständnis und Hilfe während der letzten Jahre danken.

ERKLÄRUNG

Ich versichere, dass ich die von mir vorgelegte Dissertation selbstständig angefertigt, die benutzten Quellen und Hilfsmittel vollständig angegeben und die Stellen der Arbeit – einschließlich Tabellen, Karten und Abbildungen –, die anderen Werken im Wortlaut oder dem Sinn nach entnommen sind, in jedem Einzelfall als Entlehnung kenntlich gemacht habe; dass diese Dissertation noch keiner anderen Fakultät oder Universität zur Prüfung vorgelegt hat; dass sie – abgesehen von unten angegebenen Teilpublikationen – noch nicht veröffentlicht worden ist sowie, dass ich eine solche Veröffentlichung vor Abschluss des Promotionsverfahrens nicht vornehmen werde. Die Bestimmungen der Promotionsordnung sind mir bekannt. die von mir vorgelegte Dissertation ist von PD Dr. Markus Garst betreut worden.

Köln, 6. Dezember 2017